

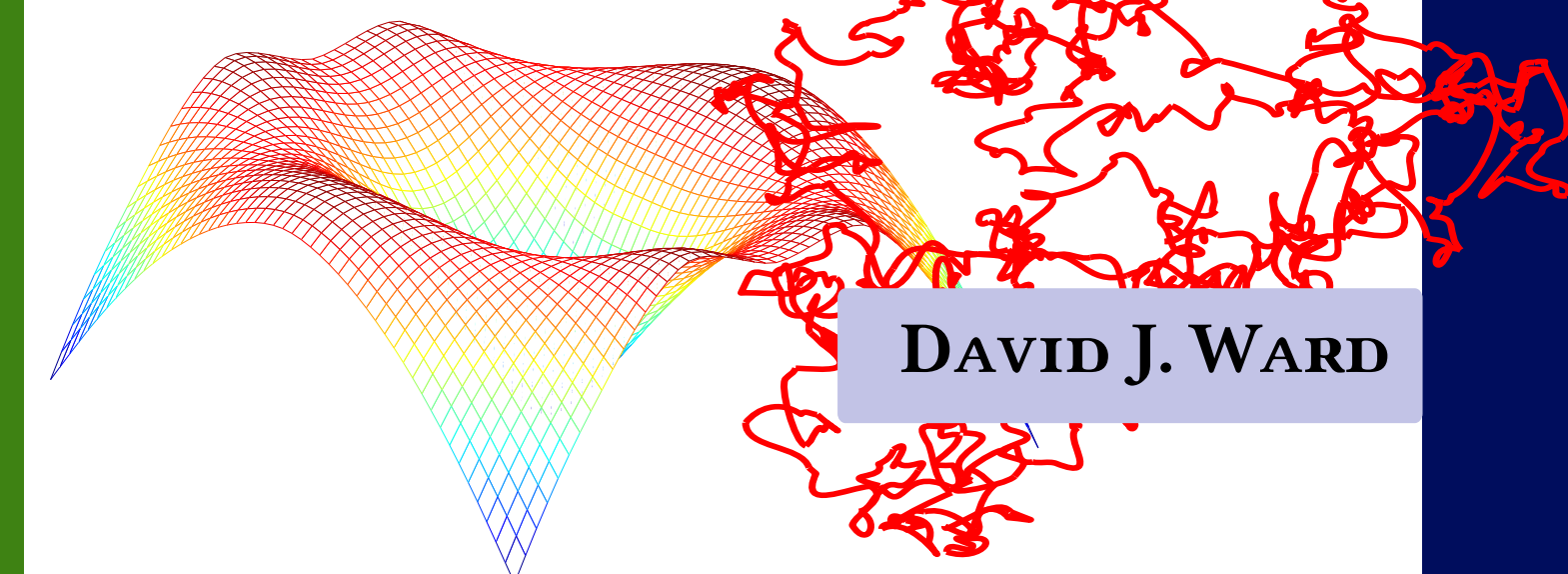
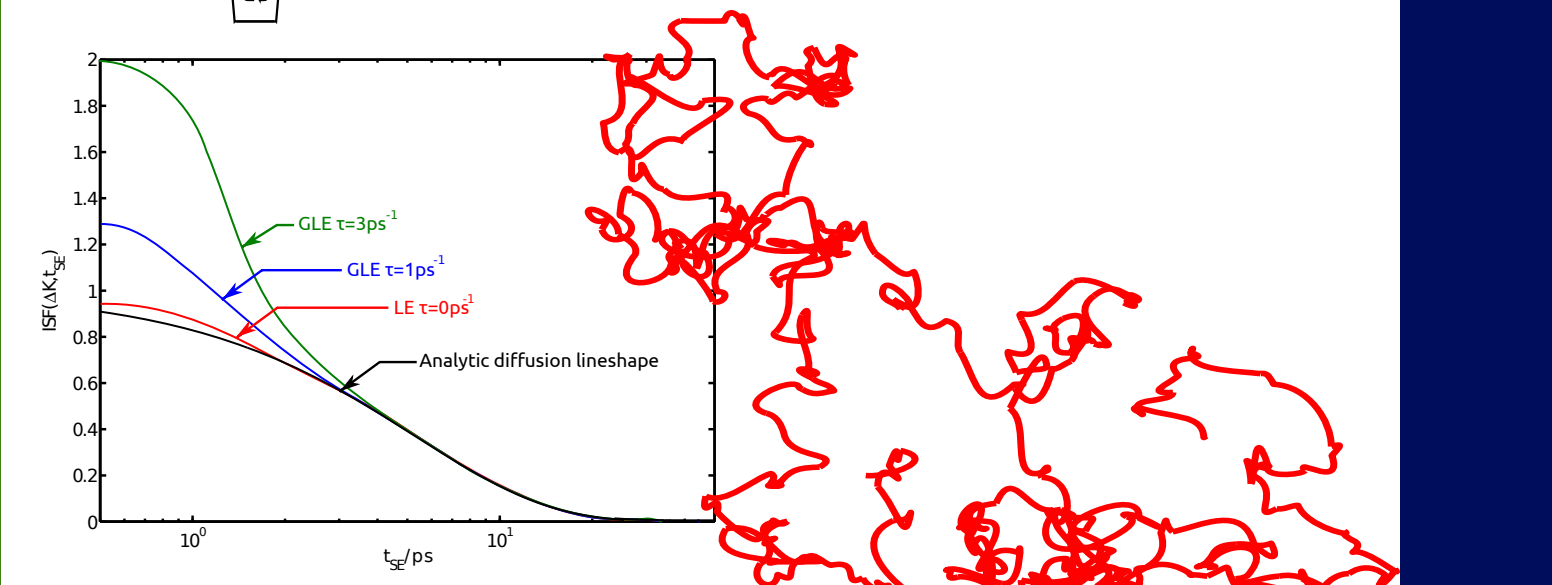
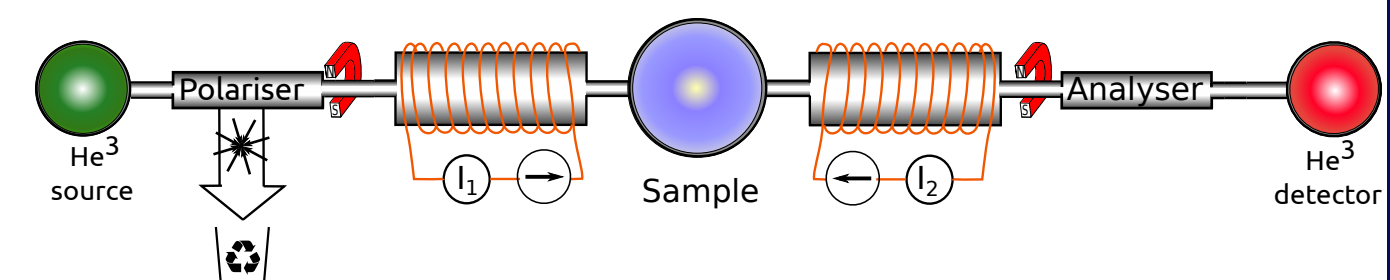
The technique of Helium spin-echo spectroscopy has been used to study the dynamics of individual atoms on pico-second time-scales and atomic length-scales. The thesis describes the modification and application of the technique, and the use of the Intermediate Scattering Function, $I(\Delta K, t)(ISF)$ to understand the range of motion from the very short times, where ballistic motion is expected, through the transition to diffusive motion, which occurs on a longer time scale. Chapter 1 introduces the experimental techniques used in the work and goes on to describe the principles of simulating surface dynamics using the generalised Langevin equation. Chapter 2 presents the dynamics of Xe on the Pt(111) surface. Experiment indicates a 2-D ideal gas-like motion and a previously unobserved jump diffusion process. The data is analysed using existing methods and it is shown that the two processes correspond to a transition between ballistic and diffusive motions. Attempts are made to explain the ballistic component through the energy landscape; however only qualitative agreement is achieved and the results indicate the need for a better calibration of the experiment, particularly at short time-scales. Chapter 3 presents improvements in measurement of the real and imaginary part of the intermediate scattering function, and the importance and implementation of a calibration procedure for the apparatus. Chapters 4 and 5 discuss experimental measurements, using the new calibration, applied to the alkali metals sodium and lithium on the Cu(111)surface, where similar phenomenology is observed as for Xe/Pt(111) in chapter 2. For the sodium experiments in chapter 4 the ISF has an asymmetric component in its imaginary part. Such a feature would normally indicate an inelastic process. Here we show the effect can be attributed to the form factor of the scattering. The dynamics of lithium are discussed in Chapter 5, and it is shown that the spectrum of excitations experienced by the lithium atoms is crucial to simulate the surface dynamics fully. A method of applying the Langevin equation with coloured noise is demonstrated to simulate the ISF over the complete timescale of motion. The work is the first complete attempt to describe the transition from ballistic to diffusive motion. In addition the work provides the first direct experimental measurement of the spectrum of excitations experienced by an adsorbate in thermal equilibrium. The thesis concludes with an outlook of future applications.



David J. Ward



Spin-echo lineshapes in helium atom scattering from adsorbates



DAVID J. WARD

A study of spin-echo lineshapes in helium atom scattering from adsorbates

A Thesis submitted to the University of Cambridge
for the degree of Doctor of Philosophy

David J. Ward
Darwin College
29th April 2013



Cavendish Laboratory
Surface Physics Group



**UNIVERSITY OF
CAMBRIDGE**

I dedicate this thesis to my parents, Stan and Barbara, whose support
has been unwavering throughout my life.

Declaration

This dissertation is the result of my own work and includes nothing which is the outcome of work done in collaboration except where specifically indicated in the text. It does not exceed the word limit prescribed by the Degree Committee for the Faculty of Physics and Chemistry and has not been submitted in whole or part for a degree, diploma or other qualification at this or any other university.

A handwritten signature in black ink, appearing to read "David Ward".

David James Ward

April 29, 2013

Abstract

The technique of Helium spin-echo spectroscopy has been used to study the dynamics of individual atoms on pico-second time-scales and atomic length-scales. The thesis describes the modification and application of the technique, and the use of the Intermediate Scattering Function, $I(\Delta K, t)$ (ISF) to understand the range of motion from the very short times, where ballistic motion is expected, through the transition to diffusive motion, which occurs on a longer time scale.

Chapter 1 introduces the experimental techniques used in the work and goes on to describe the principles of simulating surface dynamics using the generalised Langevin equation.

Chapter 2 presents the dynamics of Xe on the Pt(111) surface. Experiment indicates a 2-D ideal gas-like motion and a previously unobserved jump diffusion process. The data is analysed using existing methods and it is shown that the two processes correspond to a transition between ballistic and diffusive motions. Attempts are made to explain the ballistic component through the energy landscape; however only qualitative agreement is achieved and the results indicate the need for a better calibration of the experiment, particularly at short time-scales. Chapter 3 presents improvements in measurement of the real and imaginary part of the intermediate scattering function, and the importance and implementation of a calibration procedure for the apparatus.

Chapters 4 and 5 discuss experimental measurements, using the new calibration, applied to the alkali metals sodium and lithium on the Cu(111) surface, where similar phenomenology is observed as for Xe/Pt(111) in chapter 2. For the sodium experiments in chapter 4 the ISF has an asymmetric component in its imaginary part. Such a feature would normally

indicate an inelastic process. Here we show the effect can be attributed to the form factor of the scattering.

The dynamics of lithium are discussed in Chapter 5, and it is shown that the spectrum of excitations experienced by the lithium atoms is crucial to simulate the surface dynamics fully. A method of applying the Langevin equation with coloured noise is demonstrated to simulate the ISF over the complete timescale of motion. The work is the first complete attempt to describe the transition from ballistic to diffusive motion. In addition the work provides the first direct experimental measurement of the spectrum of excitations experienced by an adsorbate in thermal equilibrium.

The thesis concludes with an outlook of future applications.

Acknowledgements

I would like to show my appreciation for my supervisors Bill Alison and John Ellis and the benefit of their knowledge and advice throughout the course of my work. My experimental work was made possible due to the huge effort in designing and building the spin-echo apparatus, in particular I acknowledge Andrew Jardine, Gil Alexandrowicz, Peter Fouquet and Holly Hedgeland. Everett Lee taught me how to use the apparatus and the advice of Gil Alexandrowicz throughout my first and second years set the direction of the rest of the work. An implementation of Langevin molecular dynamics simulations used in chapters 2 and 4 were originally written in Fortran by Dr John Ellis. The application of coloured noise source and the Langevin simulations in chapter 5 were developed with the inspiration of Michele Parrinello and the GLE4MD project of Michele Ceriotti. The support and advice of the members and visitors of the surface physics group has been invaluable. Pepijn Kole, David Chisnall, Kane O'Donnell, Jianding Zhu, Barbara Lechner, Eliza and Andrew McIntosh, Paul Dastoor, Fay Tuddenham, Fulden Eratam, Rob Bell, James Lofthouse, Peter Townsend, Annie Weeks, Peter Wraight and Andrew Alderwick have made the Cavendish Laboratory a pleasurable place to work. I would like to acknowledge the significant contribution of my parents Barbara and Stan, my sister Jane and her husband Dominic, and my friends, Gareth, Kim and Chris who have provided a caring and supportive environment through the good and bad times. Finally Suzanne Paterson's love has given me the purpose, perspective and drive to complete this work.

Publications

Publications prepared using work performed during the course of research for this thesis include:

- *Probing molecule-surface interactions through ultra-fast adsorbate dynamics: propane/Pt(111)*, A. P. Jardine, H. Hedgeland, D. Ward, Y. Xiaoqing, W. Allison, J. Ellis, and G. Alexandrowicz, New Journal of Physics 10, 125026 (2008).
- *Determination of the Quantum Contribution to the Activated Motion of Hydrogen on a Metal Surface: H/Pt(111)* A. P. Jardine, E. Lee, D. Ward, G. Alexandrowicz, H. Hedgeland, W. Allison, J. Ellis, and E. Pollak, Physical Review Letters 105, (2010).

Presentations at international conferences relating to the work in this thesis include:

- Work from Chapter 2:
 - *Observation of a new slow dynamic process of Xe on Pt(111) using ³He Spin-echo Spectroscopy* - Poster presentation; VAS 13; Erice Italy,
 - *Investigating dynamical surface structure of Xe adsorbed on Pt(111) at low density using high resolution ³He Spinecho spectroscopy* - Contributed oral presentation; ICSOS9; Brazil,
 - *Understanding the ballistic to diffusive transition of Xe on Pt(111)* - Oral & poster presentation; WDPS13; Cambridge.
- Work from Chapter 4:

- *Dynamics of alkali metals adsorbed on Cu(111) at low density using high resolution ^3He spin-echo spectroscopy* - Contributed oral presentation; AVS56; San-Jose;
- *Surface dynamics of sodium adsorbed on Cu(111) at low density using high resolution ^3He spin-echo spectroscopy* - Contributed oral presentation; ISSC18; Reading;
- *Quantum recoil in the scattering of ^3He atoms from adsorbates.*
 - Poster presentation; ISSC18; Warwick, **Awarded best student poster prize**;
- Work from Chapter 5 has been presented at:
 - *Dynamics of alkali metals adsorbed on Cu(111) at low density using high resolution ^3He spin-echo spectroscopy* - Contributed oral presentation; AVS56; San-Jose;;
 - *How fast is fast? Experimental challenges to Markovian Langevin dynamics* ECOSS29 - Edinburgh - oral ;
 - *Quantum recoil in the scattering of ^3He atoms from adsorbates.*
 - Poster presentation; ISSC18; Warwick, **Awarded best student poster prize**.

Contents

1	Introduction and motivation	1
1.1	Experimental measurements of diffusion	3
1.2	Helium Scattering	8
1.2.1	Quasi-Elastic Helium Atom Scattering (QHAS) and the helium spin-echo method	9
1.2.2	The Intermediate Scattering Function, $I(\Delta K, t)$	12
1.3	Simulations of surface dynamics using the Langevin equation	15
2	Dynamics of xenon on platinum (111)	21
2.1	Review of literature and motivation for dynamics study	22
2.1.1	Structure and the adsorption of xenon (Xe) on platinum (Pt)(111)	22
2.1.2	Existing Dynamics Measurements	26
2.2	Experimental Procedure & Results	29
2.2.1	Adsorption: Temperature and coverage calibration	30
2.2.2	Experimental measurements of the intermediate scattering function	41
2.3	Diffusion signatures for Xe dimers and clusters	52
2.4	Langevin Simulations	56
2.5	Conclusions	68
3	The spin-echo spectrometer and instrumentation considerations	70
3.1	Precise measurement of the spin-echo point	71
3.1.1	Phase coil - Implementation and Calibration	73
3.2	Dynamical calibration of spin-echo point with precession fields	78
3.3	Further work	82

4	Jump diffusion of sodium on copper(111)	83
4.1	Motivation and background	83
4.2	Experimental methods	85
4.3	Measurements of the ISF	89
4.3.1	Application of Fourier filtering to the inelastic scattering signal in the ISF	93
4.3.2	Extraction and analysis of the diffusion parameters from the ISF	100
4.3.3	Molecular Dynamics simulations	105
4.4	The Intermediate Scattering Function $I(\Delta K, t)$ at short times	111
4.5	Summary and discussion	125
5	Observation of transition between ballistic and diffusive motion in lithium on copper(111)	126
5.1	Previous relevant work	126
5.2	Experimental methods	127
5.3	Coverage calibration	128
5.4	Measurement of Lithium dynamics	131
5.5	Simulating the ballistic/diffusive transition using the Generalised Langevin Equation (GLE)	142
5.5.1	Implementation of a digital noise filter to solve the generalised Langevin equation	143
5.6	Discussion	152
6	Outlook and future work	154
Appendices		158
A	Useful Fourier relationships	1
A.1	Relationship between the variance of a Gaussian function in time with Full Width Half Maximum in frequency and Energy	1
A.1.1	Fourier relationship	2
A.2	Relationship between α in time and Full Width Half Maximum of a Lorentzian in frequency and energy	3

A.3	Derivation of the ballistic gas line for an ISF in time	5
B	All Na/Cu(111) ISFs	7
C	All Li/Cu(111) ISFs	32
D	Protocol for Fourier filtering ISFs	41
	Acronyms	45
	References	48

Chapter 1

Introduction and motivation

The influence of technological development is apparent in virtually every aspect of daily life. In order to feed and power an increase to the quality of life for a growing population in a sustainable way there are significant challenges. From a device point of view, smarter, lower power, lower cost devices are shifting to ever smaller scales, requiring better knowledge of processes on these scales. A macroscopic knowledge of material properties is sufficient in the first stages of miniaturisation. As the size of devices approaches that of individual atoms and molecules, where the behaviour is fundamentally different, a change in approach is necessary. It becomes better to build up understanding from an atomic perspective.

The aim of the present work is to provide an understanding, on the atomic scale, of the behaviour that is relevant to nano-scale developments in device technology. Yang *et. al.* have recently reported work on development of a graphene barristor [1], a schematic image of which is shown in figure 1.1. Here the resistance of the graphene channel, between source and drain is affected by the gate electrode. Thus, there are issues such as the graphene-substrate interaction, doping and the need to control the growth of metal contacts. Bell *et. al.* [2] have studied the metal/graphene contacts. Figure 1.2, from reference [2] shows transmission electron microscope images and electron diffraction patterns of metal atoms adsorbed on graphene oxide layers. It is clear from the figure that there are a variety of different structures depending on the adsorbed metal. The authors attribute the structural differences that are driving the material properties to the differing diffusion rates of the metals on the graphene layer, highlighting the importance of understanding diffusion.

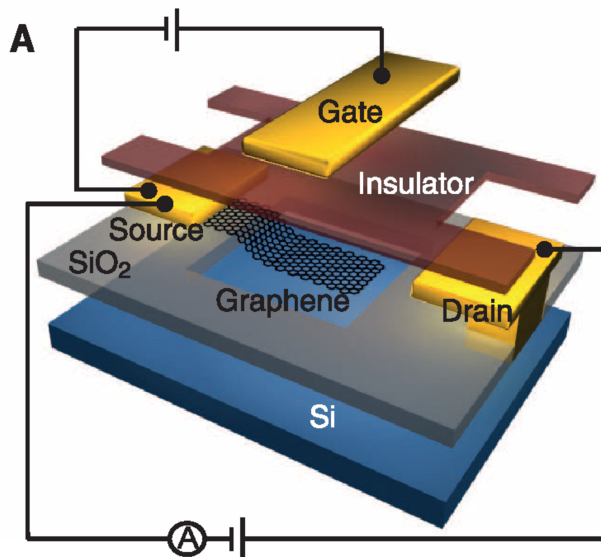


Figure 1.1: Graphene barristor recently developed by Yang *et. al.* [1].

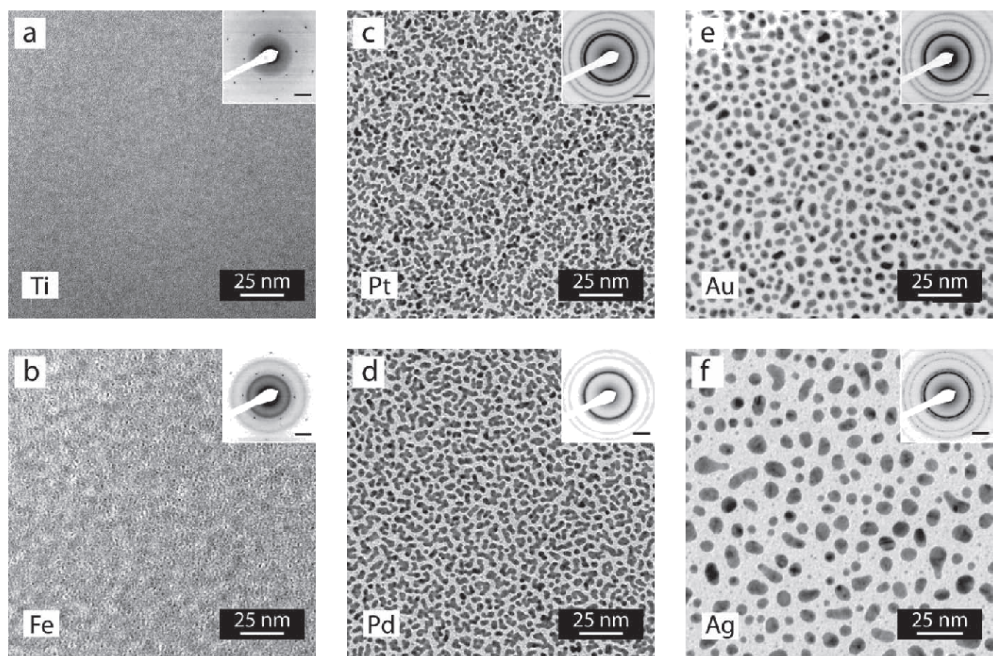


Figure 1.2: Bright-field TEM images of various metals on graphene oxide; inset in the top right of each images is the corresponding electron diffraction pattern. Taken from [2].

The work in the present thesis applies experimental measurements and simulations of scattering of helium atoms during diffusion of adsorbed species on the surface. The adsorbed atoms respond to forces from the thermal excitations of the substrate as well as forces from other adsorbates and the scattering of helium atoms responds to that motion.

In the past, a great deal of effort has been invested in describing diffusion and growth, from a macroscopic perspective, using the concept of a diffusion coefficient [3, 4]. More recently the emphasis has changed to an atomic perspective [5] where the aim is to describe the macroscopic behaviour in terms of the microscopic mechanisms. I begin with a brief overview of recent experiments

1.1 Experimental measurements of diffusion

Gomer's review of surface diffusion [5] provides an overview of some of the earliest methods of measuring surface diffusion at an atomic length scale. Initial measurements of diffusion were made using field emission [5, 6] and field ionization microscopy [7]. Microscopic techniques are attractive for the simplicity of analysis. More recently Scanning Tunnelling Microscopy (STM) has been the method of choice since it offers atomic scale resolution with fewer limitations on the surfaces that can be studied. Figure 1.3 presents state of the art images showing individual lead atoms on a lead-silicon surface, and demonstrates the strength of the technique to determine surface topology directly. Here the panels illustrate structures arising from competing attractive and repulsive interactions between the adsorbates. Helium atom scattering from the same system shows strong reflectivity, in the ordered phases [8].

In some instances, microscopy including optical, Scanning Tunnelling Microscopy (STM) and Atomic Force Microscopy (AFM) can be extended to yield information about dynamics. The simplest method is to correlate successive 'frames' of static data. More complicated methods exist, such as those described by Hahne [9], where the dynamics of copper phthalocyanine molecules on the Ag(100) surface are investigated by determining the residence time of atoms under an STM tip.

In applying scanning probe techniques to dynamic systems, it is usually necessary to work at cryogenic temperatures due to the scan time of the surface ($\approx 5\text{ ms}$ [10]) being orders of magnitude slower than the processes of interest (pico to nano-

seconds) at higher temperatures. Figure 1.4 presents recent experiments [10] demonstrating the application of frame correlations of STM images to the measurement of a ‘nano SUV’ which employs chiral molecules as nano-rotors and uses electronic excitations by the probe tip as the driving force. Data is collected at 7 K, with partial frames taken at an interval of 5 ms. The results of correlating successive frames produces the trajectory shown in the centre of the image. Akimov *et. al.* [11] have shown that in order to understand the large scale dynamics of complicated molecules, such as those employed in nano-machines, it is vital to understand the interaction of the constituent parts with each other and the surface environment on which they move.

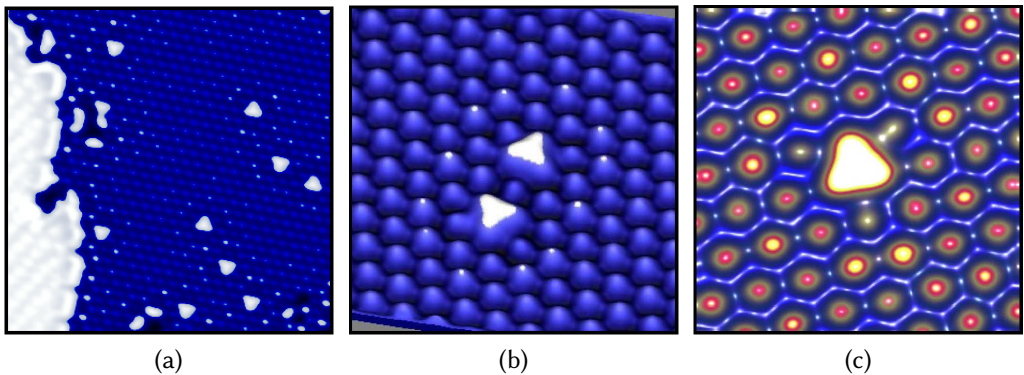


Figure 1.3: STM images of Pb atoms adsorbed on $\sqrt{3}$ -Pb/Si(111). (a) shows the surface with individual Pb atoms. (b) and (c) show two and a single Pb atoms respectively. STM images from Ref [12].

Scattering techniques are more difficult to analyse than their real space counterparts since they reveal indirect information in reciprocal space and need more substantial understanding to appreciate their significance. In physical terms the fundamental difference between the real and reciprocal space techniques is the way in which the space and time averaging occurs. In the correlation of real-space techniques, pico-second and Ångstrom scale dynamics are achieved by averaging over long trajectories or longer times, for example in laser induced thermal desorption, or field emission microscopy, atomic length and time scales are extracted by monitoring the average motion of an area orders of magnitude bigger than an atom, over time scales longer than the motion. In experiments utilising scattering techniques, the averaging is done in reciprocal space which effectively means that the length

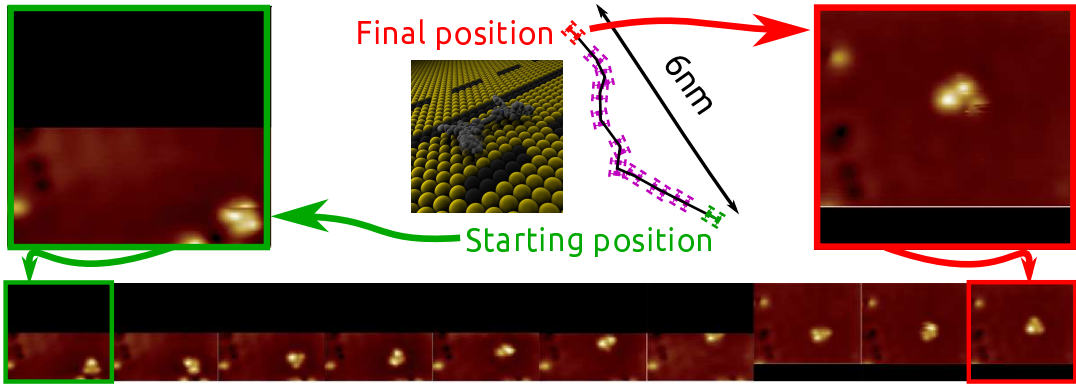


Figure 1.4: Images of “molecular SUV”, published by Kudernac et al. [10]. A chiral molecule arranged with 4 rotary motor elements which may be configured to allow driven, directional motion across a Cu(111) surface. Images are measured using STM in UHV with base pressures less than 1^{-10} mbar at a temperature of 7 K. Sequence displays 10 frames collected with the best time resolution possible.

and time-scales are averaged over the whole experiment to increase signal, however the detail of the fine scale motion is maintained.

Figure 1.5 presents a summary of experimental techniques that can be used to assess surface dynamics. The techniques are grouped into three general categories, imaging (M), optical (O) and scattering (S). The axes on the figure are logarithmic, ranging from macroscopic length scales of mm to that of individual atomic scale in Ångstroms and from time scales of seconds to nano-seconds. As can be seen in figure 1.5, the technique employed in this study, Quasi-Elastic Helium Atom Scattering (QHAS), along with Quasi-Elastic Neutron Scattering (QENS), measure atomic length scales on time scales of diffusion under thermodynamic conditions where dynamics driving reactions occur. QENS has limited application in surface studies due to its sensitivity to bulk processes in many systems, while QHAS is uniquely surface sensitive. Figure 1.6 presents a comparison of the rate of diffusion of CO on Cu(111), measured using both STM and helium spin-echo spectroscopy. It illustrates the wide range of timescales on which diffusion occurs and highlights the experimental challenge in achieving reliable numerical results. The figure is displayed on a log-log axis of the hopping rate and temperature to highlight the 13 orders of magnitude difference in hopping rate observed between the two techniques. STM is sensitive to fractions of hops per second at temperatures approaching absolute zero,

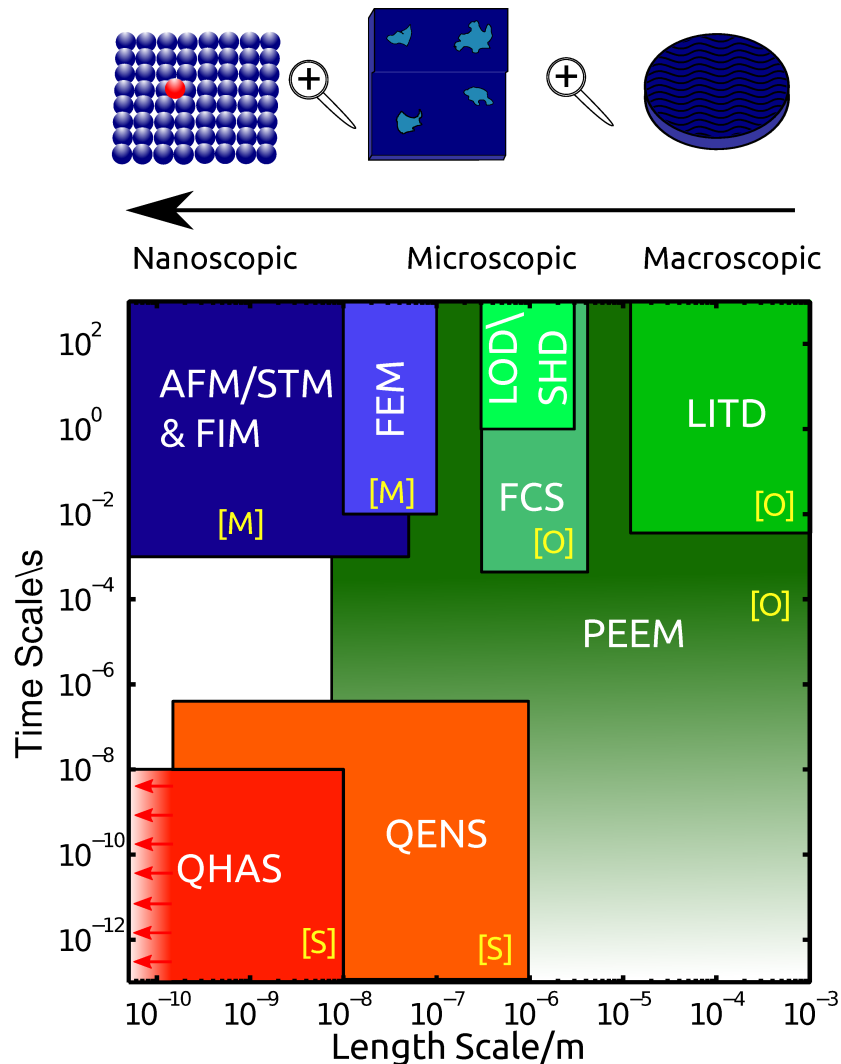


Figure 1.5: Schematic comparison of the principle experimental techniques applied to surface diffusion. Axis show time and length scales on a log axis, and therefore cover processes from mm to Ångstrom length scales and second to picosecond time scales. The colours and letters shown are used to group the techniques into primarily imaging in Blues (M), optical (O), in greens and scattering (S) in reds. QHAS is shown with a colour gradient to highlight the effort in the current study to measure faster dynamics at shorter timescales. QHAS, positioned in the bottom left hand corner of the figure, presents the only technique sensitive to surface processes on the length and time scales on which single atom diffusion occurs. The PEEM section is extended (shown by the gradient in colour) to represent sub-femtosecond scales accessible using pulse-synchronised methods. Figure Adapted from reference [13, p.7] and references therein.

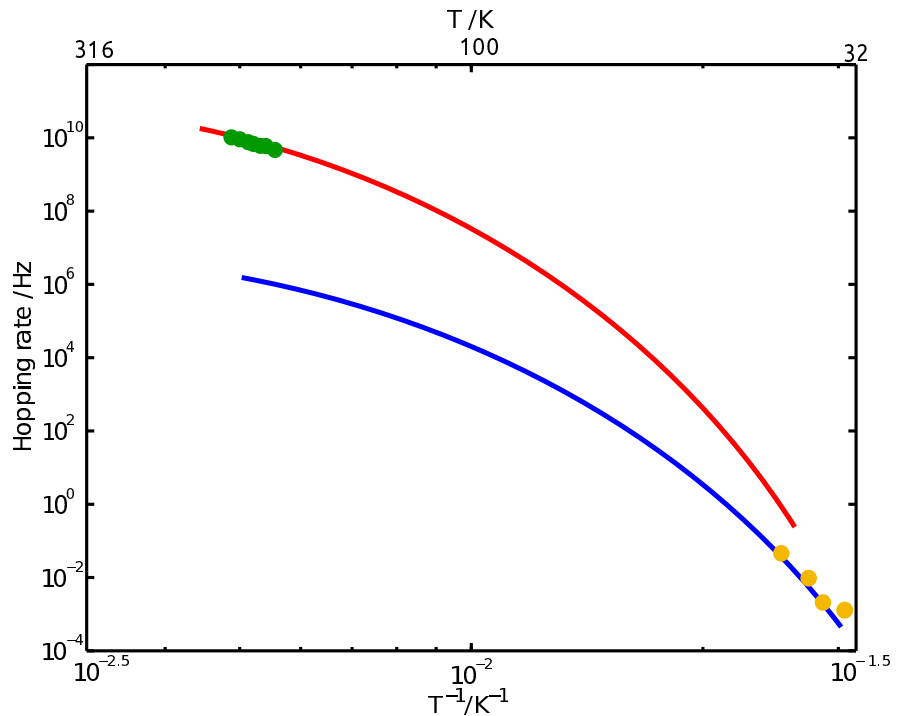


Figure 1.6: Temperature dependence of the rate of hopping of carbon monoxide on copper(111) at a coverage $\Theta = 0.04ML$. Data measured using QHAS with the spin-echo technique shown in green and STM data under the same conditions shown in yellow. The red and blue lines are based on the Arrhenius equation where the hopping rate, Γ can be written $\Gamma = \alpha_0 \exp(E_b/K_b T_s)$, where α_0 is the pre-exponential factor, related to the attempt rate for the process, E_b is the energy barrier, and T_s is the surface temperature. The red line represents a fit to the Arrhenius form for the QHAS data extrapolated to higher temperatures, where a good fit to the STM data is also achieved. The blue line shows a fit to the STM data alone, extrapolated toward lower temperatures and does not agree with the QHAS result, demonstrating the potential uncertainty in calculations of the pre-exponential factor using high temperature data, even when the process is the same. Figure adapted from [14, Fig. 5.17], where the spin-echo results are presented. STM results are from reference [15].

and spin-echo QHAS is sensitive to hopping rates of billions of hops per second at temperatures approaching room temperature. The lines in the figure represent an Arrhenius law for both of the datasets. It can be seen that the same line that fits the spin-echo data can also fit the STM data when it is extrapolated. If the STM data is fitted independently, however, as shown by the blue line, significant discrepancies in this case 4-orders of magnitude in the pre-exponential factor, can be made.

I will describe in the next section the principle of QHAS and its particular application to the current work. Interestingly both experiments give similar activation energy for the diffusion. It is the pre-exponential factors that differ drastically.

1.2 Helium Scattering

The power of scattering techniques in general has already been described. I now move on to summarise why helium is an ideal choice as a probe in the beam. Helium Atom Scattering (HAS) has been used as a probe of surface structures and lattice vibrations for many years, and more recently has been applied to measuring dynamics. Since the first recorded diffraction experiments were conducted in the 1930s by Estermann, Stern and Knauer [16, 17] there have been significant advances, particularly in the ability to generate supersonic beams with favourable energy properties for surface science. The de Broglie wavelength of helium is comparable to interatomic spacings, giving atomic resolution. It does not interfere with the processes on the surface, unlike scanning probe techniques and is completely non-destructive, unlike other scattering probes of similar size, due to the typical energy of the beams. Several excellent reviews of the technique have been published for example references [18, Ch.12] [19–23].

Figure 1.7 shows an illustration of elastic scattering from a flat surface. In this case an atom, represented as a wavepacket, interacts with the surface potential as illustrated on the right of figure 1.7. Elastic scattering occurs when there is no energy exchanged between the beam and the surface whereas inelastic scattering is observed when energy exchange occurs. Measurements of inelastic scattering are observed in some cases in the present work, and are attributed to the coupling of the helium beam to vibrational states related to surface phonons, or resonances of adsorbed scattering centres often referred to as “T-modes”. The latter processes, relating to inelastic scattering, are traditionally measured using a time of flight method

where a helium beam is generated and passed through a chopper, producing pulses which are scattered from a sample. The resultant velocity distribution is detected revealing the scattered energy distribution. The first inelastic helium scattering was presented in 1981 by the group of Toennies [24]. Since then, time of flight helium scattering has been employed to study many systems. A thorough review of studies up to 2003 is presented in Andrew Graham's 2003 review paper, reference [25].

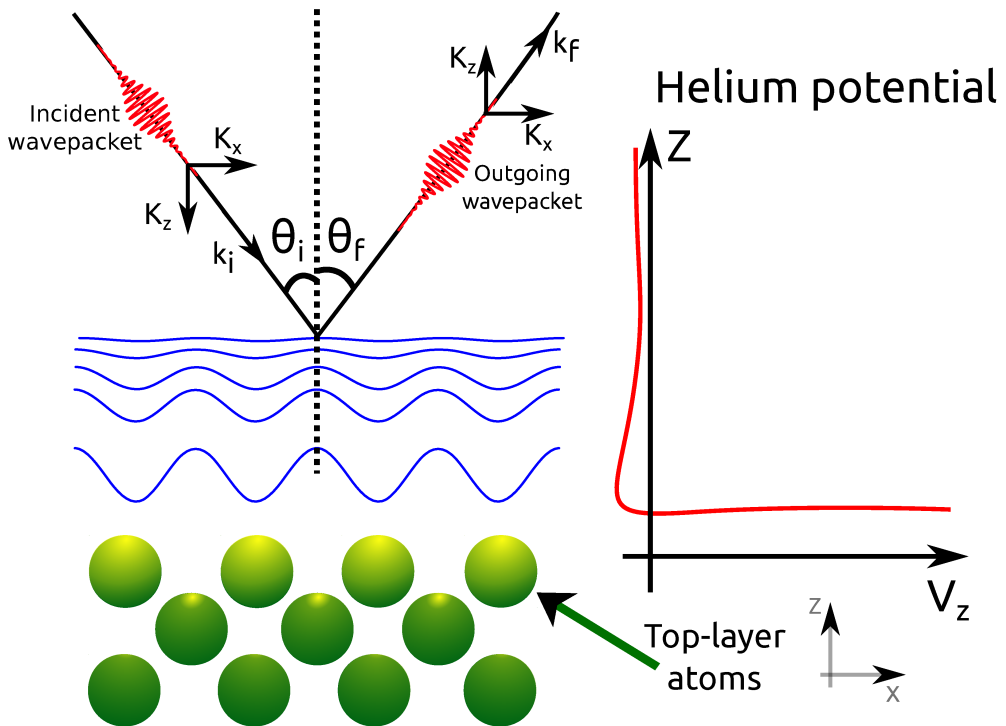


Figure 1.7: Illustration of the scattering of a helium wavepacket from a surface. Based in part on figure [26, 1.1 p.10]

1.2.1 Quasi-Elastic Helium Atom Scattering (QHAS) and the helium spin-echo method

It was established in the work of Vineyard [27] and Van-Hove [28] that scattering from moving targets causes small changes in velocity of the scattered beam which manifests itself as a broadening in the scattered elastic peak. Time of flight techniques, the benchmark in the measurement of inelastic scattering spectra, have been successfully applied to the measurement of diffusion, for example in the work of Ellis *et. al.* on the Xe/Pt(111) system [29]. Since it is a change in velocity that is measured

in the time of flight of the helium atoms, the practical limit of Time Of Flight (TOF) methods lies in the velocity spread in the beam. The practical limitation is therefore manifest as an effective limit in the speed of processes that may be observed.

The effect of the spread in the velocities is overcome in the spin-echo method, which measures velocity changes of individual atoms rather than the velocity change with respect to the mean incident velocity [18, Ch. 13]. The experimental process of performing helium-3 spin-echo experiments is outlined below. Chapter 3 describes the specific parts of the apparatus and methods that have been developed as a part of the current work.

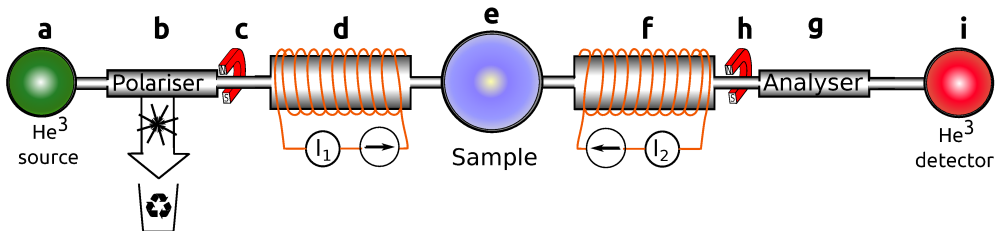


Figure 1.8: Schematic showing the principle parts of a spin-echo scattering apparatus. From **a** to **i**, there is a supersonic beam source, **a**, which produces a helium beam, which is spin polarised in region **b**, and aligned using a magnetic field at **c** in a direction perpendicular to the beam direction. The polarised beam is passed into a magnetic precession field in region **d**. Helium is scattered from the surface, **e**, and passes through a second precession field, **f**, that is usually orientated such that the precession set up in region **d** is reversed. The spin vector is then selected in regions **g** and **h** such that the component aligned with the field in region **c** proceeds to a helium atom detector, while the residual beam is pumped away.

Figure 1.8 shows a simple schematic of the significant parts of the helium-3 spin-echo apparatus, which is an established design [30]. The helium source [31] shown as **a** in the figure produces a beam by compressing helium-3 to high pressure and transmitting it through a nozzle into a vacuum chamber through a supersonic expansion. The pressure behind the nozzle (usually between 10 and 100 bar) and the temperature at which it is held defines a mean energy for the beam. The central part of the expansion passes through a skimmer to form the beam. The helium that does not pass through the skimmer is recycled through a high vacuum pumping system to a rare gas cleansing system before finally being compressed and returned to the nozzle. The most recent adaptation to the source has been presented in a work by

Lechner and co-workers [31].

The helium that leaves the source is transmitted through a polariser, the principle of which is the topic of a separate publication [32], and is shown as **b** in figure 1.8. The polariser enables the selection of one spin component, which is then further aligned perpendicular to the direction of transit in the uniform “holding” field from magnet **c**. From the point of beam polarisation at **b** to the analyser after **h**, stray magnetic fields permeating the beam path are carefully controlled using holding fields and mu-metal shielding, such that there are no uncontrolled changes to the spin vector.

The sensitivity of the spin-echo process to time-varying phenomena is instrumentally achieved in the precession solenoid, **d**, which creates a magnetic field aligned in the direction of the beam. Quantum-mechanically, the magnetic moment of the spin vector must align parallel or anti-parallel with the precession field. Assuming the moments of the spin are selected in region **c** to be perfectly in a plane perpendicular to the beam, there is no component in the beam direction, and therefore the moment ‘splits’ such that of its magnitude, exactly half is aligned and half anti-aligned with the precession field. The spin component that is aligned in a common direction with the precession field, abbreviated as the ‘+’ spin state, is accelerated and the antisymmetric component, ‘-’ state, is decelerated, causing a ‘splitting’ in time, proportional to the length of the field region and its magnitude. I emphasise that the helium atoms’ properties are split individually, i.e. each atom (or quantum-mechanical wavepacket) is split in time, not alternate atoms as might be assumed classically. A detailed mathematical definition of the temporal splitting is described in the next section.

The beam scatters from the surface in the scattering chamber, **e** and the polarised and temporally split beam is scattered according to the instantaneous state of the surface. After scattering, the beam passes through a second precession solenoid, **f**, which is traditionally connected such that it generates a magnetic field aligned in the opposite direction, but of equal magnitude to the one in **d**. If the first field causes a certain precession, and between the end of the first precession field and start of the next one there is no change in the magnetic moment, then the spin vector at the end of region **f** will be identical to that at the start of region **d**. The power of the technique comes from its immense sensitivity to changes in scattering

between **d** and **f** in the time between the two parts of the beam being scattered. For completeness, after the second precession field, **f**, the component of the magnetic moment parallel with that selected at **c**, is selected in a second hexapole field, **g** and **h**, and finally detected using a high sensitivity helium detector, at **i**.

The key parameter in a spin-echo experiment is the time difference between the arrival of the two wavepackets at the surface, known as the spin-echo time, t_{SE} , which is defined by the difference in time for the '+' and '-' spin states of the wavepacket to pass through the precession coil. The times can be calculated by considering the different kinetic energy of the two components depending on their alignment with the external precession field B

$$mv_0^2/2 \pm \mu B, \quad (1.1)$$

where μ is the magnetic moment, B is the magnetic field strength, m is the mass of helium and v_0 is the velocity. Inside the magnetic field, the velocities of the two states are given by

$$v_{\pm} = v_0 \pm \mu B / mv_0. \quad (1.2)$$

The spin component which is aligned with the field is accelerated while the other component, which is aligned anti-parallel is decelerated. Consequently, the two components take different lengths of time, t_{\pm} , to traverse the solenoid field, given by

$$t_{\pm} \approx \frac{L}{v_0} \pm \frac{\mu}{mv_0^3} \int_0^L B dl, \quad (1.3)$$

where L is the length of the magnetic field, and $\int_0^L B dl$ is the magnetic field integral. Writing μ in terms of the ${}^3\text{He}$ spin and gyromagnetic ratio, $\gamma\hbar/2$,

$$t_{SE} = t_+ - t_- = \frac{\gamma\hbar}{mv_0^3} \int_0^L B dl. \quad (1.4)$$

1.2.2 The Intermediate Scattering Function, $I(\Delta K, t)$

If we now consider scattering of a helium wavepacket from a surface; we can write the scattered amplitude from a scattering centre at position $\mathbf{R}(t)$ as

$$A \propto \exp(i\Delta\mathbf{K} \cdot \mathbf{R}(t)), \quad (1.5)$$

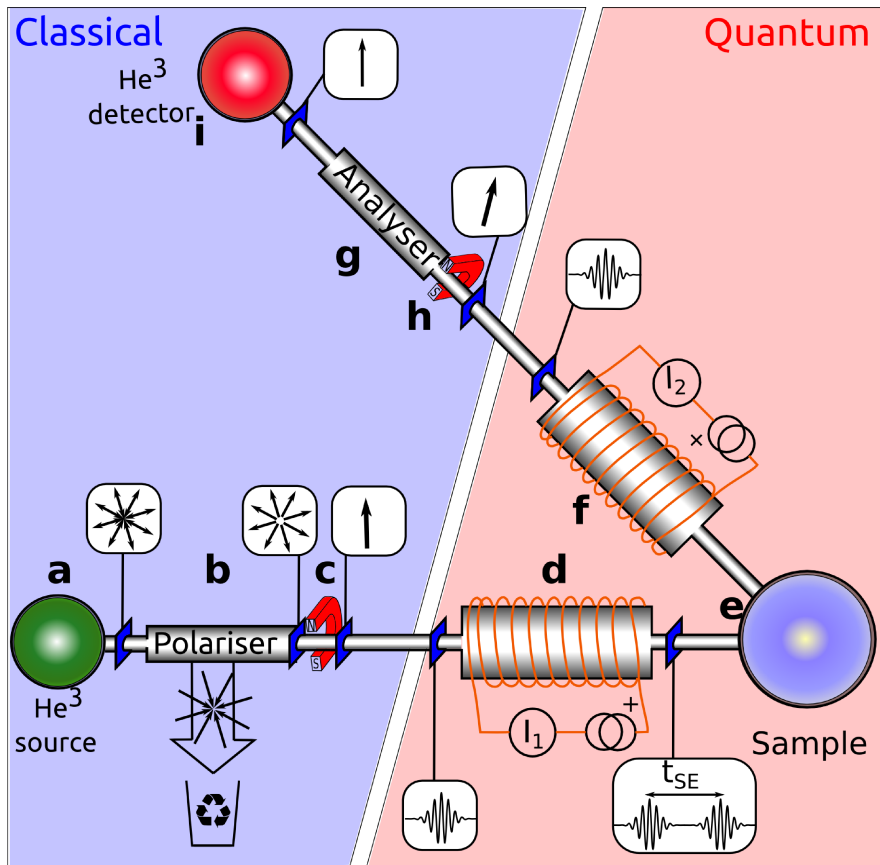


Figure 1.9: Schematic of the Cambridge spin-echo scattering apparatus. The transit of a helium beam is shown using a classical/quantum hybrid description. A beam of helium-3 is produced using an ultrasonic source **a**, which is then polarised with respect to its nuclear-spin using a hexapole magnetic field, **b**, and finally aligned to an axis perpendicular to the direction of the beam **c**. The polarised beam is passed through a magnetic field aligned to a direction of beam transit, **d**. At this point it is helpful to switch from a classical description to a quantum mechanical one, where we talk about the spin component as a single wavepacket. The wavepacket splits in the presence of the magnetic field, **d**, such that one half is accelerated and one half decelerated. The time between the two wavepackets when they scatter from the sample, **e**, defines the timescale accessible to the measurement. After scattering, the wavepacket is recombined, **f**. If there is a change in the scattering conditions between the first and second wavepacket, the classical angle of the spin vector will change on recombination. Switching back to classical spin vectors, the beam is passed through an analyser, **g**, aligned with the polariser, **h**, which rejects any signal not parallel with that produced by the polariser, and detected using a helium-3 detector, **i**. By adjusting the currents generating the magnetic fields, **d** and **f**, the relative magnitude of the polarised beam as a function of surface timescale is determined.

where the proportionality becomes equal if the scattering form factor is taken to be unity [33, Chapter 5]. Throughout the rest of the analysis the form factor is not considered. If we now consider scattering from a collection of j scattering centres

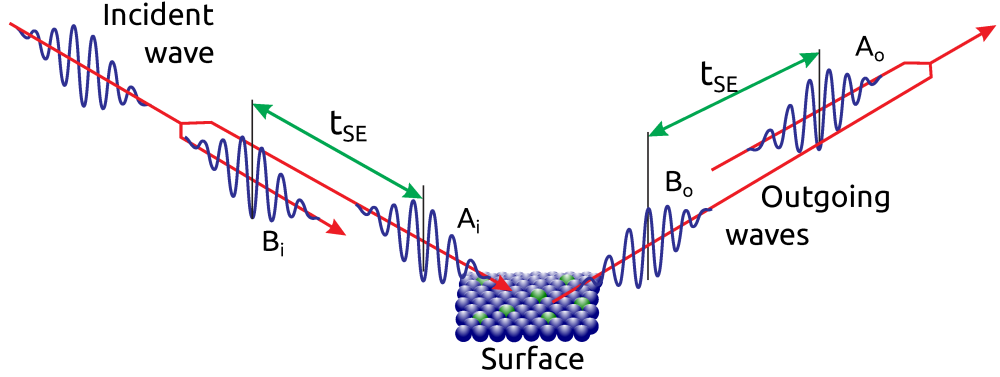


Figure 1.10: Schematic of the scattering of helium from a surface in the helium spin-echo spectrometer. The oscillating blue line represents the two spin eigenstates of the incoming helium wavepacket, separated in time by t_{SE} . After scattering from the surface, the separated wavepackets are recombined. If the scattered surface changes between the two parts of the wavepacket scattering, there is a loss of polarisation in the detected beam.

on a surface, which are at position vectors $\mathbf{R}_j(t)$ at time t , as shown in figure 1.10, which may have moved to $\mathbf{R}_j(t+t_{SE})$ at a time t_{SE} later, we can now write the total amplitude of the wavepacket as

$$A(\Delta\mathbf{K}, t, t_{SE}) \propto \sum_j \exp(i\Delta\mathbf{K} \cdot \mathbf{R}_j(t)) + \exp(i\Delta\mathbf{K} \cdot \mathbf{R}_j(t+t_{SE})). \quad (1.6)$$

We are sensitive to intensity, not amplitude, which can be written

$$I(\Delta\mathbf{K}, t, t_{SE}) \propto AA^*. \quad (1.7)$$

Intensities are the observable experimental quantity, although the corresponding polarisation, $P(\Delta\mathbf{K}, t)$, is usually presented. As usual, the magnitude of the polarisation is given by

$$P = \frac{I_{max} - I_{min}}{I_{max} + I_{min}}, \quad (1.8)$$

Where I_{max} occurs at the point when the wavepackets, shown schematically in figure 1.10, re-combine constructively at the in-phase condition and I_{min} when they combine in the out of phase condition, destructively. Jardine et. al. [34] have shown that the complex polarisation can be written

$$P(\Delta\mathbf{K}, t_{SE}) = \frac{\int G(\mathbf{R}, t_{SE}) e^{i\mathbf{K}\cdot\mathbf{R}} d\mathbf{R}}{\int G(\mathbf{R}, 0) e^{i\mathbf{K}\cdot\mathbf{R}} d\mathbf{R}} = \frac{I(\Delta\mathbf{K}, t_{SE})}{I(\Delta\mathbf{K}, 0)}, \quad (1.9)$$

where G is the Van Hove Pair correlation function $G(R, t)$ [28], the statistical probability of finding an atom at position R at t given that it was at the origin at time $t = 0$. Polarisation is a complex quantity and equation 1.9 can be written in terms of the cosine and sine, or real and imaginary components of the scattered amplitude. Experimentally the real polarisation can be measured by the scattered intensity of the in-phase recombination of the wavepackets and the imaginary polarisation at a phase angle of $\pi/2$ to the real part, which is equivalent to rotating the dipole field, \mathbf{c} in figure 1.9 to be perpendicular to that at \mathbf{h} . Hardware to rotate the spin vector is discussed in chapter 3. Equation 1.9 relates the ISF and the Van-Hove pair correlation function [28], $G(\mathbf{R}, t)$, through normalised Fourier transforms between real and reciprocal space, we can also perform a transform between time and energy to relate to the dynamic structure factor

$$G(\mathbf{R}, t) \xrightleftharpoons{\text{Spatial FT}} I(\Delta\mathbf{K}, t) \xrightleftharpoons{\text{Temporal FT}} S(\mathbf{K}, \omega). \quad (1.10)$$

Measurements of the ISF are conventionally analysed using numerical simulations based on the Langevin equation, which is discussed in the following section.

1.3 Simulations of surface dynamics using the Langevin equation

Extensive literature exists on the application of stochastic differential equations to problems in non-equilibrium statistical mechanics, see for example: [3, 35, 36]. The basis of the method arises from a distinction in the time scale of the various dynamical variables. The coordinates of the adsorbate, which are observed through the experiment, are formally separated from those of the substrate, which acts as a heat bath for the adsorbate motion. The bath coordinates are approximated under the

assumption that their characteristic time-scale is much faster than that of the adsorbate motion. Thus, the bath is represented as a frictional stochastic force [35, 37].

It can be shown that in addition to the stochastic force a dissipation term is required in order for the adsorbate's trajectory to be a true representation of the canonical ensemble [35]. An adsorbate moving in a plane and having coordinates, (x, y) , is described by the well known Langevin Equation (LE) [38, 39, p. 190]. For motion in the x direction it is

$$m\ddot{x} = -\eta m\dot{x} + \xi(t), \quad (1.11)$$

where $\xi(t)$ are fluctuating forces and $\eta m\dot{x}$ is the frictional dissipation. Here, the factor m is included so that the units of η are sec^{-1} , independent of the adsorbate mass. Both terms on the right-hand side of the equation arise from the interaction of the adsorbate and its environment; however, the partition of the external forces into a fluctuating part, $\xi(t)$, corresponding to thermal noise, and a constant factor proportional to velocity, which corresponds to the dissipation, is both helpful and convenient. The coefficient, η , describes the rate at which the bath extracts kinetic energy from a moving adsorbate, since the velocity, $v(t) = \dot{x}$, decays exponentially as $v(t) = v_0 \exp(-\eta t)$ in the absence of fluctuating forces. Thus η provides a direct measure of the rate of energy transfer between adsorbate and substrate and it determines the diffusive motion in the limit of long times [35]. Furthermore, η can be obtained from experiment, as will be shown later in the thesis. The random impulses due to the heat bath are usually assumed to vary with extreme rapidity and are taken to obey Gaussian statistics with first and second moments given by

$$\langle \xi(t) \rangle = 0, \quad (1.12)$$

$$\langle \xi(t)\xi(t') \rangle = 2B\delta(t - t'), \quad (1.13)$$

where B is a measure of the strength of the fluctuating force. The temperature of the bath determines the magnitude of B and it can be shown that $B = \eta K - BT/m$ [35], a result known as the second fluctuation-dissipation theorem. Note that the δ function in the correlation function, $\langle \xi(t)\xi(t') \rangle$, indicates that the frequency spectrum of the fluctuating force is that of white noise. Brownian motion is well

described by the Langevin equation, in that the motion is ballistic on time-scales much shorter than $1/\eta$, and diffusive on time-scales much longer than $1/\eta$ [40, 41].

For colloidal systems, such as silica spheres in water [42], the Langevin equation is a good description of reality. The macroscopic sphere receives microscopic impulses from surrounding water molecules and the impulses have a wide frequency spectrum so that, on the time-scale of observations, the motion of the sphere follows the prediction of the Langevin equation. Recent observations [42] show the transition from ballistic motion, with root mean squared (rms) displacement $\propto t$, to diffusive behaviour, with the rms displacement $\propto \sqrt{t}$ see [35, eq.1.34 & 1.35].

The approximations involved in the Langevin equation are more problematic in the case of adsorbate motion. The adsorbate is a microscopic entity and the noise due to the substrate is correspondingly larger. More importantly the frequency distribution of the noise will be represented less well by a white-noise spectrum. There exists a generalisation of the Langevin equation to account for classical motion when the noise is not “white” [35, 43]. In this Generalised Langevin Equation (GLE), the spectrum of the coloured noise is defined by its correlation function

$$\langle \zeta(t) \rangle = 0, \quad (1.14)$$

$$\langle \zeta(t) \zeta(t') \rangle = 2\eta k_B T / m K(t - t'), \quad (1.15)$$

and, to ensure the correct thermodynamic behaviour, the dissipation term becomes an integral over past times so that

$$m\ddot{x} = -m\eta \int_{-\infty}^t K(t - t')\dot{x}(t')dt' + \zeta(t). \quad (1.16)$$

The integral over the kernel, K , is usually described as a “memory” term [35, 39]. It is equivalent to a filter, in the time domain, that acts on the velocity, \dot{x} [44]. Furthermore, the filter is precisely the same as the one required to generate the coloured noise, $\zeta(t)$, from white noise, $\xi(t)$, hence

$$\zeta(t) = \int_{-\infty}^t K(t - t')\xi(t')dt'. \quad (1.17)$$

It is instructive to compare results using the LE with those from the generalised Langevin equation CLE in the case of a band limited noise spectrum. All real systems have a maximum frequency in their excitation spectrum and the effect can be described with a simple memory kernel $K(t) = \exp(-t/\tau)/\tau$, which corresponds to the frequency spectrum

$$|K(\omega)|^2 = \frac{1}{(1 + \tau^2\omega^2)}, \quad (1.18)$$

where the band limit of the noise is defined by a cut-off frequency, $\omega_c = 1/\tau$.

Figures 1.11a, (b), and (c) compare typical trajectories generated using random forces, $\zeta(t)$, generated from the same pseudo-random sequence, $\xi(t)$, with three different cut-off frequencies. Figure 1.11a, with $\tau = 0$, corresponds to the Langevin equation, while (b) and (c) have progressively larger τ and, hence lower cut-off frequencies. In all cases the friction coefficient, η , is the same and hence all three trajectories exhibit the same diffusive behaviour in the long time limit, as can be judged by comparing the starting and ending positions of the trajectories. The behaviour on a short time-scale is very different in the three trajectories. In particular, the higher noise frequencies in the Langevin simulation give rise to a more contorted trajectory, while the trajectory with the lowest cut-off frequency, fig. 1.11c, shows smoother excursions on short time-scales. The difference in the trajectories is also evident from the intermediate scattering function ISF, which can be calculated directly from the trajectory [38, p. 199] [45, eq. 47].

Fig 1.11d illustrates the effects by comparing ISFs for the trajectories shown. For times greater than approximately 4 ps, the ISFs are in the diffusive limit and they follow the same exponential dependence shown by the black curve. At short times, all trajectories deviate from the diffusive curve and the differences reflect the changes in the ballistic component to the motion. The degree to which the trajectories differ is determined by the frequency spectrum of the noise. It follows that a complete analysis of the ISF from experimental data should enable a correspondingly complete understanding of the frequency spectrum of the excitations experienced by an adsorbate, something that has not been attempted previously.

When the present work commenced, all analysis was directed at behaviour in the limit of long timescales, where we have seen that diffusive behaviour dominates. Many systems have been studied [13] and the Langevin equation played an impor-

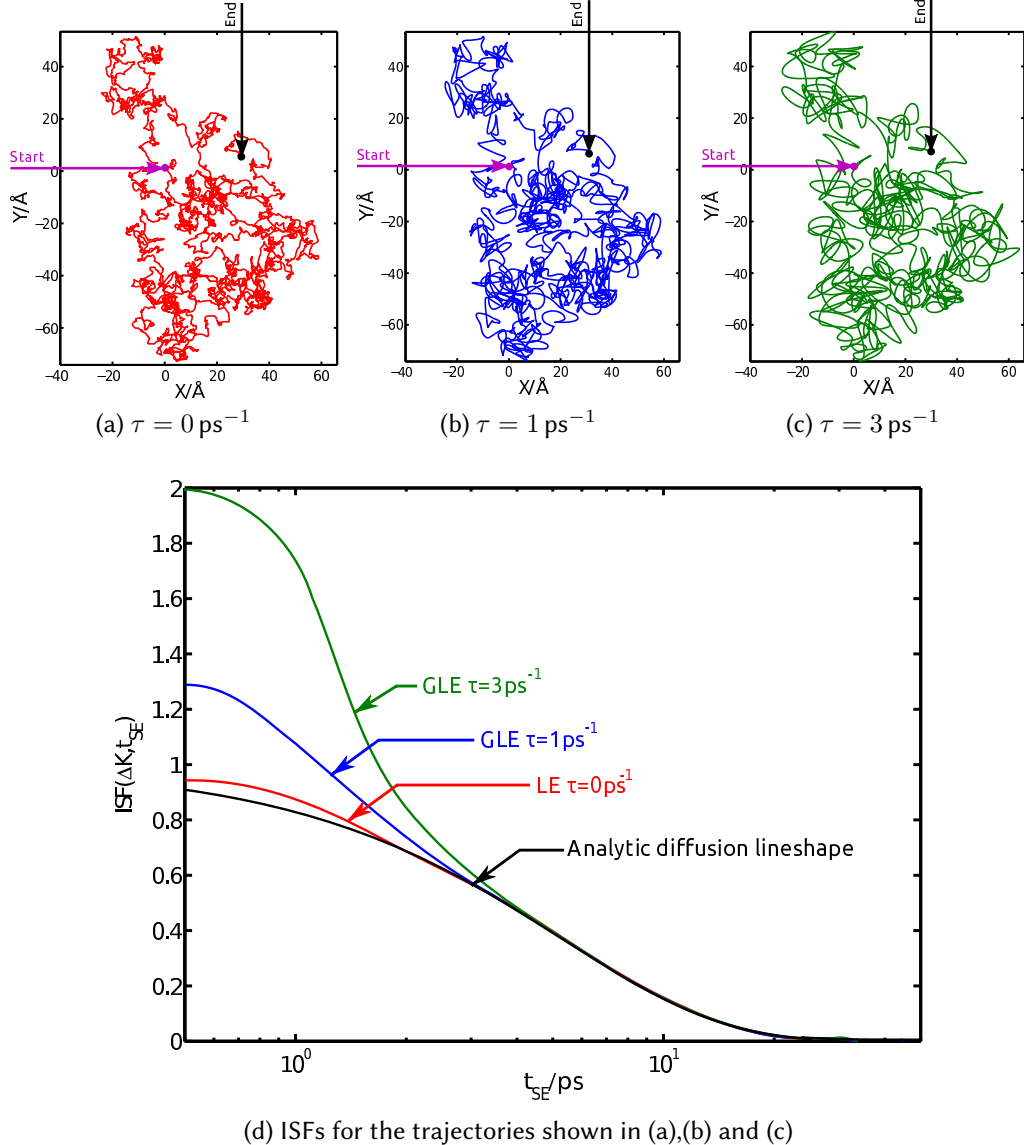


Figure 1.11: Atomic trajectories calculated using GLE molecular dynamics simulations, using a potential energy surface with $\nabla V = 0$. A filter with an exponential response of exponent τ is used to generate a coloured stochastic force so that frequency impulses are damped. The static friction η , in all of the simulations is 5 ps^{-1} and the temperature is 140 K for a particle of mass 7 amu. From right to left in panels, (a) to (c), τ is increased from 0 (white noise) to 3 ps^{-1} . In the bottom panel (d), the intermediate scattering functions calculated for the trajectories are shown normalised to the amplitude of the diffusive contribution.

tant part in the analysis [13, 29, 34]. The equations above are extended to include 2D motion in a static energy landscape, $V(\mathbf{r})$, where $\mathbf{r} = (x, y)$ is the position vector of the adsorbate and the Langevin equation becomes

$$m\ddot{\mathbf{r}} = -\nabla V(\mathbf{r}) - \eta m\dot{\mathbf{r}} + \xi_{x,y}(t), \quad (1.19)$$

a form that is widely used in the interpretation of helium-3 Spin-echo (${}^3\text{HeSE}$) experiments. In favourable cases, it is possible to extract the energy landscape and the diffusive friction with high precision [46–51].

The principal contribution of the present work is an extension of these methods to an analysis of the full ISF. The work begins with measurements of Xe motion on the Pt(111) substrate, which demonstrates that diffusive and ballistic components are not readily separable. Furthermore the work on Xe/Pt(111) highlights the experimental difficulties that occur when measuring at small spin-echo times. Later parts of the thesis describe improvements in the instrumentation and methods, followed by measurements on alkali atom motion on Cu(111). The final chapter illustrates that a complete analysis of the ISF lineshape is possible and the thesis concludes with the first experimental determination of the noise spectrum for a diffusing adsorbate, in this case, Li/Cu(111).

Chapter 2

Dynamics of xenon on platinum (111)

Xenon, and indeed all cases of rare gas adsorption on ‘flat’ surfaces, represent the simplest examples of physisorption. Such systems have been of interest since the first studies in the early 20th century which stem from the pioneering work of Langmuir [52].

The closed shell nature of rare gasses leads to an expectation that chemical interactions will be small and that adsorption forces will be dominated by weak dispersive forces, a ‘simple’ behaviour that is not in fact observed. For example, there has been controversy over the adsorption site, assumed to be the hollow site, but experimentally shown to be the on-top site, which does not maximise the adsorbate-substrate coordination as one would anticipate [53].

In this chapter the present understanding of rare gas adsorption, particularly for Xe on Pt(111), is presented with a focus on data relevant to diffusion studies. For example, the nature of the adsorbate substrate interaction, vibrational frequencies etc. I present the motivation for the current work, which concentrates on experimental measurements of the dynamics of the system studied with QHAS using the $^3\text{HeSE}$ technique and expands on a previous HAS study by Ellis and co-workers [54]. I will outline the specific technical challenges in studying this system, with reference to the $^3\text{HeSE}$ technique described in Chapter 1.

The main focus of the present work is the study of dynamics in the extremely low

coverage regime, $\Theta < 0.1ML$. Experimental results allow for the characterisation of a previously unseen and striking jump-diffusion signature, which can only now be measured because of the temporal resolution afforded by our technique. Finally I present a modified Xe/Pt energy landscape that is consistent with the experimental results and can be used to reconcile the apparently independent processes reported in the current work and presented in previous studies.

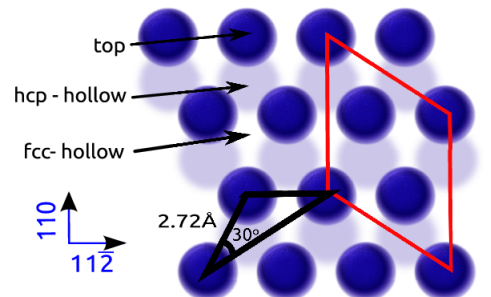
2.1 Review of literature and motivation for dynamics study

2.1.1 Structure and the adsorption of Xe on Pt(111)

It is known from experimental and theoretical studies that the majority of physisorption systems exhibit commensurate structures, where each adsorbed species occupies the same site. Rare-gas adsorption is dominated by weak, non directional, Van der Waals forces [55] due to the spherical electron distribution of the atom. It is expected that atoms will occupy sites that maximise the coordination of the adsorbate to the substrate, for fcc metals this would indicate adsorption at the 3-fold hollow site.

With the development of experimental structural surface techniques and theoretical modelling there has been some disagreement over the assumption of high-coordination physisorption. The first Low Energy Electron Diffraction (LEED) investigations by Hilgers and co-workers [56] were supportive of an fcc adsorption site, however the authors do highlight that the results are not sufficient to differentiate between hcp and fcc site preferences. The initial analysis of this experimental study, presented in 1991, relies on an assumption of high-coordination site adsorption. An analysis of the work with reference to a similar study of Xe on palladium (Pd)(111) from the same authors [57], recognises that a pure fcc site appears inconsistent, and suggests a combined fcc-hcp hollow site, with a honeycomb structure, shown in figure 2.1c, as the likely solution.

Many structures were considered in an effort to understand the competition between adsorbate-substrate and adsorbate-adsorbate interactions [58–61]. However, the picture changed dramatically when further quantitative LEED studies, particularly by Seyller and Diehl [62–65] in the late 90’s lent further experimental evi-



(a) Platinum surface with second layer atom positions shown in shadow.

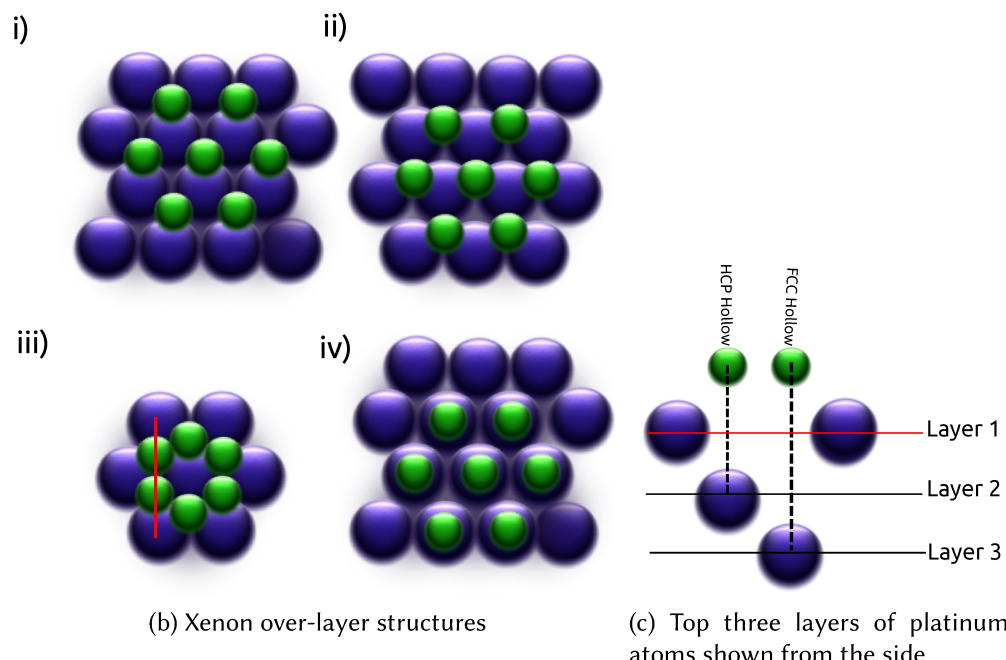


Figure 2.1: Panel 2.1a shows the top two layers of Pt atoms in the fcc structure, with unit cell shown in black. The unit cell for the $(\sqrt{3} \times \sqrt{3}) R30^\circ$ over-layer structures is shown for on-top sites in red. Panel 2.1b is a schematic diagram of desorption sites on the fcc(111) surface. Substrate atoms are shown in Blue and adsorbate atoms in green. *i*: hcp hollow sites only; *ii*: fcc hollow sites only; *iv*: ‘on-top’ sites only; *iii*: combined hcp and fcc hollow sites. 2.1c show a side-on view demonstrating the position of the degenerate hollow site with respect to the second and third layer of platinum atoms. *i,ii* and *iv* have triangular cells while *iii* exhibits a hexagonal honeycomb structure.

dence for a low-coordination on-top site as the preferred orientation for Xe on a variety of fcc crystal surfaces including Pt(111) copper (Cu)(111) and Pd(111). A summary of experimental evidence for top site adsorption is made by Zeppenfeld and Comsa [66]. At this time there arose a widespread agreement among experimentalists, using a variety of diffraction techniques as well as an STM study by Comsa and co-workers [67], against the high-coordination site adsorption argument.

In concert with the development of experimental techniques, modelling and calculation methods improved over the same time, particularly with the use of Density Functional Theory (DFT) to calculate adsorption energies. However, performing DFT on systems with long range weak forces, as are expected in this case, is fraught with difficulty and results are dependent on the technique, assumptions and functional used. Examples of some supporting DFT calculations include those of Bettancourt and Bird [68], which support a now experimentally confirmed high-coordination site preference. Although the aforementioned work supports top-site adsorption, no explanation for this finding has been proposed.

A 3D DFT simulation was calculated for Xe on Platinum by Tully, presented in reference [69], however the results of the work were limited in scope due to the available computing power and the experimental results of the system at the time. In the last decade significant progress in the application of DFT to physisorption systems has been made. An example is a recent work of Da Silva, Scheffler *et al.* [53], who have undertaken DFT calculations with both LDA and GGA functionals with respect to the Xe-Pt system. The work provides a relative adsorption potential, adapted and shown in figure 2.2, which agrees with the experimental data thus far. The authors suggest that factors such as Xe-Xe lateral interactions and spin-orbit coupling do not have a significant effect on the results, however the vibrational frequency for the model is not reproduced experimentally [70], which is expected given DFT does not take into account non-local, pairwise forces of such systems. Lazić *et al.* [71], adds the Van der Waals interactions to the DFT result, allowing a more realistic representation. The results of that work concur with the previous calculations and experimental studies that the on-top site is the preferred site, however it achieves a better approximation of the curvature of the potential minima, allowing the lateral vibrations of the xenon layer to be successfully reproduced. An in depth review on the work interaction is provided in [70, p. 1395].

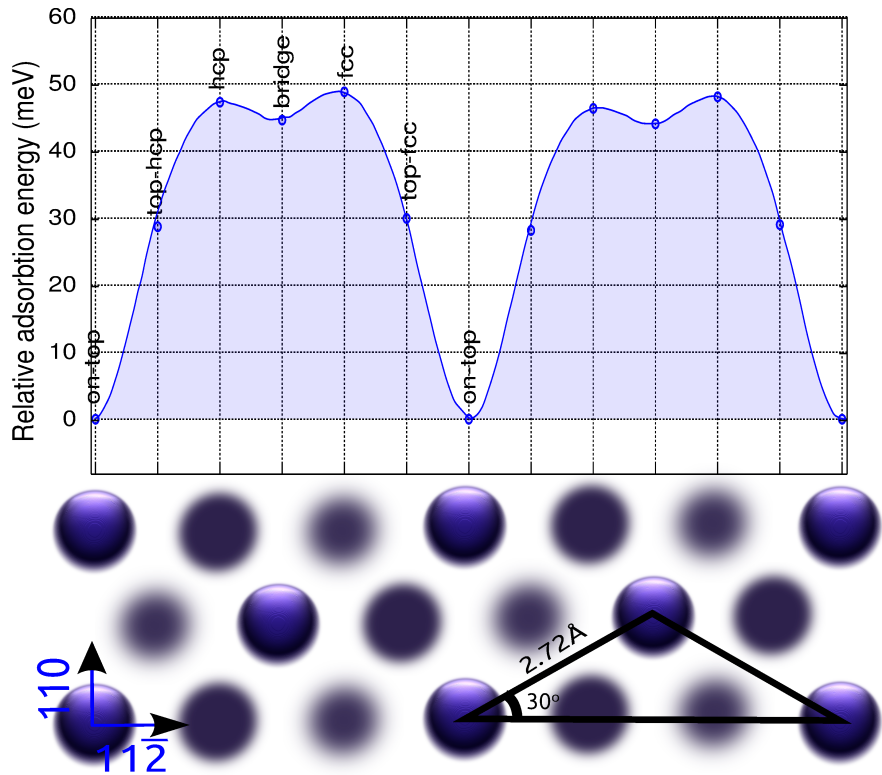


Figure 2.2: Results of DFT calculations [53], for $(\sqrt{3} \times \sqrt{3}) R30^\circ$ Xe adsorption sites on Pt(111). The top layer of Pt atoms are shown at the on-top position, with second layer atoms and third layer atoms shown at the hcp and fcc positions respectively. Adsorption energy of Xe in the on-top site is found to be -367 meV and the relative energy plotted is with the on-top site as the energy zero. The minimum potential found to be at the on-top site, which is unexpected if one assumes that there is no energy exchange between adsorbate and substrate.

An explanation for an on-top preference is that polarisation induced from the surface in the xenon atom is strongest at the on-top sites. For the clean surface of Pt, the electrons can more easily move from top site regions toward hollow-site regions and therefore when the Xe atom is at an intermediate distance it becomes more strongly polarized near the on-top site giving a stronger attractive force. The relocation of charge on the surface also leads to the reduction of Pauli repulsion at the metal atom allowing the Xe atom to move closer to the surface than at the 3-fold hollow site. This holds true for Pt-Xe distances down to approximately 1 Å where Pauli repulsion becomes significant enough to overwhelm the effects of the dipole polarisation and the 3-fold hollow site becomes the preferred site. The application of density functional theory to noble metal adsorption sites is still an active topic [72].

The surface phase diagram for xenon on platinum is fairly complex. At coverages less than 0.1 ML there is a gas to liquid transition. As the Xe concentration is increased a commensurate solid forms, which becomes an incommensurate solid and finally rotates to the $(\sqrt{3} \times \sqrt{3}) R30^\circ$ structure seen at the mono-layer with electron diffraction. Kern *et al.* have presented in-depth work on the phase transitions [73–77] which is summarised in the phase diagram shown in figure 2.3.

Data presented in this work regarding Xe dynamics is all taken at low coverage where there is only a single phase. The region investigated is shaded in red in the figure.

2.1.2 Existing Dynamics Measurements

Relevant but limited previous diffusion studies have been performed, the most recent of which is a 1999 QHAS time of flight study by Ellis *et. al.* [54]. Results from the study relate to a very low coverage investigation similar to that presented in the current work, probing single ad-atom diffusion. The major finding of the 1999 work is that Xe moves as a quasi two dimensional gas, with an activation energy and friction that could not be resolved in the work, but was shown to be less than 10 meV and $\eta = 0.25 \text{ ps}^{-1}$ respectively.

Figure 2.4 shows the key result, being that the quasi-elastic broadening increases linearly with momentum transfer. The slope of the linear relationship matches exactly that expected for a perfect 2-D gas with the mass of Xe, according to the equation 2.1, where T_s is the surface temperature, m is the adsorbate mass and ΔK is

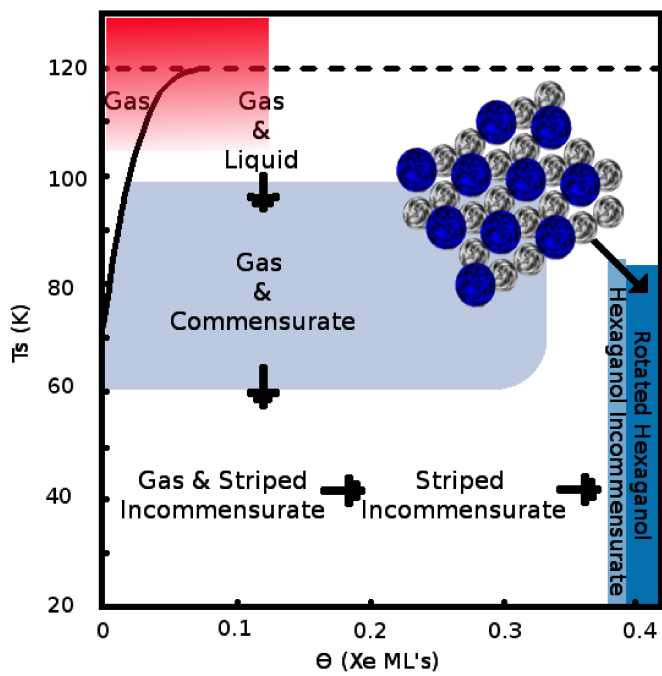


Figure 2.3: Schematic phase diagram of the ‘states’ of Xe on Pt(111) at sub mono-layer coverages. The region presented in this study is shaded in red, data from literature, e.g. Kern *et al.* [73, 75, 76].

the momentum transfer [54].

$$FWHM = 4\hbar\sqrt{\frac{K_b T_s}{m}} \Delta K \quad (2.1)$$

There are no further results pertaining to single adatom diffusion, however there have been several studies presenting results at higher coverages using STM [78] and Laser Induced Temperature Programmed Desorption (LITPD) [79]. In addition to this, higher coverage HAS measurements by Bruch *et al.* [80] which infer a different potential to that of Ellis.

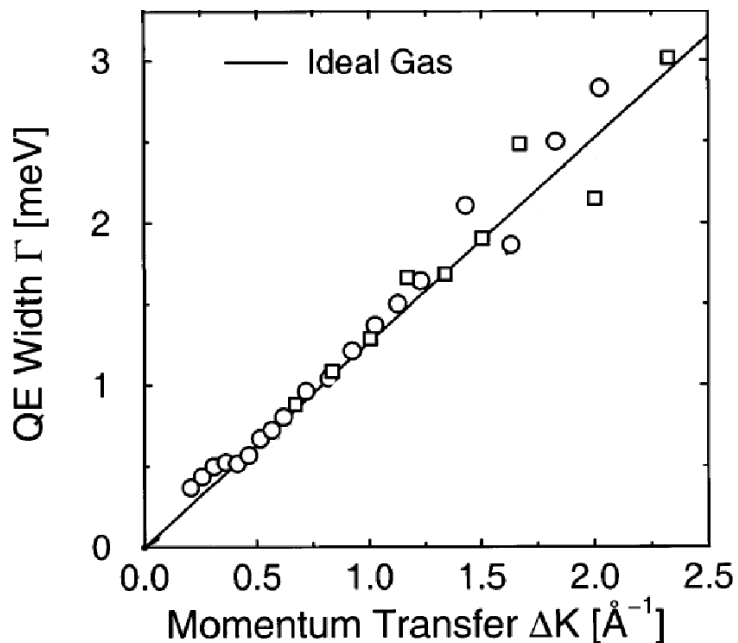


Figure 2.4: HAS Measurement of quasi-elastic broadening against momentum transfer for Xe diffusing on Pt(111) at 105 K taken from Ellis *et al.* [54]. Square and circular points are experimental data while the line relates to the ideal gas line for a species with the mass of Xe at 105 K. There is no visible energy exchange between the adsorbate and substrate, which would be indicated by a deviation of the experimental data from a linear ΔK dependence [81, Fig.10].

The results of these measurements are summarised in table 2.1. It is clear that different studies, both experimental and theoretical, predict different barrier heights for the Xe/Pt energy landscape.

The results to date present a system that appears simultaneously ballistic and

Θ	T_s	E_{diff}	Method
0.017	105	≤ 10	QHAS [54]
0.02	80	20	LITD [79]
0.08	80	52 ± 9	LITD [79]
$\frac{1}{3}$	80	56 ± 4	LITD [79]
'2D Cluster'	65-80	51 ± 5	Numerical Monte-Carlo simulation [82]
1/9 to 1/3		50-58	DFT with Van der Waals [53]

Table 2.1: Diffusion parameters for Xe/Pt(111). Θ is the coverage defined as the ratio of adatoms to top-layer substrate atoms, E_{diff} is the maximum amplitude in the potential energy landscape. The Monte-Carlo simulation is a numerical calculation based on a realistic adatom-substrate free energy. The work of Ellis [54] is unique in that it relates to single adatom diffusion, whereas other work represents diffusion in the presence of condensed phases.

diffusive, with the TOF results of Ellis *et al.* [54] showing no evidence for a surface-adatom interaction, and LITD studies [79] and DFT calculations [53, 82] providing evidence of a diffusive process with energy barrier between 20 meV and 58 meV. It would seem intractable for these two processes to be occurring simultaneously for the same system. The present work, which takes advantage of the enhanced resolution offered by $^3\text{HeSE}$ aims to provide a new insight on reconciling these behaviours.

2.2 Experimental Procedure & Results

A mechanically polished $Pt(111)$ sample (Surface Prep. Lab., NL) was installed on the manipulator. In-situ cleaning was performed with cycles of argon ion sputtering ($I_{emiss} \approx 12 \mu\text{A}/\text{cm}^2$ 800 V Ar^+ ions $T_s=450 \text{ K}$ 20 mins) and annealing (1100 K). Hydrocarbon contaminants were removed by heating the sample in an oxygen atmosphere, pressure 1×10^{-6} mbar to 800 K. Surface quality was monitored through measurement of helium reflectivity using a quadrupole mass spectrometer in the sample chamber. A high quality surface with low step and impurity density was confirmed regularly by exceptionally strong helium reflectivity $> 40\%$ throughout (measured at $T_s = 300 \text{ K}$).

The clean $Pt(111)$ crystal was aligned to the $[11\bar{2}]$ surface orientation by optimising the $c(4 \times 2)$ diffraction pattern of helium scattered from high purity Carbon Monoxide adsorbed to monolayer saturation at 150 K, and the sample re-cleaned to remove the CO from the sample and vacuum system before commencing measure-

ments. The temperature of the sample was monitored using a type-K¹ thermocouple spot welded onto a sample mount constructed from tantalum as described in chapter 3.

Temperature control was achieved with cryogenic sample cooling using either liquid nitrogen ($T_s > 120\text{ K}$) or helium, balanced against radiative heating from a coiled tungsten filament. Xe specified pure to 99.999 % is dosed using a micro-nozzle fitted to a leak valve in a linear vacuum bellows which can be inserted to a displacement of approximately 10 mm from the front of the sample holder. The precession coil current, defining the spin-echo time accessible, was selected using two power supplies optimised for range and precision. The ranges used correspond to ‘spin-echo times’ 1 – 800 and –120 to 120 pico seconds respectively. The ^3He beam was configured for 8 meV incident energy by setting the temperature of the nozzle, and was measured precisely at regular intervals. More detail on the procedures mentioned and the instrumentation specifics are detailed in the methods and instrumentation chapter 3.

2.2.1 Adsorption: Temperature and coverage calibration

Before describing new measurements on the dynamics of xenon, I describe some preliminary work designed to confirm the adsorption and coverage calibration; specifically TPD, uptake spectra, and dosage calibrations.

TPD [85] involves heating a sample in a vacuum while performing Residual Gas Analysis (RGA). As the sample is heated past the desorption temperature of the adsorbed species the rate of desorption is determined from the intensities of particular mass peaks in the detected RGA spectrum [85]. Previous TPD studies of Xe desorption from Pt(111) surface have been conducted by Meixner [79] [86] and Jansen [87] among others. The features reported have been reproduced in the current work, however one of the main uses of the technique is to calibrate the temperature scale for our system. As specified, for this study the temperature is routinely measured using a thermocouple, however careful calibration is required due to the shallow curvature of the metallic coupling voltage at low temperature [83]. Correct absolute temperature measurement is especially important with this system considering the

¹type-K thermocouple : chromel (90 % nickel and 10 % chromium) alumel (95 % nickel, 2 % manganese, 2 % aluminium and 1 % silicon) [83]

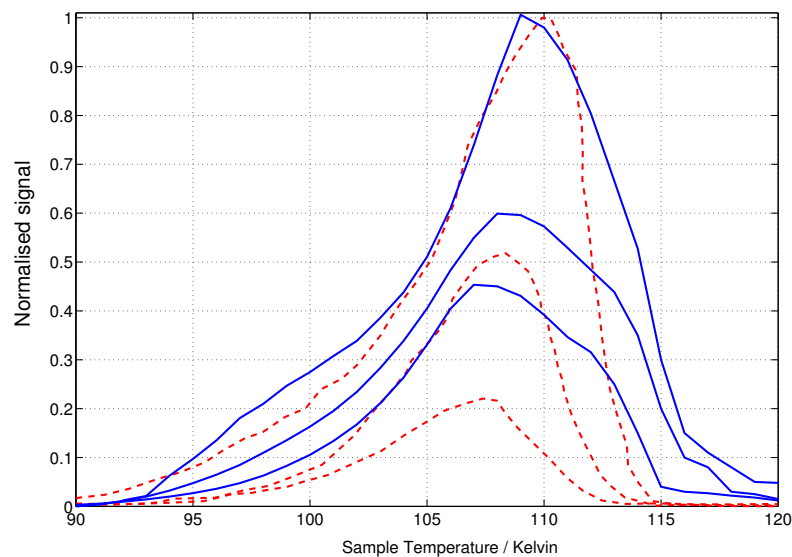


Figure 2.5: TPD spectra for Xe/Pt(111), dashed lines shown in red are taken from a previous study Meixner and George [79] at coverage $\Theta/\Theta_s=1, 0.45$, and 0.18 normalised to the $\Theta/\Theta_s=1$ maximum. Solid lines in blue are from the current work and are temperature corrected. Data is collected at coverage $\Theta/\Theta_s=1, 0.5$, and 0.1 , normalised to the $\Theta/\Theta_s=1$ maximum. In all cases the heating rate is 1.3 K/s

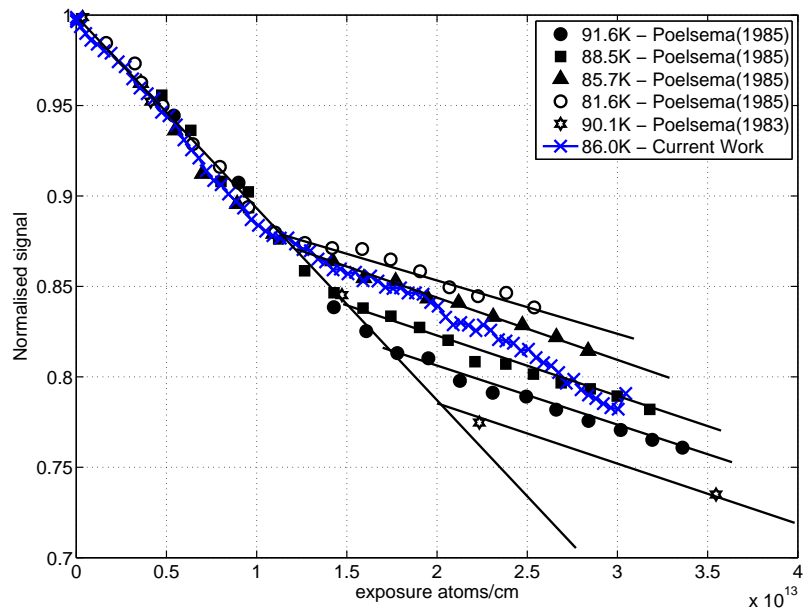


Figure 2.6: Normalised specular signal (compared to clean surface signal) as a function of dose of Xe. Black lines are taken from [84] and the blue crosses are from the current work at a surface temperature of 86 K for comparison. All data is shown in the low coverage limit, and is below the xenon desorption temperature.

complicated phase diagram 2.3.

Figure 2.5 compares the results from the present work with those of a previous study from Meixner and George [79]. The solid line shows the current results. The uncalibrated temperature values have been shifted up by 16 K compared to the indicated raw temperature. The adjusted values show excellent agreement with the previous results, shown as dashed red lines.

To confirm the calibration of the surface temperature we can compare the onset of the condensed phase from the uptake curve in the present work with similar measurements from previous works, for example [84]. If an adsorbate is deposited at the surface the order at the scattering centre is reduced as the signal is dispersed, resulting in a loss of specular reflectivity. The onset of condensation is accompanied by a change of slope in the specular reflectivity during uptake. A plot of the detector signal as the surface is exposed to the adsorbate is therefore a revealing and sensitive tool in determining structural information [22].

Figure 2.6 shows the results of Comsa & Poelsema [84] for a range of surface temperatures between 81.6 K and 91.6 K. An initial linear decaying region is observed, followed by a break at the onset of a condensed phase. The exposure at which condensation occurs changes as a function of temperature and is the experimental source for the curved line at the top left corner of the phase diagram for the system 2.3. Results of the present work are shown as blue crosses, the break corresponds to a surface temperature of between 85.7 K and 88.5 K. The temperature calibration using the TPD data, gives a surface temperature of 86 K which is again in excellent agreement with the literature. All temperatures quoted in this chapter use these calibrated results.

In the present work, most measurements are conducted at 121 K, at coverages up to $\Theta = 0.2ML$: above the xenon desorption temperature as shown in the phase diagram 2.3. In order to maintain an equilibrium dosage it is necessary to maintain a stable 'overpressure'. The primary gas dosing system on the apparatus is a 'dosing arm' as illustrated in 2.7. The purpose of the dosing arm is to increase the surface pressure locally without flooding the vacuum system with high pressures. The dosing arm is fitted with an automatic leak valve connected to a controller which senses the chamber pressure, allowing a target pressure to be maintained using feedback.

During dosing it is necessary to measure the local surface pressure in order to

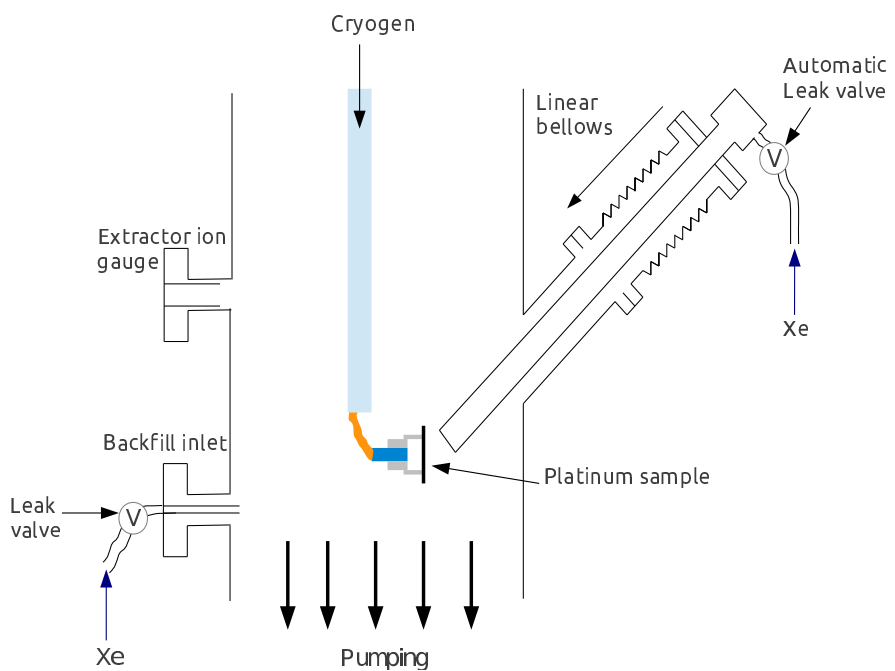


Figure 2.7: Schematic illustration of the dosing arm configuration. The sample is marked on the end of the cryogenic ‘cold finger’, the rest of the manipulator and sample chamber vacuum system are not shown for simplicity. The dosing arm is mounted on the right hand side and can move linearly in and out of the vacuum system. The pressure is measured using an ‘extractor ion gauge’ mounted on the right hand side of the chamber.

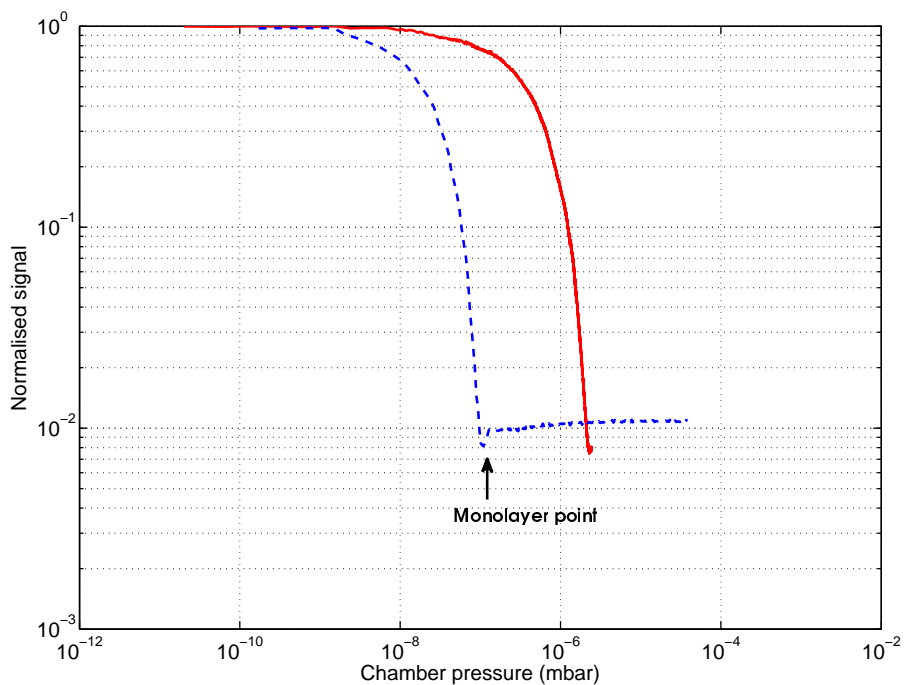


Figure 2.8: Reflected helium signal normalised to signal from the clean Pt(111) surface during Xe exposure at $T_s = 79$ K. The red solid line shows exposure by ‘back-filling’ the chamber with Xe. The blue dashed line uses the dosing arm positioned 8 mm from the surface. Prior to exposure, the specular signal was 7×10^4 Hz and the surface reflectivity was 41% and 43.8% for the backfill and arm dose methods respectively. If a factor of $\times 20$ is applied to the pressure from the arm dosing curve, the results are identical within quoted uncertainty, and are in good agreement with previous results from dosing carbon monoxide, shown in table 2.2.

Distance from Surface (± 1 mm)	Pressure multiplication factor
25	9.28 ± 0.25
13	8.91 ± 0.30
8	20.31 ± 0.21
5	14.72 ± 0.22

Table 2.2: Table showing the multiplication factor at different arm separations between the gas dosing nozzle and the surface. Multiplication factors are used to convert between chamber and surface pressure. Data is calculated by dosing carbon monoxide to a specular attenuation of 95%, at a sample temperature above the desorption temperature (340 K), with the dosing arm at different positions. The exposure is calculated using the integral of pressure with respect to time, and the pressure is adjusted using a linear factor (shown in the table) to align the uptake curves. An absolute reference is taken by backfilling the sample chamber.

assess the exposure. As illustrated in 2.7 the chamber pressure is measured remotely from the sample using an extractor ion gauge. It is necessary to calculate the relationship between the measured (remote) and local pressure. A direct determination can be made by obtaining uptake curves using both the backfill leak valve and the arm dosing method. Figure 2.8 presents these results. It is clear that the two results show the same phenomenology but the pressure difference between the chamber and the surface is obvious. If the measured pressure is ‘corrected’ by a factor of $\times 20$ ($\times 20.04 \pm 0.12$), both methods show consistent results.

In order to assess the pressure factor with respect to the arm position, the same method was employed, but with the arm at a range of positions, and the factor calculated. Carbon monoxide was used instead of xenon as the dosing gas because it has a larger accessible pressure and temperature window. A summary of the results is presented in table 2.2. As is expected the pressure increase is greater the closer the nozzle is to the sample; however, at the closest position (5 mm) the factor starts to decrease because of a small angular misalignment between the sample and dosing arm. For all measurements presented in this chapter an 8 mm arm position is maintained and factor of $\times 20$ applied where appropriate to the quoted pressures.

As the crystal rotates, it moves with respect to the dosing system, potentially varying the surface pressure and the equilibrium dose. In order to assess the effect on a measurement, the clean crystal is dosed using both chamber backfill and the dosing arm and the signal is measured as a function of angle. The backfill dose is

used as the control, as flooding of the chamber is clearly not angularly dependant. The results are presented in figure 2.9; the backfilled and dosing arm results shown in red and blue respectively are co-incident demonstrating that there is no detectable change in equilibrium coverage. The black line shows the same angular scan with a 50% attenuation dose, highlighting the method is sensitive to slight changes in coverage.

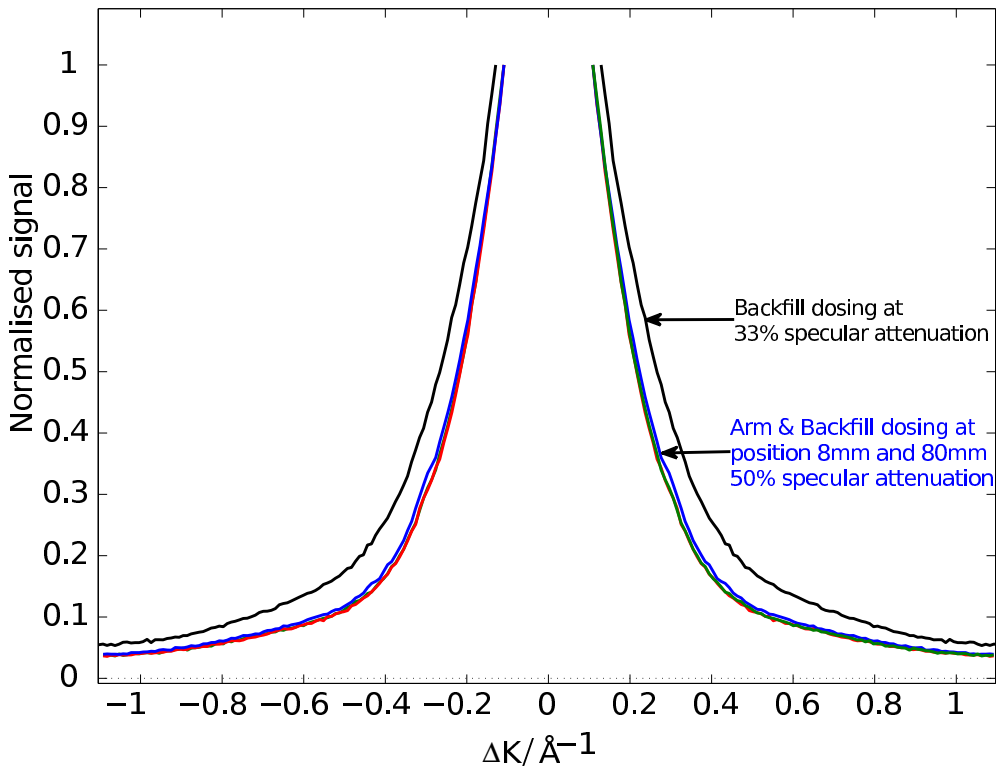


Figure 2.9: Angular scans collected at a surface temperature of 121 K. The clean crystal is dosed using both chamber backfill and the dosing arm to 33% attenuation at the specular reflectivity position (A dose $\Theta = 0.05 \text{ ML}$ where $\Theta = 1$ is saturation coverage). The sample is then moved over an angular range, equivalent to a momentum transfer between -1 to 1 \AA^{-1} (The angular range -0.1 to 0.1 \AA is avoided due to the requirement to ‘de-tune’ the detector to protect sensitive electronics from high count rates around the specular position). The results for the backfilled case, shown in red, are presented with those measured with the dosing arm in solid blue and are co-incident; demonstrating that there is no detectable change in equilibrium coverage due to the changing angle of the crystal. The sensitivity of this technique is made clear by comparing the result to the black line, which is the result for the same angular scan with a dose of 50% specular attenuation.

From the xenon phase diagram the simplest target for dynamics measurements is the single atom or gas phase motion, in the low coverage limit, at the top left of figure 2.3. It is clear from TPD measurements in section 2.5 and the literature, for example reference [79], that significant xenon desorption starts at a surface temperature of 90 K. In order to measure dynamics at temperatures above 90 K an equilibrium dose is maintained using a xenon overpressure as described.

Overpressure uptake methods used in this work are illustrated through measurements of adsorption isotherms. At a fixed temperature, the overpressure of Xe is adjusted in a series of steps while the specular reflectivity is recorded. A figure demonstrating the method, at surface temperature 121 K, is presented in figure 2.10, in which the top panel shows the count rate and the bottom panel the pressure. For each stable pressure (shown as red lines) the mean count rate is calculated. As the pressure is changed in a step-wise manner (bottom panel in figure 2.10), there are corresponding changes in the count rate (upper panel). Peaks and dips in the count rate are a result of overcorrection by the feedback system stabilising the chamber pressure.

The pressure and signal can be converted into uptake isotherms, shown in figure 2.11, which are used to locate the measurements in the phase diagram for the system. This is the same type of measurement used to define the phase boundaries such as those defining the liquid transition in 2.3, though those measurements are isobars not isotherms. At ‘very’ high pressure the count rate can be seen to increase, this is shown in the inset panel as the effect is very small, and is indicative of increased order at the surface which implies a monolayer or other condensed phase has formed.

Dynamics were not observed at the post monolayer point indicating that the surface had ‘locked’ into position, as would be expected. Any second layer atoms are apparently frozen on the first layer and do not appear to move, though this was only cursorily investigated, and could be returned to for further work in order to investigate inter-adsorbate (Xe-Xe) interactions; and the effect of a Xe monolayer on the energy landscape presented to other Xe atoms or a second adsorbate.

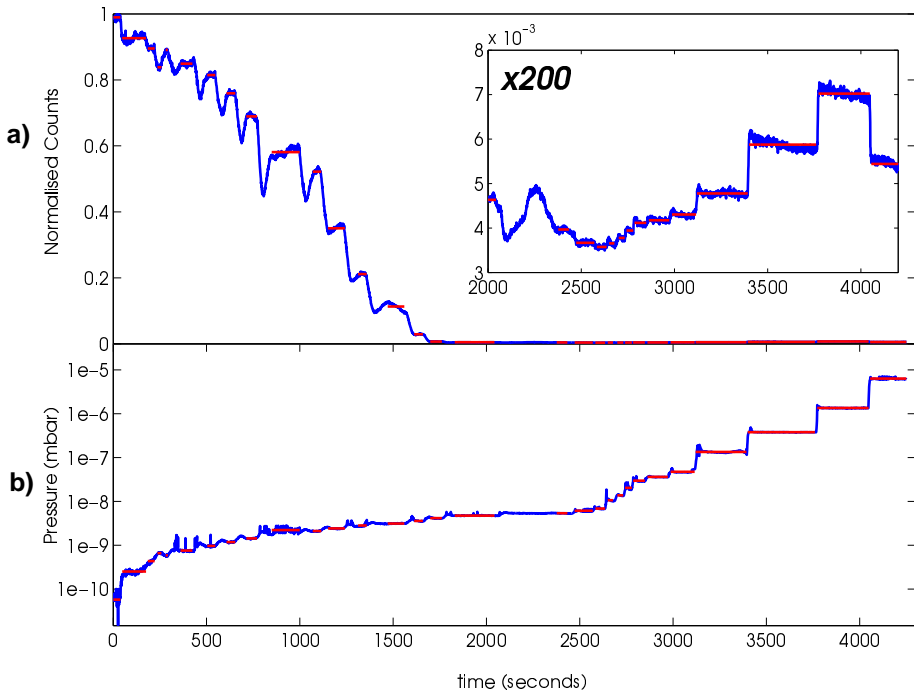


Figure 2.10: Figure demonstrating the experimental process of generating uptake isotherms. In this case the curve for $T_s = 121$ K is presented. The surface pressure is increased in steps, as can be seen in panel *b*, while monitoring the reflected signal; for each plateau (shown by red lines) the mean count rate is recorded and can be plotted against the mean pressure. These results are presented in figure 2.11. The inset in panel *a* is a magnification of the Y axis by $200\times$ the signal can be seen to *increase* in this plot demonstrating enhanced order at higher coverage, which can be associated with the onset of a more ordered phase or multi layer. The nature of the higher coverage structure is not treated in this work, but has been presented in other works for example reference [84].

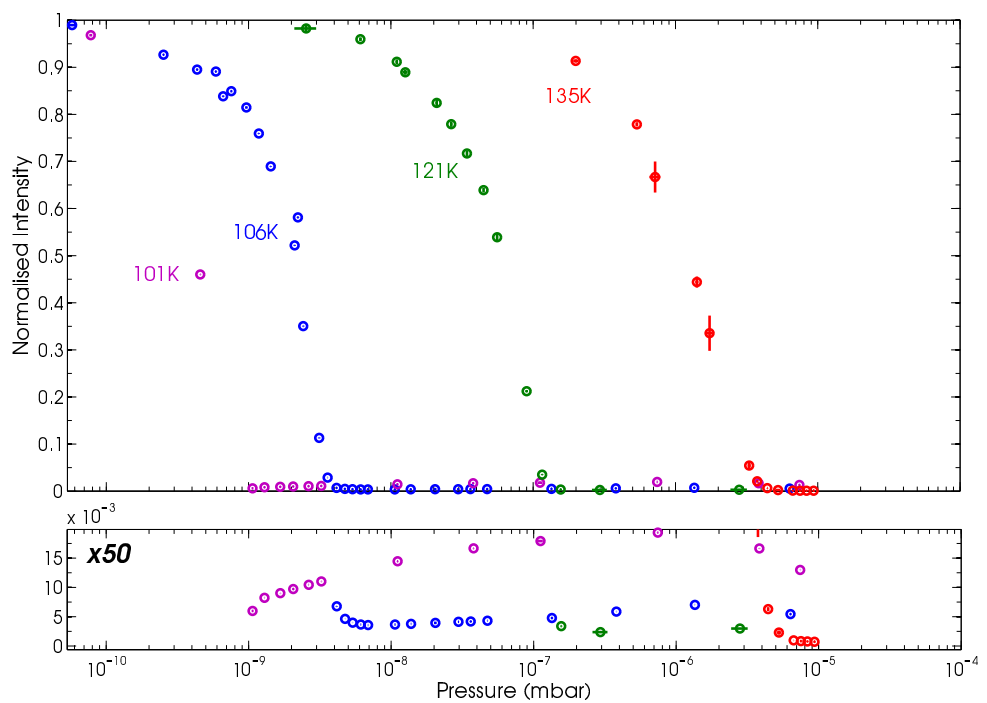


Figure 2.11: Uptake isotherms for $T_s = 101\text{ K}$ (purple), 106 K (blue), 121 K (green) and 135 K (red). The top panel shows the full scale of the uptake. The lower panel shows a $50\times$ zoom of the lowest intensity part of the uptake. The isotherm is constructed by increasing the pressure of xenon in steps and measuring the count rate, as illustrated in figure 2.10

2.2.2 Experimental measurements of the intermediate scattering function

The dynamics of xenon at low coverages $\Theta < 0.2ML$ are measured as a function of momentum transfer (ΔK) from 0.1 to 1\AA^{-1} and surface temperature between 90 and 130 K. The procedure for measuring the ISF involves setting the sample temperature, moving the crystal to the appropriate angle, equivalent to a particular ΔK , and measuring the ISF over an appropriate time scale. Several repeat measurements, or loops are usually recorded and the average spectra calculated to improve experimental statistics and reduce the effect of random noise in the experimental data. The captured spectra require very little post-processing before analysis, however there are two relatively straight forward ‘filters’ that are applied.

First, single point ‘spikes’ in the signal are sometimes recorded which are attributed to instantaneous fluctuations in the response of the system. Spikes, consisting of a single data point, orders of magnitude greater than the surrounding data, are easy to recognise and remove from the spectra by comparing multiple loops of the same measurement and analysing adjacent points in individual loops.

Secondly, variations in temperature and pressure which cause the total sensitivity to fluctuate are corrected by measuring the signal at the beginning of every loop, interpolating cubically within the loop. In the data presented here the correction is minimal, no more than 5 %.

Care was taken to avoid effects due to contaminants building up on the surface leading to potential systematic errors. Consecutive temperatures and angles were not measured in sequence. Contamination can be assessed by repeated measurements of a single ISF; each taking approximately 5 minutes. Typically the point on point signal varies by less than two standard deviations over a period of 3 hours, with statistically significant changes only occurring after more than four hours. The maximum time for a single set of measurements presented in this work is two hours from dosing. At the end of measurements the reflectivity from the sample is recorded and verified to be the same as the start, further reducing potential error.

Figure 2.12 shows a schematic representation of a typical ISF. Data is presented on linear and logarithmic time scales to demonstrate the ability to see shapes on different time scales. The plot is split into three time separated regions representing

the general shape of the experimental results to be presented. It should be noted that there is no general theory giving the functional form. Theoretical models exist only for the simplest of systems [88], and usually only cover a specific time regime. At the longest times ‘static’ scattering is seen. This is expected to change with angle, temperature and coverage and often has similar features to a diffraction scan. The slowest decaying process, typically observed after 10 ps, is an exponential decay and represents diffusion. The diffusive decay alone may be a complicated function built up of many contributions on different time scales, and its shape is discussed in greater detail later in this work. Finally the fastest decaying process represents the processes that occur *before the onset of diffusion*, in many ways the simplest physics but often the most technically challenging, as discussed later in the work. Energy gain or loss processes are not included on the figure as they add unnecessary complication.

The equation used to generate figure 2.12 is a sum of a ‘fast’ Gaussian and slower exponential, together with a constant term. Parameters have been chosen to represent the features of the experimental data; however, a point that is worth noting when estimating line-shapes is that the addition of an exponential beneath a Gaussian acts to ‘sharpen’ the roll over at the maximum of the function, effectively making it more difficult to recognise its form, as highlighted in the inset of figure 2.12.

Figure 2.13 shows experimental data taken in the low coverage regime at $\Delta K = 0.33 \text{ \AA}^{-1}$ and $T_s = 121 \text{ K}$. The first part of the spectrum is shown as an inset on a linear time-scale to emphasise the dramatic change in shape. A ‘constant’ representing the scattering from static species has been subtracted and the signal has been normalised to a spin-echo time of zero, taking into account any loss of polarisation not related to Xe dynamics.

The red dashed line in figure 2.13 shows a fit of an exponential line of the form $Ae^{-\alpha t}$ applied to the longer time process. Extracting information about diffusion from exponential signatures in ISFs is the method employed in all previous ${}^3\text{HeSE}$ measurements, for example see references [47,50,51]). It is striking that the diffusion process is the dominant contribution in this measurement, as it seems to contradict the previous QHAS work of Ellis *et al.* [54], who identified ballistic motion as the dominant effect¹.

¹An ideal gas curve would have a Gaussian profile and decay on a time-scale much quicker than

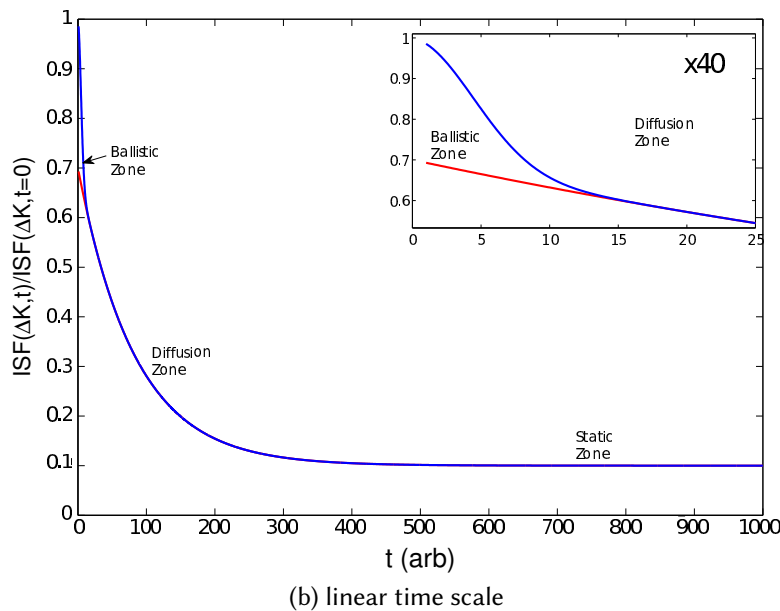
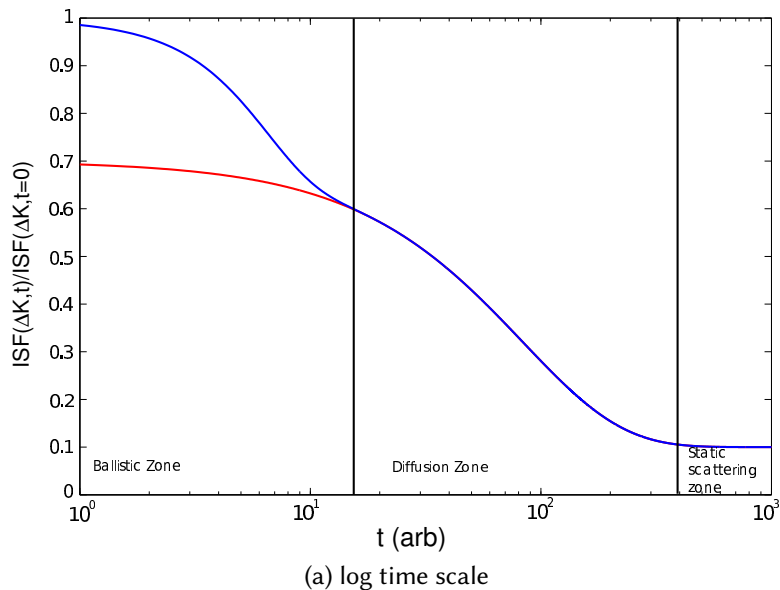


Figure 2.12: Schematic representation of the shape of a typical ISF for this system, used to highlight the different time regimes of relevant processes. The red line shows the purely diffusive signal, while the blue line contains the ballistic region and transfer region. In common with the experimental data there are two decaying processes in addition to a static signal. In this figure the value of plotting the spectra on a $\log(t)$ axis is also demonstrated

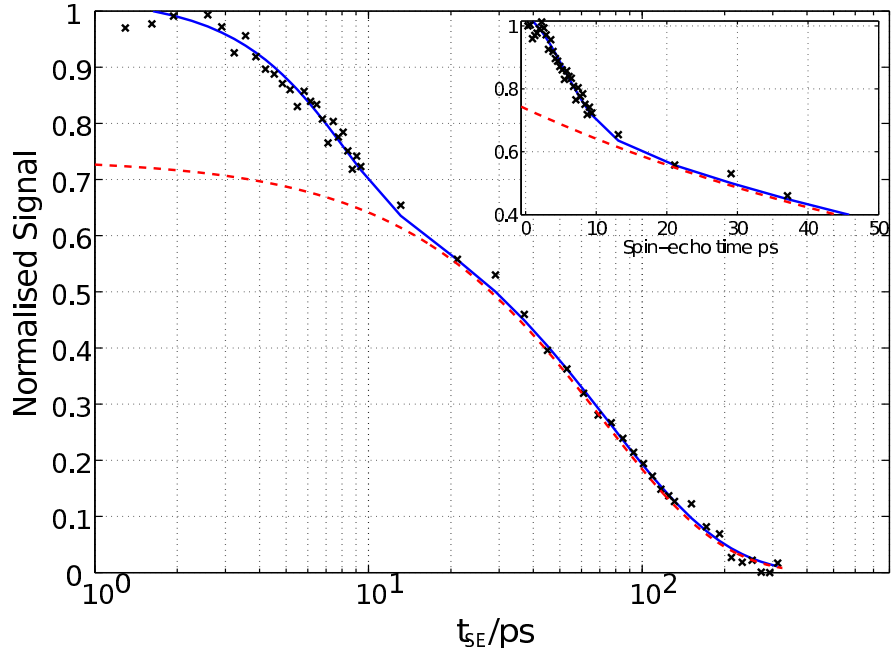


Figure 2.13: Intermediate Scattering Function, $I(\Delta K, t)$ plotted against log spin-echo time, with the inset showing the same data on a linear scale for reference. Experimental data is shown as black crosses and is taken in the $[11\bar{2}]$ direction at $\Delta K = 0.33 \text{ \AA}^{-1}$, $T_s = 121 \text{ K}$. The error on the data points in the ISF is dominated by shot noise in the counting electronics on the detector and is less than 1%, error bars are insignificant and are not shown for clarity. The static scattering signal (constant level) is removed and the signal normalised to the polarisation at $t = 0$. The red dashed line is an exponential of the form $A_0 e^{-\alpha t}$, which is applied to the longest time scale in the ISF. It is immediately clear that there is a second decay process on a faster time-scale of $t < 20 \text{ ps}$ in this case. The blue solid line is a function of the form $A_0 e^{-\alpha t} + A_1 e^{-\frac{t^2}{2\sigma^2}}$, whose purpose is to ease analysis of the two processes by combining the exponential function of the red dashed line with a second ‘faster’ decay process, the method is explained in the text.

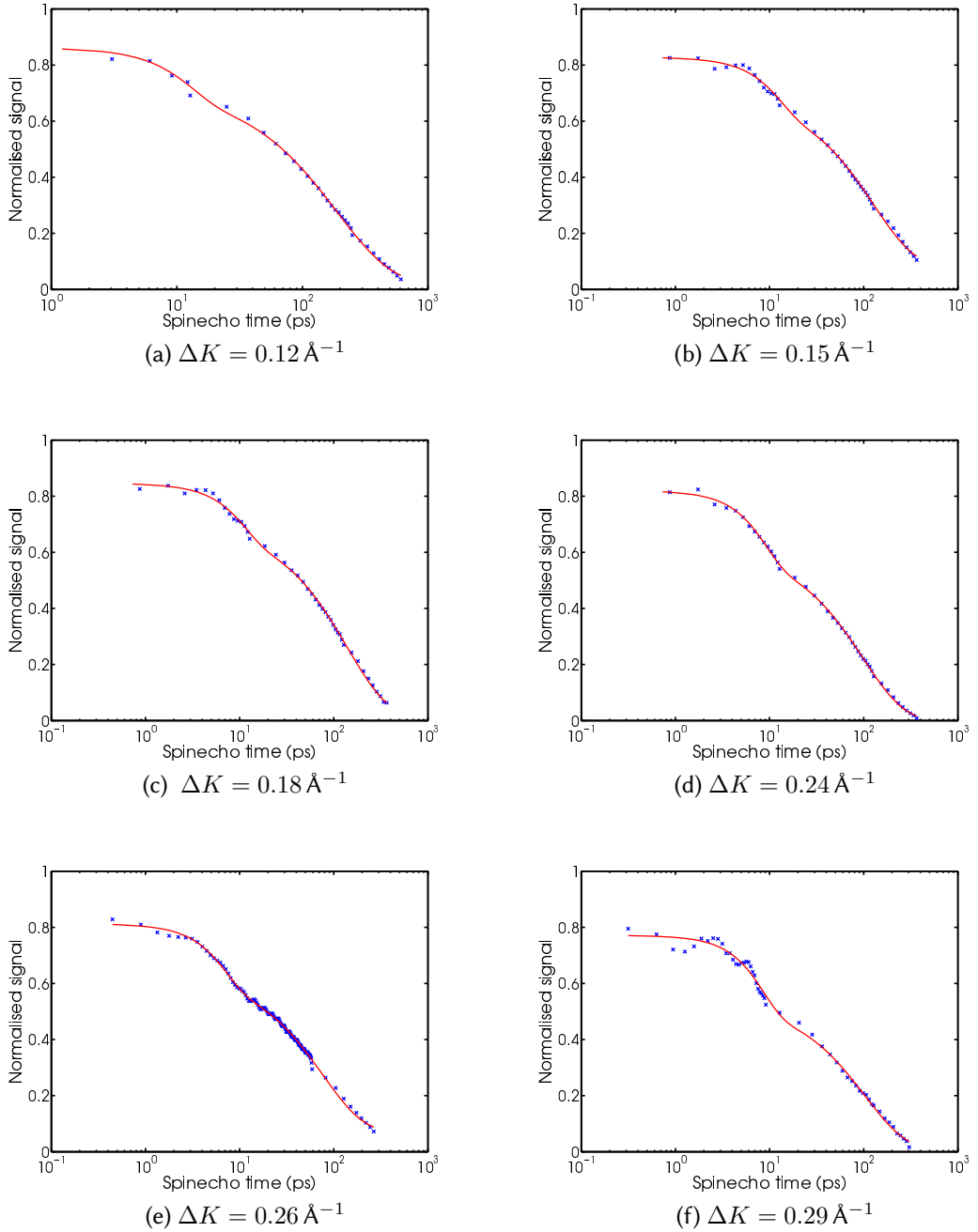


Figure 2.14: Shown as blue points are experimentally measured ISFs for Xe/Pt recorded with a sample temperature 121 K and a Xe coverage of $\theta = 0.02 \text{ ML}$. A function of the form $A_0 \exp(-\alpha t) + A_1 \exp(-t^2/2\sigma^2)$, with parameters optimised using a non-linear least squares method, is shown as a red line in the figures. In some of the figures an oscillatory component is observed, for example panel (f). Oscillations in time spectra relate to inelastic scattering, i.e. energy losses or gains proportional to the oscillation frequency, in the present work they are associated with Pt phonons and are extracted from the spectra before further analysis, using a method detailed in section 4.3.1.

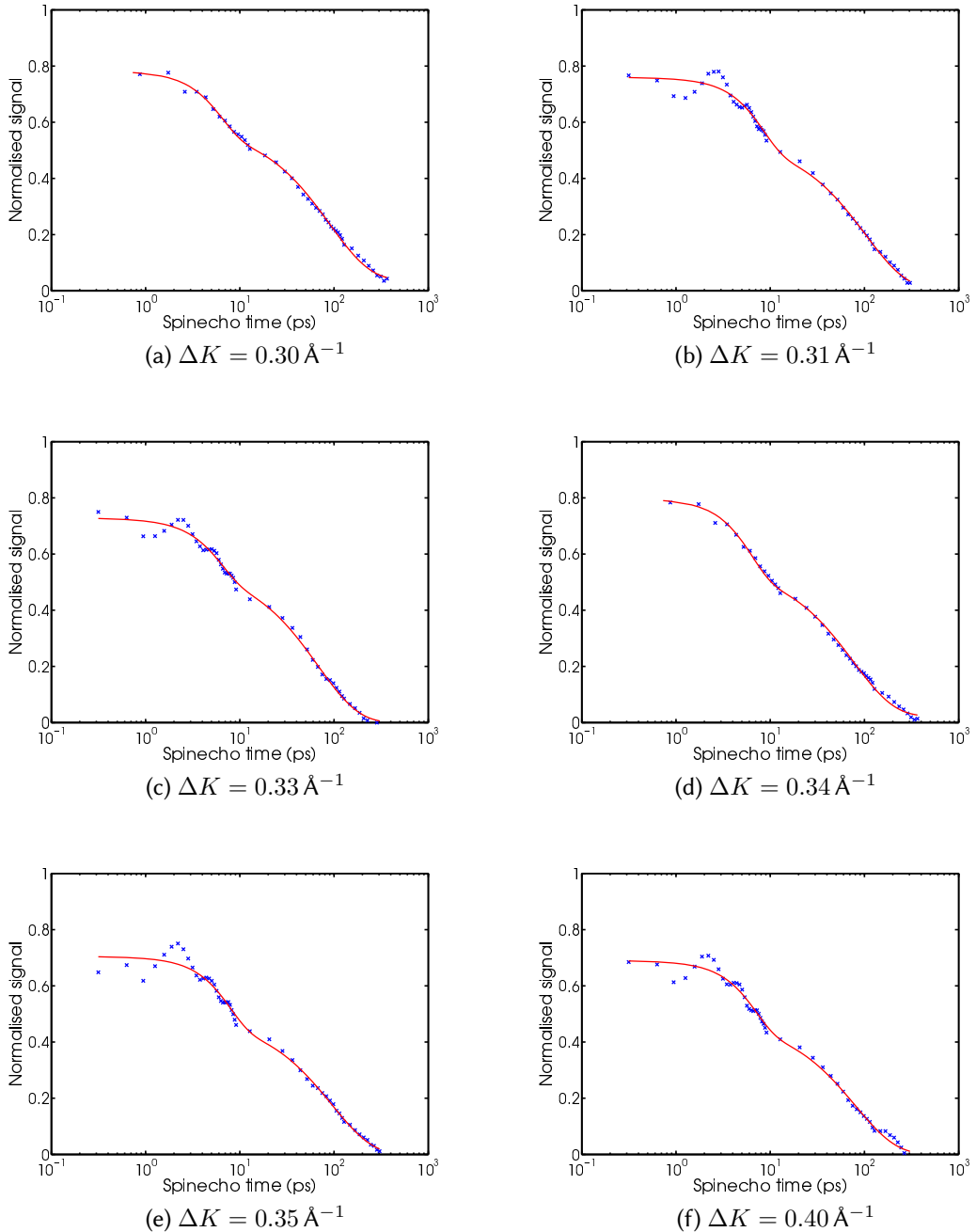


Figure 2.15: See caption of figure 2.14

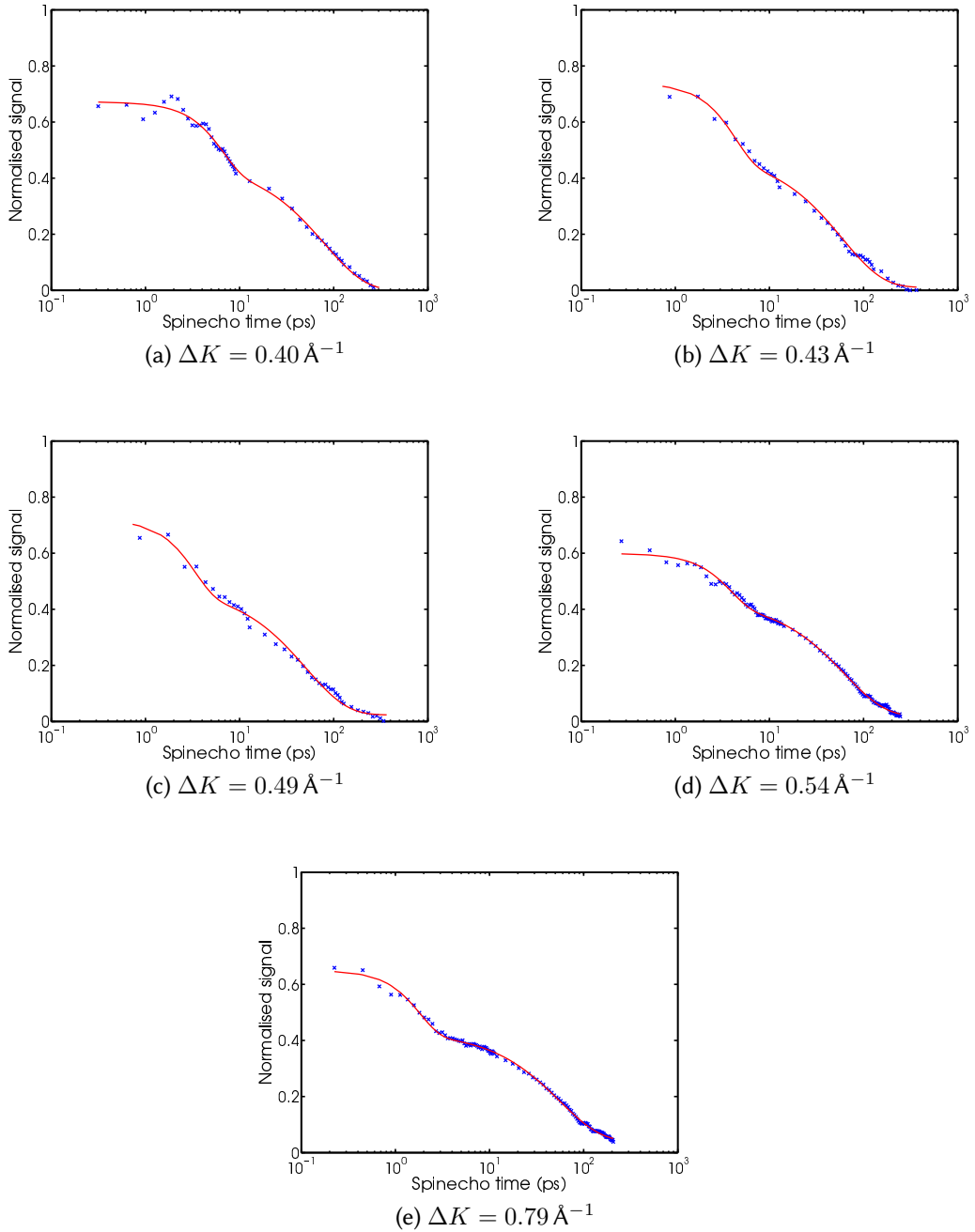


Figure 2.16: See caption of figure 2.14

Information about diffusion can be ascertained by analysing the decay rate of the ISF as a function of ΔK . At large momentum transfer the exponential term decays quickly and it is straightforward to extract the constant term in the ISF, shown in figure 2.12. The process of extracting an accurate static level is more problematic at low values of ΔK . Here the exponential decay is not complete¹ and as ΔK decreases it becomes progressively more difficult to estimate the constant term accurately. Figure 2.17 illustrates the problem. Here the red circles show the value of B in the free fit for $t > 5\text{ps}$ of the form $\text{ISF} = A_0 \exp(-\alpha t) + B$. These points are compared with data for the total scattered signal (blue line), which has been scaled to match at high ΔK . It is clear that the fits of the constant term (red circles) deviate systematically at low ΔK where the exponential decay is incomplete. In order to eliminate the systematic mis-fit, the total scattered signal (blue line in figure 2.17) is used to give the constant term, which is subtracted and the remainder of the ISF fitted to a function of the form $\text{ISF} = A_0 \exp(-\alpha t) + A_1 \exp\left(\frac{t^2}{2\sigma^2}\right)$.

The results of fitting the ISFs are shown in figures 2.14 to 2.16, and a good fit is demonstrated over a range of momentum transfers. Further analysis is performed on the parameters of these lines to characterise the diffusion.

Figure 2.18 shows the Full Width Half Maximum (FWHM) of the fast part of the ISF, σ , measured directly from the data, in this case the width is converted from time to energy units to compare with previous results, using the Fourier relationship²

$$\sigma_E = \frac{2\hbar^+ \sqrt{2\ln(2)}}{\sigma}, \quad (2.2)$$

where σ_E is the FWHM in energy and σ is the FWHM in time. It is clear from figure 2.18 that the data are consistent with the previous work [54] shown by the solid black line. The experimental data therefore shows two distinct phenomena: a diffusive component at slow times and a ballistic component at fast times, with knowledge of the Gaussian, ballistic, contribution we can reduce the parametrisation of the total process to 3 variables; the amplitude of the ballistic part A_0 , and the amplitude, A_1 ,

the exponential observed.

¹Since the present work was carried out, a significant improvement in the time resolution of the apparatus has been achieved [89], which can achieve a factor five improvement on the longest time spectra.

²Equation 2.2 is derived in detail in appendix section A.1.

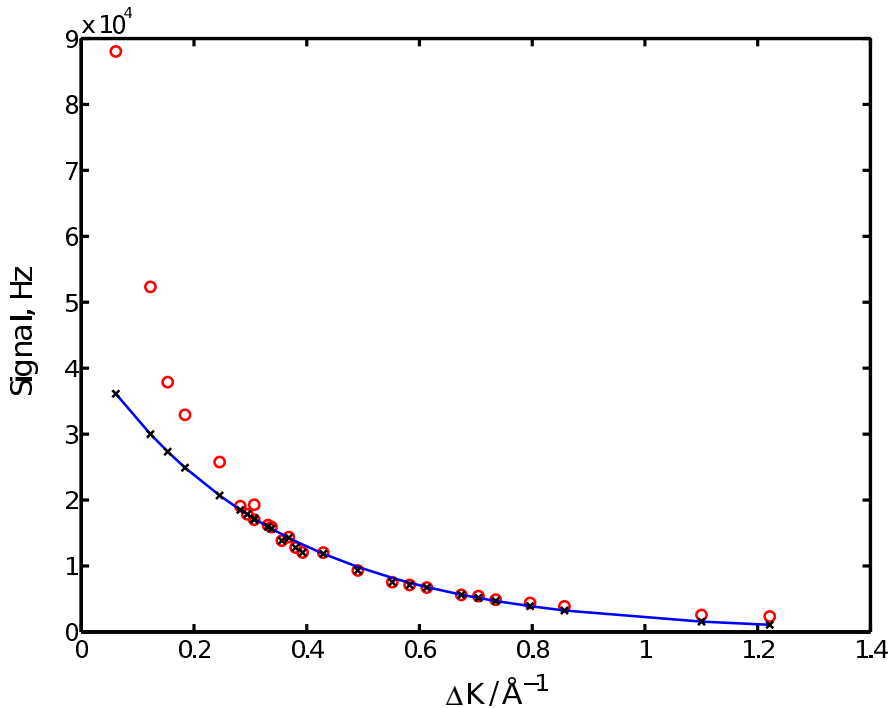


Figure 2.17: Static scattering signal as a function of ΔK , if the decay rate is low, the static scattering signal is not reached in the spin-echo time measured. A particular problem at low ΔK . The static signal that is ‘fitted’ directly from the ISF signal is shown in red circles. The blue line is the result of a static angular scan at zero current scaled to the red circles at large ΔK , and the black crosses are the intersection of the measured ΔK points with the scan line. The value from the black crosses is then used to reduce the uncertainty in the static contribution to the spectra for further functional analysis.

and decay parameter, α , of the diffusion signal.

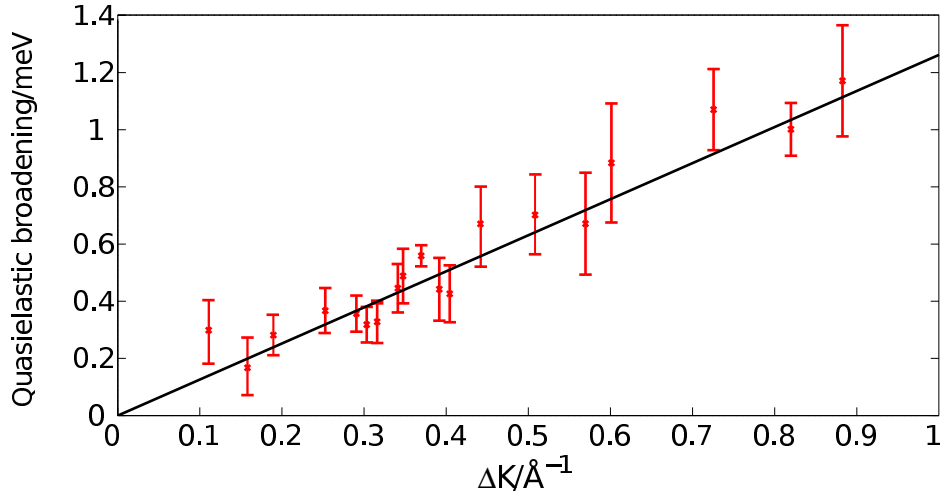


Figure 2.18: Quasi-elastic (ΔE) broadening as a function of surface parallel momentum transfer(ΔK) for the ‘fast’ decay process. The width is measured directly in time from the ISF converted to energy and plotted. The black line is the 2D ideal gas line and is the same line as used in the previous study of Ellis *et al.* [54].

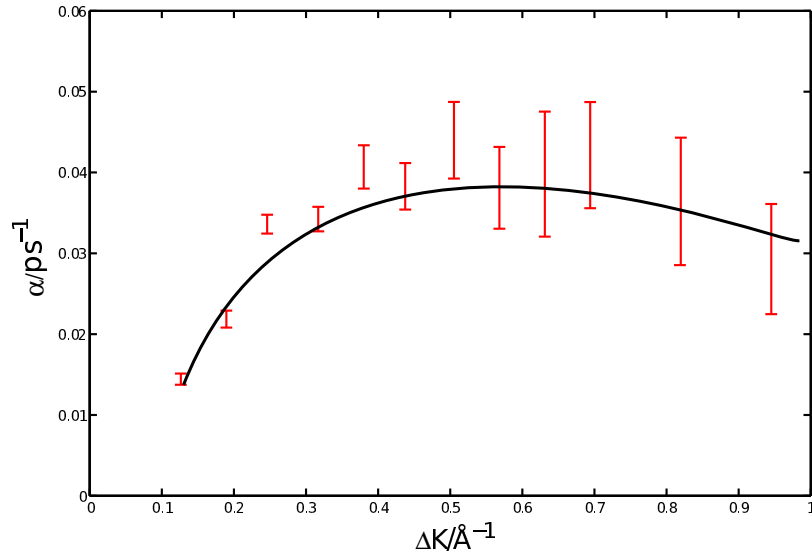
I now consider the diffusive component. Figure 2.19 presents the exponential decay rate as a function of ΔK over the accessible range of 0 to 1\AA^{-1} ¹. Figure (a) shows the data for 0.02 ML while figure (b) shows the data for 0.2 ML. Both panels in figure 2.19 exhibit the characteristic of motion dominated by the underlying periodicity of the substrate with discreet hops between adsorption sites resulting in α increasing initially and then showing evidence of periodicity as momentum transfer increases [90]. There is no discernible difference in the ΔK dependence of the decay rates implying that Xe-Xe interactions have no effect on the observations [91]. Figure 2.20 presents the temperature dependence of the same process, in an Arrhenius plot [92], the decay rate is converted to its Fourier equivalent width in energy using the equation²

$$\sigma_E = 2\hbar\alpha \quad (2.3)$$

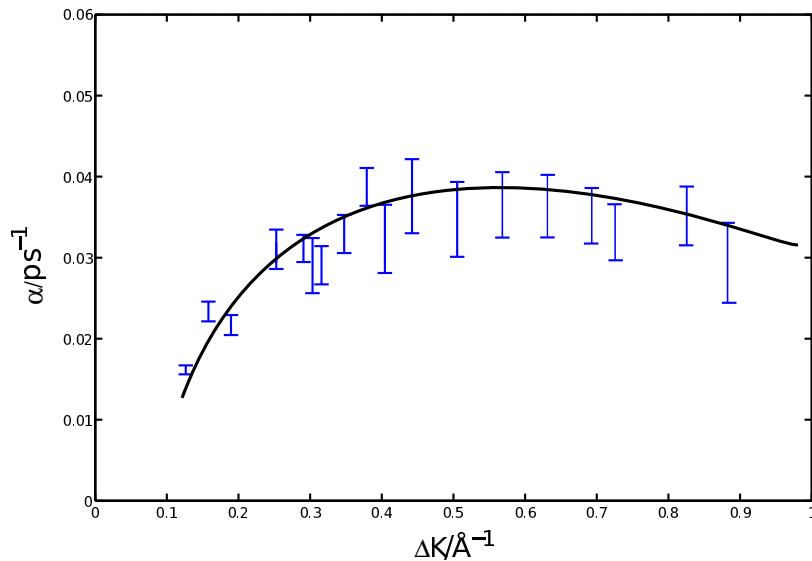
The Arrhenius plot in figure 2.20 displays a linear decay, implying that the process

¹After the current work was performed, significant improvements in the accessible experimental ranges has been achieved, as presented in chapter 3, in part inspired by the results presented in this work

²Equation 2.3 is derived in detail in appendix section A.2.



(a) Slow process $\Delta E \Delta K$ for a coverage $\Theta = 0.2ML$



(b) Slow process $\Delta E \Delta K$ for a coverage $\Theta = 0.02ML$

Figure 2.19: Plot of the quasi-elastic broadening (ΔE) as a function of surface parallel momentum transfer(ΔK) for the ‘slow’ decay process fitted to a single exponential. Panel (a) shows the highest coverage and (b) shows the lowest coverage measured on the same scale. There is no tangible difference between the two coverages demonstrating a lack of coverage dependence, indicative of a single adsorbate process.

is activated; the gradient reveals an effective activation energy, which is found to be 32 ± 8 meV in good agreement with previous experimental work and theoretical potential energy landscapes shown in table 2.1.

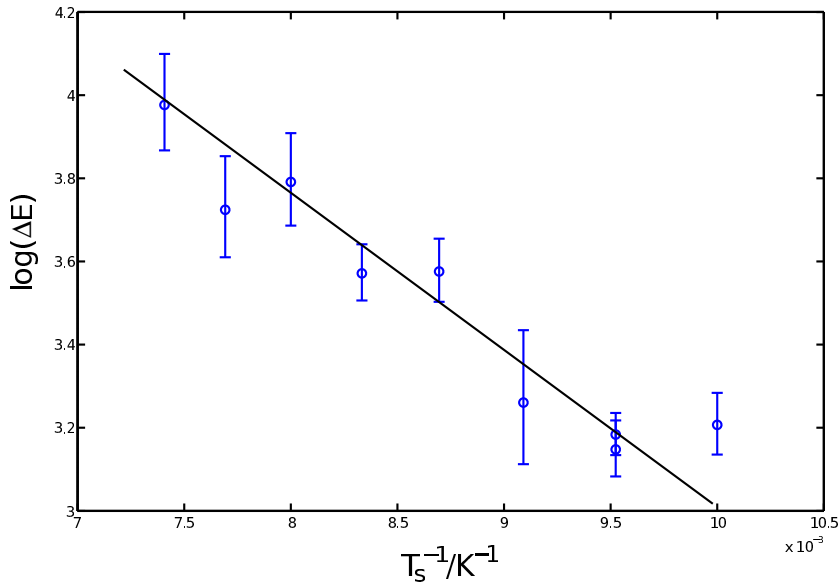


Figure 2.20: Quasi-elastic broadening (ΔE) as a function of surface temperature for the ‘slow’ decay process at a momentum transfer of $\Delta K = 0.5 \text{ \AA}^{-1}$. The width is measured by fitting an exponential in time to the slowest decay form of the ISF. The decay rate in time is converted into energy through the Fourier relationship detailed in chapter 3. The black line presents an Arrhenius law [93] with the gradient fitting an activation energy of 32 ± 8 meV.

Finally, figure 2.21 shows the ratio of the magnitude of the diffusive and ballistic portions, A_1/A_0 . At low momentum transfer, $\Delta K < 0.4 \text{ \AA}^{-1}$, the diffusive term dominates, while at higher values of ΔK the ballistic term is dominant. As will be shown later, the figure is important in getting a full understanding of the system.

2.3 Diffusion signatures for Xe dimers and clusters

The data show two dynamics processes and it is important to distinguish whether the observations are the behaviour of two independent entities or a single species that exhibits different characteristics on short and long time scales. Since there is no evidence for diffusion of a foreign species, the possibility of co-operative diffusion of dimers or larger clusters of atoms is explored. There is no evidence from

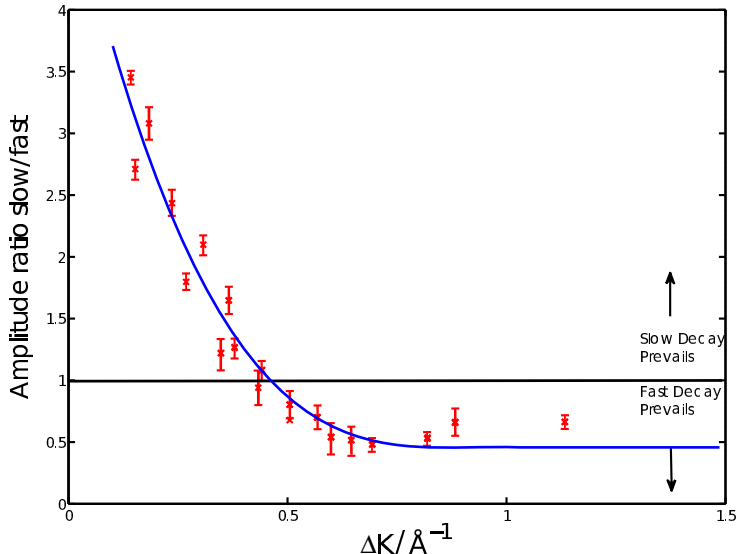


Figure 2.21: Ratio of the slow to fast amplitude, A_1/A_0 , of the phenomena observed in experimental ISFs as a function of ΔK . Below $\Delta K = 0.5 \text{ \AA}^{-1}$ the slow process dominates, a line is provided in blue to guide the eye

the Xe uptake curves shown in figure 2.8 for the formation of islands, which would be evident as a change of rate, or break, in the slope of the specular reflectivity; however, the hypothesis of the co-existence of different entities would be the dominant cause of any coverage dependence that might be expected. To explore the hypothesis of monomer/dimer co-existence, I compare the coverage dependence of the diffusive/ballistic ratio, A_1/A_0 , with a simple thermodynamic model.

If the concentration of Xe atoms and dimers respectively are specified in the usual notation as $[Xe]$ and $[Xe_2]$, and the total coverage of Xe, Θ , as the ratio of adsorbate to substrate atoms, then the equation defining the reversible transition between monomers and dimers is,

$$2[Xe] \xrightleftharpoons{k} [Xe_2], \quad (2.4)$$

where k is the rate parameter which is constant for the given extrinsic parameters of the method. In the standard notation for equilibrium reactions the rate parameter

can be specified as a function of the products and reagents, so that

$$k = \frac{[Xe_2]}{[Xe]^2}. \quad (2.5)$$

If we make the assumption that a Xe dimer has double the scattering cross-section of a Xe monomer, then the total coverage can be written as

$$\Theta = [Xe] + 2[Xe_2]. \quad (2.6)$$

Since we want the result to be a function of $[Xe]$ not $[Xe_2]$ we can re-arrange for $[Xe_2]$ and substitute into eqn 2.5:

$$[Xe_2] = \frac{\Theta - [Xe]}{2}; \quad (2.7)$$

$$k = \frac{\Theta - [Xe]}{2 \cdot [Xe]^2}; \quad (2.8)$$

which can be re-arranged to the quadratic form and solved;

$$2 \cdot k \cdot [Xe]^2 + [Xe] - \Theta = 0; \quad (2.9)$$

therefore the number of of Xe monomers can be defined as follows;

$$[Xe](k, \Theta) = \frac{-1 \pm \sqrt{1 + 8k\Theta}}{4k}.. \quad (2.10)$$

Substituting 2.10 into 2.7 gives the concentration of Xe dimers, $[Xe_2](k, \Theta)$ and therefore allows us to specify the ratio of dimers to monomers, which can be compared to the ratio of amplitudes of the measured dynamic components;

$$[Xe_2](k, \Theta) = \frac{\Theta}{2} - \frac{-1 \pm \sqrt{1 + 8k\Theta}}{8k}; \quad (2.11)$$

$$\frac{[Xe_2]}{[Xe]}(k, \Theta) = \frac{\sqrt{1 + 8k\Theta}}{4} - \frac{1}{4}. \quad (2.12)$$

If we plot $\frac{[Xe_2]}{[Xe]}(k, \Theta)$, as given in equation 2.12, for a range of values of k and compare the results to the amplitude ratio of the dynamic components of the mea-

sured data we can find the limit in k to reproduce the data, this is shown in figure 2.22.

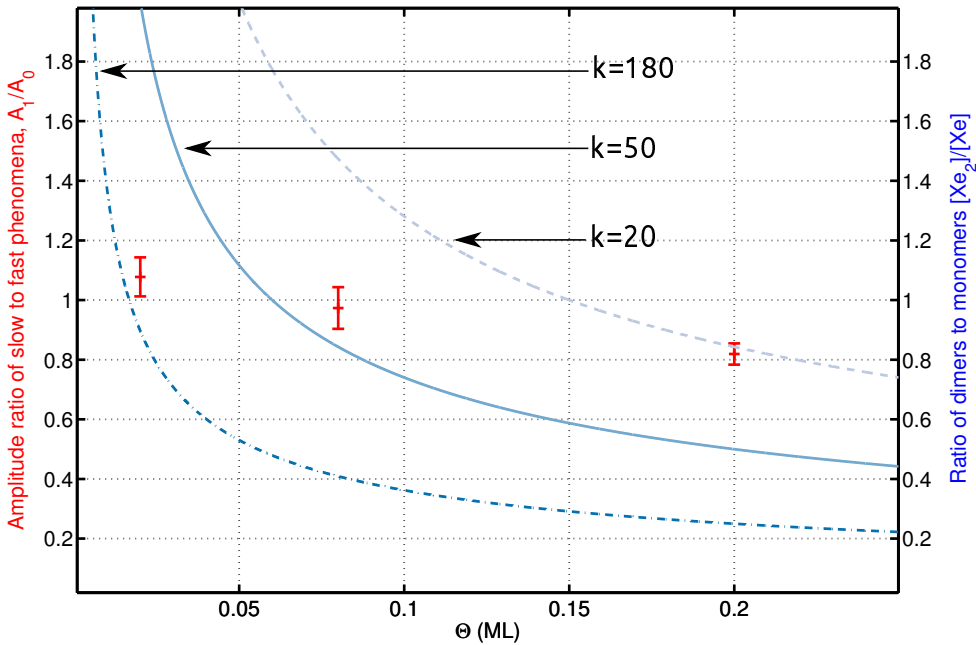


Figure 2.22: Red points show the relative amplitude of the two dynamic phenomena in the ISF measured for Xe at three coverages, 0.02, 0.08 and 0.2 ML at $\Delta K = 0.41 \text{ \AA}^{-1}$. Lines are plots of equation 2.12 as a function of Θ for three values of the rate constant, k .

Figure 2.22 presents the ratio of the amplitudes, A_1/A_0 , in the experimentally observed phenomena, at three different coverages, 0.02, 0.05 and 0.2 ML as red points. On a separate axis shown on the right hand side of figure 2.22 is the result of equation 2.12 for three values of the rate constant, k . If the phenomena are the result of the formation of dimers, and scattering from dimers and monomers is comparable, one would expect the ratio of amplitudes of the components to be in proportion to the ratio of the quantity of the species involved in each. The three lines drawn relate to values of the rate constant, k , chosen to produce lines that coincide with the experimental data. It is clear that three different values of the rate constant would be required, which would not be expected if cluster formation was the cause of the two processes. It is unlikely that dimer formation can explain the phenomenology in the experimental results.

2.4 Langevin Simulations

Having ruled out condensation as a cause of the two phenomena observed in the data, we now turn to an explanation in terms of the transition from ballistic to diffusive motion as an Ornstein-Uhlenbeck process [94] described by the Langevin equation [95]:

$$m\ddot{r} = -\nabla V(r) - \eta m\dot{r} + \epsilon(t), \quad (2.13)$$

where ∇ is the standard gradient operator, $V(r)$ is the potential energy landscape between Xe and the Pt(111) surface, m is the mass of species, r is the position vector, η is a coefficient representing the collective energy dispersing process and ϵ is the stochastic force term [3]. *On average* the stochastic term balances energy lost through the dissipative term of the equation 2.13 and assuming the system is in thermal equilibrium a scaling term can be calculated as first proposed by Kramers in 1940 [96]

$$\sqrt{2\gamma k_B T m}. \quad (2.14)$$

The Langevin equation can be solved analytically for flat surfaces [88]. The resulting formalism is an extension of the thermodynamic solution of motion used by Ellis *et al.* [54] to describe the ballistic motion of a 2D gas to include diffusion on the flat surface but with an effective friction. The key result of Miret-Artés *et al.* [88] is that it is the solution of a Ornstein-Uhlenbeck [94] process, not the equivalent Wiener process which is limited to the long time behaviour, thus allowing analysis of the transition from ballistic to diffusive motion. Unfortunately it is not possible to derive a similar analytical result for an arbitrary potential energy surface, and one must perform molecular dynamics simulations where a sampling time-step is employed and all of the forces on a Xe atom at its instantaneous position vector, $r(t)$, is calculated. From the force vector the acceleration and velocity can be calculated algebraically and the atom's motion propagated for the time-step δt along a ballistic trajectory; subsequently its new position is calculated and the process is repeated.

The absolute position of an atom is mapped onto a simulation unit cell. In the case of this study for the Pt(111) surface, the cell takes a rectangular form with dimensions twice the primitive unit cell¹. The starting conditions for the system places an atom at a random position r_0 in the simulation cell and gives it a random

¹A rectangular unit cell is used to make integration simpler in the simulation cell

velocity from the thermal distribution for the simulation temperature. The system is allowed to propagate for 2 ps to allow the ensemble to thermally equilibrate before data are recorded.

The output of the simulation consists of the ad-atom position at each time step, forming a trajectory. If at each time-step of the simulation the trajectory equates to the position of a scattering centre then we can write the total scattered amplitude at that time as:

$$A(K, t) = \exp(-i(k_x \cdot x(t) + k_y \cdot y(t))); \quad (2.15)$$

$A(K, t)$ is accumulated through the position vector $r(t)$, which in Cartesian co-ordinates is $\sqrt{x(t)^2 + y(t)^2}$, at each time-step, δt , of the simulation. $A(K, t)$ is multiplied by the form factor, F , which for these studies is assumed to be unity for all values of ΔK , and can be Fourier transformed to determine the amplitude in energy space,

$$A(K, \omega) = \hat{F}(F \cdot A(K, t)); \quad (2.16)$$

where \hat{F} denotes the forward Fourier transform, in Cartesian co-ordinates, and k_x and k_y define the momentum vector in Cartesian co-ordinates, defining the surface direction. If $A(K, \omega)$ is multiplied by its complex conjugate, the energy self correlation function is recovered, which can then be inverse transformed to recover the self correlation function in time, the ISF:

$$I(K, t) = \hat{f}(A(K, \omega)A^*(K, \omega)), \quad (2.17)$$

where \hat{f} is the inverse Fourier transform.

The simulation results presented are calculated using a Fortran molecular dynamics code. For this work the Fortran code was ‘wrapped’ in a Matlab function which allows high level functionality such as complex fitting routines and plotting facilities to be accessed while optimising run parameters. The processor time on a quad core Intel desktop computer is of the order 20 sec for a 2 ns simulation with a time-step 1.6 fs.

For numerical calculations the simulation time-step is not a parameter reflecting any physics but it must be carefully chosen for the systems of interest: as the NyquistShannon sampling theorem [97] states, it must be at least double the fre-

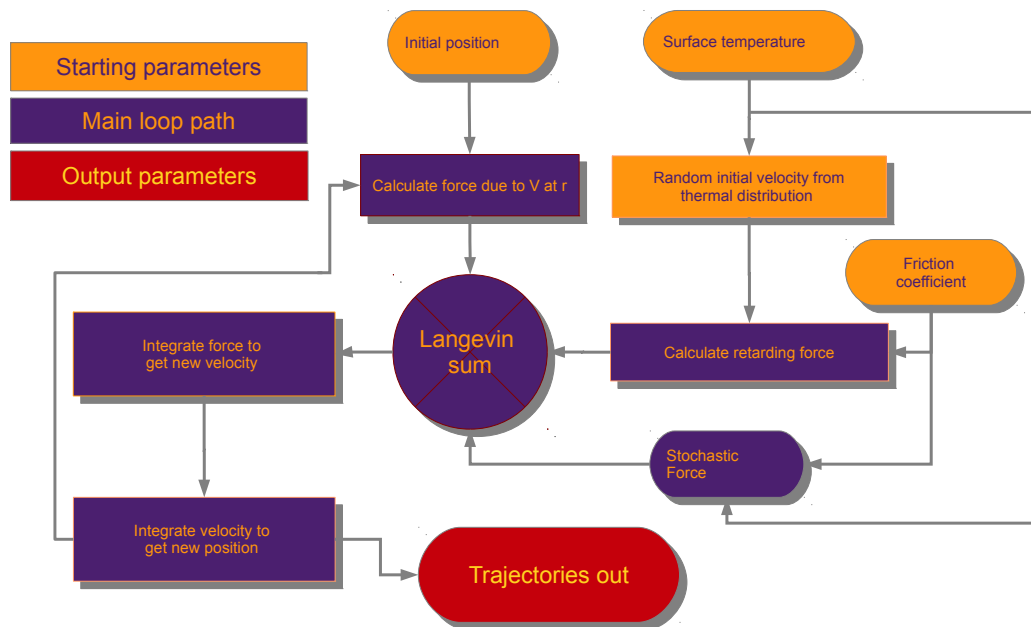


Figure 2.23: Flow diagram illustrating the procedure for performing molecular dynamics simulations using a brute force approach. The sum of all of the force contributions on the atom are calculated at position r at time t , allowing the resultant velocity to be determined with calculus. The ballistic path can be determined using its velocity and the simulation time-step δt . At the end of the time-step the new position is determined and the process repeated for the number of steps in the simulation.

quency of the process of interest. The calculations presented here use a time-step of 1.6 fs which can completely sample processes of frequencies up to 0.3 PHz. Reducing the time-step increases the simulation time linearly, so care must be taken to pick an appropriate value.

The potential and friction terms in the Markovian Langevin equation 2.13 are optimised to tune the simulation results to experimental data. The friction is a fairly straightforward parameter as it is a numerical co-efficient, however the potential energy surface is more difficult to estimate accurately. The activation energy of the diffusion signature in the Arrhenius data in figure 2.20 provides some insight on the amplitude of the Potential Energy Surface (PES) and is a starting point to develop model potentials. One of the simplest ways of calculating a PES is to map a cosine function symmetrically from each adsorption site mapping out the periodicity of the surface. For a cosine potential in the Markovian Langevin equation there are two optimisation parameters (V_{max} and η) for the whole calculation, assuming that the sample temperature and adsorbate mass are fixed.

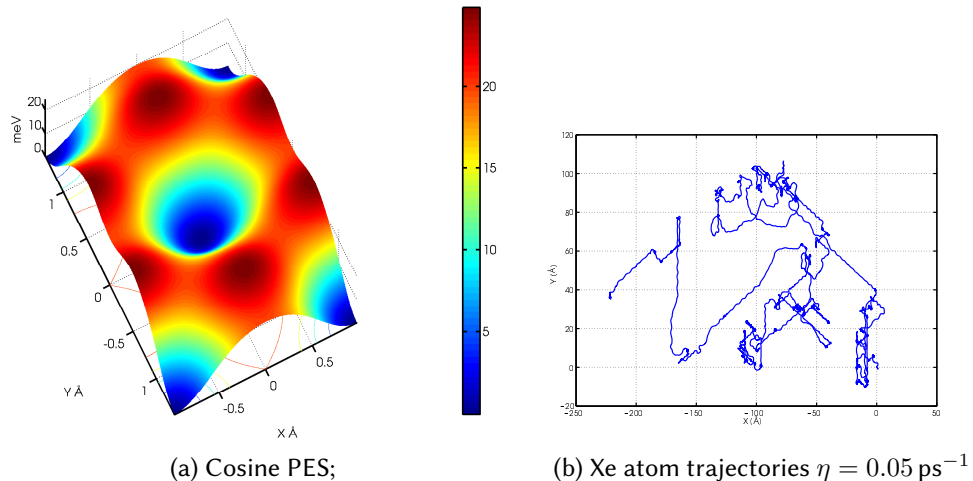


Figure 2.24: Xe-Pt(111) potential energy surface defined by a cosine corrugation with on-top to bridge amplitude 20 meV. Trajectory of a xenon atom with friction co-efficient $\eta = 0.05 \text{ ps}^{-1}$ and surface temperature $T_s = 121 \text{ K}$.

Figure 2.24, panel (a) presents the corrugation for a sample cosine potential energy surface. Panel 2.24b is a representation of a trajectory for a Xe atom for a single 2500 ps run, at a temperature of 121 K and friction of 0.08 ps^{-1} , traversing the PES.

The points with a high concentration of data are the top-sites, where the atoms sit for multiple time steps before being activated and then moving across the surface. Simulations have been performed for a range of temperatures, PES amplitudes and friction coefficients. Calculated results are in the form of ISF, which are then parametrised using the same techniques employed for the experimental data, using a function $A_0 \exp(-\alpha t) + A_1 \exp\left(\frac{t^2}{2\sigma^2}\right) + B$, with σ fixed using the thermodynamic result for ballistic motion, reported by Ellis *et al.* [54]. Any inelasticity observed in the results, as an oscillation in time or separate peak in frequency space, is filtered from the signal using a simple filtering process described later in chapter 4 and appendix D, as they are, in general, due to oscillations within the hollows of the potential.

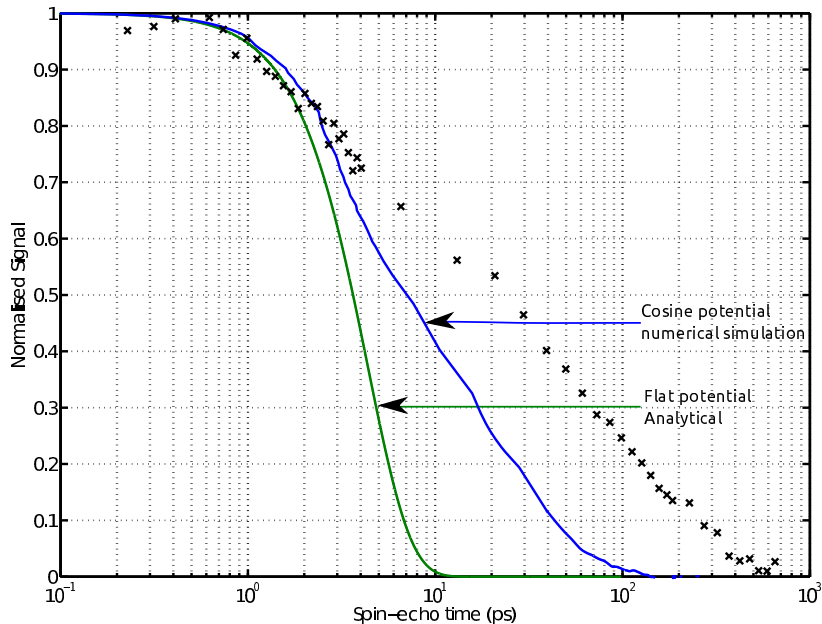


Figure 2.25: Simulated ISF shown in blue for a molecular dynamics simulation using a cosine PES with top-site to fcc-hollow amplitude 20 meV, as shown in figure 2.24a. The ISF presented, shown as black crosses, is taken at $\Delta K = 0.4 \text{ \AA}^{-1}$ at 121 K, with friction coefficient, $\eta = 0.05 \text{ ps}^{-1}$, and time-step δt , 1.6 fs. The green line presents the analytical solution to the Langevin equation for diffusion on a flat surface as presented in reference [88] under the same conditions for comparison.

The blue line in figure 2.25 shows a simulated ISF for a 20 meV cosine potential energy surface at surface temperature 121 K, coefficient of friction 0.05 ps^{-1} and

momentum transfer 0.4 \AA^{-1} . The green line is the analytical result of the Langevin equation for the flat surface [88] under the same conditions. The addition of the potential in the simulation slows the diffusion while the width of the ballistic component, being independent of the potential and friction remains constant and in agreement with the experimental result of this work and the previous study of Ellis *et al.* [54]. The parameters of the line shape are plotted as a function of momentum transfer and temperature and compared with experimental results.

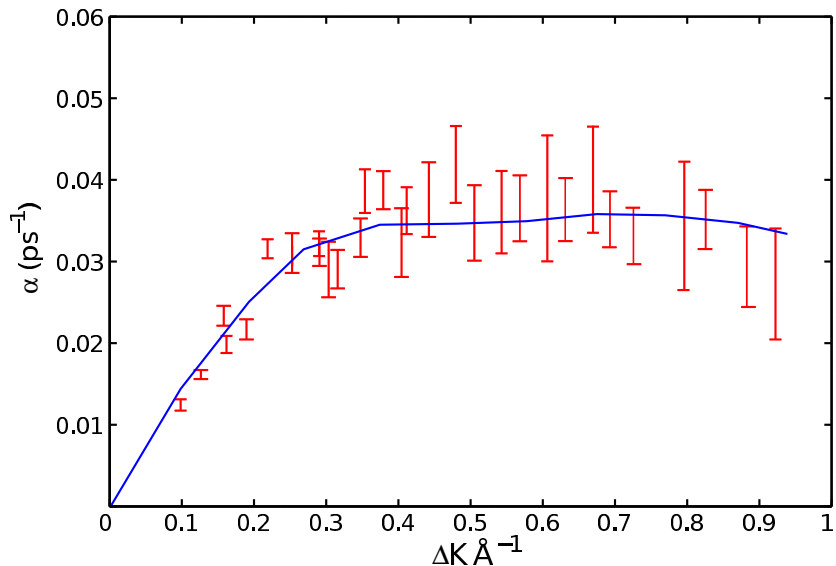


Figure 2.26: Graph showing the decay rate, α as a function of momentum transfer at sample temperature 121 K, red points are experimental data. The blue line is the result of molecular dynamics simulations using a cosine potential energy surface with amplitude 20 meV with friction coefficient 0.05 ps^{-1} . The diffusion results fit the experimental data exceptionally well in this case.

Figure 2.26 presents exponential decay rates for the diffusion process as a function of momentum transfer. Experimental data is shown in red and the results of a molecular dynamics calculation shown as a blue line for the conditions of sample temperature 121 K, 20 meV PES and friction coefficient 0.05 ps^{-1} . The agreement between simulation and the experimental decay rates is very good across the momentum transfer range accessible. Similar agreement is achieved for the temperature dependence of the process. The friction coefficient implies that diffusive motion will not become predominant until times greater than 20 ps, which again concurs with

the observations in the measured ISFs; for example 2.13.

When comparing the total shape for the ISF, good agreement between cosine PES molecular dynamics simulations and experimental data is observed for the width of the Gaussian ballistic component and the decay rate of the exponential with respect to momentum transfer and temperature; however the relative fraction of the ISF is more significantly skewed to diffusion in the simulation than observed for experimental data in general. Figure 2.27 presents the relative amplitude of the diffusion to ballistic components of the experimental data and molecular dynamics simulations, conducted using the cosine PES with parameters that give the best affinity with the experimental diffusion properties. There are systematic deviations from the experimental data, demonstrating a greater proportion of the atoms in the transition state than the simulation. There is nothing that can be changed within the cosine PES or friction coefficient that will improve the ballistic amplitude without compromising other aspects of the data.

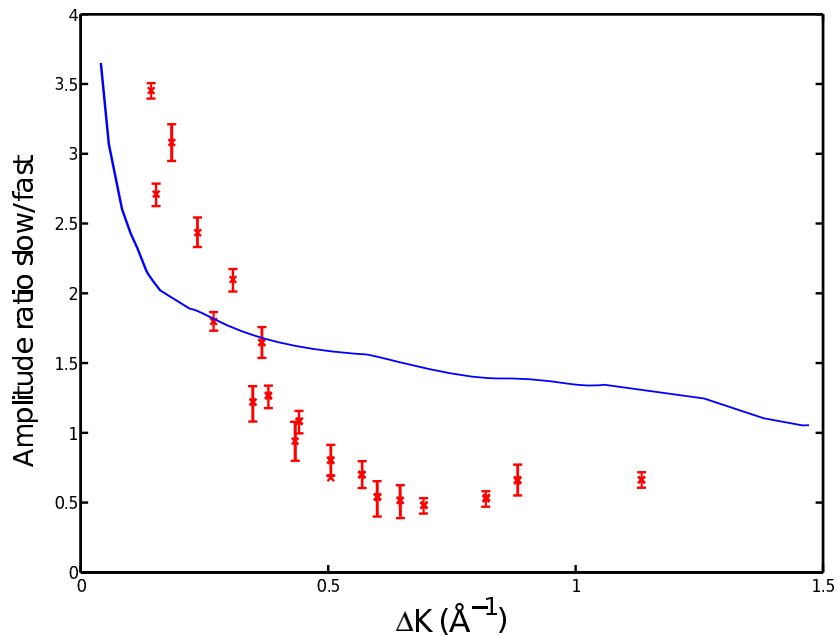


Figure 2.27: Ratio of amplitude of diffusive component to the ballistic one; experimental data is shown as red points and molecular dynamics simulations as a blue line. Simulations use a cosine PES of amplitude 20 meV and friction co-efficient 0.05 ps^{-1} . All data has a surface temperature of 121 K.

Comparison of the slow decay process with simulations, figure 2.26, shows that

the behaviour at longer times, which correspond to the diffusive regime, is well described by the cosine potential. However, figure 2.27 shows that the cosine potential fails to describe the ratio of slow to fast components in the ISF. Specifically, at large ΔK the model (blue curve in fig 2.27) shows the amplitude of the slow component larger than that of the fast component, whereas the data has the slow component smaller than that of the fast component. Clearly the model needs to be changed in order to increase the relative number of atoms in the ballistic motion phase. Later in the thesis I investigate how this might be achieved by modifying the noise spectrum, which requires a treatment beyond the approximation inherent in the Markovian Langevin equation. Here, I retain the ohmic friction co-efficient and examine whether changes in the potential can explain the data. One obvious approach is to increase the short-time, ballistic component, at the expense of the long-time, diffusive component by flattening the landscape over a significant area of the unit cell. The adsorption sites and barrier to diffusive motion can be retained while the particle spends a longer time in the flat regions, where it behaves ballistically. Such a potential, termed a ‘tabletop’ potential, has been created by starting with a potential plateau at a fixed position, and then defining a critical radius around the adsorption sites inside of which a cosine shape is applied. Critical radii of $1/8$ to 1 atomic spacings have been used and radius of $1/3$ of the atomic spacing is found to produce the best results. The potential with the optimum radius is shown in figure 2.28 panel (a), and a trajectory calculated using the potential in panel (b), which may be compared to the cosine potential shown in figure 2.24.

Figure 2.29 presents the simulated ISFs for the cosine potential presented in 2.24a as a blue line, tabletop potential presented in 2.28a as a red line, and flat surface analytical result reported by Miret Artés *et al.* [88] as a green line. Experimental data is shown as black crosses. The diffusion parameters for the two simulated potentials show similar decay rates and the width of the Gaussian component is the same for all three line types. As desired, the effect of the tabletop potential in this case is to modify the relative amplitude of the ballistic to Gaussian contribution. To investigate the parameters of the simulation, and similarly to the results of the cosine potential and experimental results, the output of the simulations are analysed and the parameters compared to the experimental data.

Figure 2.30 presents the $\alpha/\Delta K$ results, and figure 2.31 the temperature depen-

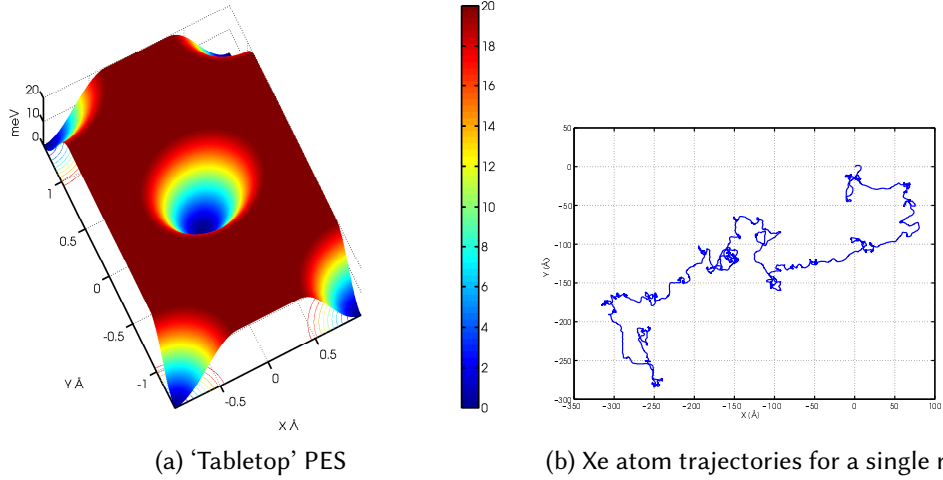


Figure 2.28: Xe-Pt(111) potential energy surface defined by a tabletop of critical radius $a_n/3$, where a_n is the closest atomic spacing. On-top to bridge amplitude is 20 meV. Trajectory of a xenon atom with friction co-efficient 0.05 ps^{-1} and surface temperature 121 K is shown in the right panel.

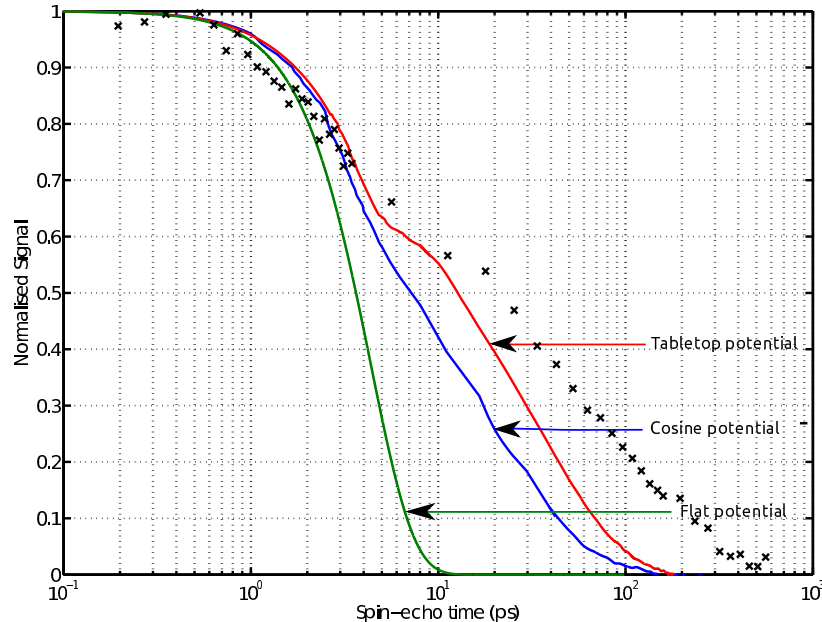


Figure 2.29: Molecular dynamics simulation ISFs for $\Delta K = 0.4 \text{ \AA}^{-1}$ at surface temperature 121 K and friction co-efficient $\eta = 0.05 \text{ ps}^{-1}$. The line shown in blue uses a cosine potential of amplitude 20 meV (figure 2.24a). The Red line produced using a tabletop potential (figure 2.28a) amplitude 20 meV and in green, the analytical solution for an Ornstein-Uhlenbeck [94] process on a flat surface [88].

dence, as an Arrhenius plot, with experimental results shown in red, cosine potential molecular dynamics simulations shown as a blue line and $a_n/3$ tabletop potential results shown in black. The yellow shaded region encapsulates the results of tabletop PESs with amplitudes between 18 and 22 meV and coefficients of friction, η of 0.01 ps^{-1} to 0.1 ps^{-1} , the optimum values are 20 meV and 0.05 ps^{-1} , highlighted by the black line and the results of the tabletop potential demonstrate equivalent agreement with the diffusion parameters compared to the cosine potential.

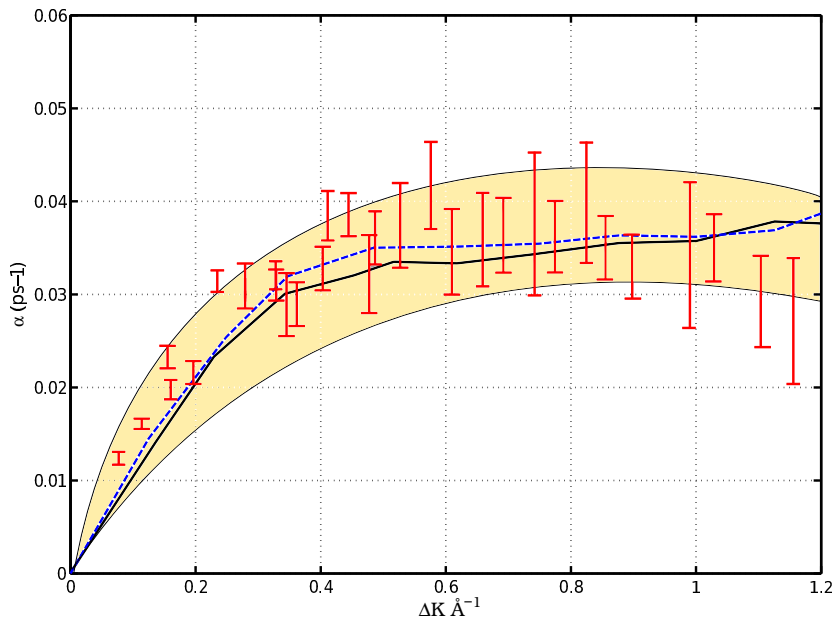


Figure 2.30: Graph showing the decay rate, α as a function of momentum transfer at sample temperature 121 K, red points are experimental data. The yellow shaded region represents the regime of results for molecular dynamics simulations using a cosine and ‘tabletop’ potential energy surfaces. On-top to bridge site amplitudes of 18 to 22 meV and friction coefficients of 0.02 to 0.13 ps^{-1} are used to highlight the sensitivity of the results to the parameters. The dashed blue line is the result of molecular dynamics simulations for the cosine potential and the black line a tabletop potential with a critical radius $a_n/3$; both have potential amplitude 20 meV and friction 0.05 ps^{-1} . The diffusion results fit the experimental data well in either potential model.

Figure 2.32 presents the ratio of slow to fast amplitude (A_1/A_0) of the two phenomena observed. The Black line is the result for the tabletop molecular dynamics simulation analysed using the same method as that used for the experimental data,

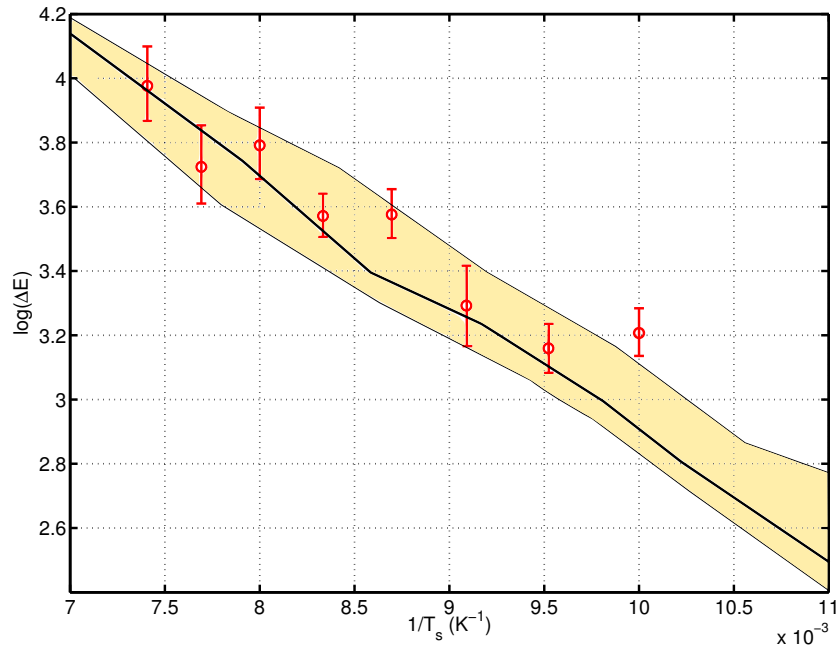


Figure 2.31: Plot of the temperature dependence of the diffusion fit parameters. Experimental data is shown in red with simulations using a tabletop potential with cosine profile ‘holes’ of radius $a_n/3$ shown as a black line. The yellow shaded region presents the sensitivity to the parameters encapsulating all results for potential amplitudes 18 to 22 meV and friction coefficients of 0.02 to 0.13 ps^{-1} .

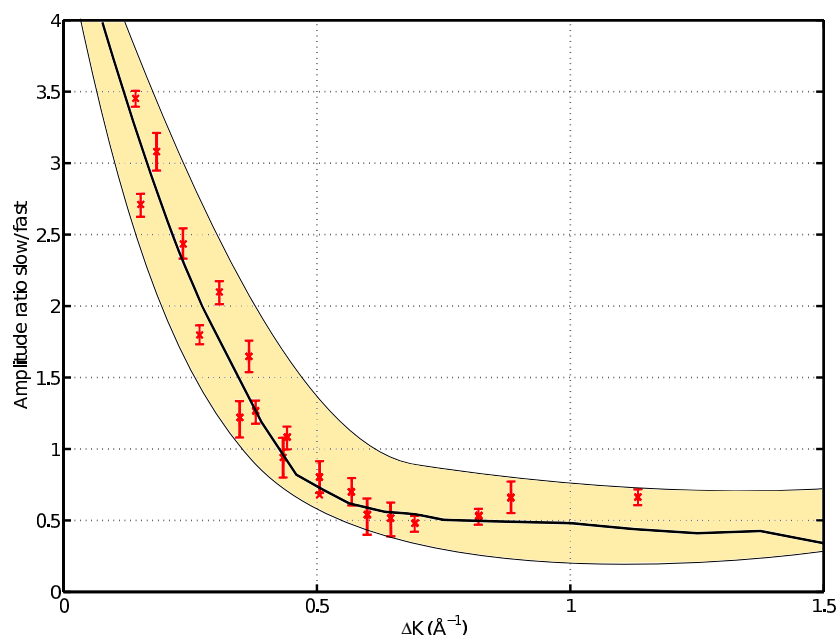


Figure 2.32: Amplitude ratio of slow over fast phenomena as a function of ΔK . Experimental data is shown in red points, the black line is the result of the optimised parameters of Langevin molecular dynamics simulations using a ‘tabletop’ potential with a critical radius $a_n/3$, with an amplitude 20 meV, friction coefficient 0.05 ps^{-1} , temperature 121 K. The yellow shaded region represents the results for the same simulation with potential amplitude ranging from 18 to 22 meV and friction 0.05 ps^{-1} .

i.e. fitted to a functional form $ISF = A_0 \exp(-\alpha t) + A_1 \exp\left(\frac{t^2}{2\sigma^2}\right)$, where σ is defined by the thermodynamic equation for the ΔK and temperature [54]. There is an exceptionally good agreement for all of the data with the tabletop potential model, particularly the amplitude ratio, which did not reproduce the experimental data with the simple cosine model initially used, as illustrated in figure 2.27.

2.5 Conclusions

Xenon dynamics on the platinum(111) surface have been measured with unprecedented precision, at temperatures between 90 and 140 K and coverages less than 0.2 monolayers for length scales equivalent to momentum transfers up to 1.1 \AA^{-1} . The first good combined analysis of ballistic and diffusive motion using ${}^3\text{HeSE}$ is presented as a result of this work. Experimental evidence shows a significant ballistic contribution to dynamics in a corrugated landscape, reconciling existing work and explaining that of Ellis *et al.* [54]. The work is consistent with that of theory and LEED. Langevin molecular dynamics simulations have enabled an energy landscape to be proposed where an enhanced ballistic component is achieved through the use of a ‘tabletop’ potential. It is interesting to compare the table-top model with the results of DFT calculations; see figure 2.33 for a comparison of the potential models.

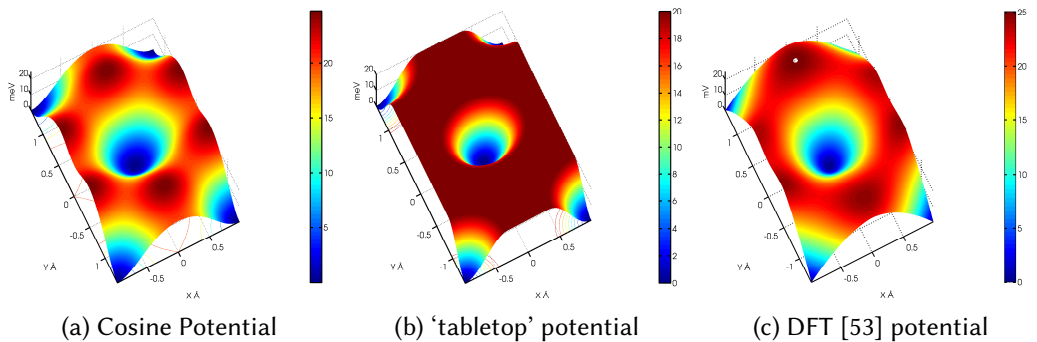


Figure 2.33: Calculated DFT potential from Scheffler *et al.* [53], compared with the tabletop and cosine potentials used in this work

It is clear from the present work that there are significant challenges in measuring relatively simple systems. It is particularly difficult to describe the ballistic and diffusive components with a simple energy landscape and friction within the Langevin framework. The remainder of the work addresses these issues through the

improvements necessary in experimental procedures to capture ISFs in a more precise way and in the analysis and identification of phenomenology within line-shapes and methods of simulation of more realistic systems.

Chapter 3

The spin-echo spectrometer and instrumentation considerations

In chapter 2, spin-echo measurements of the diffusion of Xe/Pt(111) have shown that the ISF can be used to characterise dynamics on different length and time scales and that in order to understand the dynamic processes it is often desirable to measure the ISF on short ($t_{SE} < 5 \text{ ps}$) as well as long timescales.

In order to properly measure the ISF at small spin-echo times, it is necessary to perform more precise measurements than may be performed at longer times. As has been seen in the work of chapter 2, inelastic scattering from substrate phonons (and in fact any inelastic scattering) is observed as a decaying oscillation in time, which will have the greatest magnitude as the spin-echo time tends to zero. When considering simple diffusion processes, such as jump diffusion or 2D Brownian motion; on the smallest timescales they must appear ballistic between interactions, and the shape of the ISF at smallest times should reflect this. In order to ease the separation of the contributions to the ISF at small times it is necessary to measure the precise polarisation, which means using high resolution power supplies to control the precession fields, and making sure that the magnitude and phase of the polarisation, i.e. the complex polarisation vector, is measured precisely. A practical method for improving the measurement of the complex polarisation vector is now addressed.

3.1 Precise measurement of the spin-echo point

It has been shown in section 1.2.2 that the ISF can be written in terms of a real and imaginary polarisation: $Re[P] = Re[ISF(\Delta K, t)/ISF(\Delta K, t = 0)]$ and $Im[P] = Im[ISF(\Delta K, t)/ISF(\Delta K, t = 0)]$, and it is therefore necessary to determine the ISF at $t = 0$ precisely to calculate $ISF(\Delta K, t_{SE})$, at an arbitrary t_{SE} . If the current in the incoming solenoid shown as \mathbf{d} in figure 1.9 is defined as I_1 , and the outgoing solenoid I_2 , then naively, one would expect the maximum polarisation to occur at $I_1 = I_2 = 0$ since that would correspond to no rotation of the polarisation vector, however, experimentally this is not observed to be the case. Practical hardware implementations that affect the magnetic fields between the polariser and analyser will cause changes to the polarisation vector, these include:

- misalignment of magnetic elements;
- differences between the two coils and their driving circuits;
- supply current mismatch when the coils are supplied from different power supplies;
- external magnetic fields penetrating the beam path.

The issue is illustrated in figure 3.1 which shows schematically three lines corresponding to measurements of polarisation in an ideal measurement (black dashed), real elastic measurement (blue) and QHAS dynamics measurement (red). An experimental measurement made by scanning one of the precession fields while maintaining the other at the zero field condition is shown in figure 3.2, a shift of the centre of the spectrum from $I_1 = 0$ is clear. Further to the presence of a shift in the spin-echo point, some effects are observed to vary with time and other environmental factors, particularly precession current and local temperature, and we need to measure and calibrate the spin-echo point to ensure accurate dynamics measurements. The method of calibration involves making small adjustments to the polarisation vector shown in figure 3.1. In the remainder of this section a method is outlined to determine the complex polarisation vector given the beam energy and energy distribution outlined already, used both for calibration at the start of a measurement and to determine dynamics measurements.

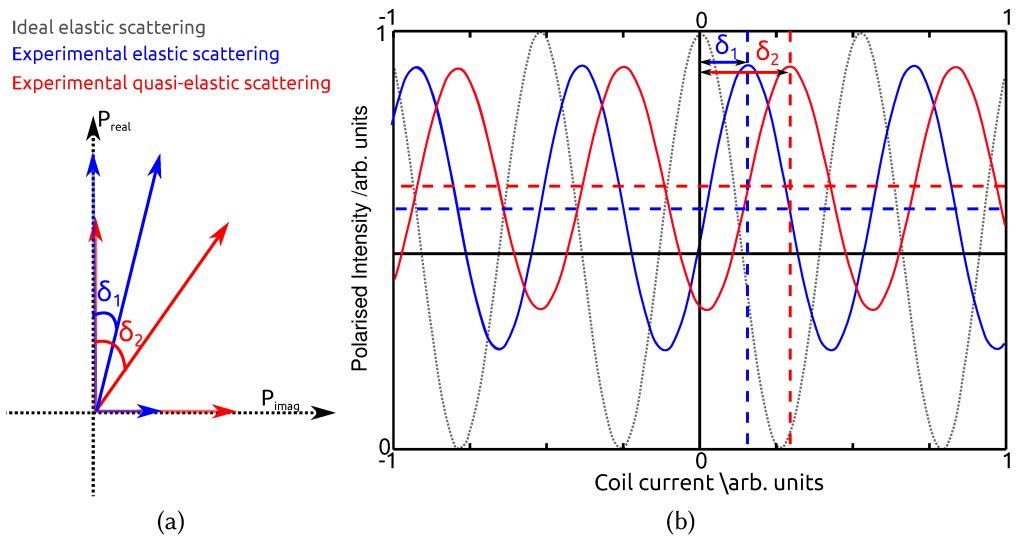


Figure 3.1: Schematic representation of the spin echo point. Panel (a) represents the polarisation with magnitude and phase angle looking along the beam direction. (b) shows a representation of the signal as the precession field varies and the phase angle in panel (a) rotates, and is similar to the data collected experimentally and shown in figure 3.2. The beam spread σ is large compared with the frequency ω for typical beam conditions and therefore the envelope is not displayed on this schematic for simplicity. For an ideal measurement of a static, clean surface at low temperature, that only exhibits elastic scattering, the polarisation would be aligned on the vertical axis, and the curve would take the form of the black, dashed line. The blue line represents a typical experimental measurement of an elastic process, and has a non-zero phase and a reduced amplitude due to a total polarisation of less than 100%. The red line shows a representation of the measurement of an oscillation when dynamics measurements are being made, with dynamical information related to the difference between the curves.

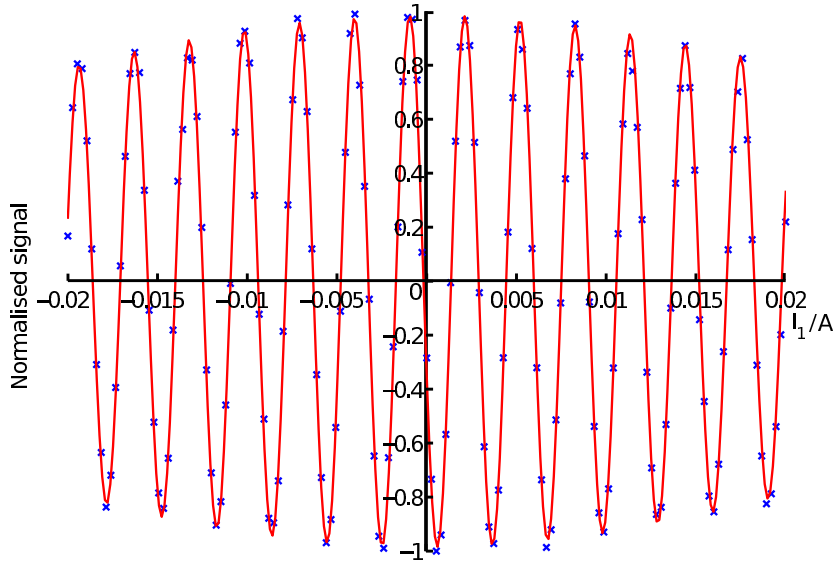


Figure 3.2: Sinusoidal variation of the signal at the detector as a function of the incoming precession current, I_1 , varying from -0.02 to 0.02 A, with I_2 held at 0 A.

3.1.1 Phase coil - Implementation and Calibration

In principle the simplest way of measuring the complex polarisation is to rotate the polariser (**b** in figure 3.3), in the plane perpendicular to the direction of the beam; between the angles 0 to 2π with respect to the analyser. Mechanical rotation of magnetic devices on the instrument is virtually impossible and in practice there are simpler solutions. Classically, the precession fields can be considered as spin-encoding and decoding regions where the spin vector is rotated by a fixed number of turns in opposite directions in each of the precession fields. Assuming that the beam is mono-energetic, the ingoing spin vector may be rotated with respect to the outgoing one by increasing the magnetic field integral in the ingoing precession field, either by increasing the length of the coil or by increasing the field strength in the ingoing coil¹. The most convenient approach is to add an additional ‘phase coil’ in the region before the ingoing precession region, shown as **j** in figure 3.3. The

¹A mono-energetic beam is an acceptable assumption for these measurements as the beam energy is typically 8 meV, and the beam spread is typically less than 2%. With extensive measurements over a long period of time, it is found that for stable source configurations, and stable local temperatures, there is a standard deviation in the beam energy of less than 1% over a period of several days.

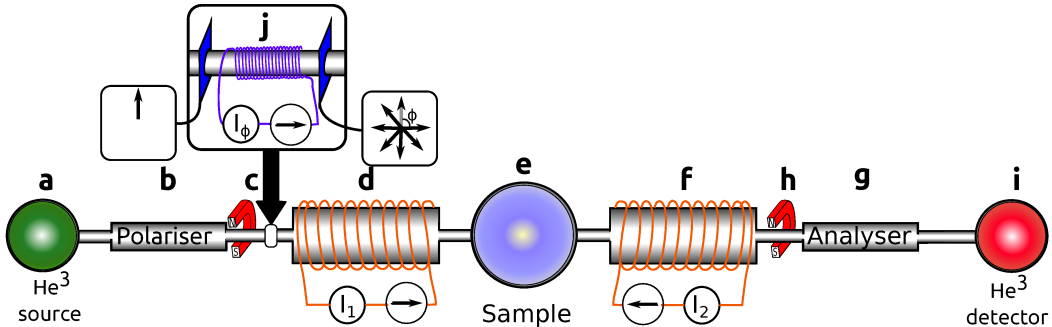


Figure 3.3: Schematic, plan view of the spin-echo apparatus, shown without the fixed 45° scattering geometry for simplicity. **a** to **i** are described in figure 1.9, and **j** shows the position of the phase coil, which is used to rotate the polarisation vector, after it has been aligned at **c**, and before it enters the precession field **d**.

Parameter	Value
Coil length	$22 \pm 1 \text{ mm}$
Wire diameter	24 SWG ($\approx 0.5 \text{ mm diameter}$)
Number of turns	25
Inner diameter of coil	90 mm
Coil Resistance	$0.22 \pm 0.02 \Omega$

Table 3.1: Physical properties of the phase coil as installed in the spin-echo apparatus, shown in figure 3.3.

physical parameters of the phase coil are shown in table 3.1. A commercial power supply (35V,5A) is used to pass current through the phase coil and it is desirable to utilise the full resolution of the power supply to get the maximum sensitivity for calibrating the phase.

For a typical beam energy of 8 meV it was determined that the period of a full spin rotation is approximately 0.7 A and the full scale of the current supply used is 5 A. A current divider circuit is implemented, shown in figure 3.4, with resistors attached to a water cooled heat sink to increase temperature stability. It is necessary to determine the relationship between the phase coil field and the main precession field, so that the properties of the beam can be measured with either coil without direct knowledge of the magnetic fields, which are difficult to measure inside the vacuum system. Figure 3.5a shows a measurement similar to figure 3.2, measured over many periods between $\pm 0.02 \text{ A}$ with ≈ 101 data points. Figure (b) shows the

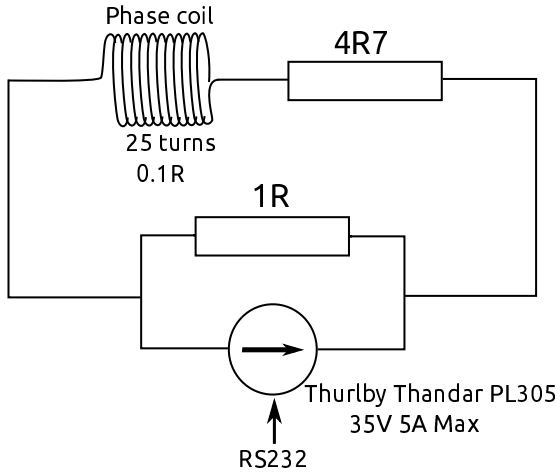


Figure 3.4: Power supply for phase coil. The two resistors act to divide the total current in a ratio of approximately 5:1. The current from the supply varies from 0 to 5 A utilising the full precision of the supply, while the current through the coil varies between approximately 0 to 1 A. The precise value of the current is unimportant in this work as addressed in the text.

same measurement made using the phase coil power supply over a range $I\phi = \pm 4 \text{ A}$ ¹. For an ideal measurement of a clean crystal at low temperature, the polarisation would be proportional to the amplitude of the cosine signal, and the amplitude of the imaginary signal would be 0. In both panels of figure 3.5 there is a clear non-zero sine component in the spectrum, shifting in the spin echo point from the 0 current position. The red line in panel (a) can be obtained by optimising the parameters of the model

$$In(I) = \alpha \exp\left(\frac{-I^2}{2\sigma^2}\right) [\cos(\omega I + \delta)] + (C + Bkg), \quad (3.1)$$

$$= \exp\left(\frac{-I^2}{2\sigma^2}\right) [A \cos(\omega I) + B \sin(\omega I)] + (C + Bkg), \quad (3.2)$$

where I is the current through either the precession or phase coils, using a non-linear least squares method, applied in Matlab curve fitting toolbox. Ignoring all of the parameters apart from the oscillation frequency, ω , for now, from figure 3.5 we

¹For the displayed measurements both polarities were measured by manually inverting the output of the power supply, as the available power supply is not bi-polar.

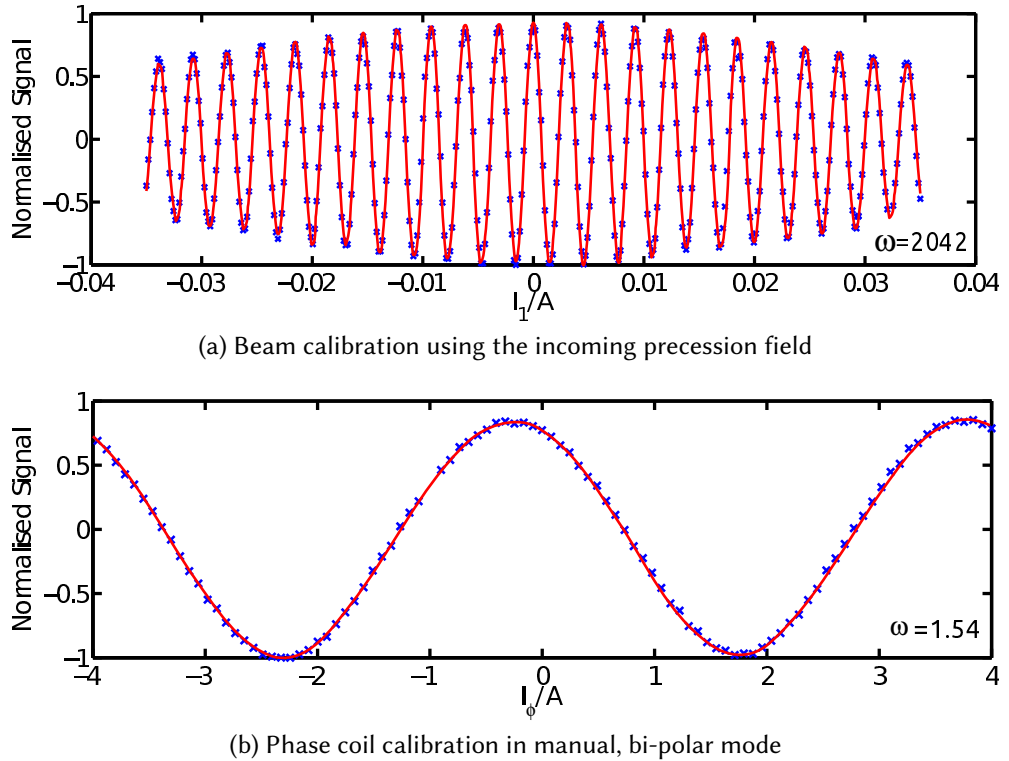


Figure 3.5: Comparison between a polarisation measurement using the main precession coil power supply and the phase coil power supply for Cu(111) at 100K. Panel (a) is used to determine the beam energy distribution, the width of which is defined by the envelope function clearly visible in panel (a). It is clear from panel (a) that in comparison to the period of oscillation, the rate of decay in amplitude is small, indicating a narrow energy distribution. Panel (b) shows a similar measurement using the phase coil power supply, which has a much smaller range, and at typical beam conditions can measure a maximum of two oscillation periods. The red line in each figure is the result of optimising a function shown in figure 3.2, and the results are used to calculate the ratio of frequencies, which is equivalent to the ratio of magnetic field integrals for the two regions allowing the beam properties measured accurately using panel (a) to be applied to the spin-echo point measurements in panel (b).

determine the ratio of the field integrals to be;

$$\frac{\int_0^{L_1} B_1 \cdot dl}{\int_0^{L_\phi} B_\phi \cdot dl} = 1323.0 \pm 2.1 \quad (3.3)$$

Using this information we can translate the beam properties ω and σ , measured using the high precision precession coil as a function of I_0 to I_ϕ which can be used to measure the spin-echo point rapidly and independently of the precession field coils. There is no expected time variation of σ and ω . Experimental evidence has shown the variation in beam energy and standard deviation to be less than 1% for the same source configuration. It is therefore straightforward to determine σ and ω using an infrequent precise measurement over many oscillations, such as the one shown in figure 3.5a, which takes ≈ 20 min to perform each time the beam is adjusted; for example each time it is turned on at the start of a session

Now looking to the rest of the parameters of equation 3.2. If the properties of the beam are known, there are 4 remaining variables in equation 3.2; A and B are related to the perpendicular components of the polarisation vector, which may be termed real and imaginary polarisation. C is related to the constant level combined with Bkg which is the signal arising from non-polarisable species with a mass/charge ratio of 3 amu, such as HD from the background gasses and the dark detector background. A , B and $C + Bkg$ in equation 3.2 can be determined by measuring three values of In over one oscillation period and solving the resulting set of linear equations. In practice we measure 4 points and therefore have an over constrained set of linear equations which is solved using a least squared optimisation. There is no way to separate C and Bkg from the 4 data points, and therefore the background signal is measured before each cycle of the main solenoid with a closed beam stop, the measured signal is recorded and then subtracted from the measured data in analysis.

From equation 3.2 the real polarisation is $Re[P] = A/(C - Bkg)$ and the imaginary polarisation is $Im[P] = B/(C - Bkg)$. The spin-echo point, defined as the

current offset required to achieve the maximum in the cosine curve defining the real polarisation, is related to the phase angle, δ_1 shown in figure 3.1, which can be obtained by taking the four quadrant inverse tangent of the real and imaginary polarisation vectors, $\arctan(Re[P]/Im[P])$. Using this method the spin-echo point may be calculated and assessed independently of other environmental considerations.

The procedure for measuring the polarisation due to surface processes is the same process as measuring the spin-echo point. In practice, the measurement consists of measuring the spin-echo point before the experiment as outlined above, and then again during dynamics experiments, taking into account the pre-existing calibration. Equation 3.2 can be expanded to include the calibration, and written:

$$In(I_\phi) = \exp\left(\frac{-(I_\phi - I_0)^2}{2\sigma_\phi^2}\right) [A \cos(\omega_\phi I_\phi - I_0) + B \sin(\omega_\phi I_\phi - I_0)] + (C + Bkg); \quad (3.4)$$

subscript ϕ is used to indicate values that are measured with respect to the current in the phase coil. σ_ϕ and ω_ϕ are known from beam calibration. I_0 is the value measured during spin-echo point calibration, and is a function of environmental conditions. As before equation 3.4 is a linear equation with terms A , B and $(C + Bkg)$.

3.2 Dynamical calibration of spin-echo point with precession fields

I first investigate the variation of the spin-echo point with respect to magnetic field in the precession coils. There are several related mechanisms through which the field may affect precession including mechanical misalignment, field or current leakage, and driving circuit mismatch, however all of these processes will cause an unexpected phase change as a function of current. If we consider the standard quasi-elastic dynamics measurement where the currents are equal magnitude in each coil, I_0 in equation 3.4 becomes $I_0(I)$, where $I = I_1 = -I_2$. If the procedure highlighted in the previous section is used over the range of I employed in a dynamics measurement, any instrumental effects causing a polarisation change can be measured and discounted in later analysis.

Figure 3.6 shows a typical calibration measurement of spin-echo point in phase-coil amps (I_ϕ) as a function of current in the main precession coil current ($I = I_1 =$

$-I_2$), for the two different power supplies commonly employed on the apparatus. The sample in this case was a copper(111) crystal at temperature 55 K. The red line is measured using a bipolar power supply with range of $I = \pm 1$ A, while the blue line represents data measured using a single polarity supply with range $I = 0 - 12$ A. Several things become clear from the figure: firstly the calibrated spin-echo point varies as a function of main solenoid current, from initial impressions, in a linear way, and secondly the variation changes in gradient and intercept depending on the power supply used, suggesting that there is some fluctuation from the circuitry connecting the power supply to the solenoids. We now turn to investigate the time

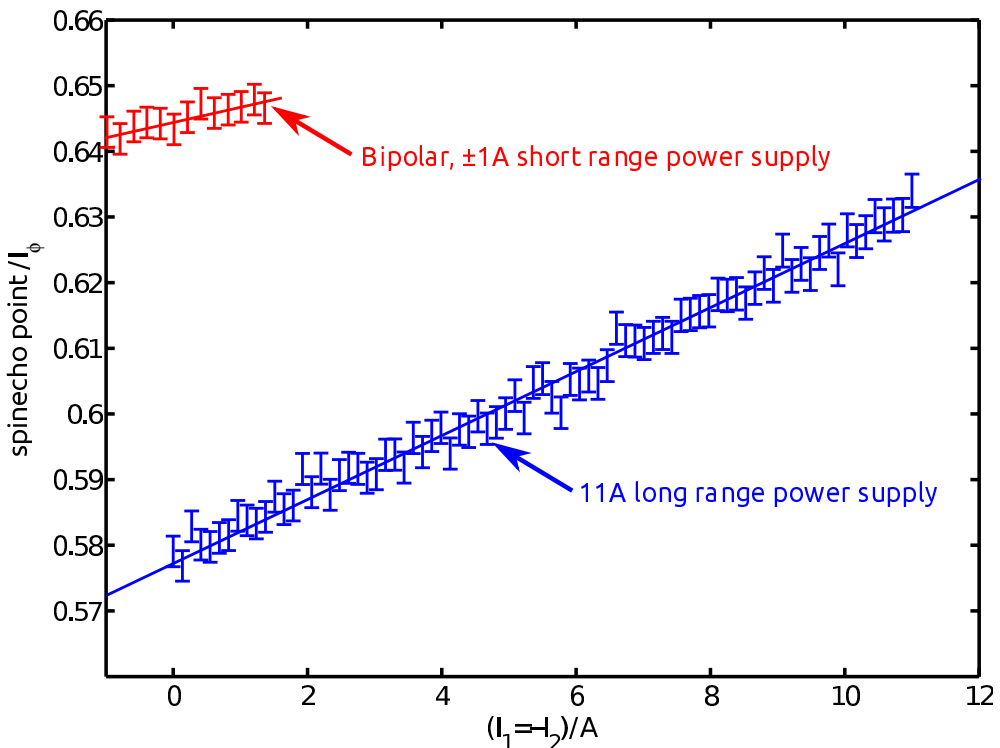


Figure 3.6: Calibrated spin-echo point, measured using the phase coil power supply current, as a function of current in the main precession power supplies, for a range of $I = \pm 1$ A shown in red, and $I = 0 - 12$ A shown in blue. The sample in this case was a $Cu(111)$ crystal at 55 K on the specular reflection peak. Both of the main power supplies appear to cause a linear shift in the calibrated spin-echo point, with different gradients and intercepts, highlighting the importance of taking the effect into account through effective calibration.

stability of the calibration system by repeatedly measuring the spin-echo calibration at a range of main solenoid currents over a long period of time. The results of a typical time calibration for $I = 0.5A$ measured using the bipolar power supplies are shown in figure 3.7. The striking result of the data is that there are long periods of $\approx 5\text{hrs}$ where the spin-echo point remains stable, followed by regular and apparently instantaneous discontinuities. Correlations between environmental factors in the Laboratory environment have been discounted and at present the cause of the discontinuities are unknown and being investigated further.

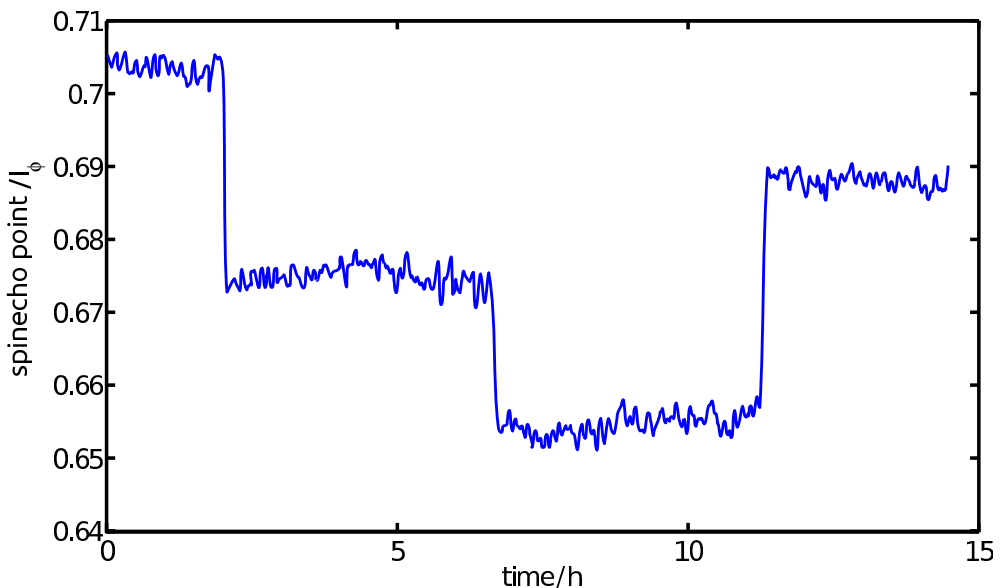


Figure 3.7: Typical time stability of the calibration of the spin-echo point measured over 15 hrs using 0.5 A current through the main precession power supply in this case.

Finally, we investigate the variation of the spin-echo point with momentum transfer, or angle of the crystal. The measurement is useful as it probes the effect on the spin-echo condition of forming slightly different paths through the precession fields. Typical results are shown in figure 3.8, which shows a measurement similar to the one presented for the specular beam in figure 3.6, but measured at three different angles. Measurements similar to the one presented have been repeated for a variety of systems and conditions and a variation in the spin-echo point typically less than 2%, with respect to the crystal angle, is observed, indicating that there is

no effect at the angles used in typical dynamics measurements.

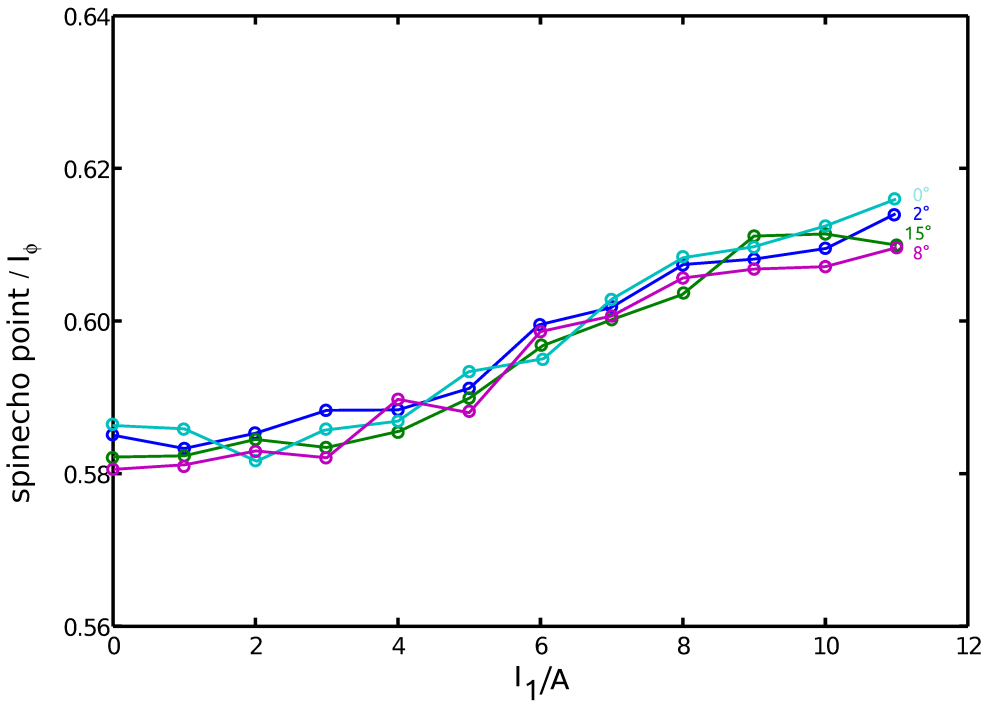


Figure 3.8: Calibration of the spin-echo point as a function of current measured on specular and at three different angles (2° , 8° , and 15° from the specular reflection angle) measured using a graphene/ruthenium(0001) surface at a temperature 55K with notional 8 meV beam energy, using the bipolar power supplies. Although there is a clear variation in the calibration with main current, I , there is no observable variation with angle.

In light of the variation with main current shown in figure 3.6 and the lack of any variation with angle in figure 3.8, in practice the spin-echo point is calibrated regularly and the spin-echo point with no dynamics occurring noted and considered in further analysis.

The method used to calibrate and measure the spin-echo point outlined in this chapter is now the standard way of performing dynamics measurements, and works measured using it have been published, for example references [14, 46, 98–103].

3.3 Further work

The phase coil method of rotating the spin vector is ideal for measurements where the velocity spread of the beam is small; however if one wishes to study processes with larger energy shifts, and especially inelastic phenomena, it is desirable to increase the beam energy and spread to excite more processes. In particular for these measurements it is desirable, though not essential, to implement a solution for rotating the polarisation vector. A method for achieving this is to install flipper coils that produce an additional alignment field, between stage **c** and **d** in figure 3.3. A mechanism for measuring the two perpendicular components, notionally the real and imaginary parts of the spectrum, has been implemented as part of an earlier work [104], however this method is currently limited to measuring two points and requires a more complete magnetic field analysis and mechanical design to be extended to measuring 4 points.

Chapter 4

Jump diffusion of sodium on copper(111)

4.1 Motivation and background

Alkali metal adsorption on metallic substrates has a significant technological impact. The effect on heterogeneous catalysts has been recognised since 1945 when Dobereiner [105] discovered that “*the effectiveness of platinum sponge is increased to such an extent when it is moistened with caustic soda or caustic potash that, like platinum black, it acts upon alcohol and wood spirit even at room temperature. In the case of platinum black the increase is so great that one can decompose any fermentable sugar with it to carbon dioxide and water*”.

Simple, prototypical systems can offer insights into complex phenomena. Ertl’s 2007 Nobel prize work on the Haber-Bosch process from the 1970’s is an example [106–108]. Here, the macroscopic kinetics of an empirically optimised industrial process was related to the kinetics of individual steps of the reaction observed on simplified systems under idealised conditions. It is particularly relevant as it explains why the presence of potassium ions in the catalyst promotes product formation. The industrial process had been empirically optimised with relatively complicated catalysts at high pressure and temperature, but the detailed nature of the mechanisms were not understood. Ertl brought the surface science techniques that he had applied to simple atomic systems such as hydrogen adsorption and demonstrated that the insights were relevant to the complicated catalysts used, providing experimental

evidence of the correct formation pathway and the energetics of the steps. The work is particularly relevant on the topic of alkali metal studies as the rate limiting step in the ammonia formation is the adsorption of N_2 on the iron catalyst surface. It had been found empirically that the overall reaction rate was improved in the presence of potassium in the catalyst. Ertl reported an increase in the nitrogen adsorption energy by 10 – 15 kJ/mol with the presence of potassium ions at the iron surface, and attributed the increase to the donation of electrons by potassium to neighbouring iron atoms [106]. It has since been found that a variety of heterogeneous catalytic processes are enhanced in the presence of controlled quantities of alkalis. Mross presents a detailed review of the impact of alkali dosing on industrial catalytic processes [109].

There have been many experimental and theoretical studies, including two review papers by Diehl *et al.* [110] [111] which present a thorough overview of the known adsorption properties for a variety of substrates. Alkali metals have simple electronic structures and tend to chemisorb at high symmetry sites without disturbing the underlying substrate. It is generally accepted that, at low coverage, the valence charge of the alkali is displaced towards the substrate due to the difference in electron affinity, creating a dipole moment [112]. As the coverage is increased the dipole moments become de-polarised and the alkali layer becomes metallic [113], a transition that has been observed by Fouquet *et al* and Huang *et al* [42, 114].

A number of studies have been conducted on the dynamics of alkali atoms on a copper (001) surface; Na/Cu(001) [50], Cs/Cu(001) [49], K/Cu(001) [48]. In all cases activated diffusion is observed at low coverages with a systematic trend seen in activation energy and friction. As the coverage increases some perpendicular motion is observed [50], which has been attributed to changes in the classical turning point of the scattered helium atom [115]. Fratesi has performed a series of DFT calculations [116] for a range of alkali atoms a Cu(001), which confirms the trends observed in experimental work. There are no previous measurements of the dynamics of alkali metals on Cu(111) using helium scattering. However LEED and TPD measurements have been reported [111, 117, 118], with results showing a 3×3 periodic structure, but with 4 adatoms per unit cell, as reproduced in figure 4.1.

The present study extends previous work through the improvements in instrumentation described in chapter 3. Specifically, the experiment allows a careful anal-

ysis of the ISF at small spin-echo time (< 5 ps). The results confirm the validity of the methods used previously to analyse jump diffusion using the exponential dependence of the ISF at long spin-echo times. Values for the activation energy and friction are obtained. In addition, at short spin-echo times, we observe an unusual line shape with an unexpected asymmetry that is suggestive of an inelastic process. We argue that there is negligible inelasticity and explain the observations in terms of the form factor of the scattering.

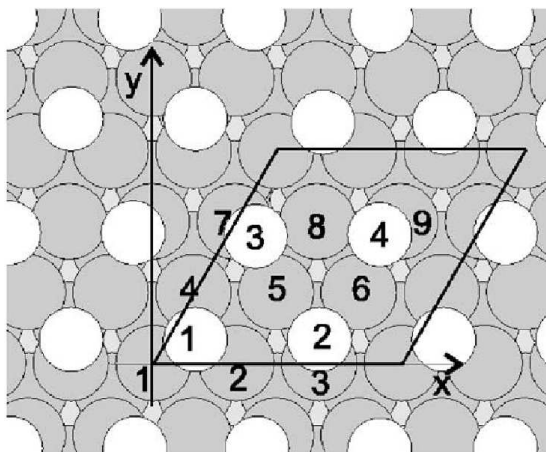


Figure 4.1: Schematic diagram of the coverage at saturation of the first monolayer of Na/Cu(111) taken from [119]. Na atoms, shown as open circles, occupy a variety of sites: 1 and 2 are in threefold sites (fcc and hcp respectively), while those indicated by 3 and 4, are displaced slightly. The structure has (3×3) periodicity, with 4 adatoms per unit cell and coverage corresponding to $4/9$ of the number of top layer copper atoms.

4.2 Experimental methods

A mechanically polished single crystal Cu(111) sample (Surface Prep. Lab., NL) used in this study was mounted on a sample manipulator, allowing translational, polar and azimuthal rotations as well as temperature control. The manipulator is fitted into the scattering chamber which is evacuated to 2×10^{-11} mbar base pressure post baking. Preparation of the surface was performed by repeated cycles of argon ion sputtering ($I_{emiss} \approx 6 \mu\text{A}/\text{cm}^2$, 800 V Ar^+ ions, $T_s = 300 \text{ K}$ for 30 mins) followed by surface annealing ($T_s = 800 \text{ K}$, 30 secs). Surface quality was monitored though measurement of helium reflectivity using a quadrupole mass spectrometer in the sample

chamber. A high quality surface was confirmed regularly by exceptionally strong helium reflectivity ($> 34\%$) throughout, (measured at $T_s = 300$ K). The temperature of the nozzle was set at 37 K, giving a typical incident energy of 8 meV, with the beam energy recorded at regular intervals. More detail on the procedures and instrumentation specifics are detailed in chapter 3. The clean crystal is aligned to the [11 $\bar{2}$] surface azimuth, by optimising the pattern of helium scattered from high purity carbon monoxide adsorbed to monolayer saturation. The temperature of the sample is monitored using a type-K¹ thermocouple spot welded onto a sample mount constructed from tantalum as described in chapter 3. Temperature control is achieved with cryogenic sample cooling using liquid nitrogen ($T_s > 120$ K), balanced against radiative heating from a coiled tungsten filament.

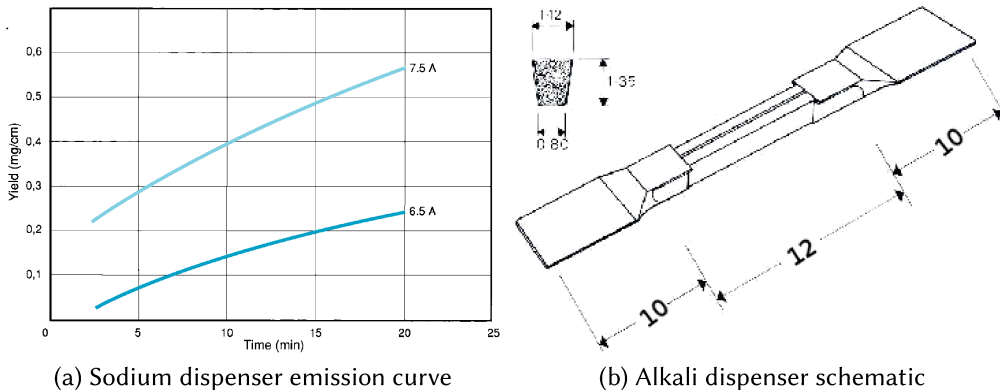


Figure 4.2: Left panel shows sodium dispensing capacity as cumulative yield per unit length of the dispenser, as a function of time at 6.5 and 7.5 Å. The dispenser contains 1.8 mg of sodium in total. In this study a current of 5 A is used during dosing. Right panel shows a schematic diagram of the dispenser with dimensions. All information from [120].

Alkali metals are dosed onto the Cu(111) sample from dispensers supplied by SAES Getters [120]. Figure 4.2b shows a profile of the dispenser; the metal tabs visible on the ends, allow good electrical and mechanical connectivity. In the current study the dispenser is spot welded to the tube shown in panel (c) of figure 4.3. The

¹type-K thermocouple : chromel (90 % nickel and 10 % chromium) alumel (95 % nickel, 2 % manganese, 2 % aluminium and 1 % silicon) [83]

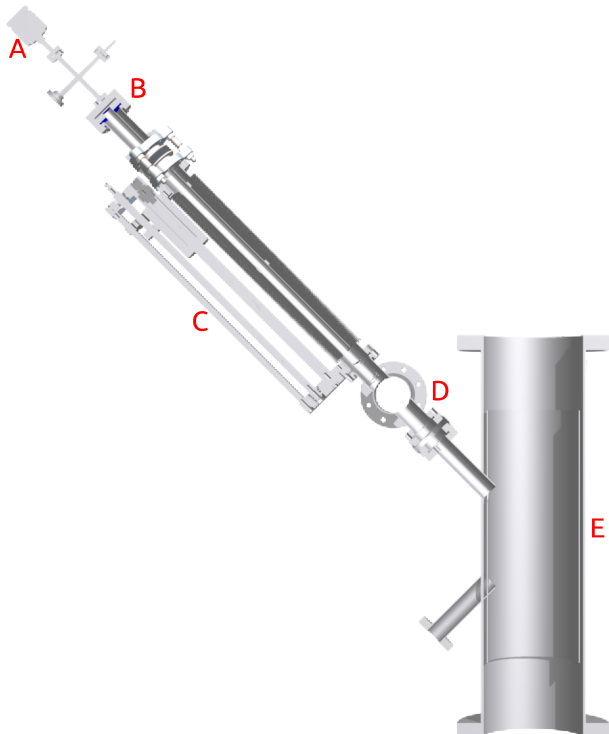
alkali metal itself is contained in the centre section and is released when a current is passed through the dispenser from the slit visible in the top. Before starting to dose with a new dispenser it is degassed to remove adsorbed gasses from the casting and support mountings. The dispenser is gently heated to 500 K by gradually increasing the current, achieving higher temperature than normal ‘rapid’ use but without reaching the higher currents where the dispensing occurs shown in figure 4.2a, maintaining maximum productive output of the dispenser.¹

The design of the alkali dosing system was optimized during the course of the present work. It has been used for a number of subsequent studies, such as those presented in reference [101], and is the standard method for dosing alkali metals in the scattering experiments in Cambridge. In order to deliver alkali vapour efficiently, the front edge of the dispenser and the surface must be brought into close proximity. Figure 4.3 shows a linear bellows, fitted with a dosing insert. Panel 4.3a shows a schematic cross-section of the scattering chamber with the alkali dispenser dosing arm fitted in the retracted position. Panels (b) and (c) of figure 4.3 illustrate the arm insert and a magnification of the end of the insert showing the dispensers. The blue part at the tip of the insert, best observed in panel (c) is a titanium flag that is connected to a rotary vacuum feed-through. When the flag is closed the sample is shielded from the dispenser. Opening and closing the flag allows precise initiation and termination of dosing irrespective of the dispenser warm up time.

In order to dose the sample, the gate valve, D, in figure 4.3, between the dosing arm and scattering chamber is opened and the dosing insert, A, moved to the optimum position, 10 cm from the surface, using the bellows mechanism, C. The dispenser current is then increased to the operational level, typically 5 A, and allowed to stabilise for approx 5 mins before opening the flag to commence dosing. When the desired dose level is reached, the flag is closed to stop dosing and the dispenser current is turned off, before retracting the arm. Throughout the dosing procedure the helium reflectivity and chamber pressure are monitored to quantify the dose and to confirm that there is no contamination in the non-exposed periods.

Figure 4.4a shows an uptake curve taken to a coverage greater than monolayer

¹In operation a current is passed through the dispenser which is filled with a sodium salt of chromic acid ($\text{Na}_2\text{-CrO}_4$) and a reducing agent (Zr 84%-Al 16%); producing an ultra pure vapour of alkali metal; the reactive products created in the process are irreversibly sorbed by the reducing alloy. Alkali dispensers are a convenient method for introducing high purity films in vacuum [120].



(a) Scattering chamber with dosing arm and alkali insert



(b) Alkali dosing insert (A)

(c) Alkali dispensers detail

Figure 4.3: Dosing arm fitted with alkali metal insert, A, fitted to the spin-echo spectrometer sample chamber, E. Panel (a) shows a cut through overview of the chamber with the bellows, C, in the retracted position. A, marks the alkali dosing insert which is connected to a port aligner, B, which enables the precise position of the dispensers, G, to be adjusted to allow safe passage through the vacuum system into the correct position in the chamber. D, marks the location of turbo-molecular vacuum pump connection and a gate valve fitted to a port on the scattering chamber, E. The alkali insert is shown in detail in panel (b), with a rotary feedthrough, F, which can turn a titanium flag, H, to shield the sample from the dispensers, G.

saturation. The period marked A through C demonstrates that there is no change in specular reflectivity between opening the dosing arm chamber and opening the flag. Sodium is deposited from a clean surface at C to monolayer saturation at E and beyond. In order to work at a specific coverage the dosage may be stopped virtually instantaneously by closing the flag, as demonstrated in figure 4.4b, where the sample is dosed to a specular attenuation of $I_0/3$.

From the uptake curve, 4.4a, and assuming a unity sticking co-efficient, as in the coverage dependant LEED/TPD studies conducted by Tang *et al.* [118], and photo emission spectra in reference [121], the coverage can be linearly interpolated from the region C through E on figure 4.4a. Most dynamics measurements were collected at a coverage corresponding to an attenuation such that $I = I_0/3$, as shown in figure 4.4b, which translates to a coverage of 0.045 % of the atoms at saturation coverage. The structure at monolayer coverage, taken from [119] is shown in figure 4.1. The periodicity is 3×3 [118], but with 4 adatoms per unit cell, so the coverage, defined with respect to the number of substrate atoms in the top most layer, [119] is $4/9$. Using the known monolayer structure and uptake curve the coverage with respect to the number of substrate atoms is $\Theta = 0.025$ ML. The coverage calibration can be cross-checked using the location of diffraction features. An angular intensity scan taken at the same coverage is presented in figure 4.5, which shows a strong, sharp specular signal at $\Delta K = 0$ together with broader, weaker diffraction-peaks. The observed features correspond to isotropic diffraction rings that result from the quasi-hexagonal distribution of sodium atoms with well defined nearest-neighbour distance but no long-range orientation order. The radius of the inner ring, K_{ring} , is related to the average nearest-neighbour distance, r , by $K_{ring} = 4\pi/\sqrt{3}r$ [122]. The data gives $\Theta = r^2/a^2 = 0.025$ ML, which is in good agreement with the coverage calculated using the uptake curve. Other coverages that are used in this work are calculated using the same methods.

4.3 Measurements of the ISF

During measurements care is taken to avoid contamination. The variation of helium-3 reflectivity of the clean copper surface over a period over 5 hours; longer than the maximum measurement session of 3 hours shows no significant variation. ISFs are measured non-sequentially in momentum transfer or temperature, and spectra

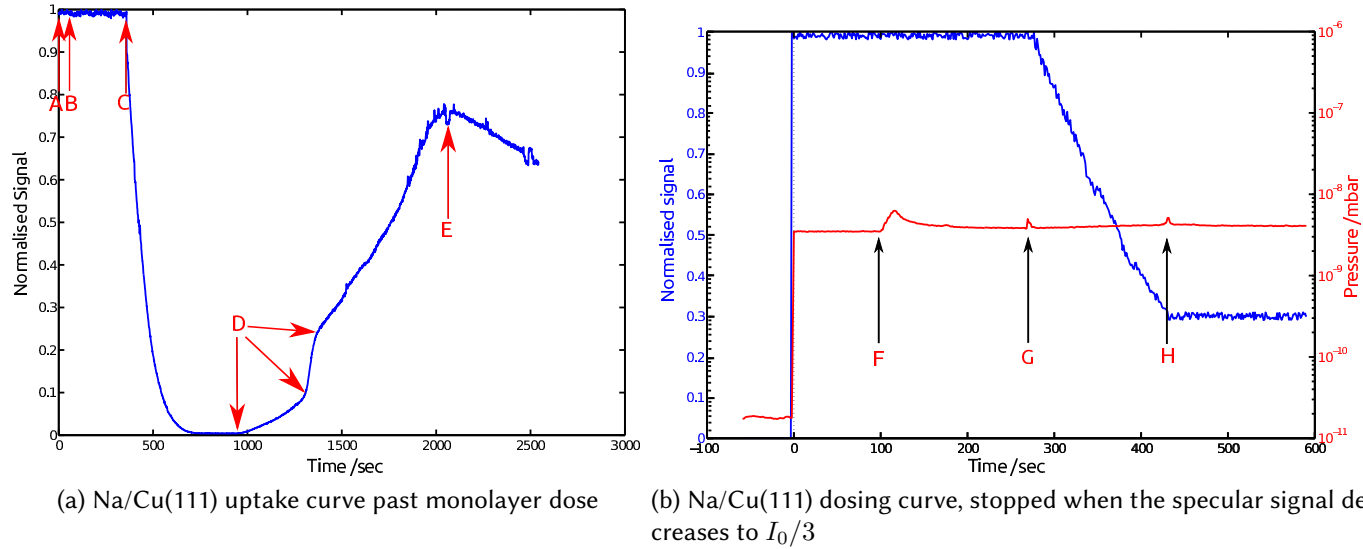


Figure 4.4: Normalised uptake curves of Na/Cu(111) taken at a surface temperature of 200 K. (a) shows specular helium reflectivity to a point past monolayer saturation. The curve is used to investigate surface structures and to calibrate coverage. The gate valve between the scattering chamber and dosing arm is opened at A ($t=0$), the dispenser current is enabled at B (50 s), but no loss of specular reflectivity is observed until the flag is opened at C ($t=350\text{ sec}$). In the period C onwards sodium is deposited on the surface, demonstrated by an initial decrease in helium reflectivity as the surface entropy increases and then an increase as the surface stabilises, D, approaching the complete monolayer, highlighted at E. At the points indicated by D different compressed surface structures are formed. (b) shows helium reflectivity and chamber pressure, in blue and red respectively, in this instance the dose is stopped by closing the dosing flag at H, where the specular signal is $I_0/3$. The points F and G indicate the times when the dispensing current is enabled and the flag opened, respectively

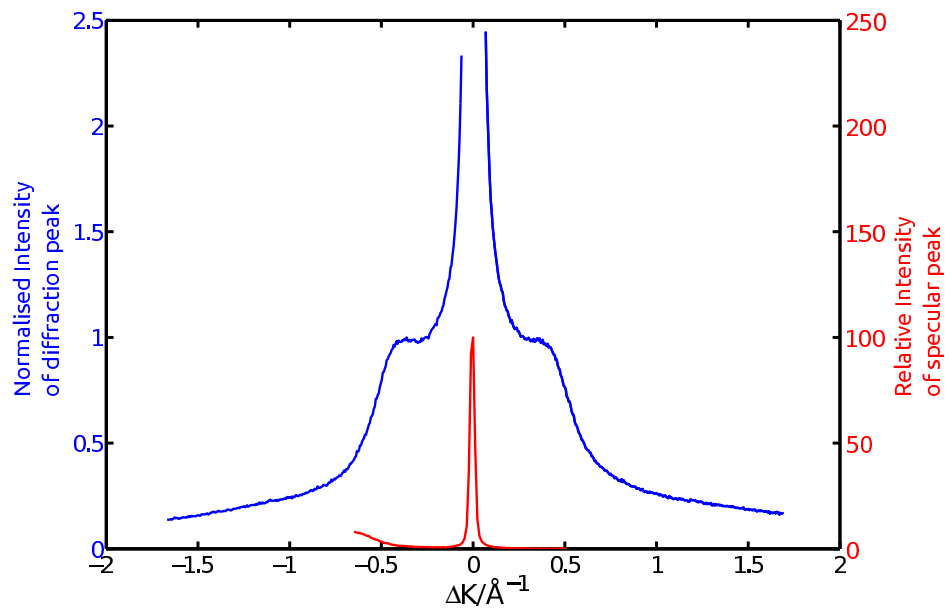


Figure 4.5: ^3He diffraction scan for Na on Cu(111), along the $[11\bar{2}]$ substrate direction, at coverage of $\Theta = 0.025 \text{ ML}$. Signal is normalised to one at the peak of the diffraction ring. The total scattering angle and beam energy are fixed at 44.4° and 8 meV respectively, while the angle of incidence is varied in order to obtain the diffraction pattern. The central peak, shown as a red line, is the specular reflected beam and the weak diffraction features are apparent in the expanded curve (blue line). The diffraction features do not vary significantly with azimuthal sample orientation, indicating an absence of azimuthal ordering.

recorded at the beginning of each measurement session are repeated at the end with no variation noted.

Having established the structural characteristics of Na/Cu(111), we now consider dynamics and present surface spin-echo data and analysis. ISFs are recorded at coverages between 0.025 and 0.12ML at typically 155 K sample temperature. Figure 4.6 presents a typical ISF as red circles. The raw data in the form of helium count rate as a function of solenoid current is converted to $ISF(\Delta K, t)$ as previously described in chapter 1, section 1.2.2. In addition to the expected exponential decay at long times, there is an oscillatory contribution to the ISF that is clearly visible in figure 4.6, particularly at spin-echo times less than 25 ps. Inelastic scattering from phonons in the sample is a common cause of inelastic scattering [21], but the process is not treated in the present work. In the data shown in figure 4.6 the decay rates of the quasielastic dynamics and oscillating component are similar and it is challenging to separate the contributions in time. In the next section the inelastic contributions are filtered from the ISF in Fourier space and the result presented in figure 4.11.

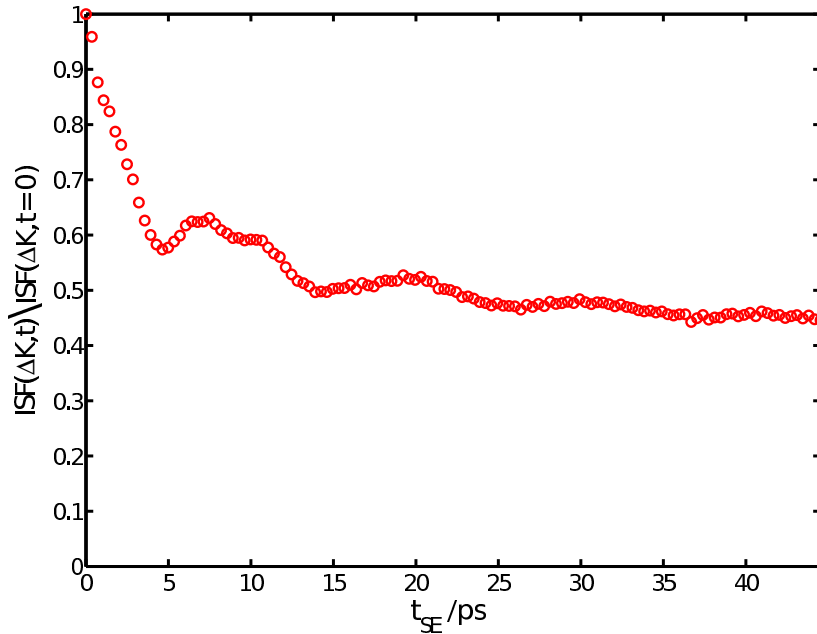


Figure 4.6: A typical Na/Cu(111)ISF measured on the $[11\bar{2}]$ surface direction and presented for a momentum transfer $\Delta K = 0.08 \text{ \AA}^{-1}$ at a coverage of $\Theta = 0.025 \text{ ML}$ and temperature 155 K.

4.3.1 Application of Fourier filtering to the inelastic scattering signal in the ISF

Firstly we need to remove contributions from inelastic scattering, typically attributed to the interaction of the beam with substrate phonons. It is helpful to consider some model ISFs created with simple analytical functions and their Fourier transforms. Figure 4.7a presents an exponential decay,

$$I(t) = e^{-\alpha t}; \quad (4.1)$$

representing a quasielastic scattering signal, which has no imaginary contribution. The Fourier transform of equation 4.1 is presented in figure 4.7b. The peak in the Fourier spectrum is symmetrically located around ω_0 and also has no imaginary component. Now, considering a purely inelastic scattering event, the Fourier spectrum will form a peak shifted from ω_0 , where the shift corresponds to the energy change on scattering, an example of which is depicted in figure 4.7d. The time spectrum representing inelastic scattering comprises a decaying oscillation, of the form;

$$I(t) = A_2 e^{-\alpha_2 t} [\cos(\omega, t) + i \sin(\omega, t)]; \quad (4.2)$$

as shown in figure 4.7c. The real component of this oscillation is symmetric around $t = 0$, while the imaginary component is antisymmetric. In the experimental spectra we observe a combination of quasielastic and inelastic contributions as in figure 4.8a, which constitutes a sum of quasielastic and inelastic contributions;

$$I(t) = A_1 e^{-\alpha t} + A_2 e^{-\alpha_2 t} [\cos(\omega, t) + i \sin(\omega, t)]. \quad (4.3)$$

The combined data has a Fourier spectrum shown in 4.8b, which is a superposition of the two spectra we have looked at already in figures 4.7b and 4.7d. Even though the decay rate of the inelastic and quasielastic contributions are the same, they are separated in Fourier space due to the shift in energy of the inelastic component. In time spectra, where the lifetime of multiple processes are similar but there is an energy change on scattering, the phenomena can be separated in Fourier space.

It is convenient to analyse the ISF directly in time and therefore a mechanism

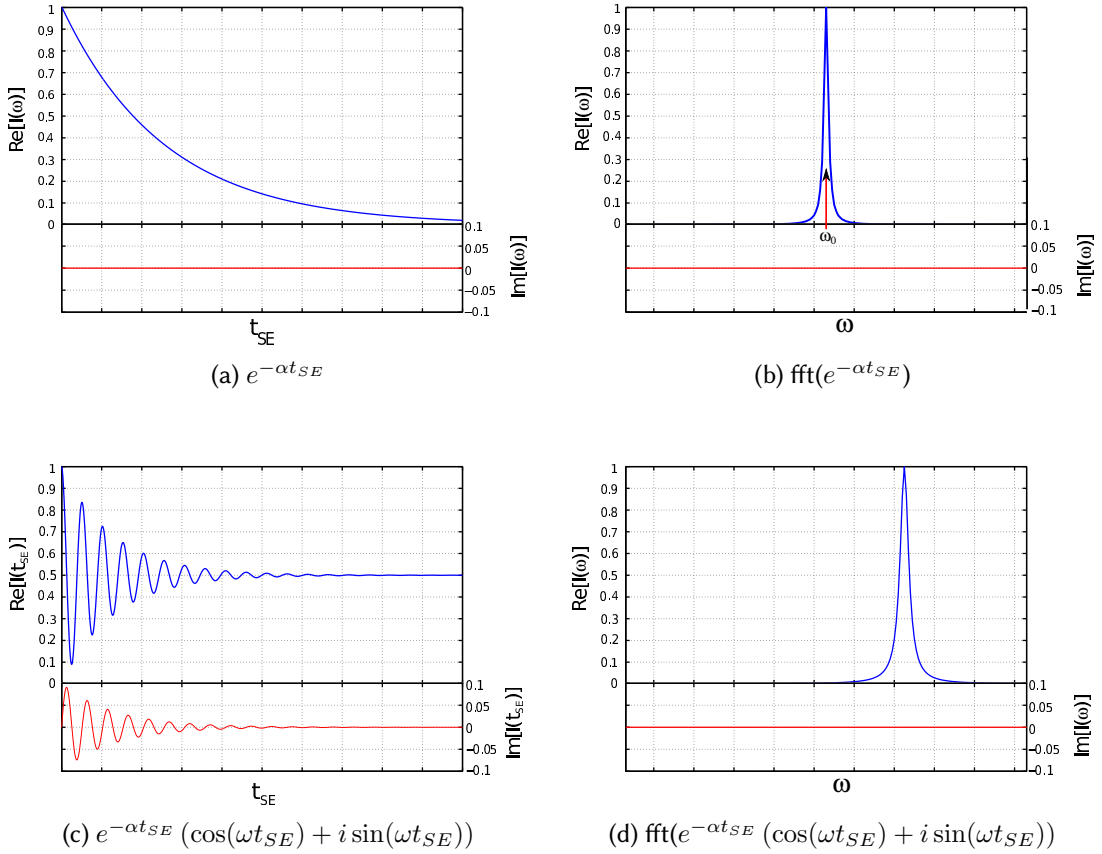


Figure 4.7: Simulated QHAS and inelastic scattering spectra presented on the left with real and imaginary components displayed as blue and red lines respectively. Right hand panels show the Fourier transforms of the spectra in the left hand panels. There is no physical process identified that has a $\text{Im}(I(\omega))$ component, and therefore as expected the imaginary component remains zero in the spectra, by extension it is necessary that $\text{Re}(I(t))$ must be symmetric about $t = 0$ and $\text{Im}(I(t))$ must be antisymmetric about $t = 0$.

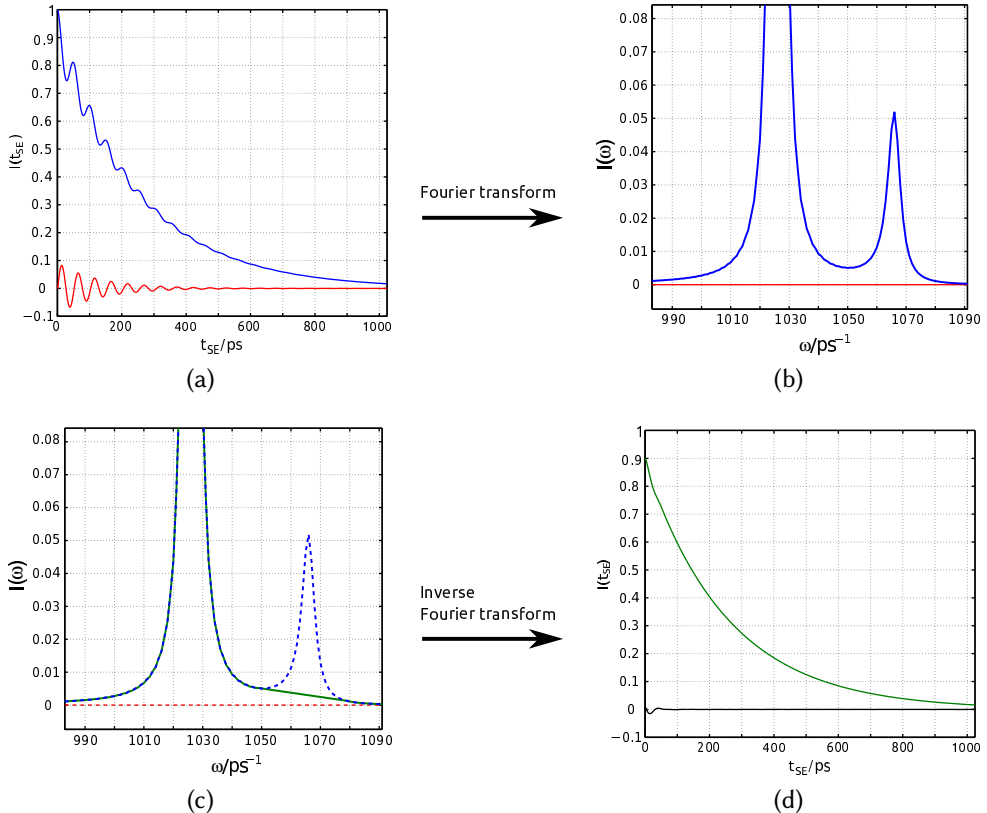


Figure 4.8: Application of Fourier transform filter to simulated ISF with quasielastic and inelastic phenomena of the form $A_1 e^{-\alpha_1 t} + A_2 e^{-\alpha_2 t} [\cos(\omega, t) + i \sin(\omega, t)]$, shown in figure (a). The Fourier transform is shown in figure (b), which is then filtered by linearly interpolating the signal as shown by the green line in figure (c), which, via an inverse Fourier transform gives the ISF shown in green (real) and black (imaginary) in figure (d). The blue and red dashed lines show the original data.

Lineshape	$\alpha (\times 10^{-4} ps^{-1})$	Figure reference
Exponential quasielastic (Eqn:4.1)	39	Blue line in figure 4.7a
Inelastic+quasielastic (Eqn:4.2)	38.53 ± 0.12	4.9a
Filtered Inelastic+quasielastic	39.02 ± 0.05	4.9b

Table 4.1: Results of the application of a nonlinear least squares fit of a model described by equation 4.1. The top row of the table represents the model function and the second two rows show the result of fitting the same model to a simulated ISF of the form shown in equation 4.2, before and after the application of Fourier filtering. Comparing the results of the fits it is clear that without filtering the inelastic component, there is an underestimate of the value of α within the 66% confidence interval indicated, while the filtered result gives a fit with the correct value specified with a smaller bound.

is necessary for removing the phonon. In the present work, we apply a simple filter in the Fourier domain. The process is illustrated in figure 4.8 and described in appendix D. Figure 4.8a and 4.8b show, respectively the ISF and its Fourier transform. The inelastic scattering peak in figure 4.8b is easily removed by the straight line interpolation shown as a solid green line in panel (c). The inverse Fourier transform leads to the filtered ISF shown in panel (d). It is clear that the inelastic contribution has been reduced significantly by comparing figures 4.8a and 4.8d.

We must also consider the effect that the filtering has on the determination of the decay parameter, α . Figure 4.9 compares nonlinear least-square fits of a single exponential, 4.1, to both the filtered data, figure 4.9a, and the unfiltered data, figure 4.9b. The dashed lines in the fit give the 66 % confidence limits of the fit. Quantitative results for the two fits are compared in table 4.1. The figure shows; first, that plausible fits are possible for both the unfiltered and the filtered data; second, the confidence of the fit is much better for the filtered data. Finally, when one compares the values given by the two fits (see table 4.1) it is clear that the fit to the unfiltered data systematically underestimates α , at the 66% confidence level. In contrast, the filtered data gives the expected value of α to high precision. Figure 4.10 presents the results of the Fourier filter applied to experimental data. Plots, (a) and (b), present the real and imaginary raw data and (c) and (d) present the same data after removing the inelastic signatures. The final spectra in (e) and (f), show the filtered contribution. The ability to perform further analysis on both the quasielastic and inelastic

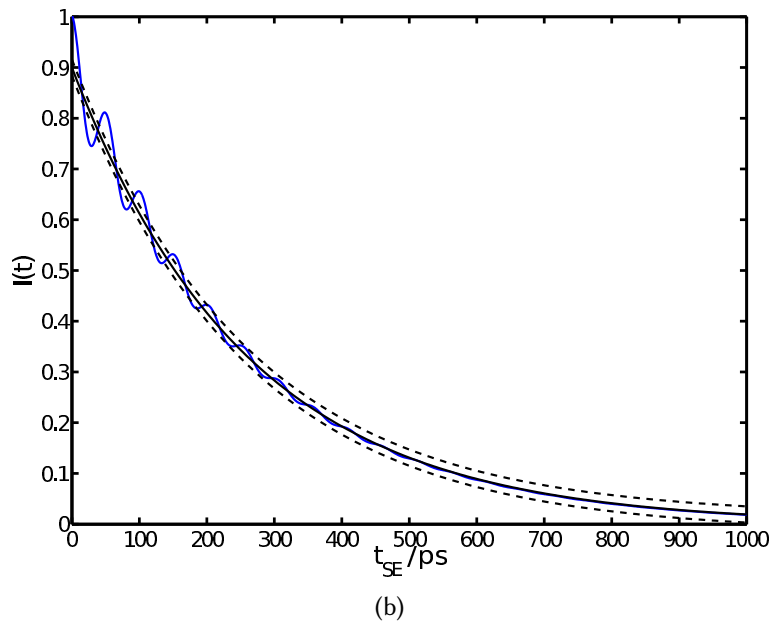
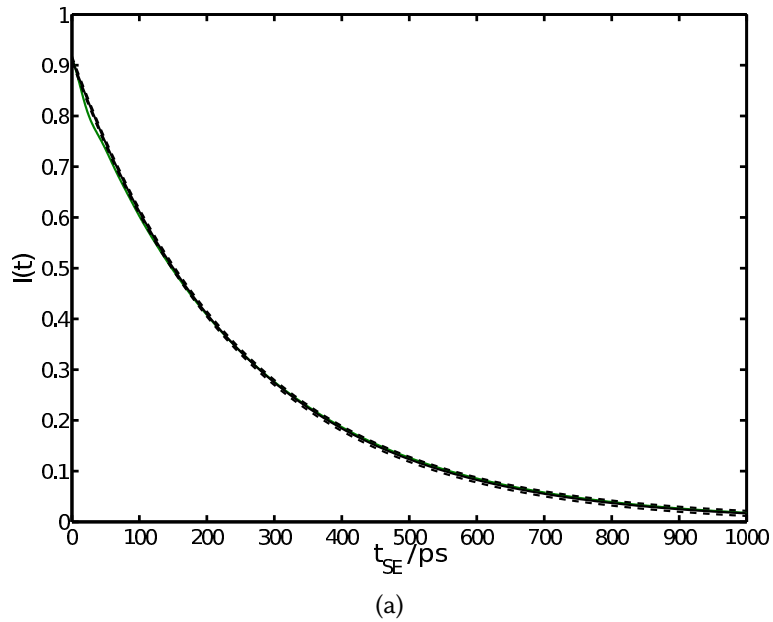


Figure 4.9: Fitting of the the filtered (panel (a)) and unfiltered (panel (b)) ISF of the form in equation 4.3, with $\alpha_1 = \alpha_2 = 39 \times 10^{-4} \text{ ps}^{-1}$ and the amplitude of the inelastic contribution 1/10 of the elastic contribution. The results of the fit are presented in table 4.1.

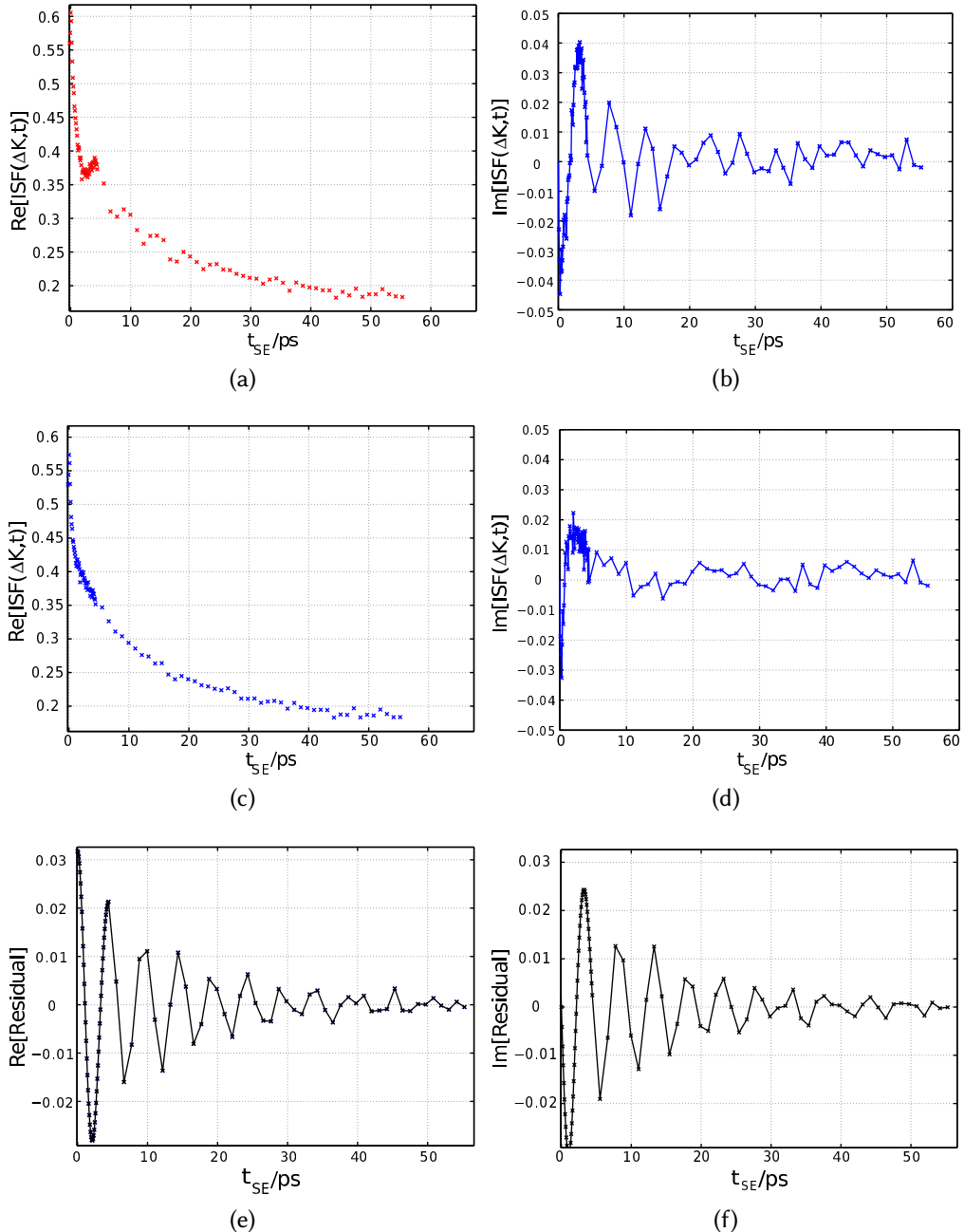


Figure 4.10: Effect of application of a Fourier filter on an ISF of Na/Cu(111), taken at $\Delta K = 0.15 \text{ \AA}^{-1}$ and a temperature of 122 K. Panels (a) and (b) presents the real and imaginary components of the unfiltered ISF while panels (c) and (d) present the same data after processing with the filter. Panels (e) and (f) presents, as a black line, the inelastic scattering spectrum that has been filtered.

phenomena is significantly improved by the method employed, which is simple yet robust. All presented data has been analysed using this filtering method.

Whilst necessary to understand the inelastically scattered energy spectra, calculating the spectrum in specific units is not fundamental to the filtering method, in principle any reversible transform may be applied. The frequency spectrum for a oscillatory signal, symmetric about $t=0$, where there is no imaginary contribution, will present intensity on both sides of the central peak, whereas the complex spectrum would present on one side depending upon the sign of the sinusoidal component. The same method is employed for data in which the imaginary signal was not collected, but both peaks were removed.

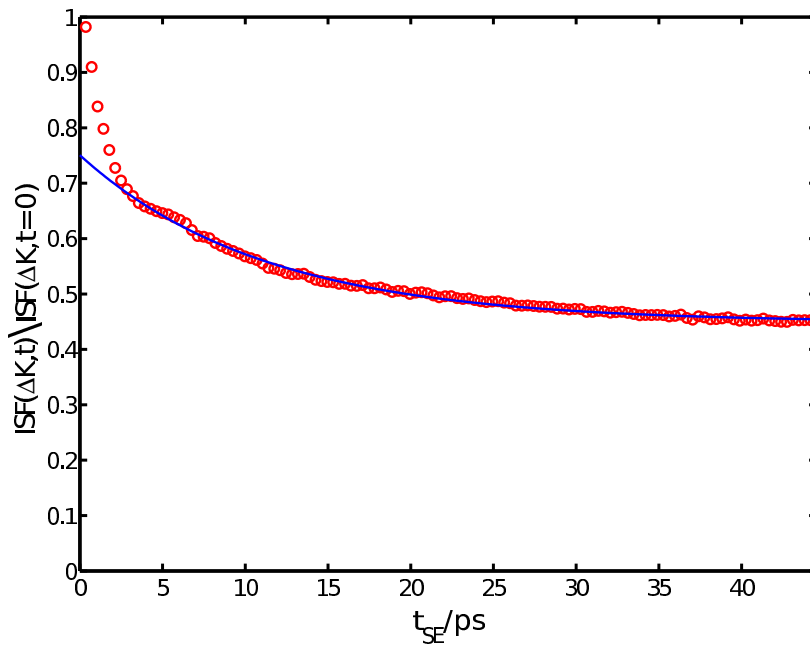


Figure 4.11: A typical Na/Cu(111) ISF measured on the [11 $\bar{2}$] surface direction and presented for a momentum transfer $\Delta K = 0.08 \text{ \AA}^{-1}$ at a coverage of $\Theta = 0.025 \text{ ML}$ and temperature 155 K. The data has been filtered using a Fourier inelastic filter as detailed in section 4.3.1. The blue line shown is of the form $A_1 e^{-\alpha t} + A_2$ where A_1 , A_2 and α are determined using a nonlinear least squares fit. The line is in excellent agreement with the data for $t_{SE} > 5 \text{ ps}$.

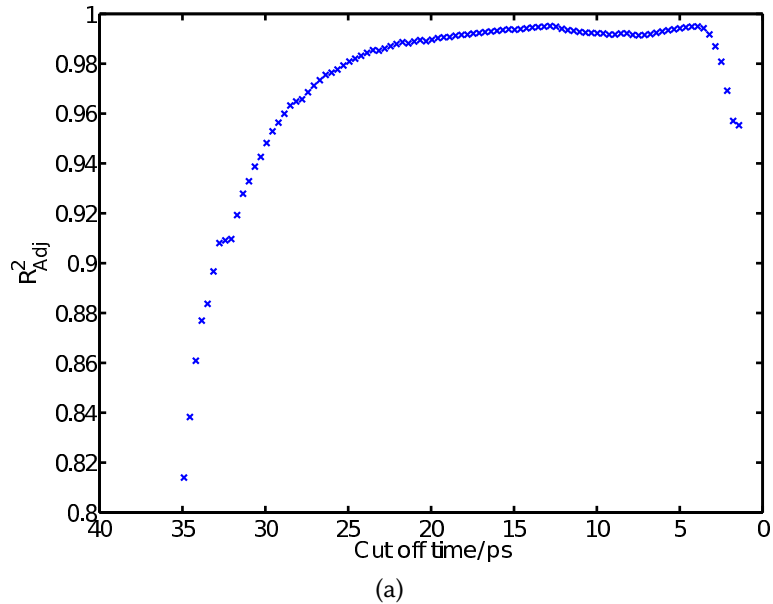
q

4.3.2 Extraction and analysis of the diffusion parameters from the ISF

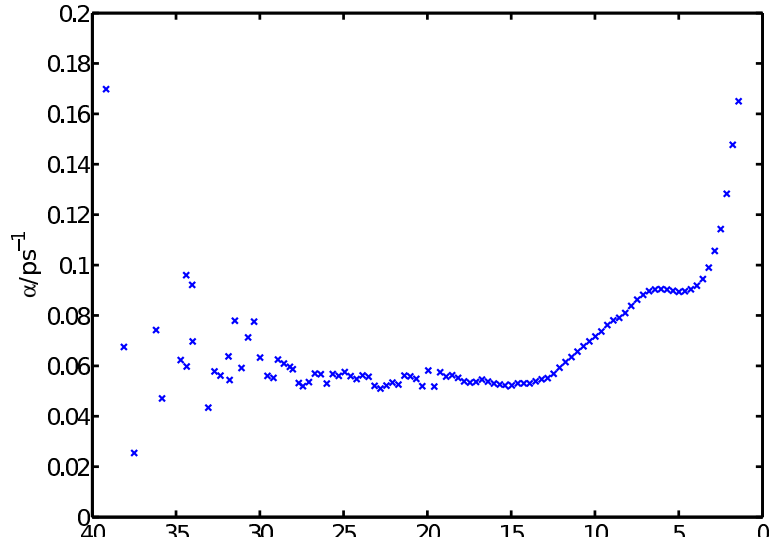
Having removed the inelastic features of the ISF we now turn to analyse the quasielastic lineshape, starting with the slower decay process. The blue line in figure 4.11 represents a model of the form $A_1 e^{-\alpha t} + A_2$, with the free parameters A_1 , A_2 and α , optimised using a nonlinear least squares method implemented using the Matlab™ curve fitting toolbox. The model does not represent the data at small times, $t_{SE} < 10\text{ps}$, which are therefore excluded, using an iterative routine to find the optimum exclusion limit. We quantify the quality of the fit using the R squared value, R_{adj}^2 , adjusted for the number of degrees of freedom, m , where R^2 is the square of the correlation between the response values of the data and the predicted response values of the model. If we define the data as a series $y_{i=1}^n$ and the fit as $f_{i=1}^n$, then R_{adj}^2 is defined:

$$R_{adj}^2 = 1 - \frac{(n-1) \sum_{i=1}^n (y_i - f_i)^2}{(n-m) \sum_{i=1}^n (y_i - \bar{y})^2}. \quad (4.4)$$

Figure 4.12 shows the quality of the fit and the decay rate α for the blue line shown in figure 4.11, as a function of the cut off time, starting with the slowest 5 data points and incrementing towards $t=0$. Figure 4.12a displays the quality of the fit measured using R_{adj}^2 defined in equation 4.4. At large cut-off times, the quality of the fit is limited by the lack of data and therefore the R_{adj}^2 value starts small, and the value of α varies over a relatively large range. As the number of data points increases, α stabilises around 0.05 ps and R_{adj}^2 increases, indicating that the model represents the data. At times less than 12 ps there is a slight reduction in R_{adj}^2 , which is attributable to the incomplete removal of the inelastic scattering signal in this case. At times less than 5 ps R_{adj}^2 decreases rapidly as the quantity of data not described by the exponential model increases, which is consistent with the clear fast decay process in figure 4.11. A cut off limit for the dataset is found to be 18 ps , yielding a value for α of $0.055 \pm 0.005\text{ ps}^{-1}$. The same method is applied to analyse the diffusion signal in the rest of the dataset. Figures B.1 to B.10 in appendix B present all of the ISFs collected in the current study, the red circles present the data before any filtering has been performed, and the blue lines present the fits to the filtered data. The features



(a)



(b)

Figure 4.12: Sensitivity of the time cut off, when optimising an exponential model $A_1 \exp(-\alpha t)$ to experimental data. The resultant model and data are shown as a blue line and red points, respectively in figure 4.11. (a) shows the degrees of freedom adjusted R^2 value, and (b) the value of α as a function of the cut-off time. It is clear that at large cut off time the fit to the exponential is weak, and as at small times the influence of the clearly defined faster decay distorts the result. The starting point of the current work is 18 ps, yielding a value for α of $0.055 \pm 0.005 \text{ ps}^{-1}$.

presented and described in figure 4.11 are typical for the whole dataset, and can be summarised as a rapidly decaying contribution at times less than 5 ps, followed by a slower decay process. There is a strong inelastic component present in some spectra, for example figures B.5 and B.1a. It is clear that there is a significant deviation from the exponential fit at small times, typically below 5 ps, which is considered later in section 4.3.1. The focus for the rest of this section is the longer timescale process, consistently well characterised by an exponential function.

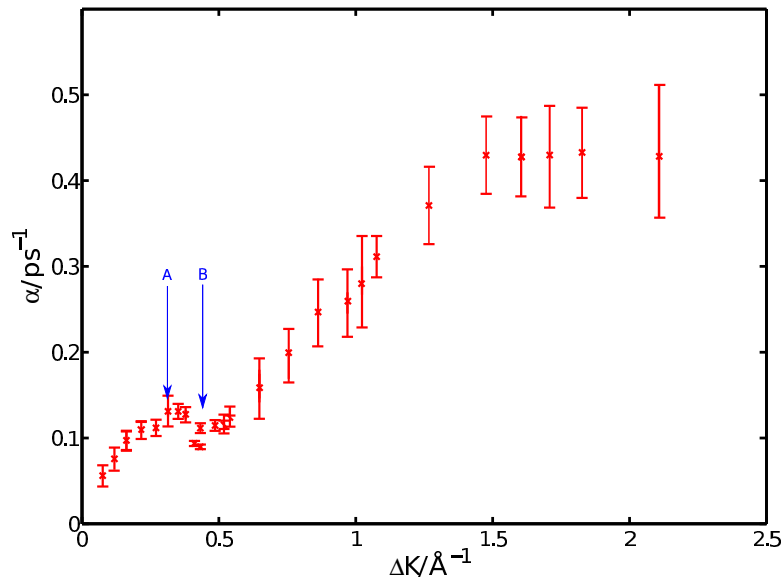


Figure 4.13: Plot of dephasing rate, α , as a function of momentum transfer (ΔK) for the decay process fitted to a single exponential, at a coverage $\Theta = 0.025$ ML. All of the data is collected at a surface temperature of 155 K

Figure 4.13 presents the decay rate, α , from fitting the slowest exponential decay in the ISFs, collected at a coverage of $\Theta = 0.025$ ML and temperature 155 K. The data has many of the same characteristics of other alkali atoms on metal surfaces [29, 48–50, 123, 124]. Firstly the dephasing rate rises to a broad maximum near 1.8\AA^{-1} , which is consistent with hopping to nearest neighbour adsorption sites [90]. Secondly at momentum transfers, $\Delta K < 0.7 \text{\AA}^{-1}$ an additional peak is evident, there is initially an increase in α at low ΔK , marked A, followed by a decrease marked B. These features are typical for systems where inter-adsorbate interactions are present, as shown for similar systems for example in Na/Cu(001) [50]. Figures 4.14a and 4.14b present the dephasing rate for higher coverages of $\Theta = 0.08$ ML and $\Theta = 0.12$ ML.

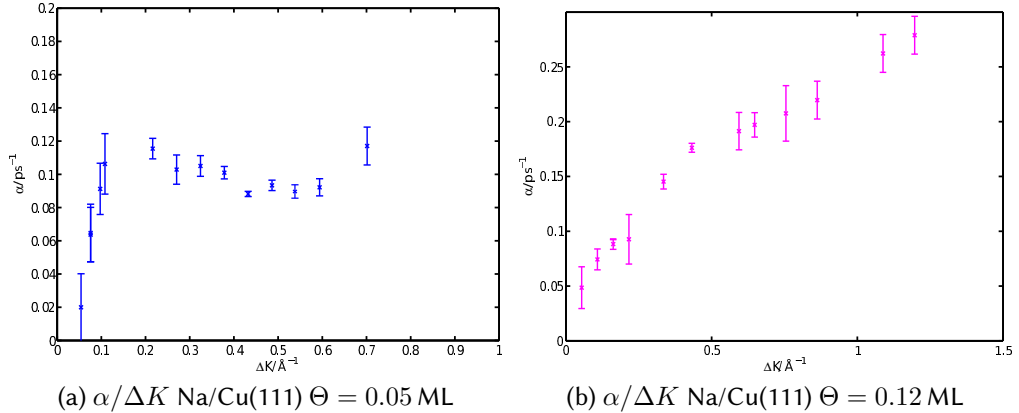


Figure 4.14: Plot of dephasing rate, α , as a function of momentum transfer (ΔK) for the decay process fitted to a single exponential, (a) shows a $\Theta = 0.05$ ML coverage and (b) shows a $\Theta = 0.12$ ML coverage. All of the data is collected at a surface temperature of 155 K

At the intermediate coverage of 0.08 ML, figure 4.14a, the peak and dip structure at low coverage is more strongly marked, as might be expected from a closer spacing of adsorbates and correspondingly stronger dipole repulsion. However, the data at the higher coverage of 0.12 ML, figure 4.14b, shows a significantly weaker peak and dip. The clear implication is that the interadsorbate repulsion is reduced at the highest coverage studied here. It is possible that the reduced strength of the inter-adsorbate repulsion is related directly to the metallisation of the surface, which is accompanied by charge rearrangement and depolaristaion of the adsorbate-surface bonds [42, 125]. The low coverage data is the focus of the present work, and the remainder of this chapter treats the dynamics observed for the $\Theta = 0.025$ ML coverage.

First, we turn to the temperature dependence of the dephasing rate, which is related to the activation energy for hopping [13]. The measured temperature dependence for $\Theta = 0.025$ ML coverage at a momentum transfer of $\Delta K = 1.0 \text{ \AA}^{-1}$ is presented in figure 4.15, with the constituent ISFs presented in appendix B, figure B.10. The data points with associated uncertainty are displayed in blue, the line shown in black is an Arrhenius law relating the decay rate to the temperature

according to

$$\alpha = \alpha_0 \exp\left(-\frac{E_a}{k_B T}\right), \quad (4.5)$$

where α is the dephasing rate, E_a is the activation energy, k_B is the Boltzmann constant and T is the surface temperature. In order to access the activation energy we can re-arrange equation 4.5 to a linear equation in $1/T$,

$$\ln(\alpha) = -\frac{E_a}{k_B T} + \ln(\alpha_0), \quad (4.6)$$

such that if we plot $\ln(\alpha)$ against $1/T$, as in figure 4.15, the activation energy will be the product of the gradient and the Boltzmann constant. The data and Arrhenius law shown in figure 4.15 show good agreement over the temperature range studied, revealing an activation energy of 12 ± 3 meV.

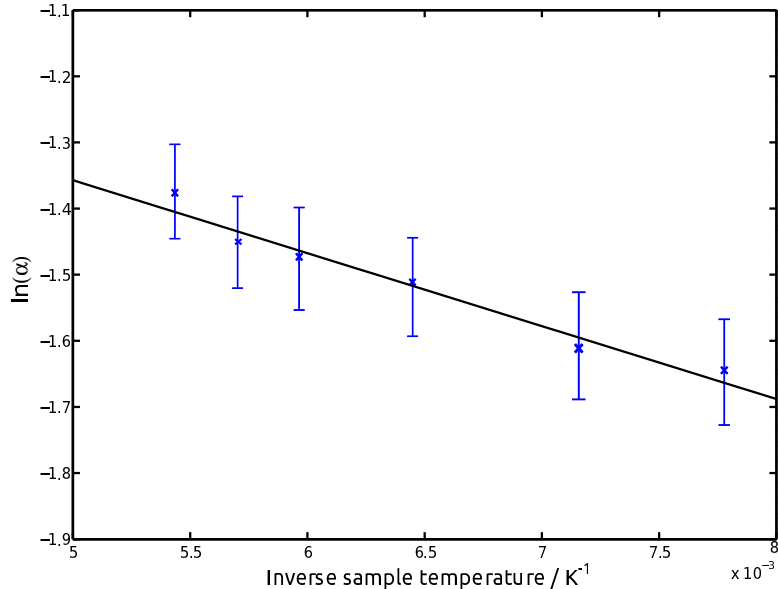


Figure 4.15: Log dephasing rate, $\ln(\alpha)$, as a function of surface temperature for the decay process at an momentum transfer of $\Delta K = 1.0 \text{ \AA}^{-1}$. The width is measured by fitting an exponential in time to the slowest decay in the ISFs. The black line is a weighted linear regression representing an Arrhenius law with gradient of activation energy 12 ± 3 meV.

4.3.3 Molecular Dynamics simulations

Having considered the experimental observations, showing evidence of a jump diffusion process with indications of repulsive interactions, we now look at computer simulations to help characterise the details of the observed motion, specifically with the aim of determining the effects of nano-scale friction and adsorbate substrate interactions.

The simulation results are generated using a Fortran molecular dynamics code, originally written by Dr J. Ellis, and modified as part of this work. The simulation system consists of a collection of interacting atoms, each moving in a two dimensional landscape that describes the interaction with the substrate. Pairwise interactions between the adsorbates are included and the substrate heat-bath is represented by a stochastic force. Using these ideas, the force on the i th adsorbate atom, can be described classically by the Langevin equation:

$$m\ddot{r}_i = -\nabla V(r_i) - \eta m\dot{r}_i + \epsilon(t) + \sum_{i \neq j} F(r_j - r_i), \quad (4.7)$$

where ∇ is the standard gradient operator, $V(r)$ is the potential energy surface between a Na adsorbate and the Cu(111) surface, m is the mass of Na, r_i is the position vector, η is a coefficient representing the collective energy dispersing process and ϵ is the stochastic force term [3]. F is the sum of forces due to neighbouring atoms, j . On average, the stochastic force balances energy lost through the dissipative term. Assuming the system is in thermal equilibrium a scaling term can be calculated using the fluctuation dissipation theorem [126], which, in the case of no time correlation between simulation steps, (i.e. the Markovian approximation described in section 1.3) gives the average magnitude of the impulsive force, q , as;

$$q = \sqrt{2\eta k_B T m}, \quad (4.8)$$

which gives consistency with Einstein's theory of Brownian motion.

The simplest PES is perhaps that described using a sinusoidal potential with the periodicity of the substrate and a single Fourier component. Mathematically we

describe the potential;

$$V(r) = - \sum_i A \cos(\mathbf{g}_i \cdot \mathbf{r}), \quad (4.9)$$

where A is the amplitude between the top and 3-fold hollow site and the index i represents the 3 vector directions required to give the correct hexagonal symmetry. The \mathbf{g} vectors are defined as

$$\begin{aligned} \mathbf{g}_1 &= (\zeta, 0), \\ \mathbf{g}_2 &= (\zeta \cos(\pi/3), \zeta \sin(\pi/3)), \\ \mathbf{g}_3 &= (-\zeta \cos(\pi/3), \zeta \sin(\pi/3)), \end{aligned} \quad (4.10)$$

where $\zeta = 4\pi/\sqrt{3}a$ with a being the lattice constant. Figure 4.16 shows the form of the resulting potential. Note that, with a single Fourier coefficient, it is impossible to vary the barrier and the curvature around the minima independently. Note also that, by changing the sign of the Fourier coefficient it is possible to change the number and nature of the adsorption sites. Here, we choose the form that gives adsorption at three-fold sites, where the energy of the fcc and hcp sites are degenerate. Higher Fourier components could be used to lift the degeneracy; however, their inclusion was found unnecessary.

We now consider the forces between adatoms which are evident in the results. It is well known that electrons in metals generate long range forces between adatoms, and the work of Lau and Kohn [127] predicts an inverse cube law governing a repulsive force between the dipoles of adjacent adatoms. We determine the value of the dipole moment and polarisability, α_p , of sodium on Cu(111), by fitting the Topping model [128] of dipole induced depolarization to existing measurements of the change in work function with coverage. Topping states that the work function $\Delta\phi$ varies with coverage Θ according to the equation,

$$\Delta\phi = \frac{p_0 \frac{\Theta}{a^2}}{\epsilon_0 \left[1 + 9\alpha_p \left(\frac{\Theta}{a^2} \right)^{\frac{3}{2}} \right]} \quad (4.11)$$

where p_0 is the sodium dipole moment at zero coverage and a is the primitive copper lattice spacing. Figure 4.17 shows work function measurements on Cu(111) as a

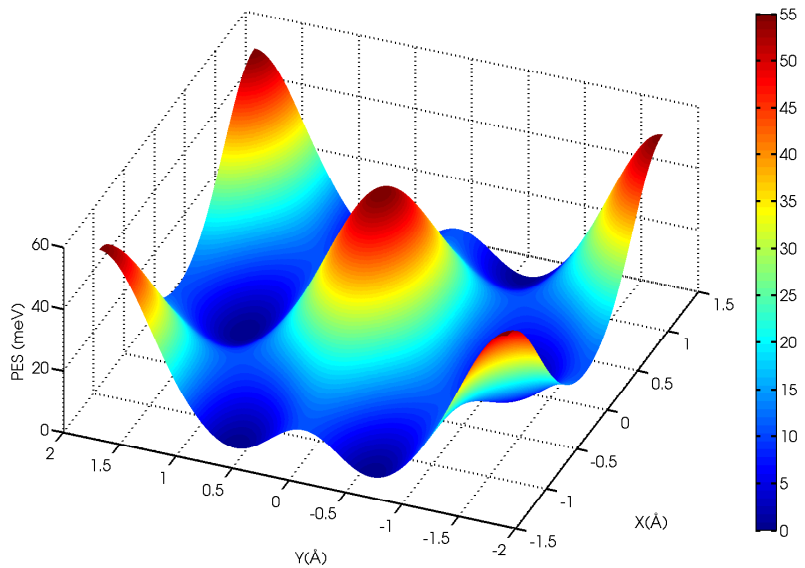


Figure 4.16: Sinusoidal potential energy surface used in Langevin molecular dynamics simulations. The hollow sites are equivalent in this case and the amplitude between the top and hollow sites is 55 meV.

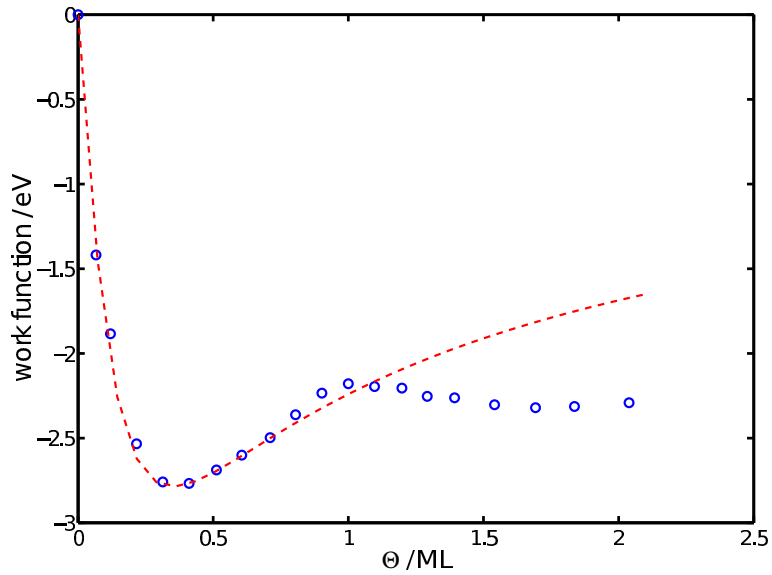


Figure 4.17: Work function variation with coverage (blue circles) for Na on Cu(111) by Fischer *et al.* [129]. A fit to the Topping model [128] is shown (red dashed line), which yields a zero coverage dipole moment, p_0 , of 4 D and a polarisability, α_p , of 17 \AA^3 .

function of sodium coverage, obtained by Fischer *et al.* [129]. The Topping model fit to the initial drop of the curve requires a dipole moment in the limit of zero coverage, p_0 , of 4 D and a polarisability, α_p , of 17 \AA^3 . The mean dipole moment, p at a particular coverage can then be calculated by the relation,

$$p = \frac{p_0}{1 + 9\alpha_p \left(\frac{\Theta}{\alpha^2}\right)^{\frac{3}{2}}} \quad (4.12)$$

which is used with the Lau and Kohn dipole repulsion potential [127] to calculate the inter-atomic repulsion in the Langevin simulations. At coverages above 1 ML, the fit to the Topping model doesn't provide good agreement with the work function data, however the current work is confined to significantly lower coverages.

Trajectories from the Molecular Dynamics (MD) calculations are used to generate the simulated ISFs, which are analysed using the same procedure as the experimental data. The slowest process in the calculated ISF is then fitted with an exponential decay model. Figure 4.18 shows a comparison of experiment and simulation, experimental data points are shown in blue and the Langevin simulation in red with the line indicating the parameters matching the experimental data closest and the shaded region representing the confidence in the result. The peak and dip between 0.25 and 0.5 \AA^{-1} is reproduced in the simulation results and confirms the presence of interadsorbate repulsive interactions, as described by the Topping model [128]. At low ΔK values the simulations agree very well with the experimental data. At larger momentum transfer the experimental results have a consistently larger decay rate, implying that the atoms are moving faster than expected on shorter length scales (larger momentum transfers). It is not possible to reproduce the data by simply changing the amplitude of the PES and varying the friction co-efficient, implying that the real PES is more complicated than a single Fourier component. In future work, the experimental data could be extended to larger momentum transfers and sinusoidal potentials with higher order Fourier components used to determine the precise difference between the fcc and hcp hollow sites. Recent success in this area has been achieved with pyrrole on Cu(111) [89], although in the case of Na/Cu(111) the difference is likely to be much smaller as the existing equipotential model for the hollow sites provides a good fit to the majority of the data.

As shown in figure 4.19, the temperature dependence of the data is reproduced

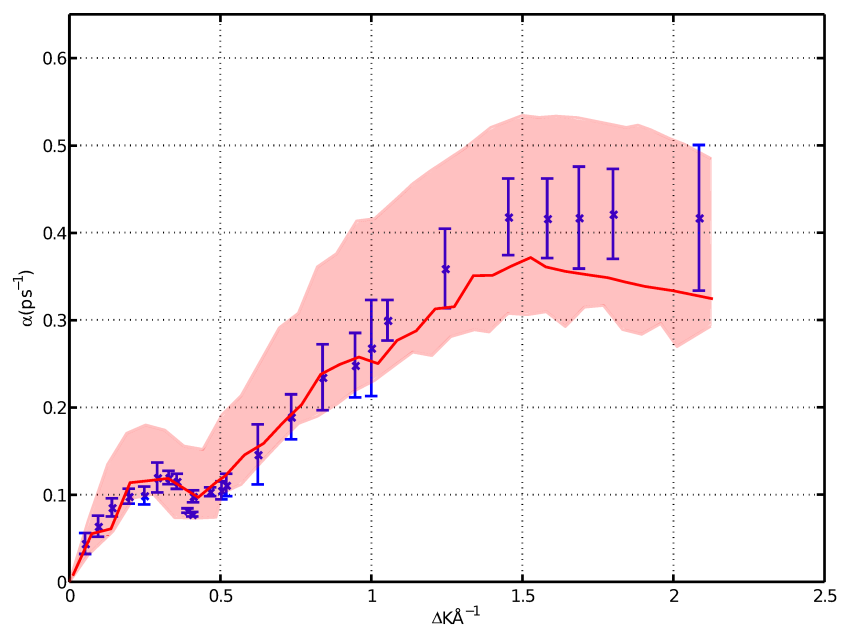


Figure 4.18: Dephasing rate, α , as a function of momentum transfer (ΔK), at a coverage $\Theta = 0.025$ ML. Experimental data is presented in blue. Langevin molecular dynamics simulations for a sinusoidal PES, friction co-efficient $\eta = 0.2 \text{ ps}^{-1}$ with interadsorbate interactions is shown with a red line. The red shaded area represents molecular dynamics results for frictions $0.12 - 0.24 \text{ ps}^{-1}$ and top to hollow site potential $50 - 60 \text{ meV}$. All of the data is presented for a surface temperature of 155 K.

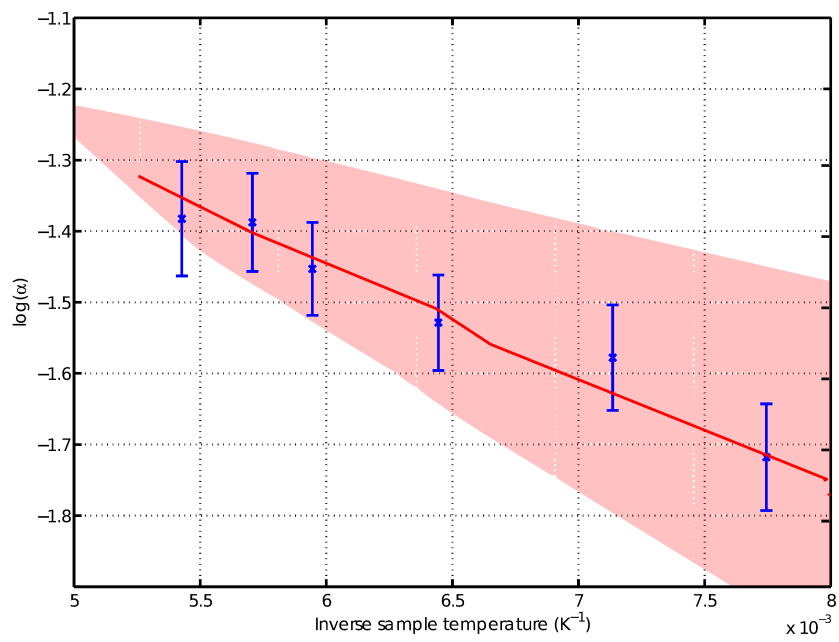


Figure 4.19: Temperature dependence shown as the natural log of the dephasing rate, $\ln(\alpha)$, as a function of inverse temperature, at a coverage $\Theta = 0.025$ ML. Experimental data is presented as Blue points. Langevin molecular dynamics simulations for a sinusoidal PES shown in figure 4.16, amplitude 55 meV, friction coefficient $\eta = 0.20 \text{ ps}^{-1}$ with interadsorbate dipole interactions shown with a red line. The red shaded area represents molecular dynamics results for frictions $0.12 - 0.24 \text{ ps}^{-1}$ and top to hollow site potential 50 – 60 meV.

extremely well with the same parameters used in figure 4.18. The activation energy of the experiment and simulation are identical within the precision of the results, and have a value of ≈ 12 meV, which is significantly lower than the top to bottom site potential of 55 meV. When analysing the trajectories of the atoms, it is noted that the diffusion pathway is over the bridge, not over the top sites, which, as shown in figure 4.16 has a barrier of ≈ 14 meV, much closer to the measured activation energy.

4.4 The Intermediate Scattering Function $I(\Delta K, t)$ at short times

Having considered observations of the ISF on the timescale of diffusion, we now move on to consider behaviour at much smaller times, in the pico-second and sub picosecond range. In order to make accurate measurements we employ the improvements to the measurement technique presented in chapter 3.

The data is taken with power supplies offering higher resolution and better stability than that considered so far. Specifically, the results include spin-echo times, t_{SE} , taken symmetrically about zero up to approximately 50 ps. Thus, the results show the behaviour both at short times, less than about 5 ps, as well as the exponential decays, analysed above, which dominate above 5 ps. In addition, the results include both the real and the imaginary parts of the ISF. Data presented in this section is representative of the complete dataset, which is reproduced in full in appendix B. All of the data has been filtered according to the method in section 4.3.1 and therefore inelastic signals are not presented in the data. Figure 4.20 shows the real (red circles) and imaginary (blue crosses) parts of a typical ISF measured using the enhanced resolution of the spectrometer developed during this work. The higher point density at spin-echo times less than 5 ps was chosen to sample the processes fully, while maintaining an efficient total measurement time. In figure 4.20, the real part of the ISF (red circles) is characterised by a fast decay at times less than two picoseconds followed by a slower, exponential decay. The imaginary signal (blue crosses) in the data is an antisymmetric peak confined to a time scale similar to that of the fast process in the real data. The amplitude of the imaginary component is $\approx 1/2$ that of the real signal, over the same time scale, after the exponential part of the

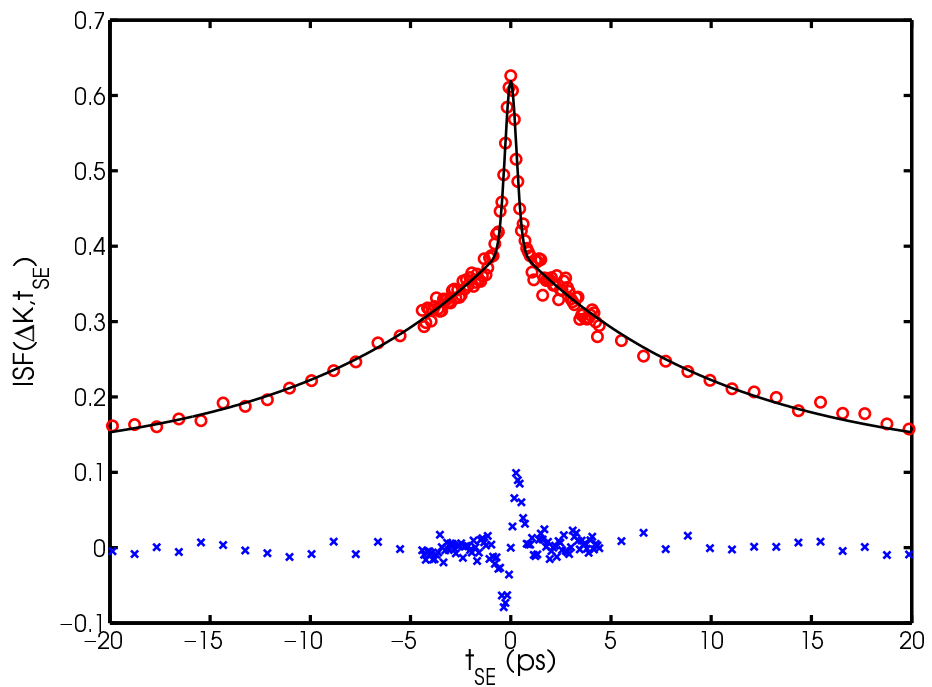


Figure 4.20: Real (red circles) and imaginary (blue crosses) ISF of Na/Cu(111) in the $[11\bar{2}]$ direction at coverage $\Theta = 0.025$ ML at a temperature of 155 K and momentum transfer of $\Delta K = -0.2 \text{ \AA}^{-1}$, presented at spin-echo times of ± 20 ps. The black line is the form $A_0 e^{-t^2/2\sigma^2} + A_1 e^{-\alpha t} + A_2$ with A_0, A_1, A_2, σ , and α obtained through a non-linear least squares fit.

decay has been subtracted (see figure 4.23). Before concentrating on the fastest part of the data we confirm that the exponential part, $A_1 e^{-\alpha t} + A_2$, of the total model, $A_0 e^{-t^2/2\sigma^2} + A_1 e^{-\alpha t} + A_2$, is consistent with the data presented in section 4.3. Figure 4.21 presents the extracted value of α from the fast data as blue crosses and in red is the data extracted previously in section 4.3 under the same conditions. It is clear that the lineshape is in excellent agreement, and hence can also be characterised with the molecular dynamics simulations presented in figure 4.18.

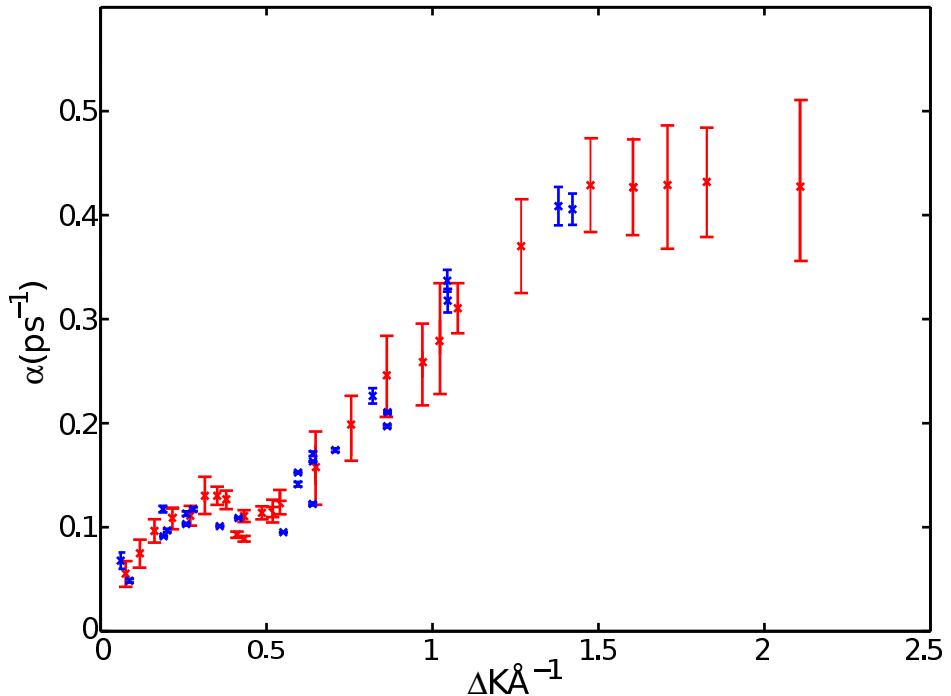


Figure 4.21: Depolarization rate, α , as a function of momentum transfer, ΔK , for coverage $\Theta = 0.025 \text{ ML}$. Blue points are extracted from the 'fast' measurements and red points are extracted from the equivalent slow measurements under the same conditions.

Moving on to the analysis of the faster process, we expect to observe a fast decay due to ballistic motion which should have a Gaussian form in time and energy [88]. In figure 4.20, the real part of the spectrum is shown as red circles with black line showing the model of the form $A_0 e^{-t^2/2\sigma^2} + A_1 e^{-\alpha t} + A_2$ with A_0, A_1, A_2, σ , and α obtained through a nonlinear least squares optimisation. The agreement between the model and data supports the proposed lineshape. Further support comes from the dependence of the Gaussian width on the momentum transfer. Figure 4.22 shows

the outcome of analysing the complete dataset. The data points are compared with the simplest model for ballistic motion, that of an ideal 2-D gas [54]. For a perfect 2-D gas, the ISF has the form¹:

$$I(\Delta K, t) = \exp\left(-\frac{\Delta K^2 \nu_0^2 t^2}{4}\right), \quad (4.13)$$

where $\nu_0 = \sqrt{2k_B T/m^*}$ and m^* is the effective mass of the gas particle. Thus, the width, σ should increase inversely with ΔK ;

$$\sigma = \frac{\sqrt{2}}{\Delta K \nu_0}. \quad (4.14)$$

In understanding the lineshape we usually consider decay rates which are directly proportional to the speed of a surface process. As the variance, σ of a Gaussian gets narrower the process is getting faster, therefore we consider $1/\sigma$. The red line in figure 4.22 presents the 2D ideal gas line with a slope chosen for an effective mass $m^* = 30$ amu, to match the data, and is close to the mass of a free sodium atom, 23 amu. The data follows the 2-D gas line at large values of ΔK , however there is clearly a deviation away from a linear relationship at low ΔK attributable to the effect of friction in the intra-cell region reported previously [130, p.8727]. The comparison, between data and simple 2-D gas theory, shown in figure 4.22 is compelling evidence that the behaviour of the ISF, at short times, corresponds to ballistic motion.

We now move on to consider the imaginary part of the spectrum in figure 4.20, and specifically to the phenomena that might generate an imaginary component. Figure 4.23 shows the real (red points) and the imaginary (blue crosses) parts of the ISF after removing the phonon, diffusive and static components. The real part is symmetric and the imaginary part is antisymmetric. Thus, the dynamical structure factor, $S(K, \omega)$, is real, as it must be, but shifted in frequency, or equivalently energy, by $\Delta\omega$. The argument is illustrated in Figure 4.24a, where a Gaussian ISF that is completely real is shown. Its Fourier transform, also a Gaussian with known width is shown in (b). If there is a small energy shift, the peak will be convoluted with a

¹See Appendix A section A.3 for a detailed derivation of the relationship between σ and ΔK .

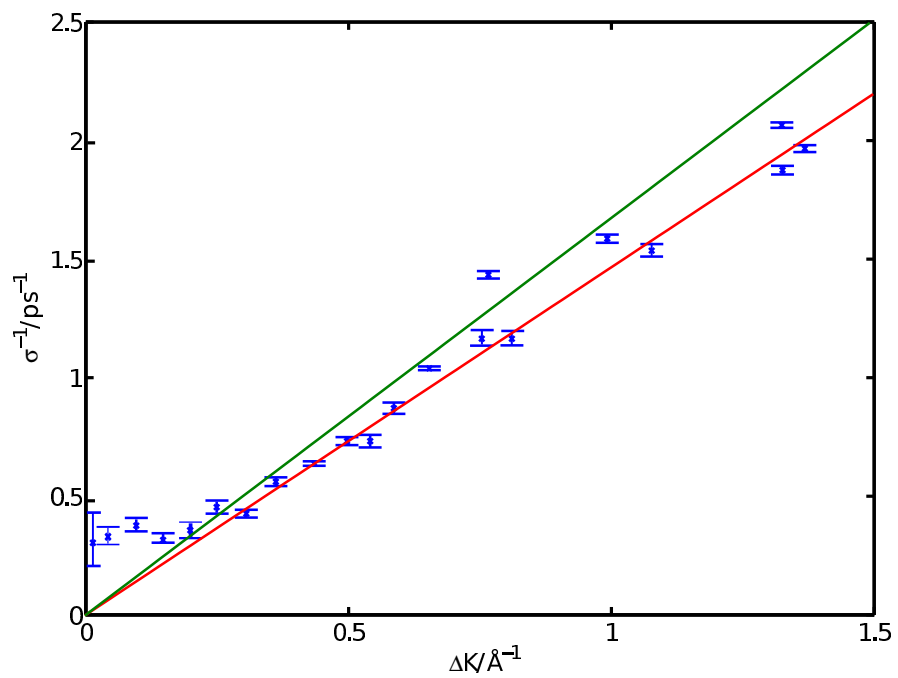


Figure 4.22: Gaussian variance, σ , as a function of momentum transfer, ΔK , for Na/Cu(111) [11\bar{2}] direction, at a coverage $\Theta = 0.025$ ML. Experimental data is presented in blue. The 2-D ideal gas line for the mass of sodium is presented in green and for an effective mass of 30 amu, in red.

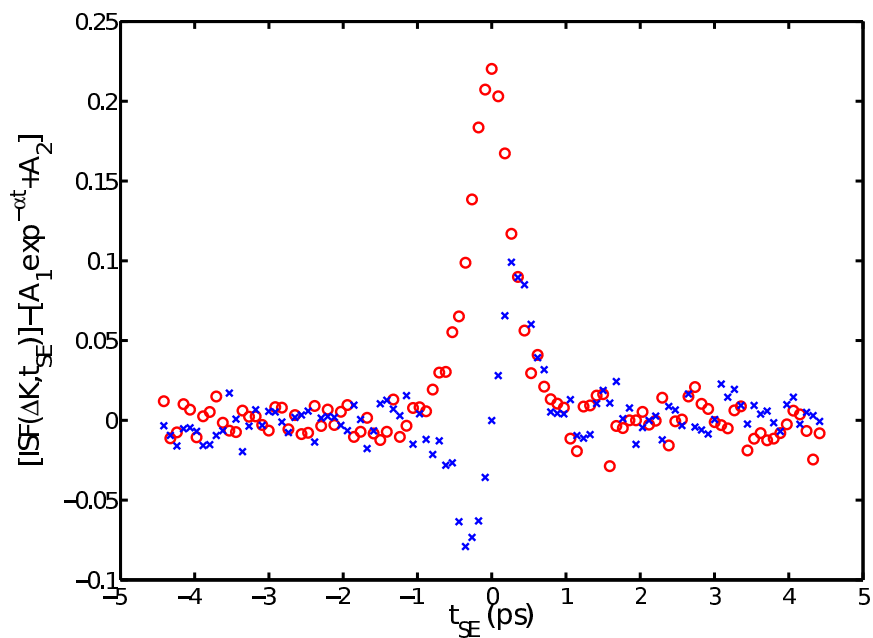


Figure 4.23: Real (red circles) and imaginary (blue crosses) ISF of Na/Cu(111) in the $[11\bar{2}]$ direction at coverage $\Theta = 0.025$ ML at a temperature 155 K ant momentum transfer of $\Delta K = -0.2 \text{ \AA}^{-1}$, presented at spin-echo times of ± 5 ps. The elastic (A_2) and diffusion ($A_1 \exp^{-\alpha|t|}$) components are subtracted leaving a Gaussian function, symmetric about $t = 0$ in the real and asymmetric in the imaginary.)

delta function, as shown in (d) as the difference between the solid and dashed lines. Finally (d) shows that the time spectrum of the shifted peak, which consists of the original data shown in figure (a) multiplied by $\cos(\Delta\omega t) + i \sin(\Delta\omega t)$. From the ana-

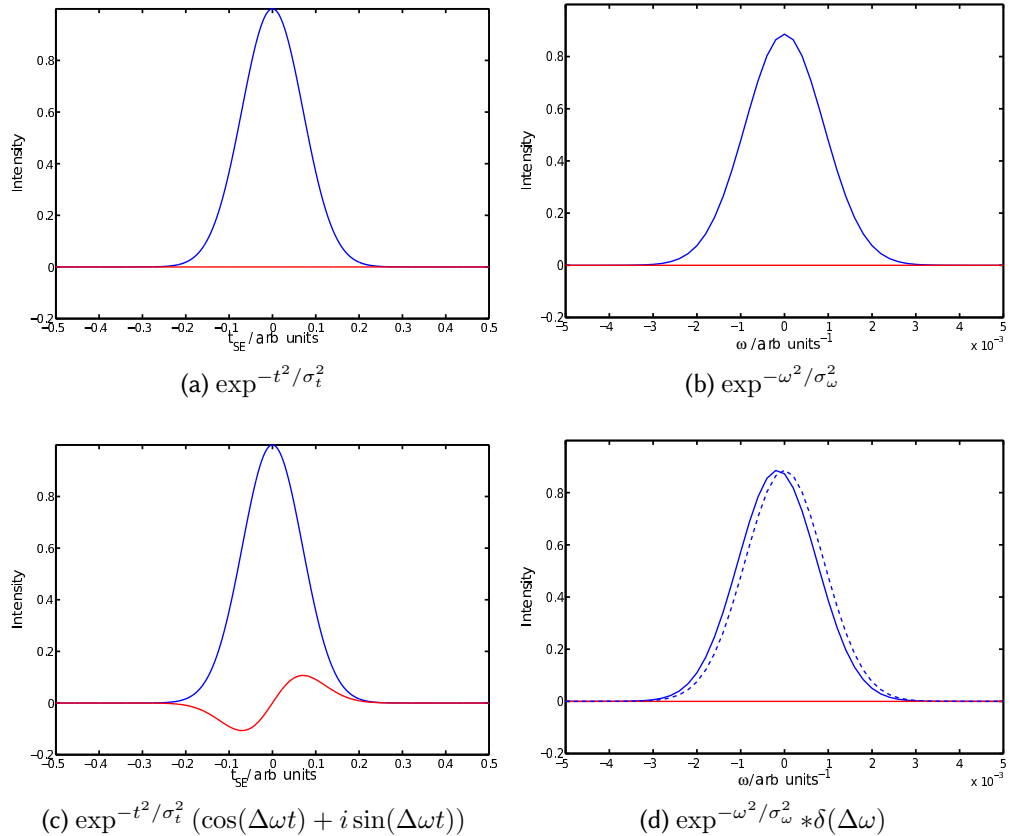


Figure 4.24: Analytical representation of the ISF in time on the left and frequency on the right, the real part of the spectra are shown in blue and the imaginary part in red. Panel (a) shows a completely real Gaussian function in time and panel (b) shows the Fourier transform, which is a completely real Gaussian. Panel (d) presents the effect of a small frequency shift, achieved by convolving a delta function at $\Delta\omega$ on the data in panel (b) shown as a blue dashed line. Panel (c) shows the transform of figure (d) in time, and demonstrates a complex function of the form $\exp^{-t^2/\sigma_t^2} (\cos(\Delta\omega t) + i \sin(\Delta\omega t))$. By dividing the data in figure (c) by $\cos(\Delta\omega t) + i \sin(\Delta\omega t)$ the value of the frequency shift $\Delta\omega$ can be determined that reproduces the data in panel (a).

lytic plots in figure 4.24 it is possible to take the ISF presented in figure 4.24c, divide by $\cos(\Delta\omega t) + i \sin(\Delta\omega t)$, optimise the value of $\Delta\omega$ to make the function completely

real, and thereby directly calculate the optimal magnitude of the frequency shift.

The procedure has been applied to all the experimental ISFs, the results for the spectrum presented in figure 4.23 are shown in figure 4.25, which demonstrates that the imaginary part can be eliminated very effectively by such a shift. The same

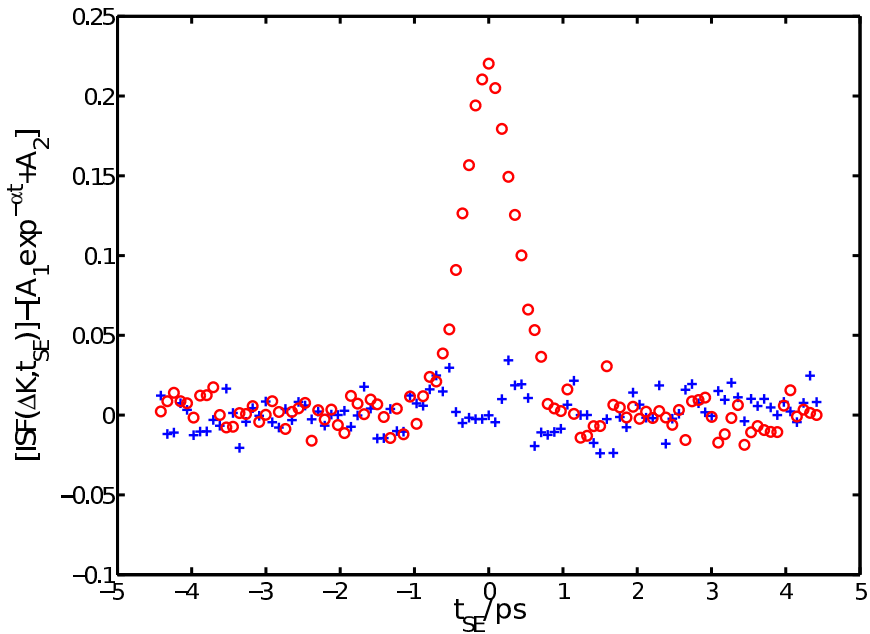


Figure 4.25: Real (red circles) and imaginary (blue crosses) ISF of Na/Cu(111) in the $[1\bar{1}\bar{2}]$ direction at coverage $\Theta = 0.025$ ML, Temperature 155 K, $\Delta K = -0.2 \text{ \AA}^{-1}$, presented at spin-echo times of ± 5 ps. The elastic (A_2) and diffusion ($A_1 \exp^{-\alpha|t|}$) components are subtracted leaving a Gaussian function, symmetric about $t = 0$ in the real and asymmetric in the imaginary. The purple and green points represent the original ISF divided by $\cos(\Delta\omega t) + i \sin(\Delta\omega t)$ with an optimal value of $\Delta\omega$ that reduces the imaginary signal shown as blue crosses to that shown by green circles

process is performed across all of the spectra, and figure 4.26 shows the results for the whole range of momentum transfer in the dataset. The most striking feature of figure 4.26 is the sudden change from energy gain, $\Delta K < 0$, to energy loss for $\Delta K > 0$. Also, we note that the red line, drawn through the data points, suggests that the magnitude of the energy change is approximately the same on both sides of the origin, being slightly larger for $\Delta K < 0$. A number of explanations are candidates to explain the origin of the energy shift. Most can be ruled out on the basis that there is no obvious reason for a sudden change in sign at $\Delta K = 0$. Thus, excitation

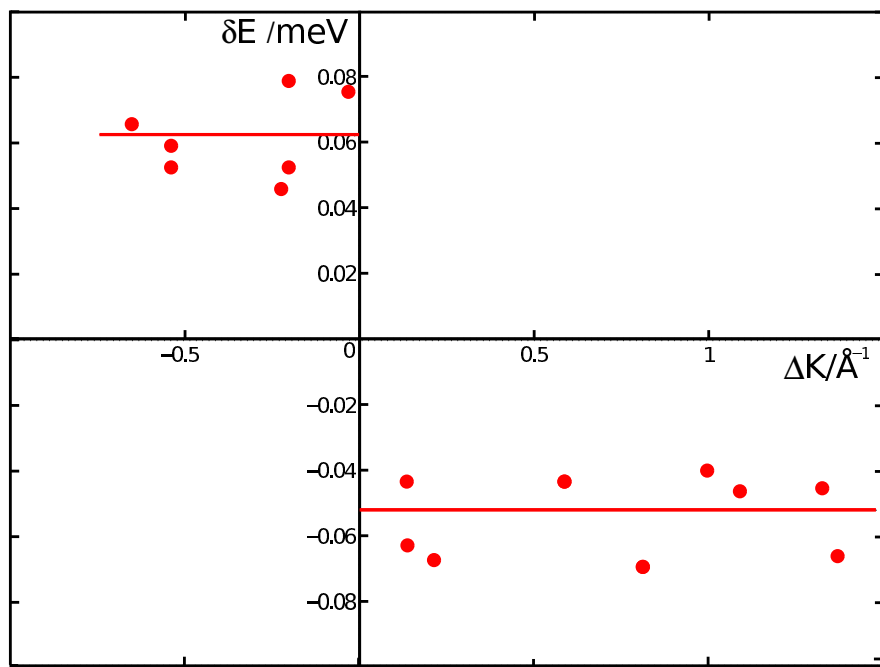


Figure 4.26: Dependence of the energy shift, δE in the quasielastically scattered peak with respect to momentum transfer, ΔK , for Na/Cu(111) [11 $\bar{2}$] direction, coverage $\Theta = 0.025$ ML determined from experimental ISFs measured at surface temperature 155 K with a He^3 beam of incident energy 8 ± 0.4 meV. The solid red line is a guide to the eye and it suggests that the energy shift is approximately independent of ΔK . It is evident that the sign of the energy shift changes discontinuously about $\Delta K = 0$.

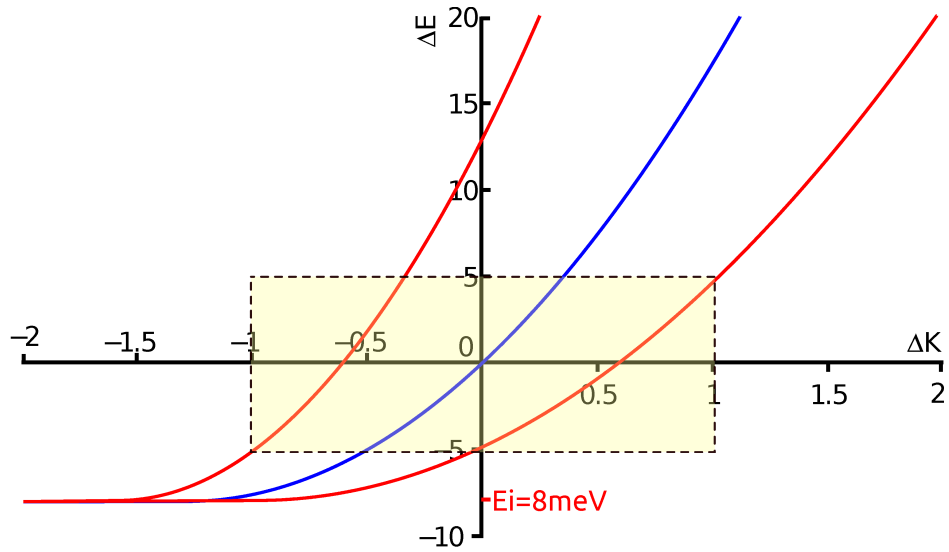
of perpendicular or parallel vibrational modes of the adsorbate are unlikely to be candidates. Adsorbate recoil has been suggested as a possible explanation and a complete theory has been published [131]. The analytic theory, which applies to a 2-D flat energy landscape, predicts a specific dependence on ΔK , specifically $\Delta E \propto \Delta K^2$. The observations in figure 4.26 do not support the hypothesis. It can be argued that, in an energy landscape where the adsorbate spends most time localised in an adsorption well, the recoil should be identically zero. Only discrete energy losses, corresponding to single quanta excitations should be observable and we have already argued they cannot explain the data. As in the Mössbauer effect [132], there should be no recoil observable in the quasi-elastic signal. The most likely explanation lies in the form-factor for scattering. A similar effect has been observed previously in TOF experiments in the Xe/Pt(111) system [54].

Here we expand on the methods from [54] to extract quantitative information on the form factor for scattering from the adsorbate. It is important to recognise that for a given scattering angle the energy, ΔE , and momentum transfer, ΔK , are related by kinematics [18], such that,

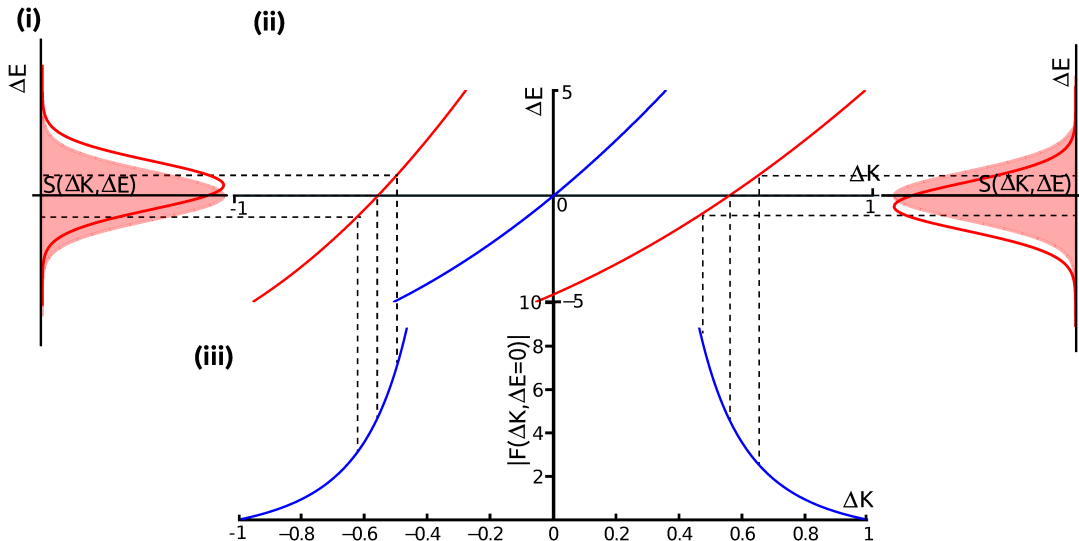
$$\Delta E = \frac{\hbar^2}{2m} \left(\frac{|K_i + \Delta K|^2}{\sin^2 \Theta_f} - k_i^2 \right) \quad (4.15)$$

known as the instrument scan curve.

Figure 4.27a shows scan curves for specular and off-specular scattering. The blue curve, which intersects $\Delta E = \Delta K = 0$, is the case for specular scattering while the red curves correspond to $\pm 5^\circ$ off specular. In the figure the beam energy is 8 meV, which is seen as the asymptotic value of all three curves at the left of the figure. The central, shaded portion of figure 4.27a, is drawn magnified in the centre of figure 4.27b, marked (ii). In addition the lower part of the figure 4.27b(iii) shows a schematic of the form factor, F . The key feature is the general trend to decrease strongly with $|\Delta K|$ [54, 133]. The origin of energy shifts can now be seen on 4.27b(i). The shaded Gaussian corresponds to the true QHAS centred, in the absence of energy loss, at $\Delta E = 0$. The measured intensity is $S \times F$ which is shown as the shaded curve, in this case shifted to positive ΔE by the form of F . For positive ΔK , the gradient of F is reversed and the energy shift becomes negative. The effects can be compared quantitatively with the data, which we analyse next.



(a) Scan curve for an 8 meV helium beam, on specular in red and $\pm 5^\circ$ off specular in red



(b) Effect of the scan curve (ii) and a typical form factor line [133] (iii), resulting in the energy shift shown in (i)

Figure 4.27: Panel (a) shows the scan curve for an 8 meV beam of He^3 at specular (blue) and $\pm 5^\circ$ off specular. The portion of the scan curve shown in the yellow box is expanded in section (ii) of the lower panel (b). Section (iii) shows a typical shape for the form factor [133] which is multiplied by the scan curve. The red shaded region of panel (b) represents a Gaussian QHAS peak, which is shifted by the effect of the form factor and scan curve to the red curve, which for positive ΔK , causes a negative shift in ΔE , and for negative momentum transfers a positive ΔE shift.

In a small range of ΔK the form factor can be written as a linear approximation

$$F(\Delta K) \approx F(\Delta K_0) + (\Delta K - \Delta K_0) \frac{\delta F}{\delta \Delta K} \Big|_{\Delta K_0} + \dots \quad (4.16)$$

Similarly the scan curve, equation 4.15, can be approximated as

$$\Delta E = \frac{\delta \Delta E}{\delta (\Delta K)} \Big|_{\Delta K_0} (\Delta K - \Delta K_0) = \beta(\Delta K_0)(\Delta K - \Delta K_0) \quad (4.17)$$

So that F varies linearly with ΔE .

$$F = F(\Delta K_0) + \frac{\delta F}{\delta (\Delta K)} \Big|_{\Delta K_0} \frac{\Delta E}{\beta}, \quad (4.18)$$

$$= F(\Delta K_0) [1 + \alpha \Delta E], \quad (4.19)$$

where

$$\alpha = \frac{\delta F}{\delta (\Delta K)} \Big|_{\Delta K_0} / (\beta F(\Delta K)). \quad (4.20)$$

The gradient α is related to the measured shift in the quasielastic scattering. If the dynamical structure factor $S(\Delta E)$, has a Gaussian form,

$$S(\Delta E) = A \exp\left(-\frac{\Delta E^2}{2\sigma^2}\right). \quad (4.21)$$

The measured signal, I , is equation 4.21 multiplied by equation 4.19 so

$$I(\Delta E) = F \times S = AF(\Delta K_0) \exp\left(-\frac{\Delta E^2}{2\sigma^2}\right) [1 + \alpha \Delta E], \quad (4.22)$$

This corresponds to a peak shifted away from $\Delta E = 0$. The position of the new maximum can be found by differentiation

$$\frac{dI}{d(\Delta E)} = AF(\Delta K_0) \exp\left(-\frac{\Delta E^2}{2\sigma^2}\right) \left\{ \alpha - \frac{\Delta E}{\sigma^2} - \frac{\alpha \Delta E^2}{\sigma^2} \right\}, \quad (4.23)$$

which is a maximum ($dE/d(\Delta E) = 0$) when

$$\alpha\Delta E^2 + \Delta E - \alpha\sigma^2 = 0 \quad (4.24)$$

so that

$$\Delta E_{max} = \frac{-1 + \sqrt{1 + 4\alpha^2\sigma^2}}{2\alpha} \quad (4.25)$$

at small values of ΔE

$$\approx \alpha\sigma^2 \quad (4.26)$$

The values, ΔE_{max} given in equation 4.26 are those that are measured and plotted in figure 4.26. Corresponding values of the Gaussian width, σ are given in figure 4.22, which allows values of α to be determined as a function of ΔK . The results are plotted in figure 4.28. The data points as shown as red symbols and the blue curve is a best fit power law to the data. The curve indicates that $\alpha \propto \Delta K^{-2.7 \pm 0.1}$ with good accuracy.

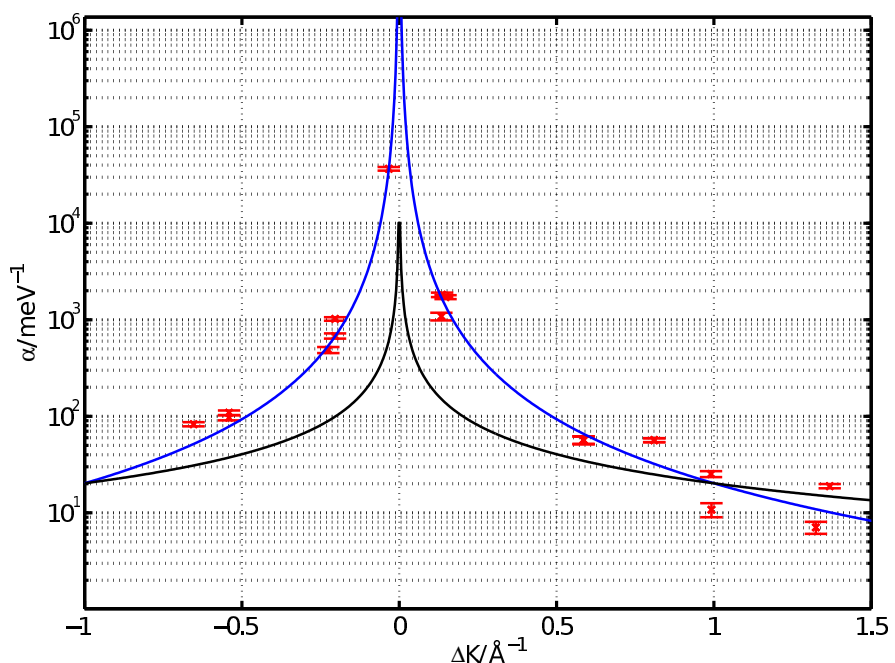


Figure 4.28: Red points show α , the ratio of energy shift, ΔE , to the square of the width of the quasielastic peak, σ , as a function of momentum transfer, ΔK , extracted from the experimental ISFs for Na/Cu(111) on the $[11\bar{2}]$ direction at coverage $\Theta = 0.025$ ML at surface temperature 155 K with a He^3 beam of incident energy 8 meV. The blue line is a best fit of the form $\alpha \propto \Delta K^{-2.7 \pm 0.1}$. The black line is the form for a form factor following a power law where $\alpha \propto \Delta K^{-1}$.

4.5 Summary and discussion

In this chapter I have shown that it is possible to extract small time-scale data on the 1 – 10 ps timescale for both the real and imaginary spectra using the methods outlined in chapter 3. As in the earlier work, we observe a clear ballistic motion characterised by a Gaussian lineshape, however for the Sodium case we also observe a significant energy shift in the spectrum which we attribute to scattering from the form factor, exacerbated by large energy broadening, equivalent to a fast decay process.

In previous work [54, 133] the form factor has been assumed to follow a power law in ΔK .

$$F(\Delta K) \approx F_0 \Delta K^{-n}, \quad (4.27)$$

where $n = 2 \text{ meV}^{-1}$ corresponds to a hard sphere. These simple models assume hard wall scattering. It is straight forward to calculate the effect of such a form factor. Equation 4.20 gives

$$\alpha = -\frac{n}{\beta} \Delta K^{-1} \quad (4.28)$$

β is related to the properties of the beam, and varies slowly with ΔK , so that the ΔK dependence in equation 4.28 does not change with n , although the magnitude of α is directly proportional to n . It is interesting to note that the observed dependence on ΔK differs significantly for the prediction in equation 4.28. The black line in figure 4.28 shows the prediction for $n=1$.

The fact that the data cannot be described by a simple form factor for hard wall scattering suggests that further work utilising soft-wall theories for scattering are necessary. As a consequence further analysis of ballistic motion is not made at this stage. In the next chapter a similar study of lithium on the same substrate is presented. The form factor is shown to be less important in the case of lithium and a quantitative investigation of the ballistic motion can be performed for that case.

Chapter 5

Observation of transition between ballistic and diffusive motion in lithium on copper(111)

Previous chapters have shown the importance of the detailed lineshape of the ISF, specifically the transition of ballistic to diffusive motions. In chapter 4 it was concluded that the effects of the form factor on the scattered signal were significant for sodium which made analysis more difficult. In the present chapter the same measurement techniques, that were applied to the faster part of the ISF for sodium, are applied to lithium on the same copper(111) surface. The effects of the form factor are shown to be less significant and the data reveals a clear transition from ballistic to diffusive motion. The data is analysed in terms of a generalised Langevin equation and, for the first time, we are able to identify the effects arising from the limited bandwidth of the thermal excitations.

5.1 Previous relevant work

Adsorption of lithium on copper(111) at temperatures of above 300K has been reported to result in Cu(111)-(2x2)-3Li RT intermixed surface structure using LEED [134] and photoemission spectroscopy [135]. At lower temperatures and coverages, a simpler commensurate p(2x2) overlayer structure is formed [136] where the lithium atoms sit in fcc hollow sites. Experimental results are supported by ab-initio Hartree-Fock and DFT calculations [137]. A diagram showing the low temperature first layer

saturation structure is shown in figure 5.1 and demonstrates that, at first layer saturation, there is one lithium atom for every four copper atoms in the topmost layer.

In addition to structural measurement there have been a number of studies of vibrational properties and phonon spectra. A feature of lithium measurements arises from its low mass, leading to a higher vibrational frequency than that for sodium. An recent electron energy loss spectra (EELS) study by Lindgren et. al. [136], presents results for coverage dependance of the vibrational frequency of lithium on copper(111). The energy loss peak shifts from 38 meV at low coverage to 43 meV at 0.3 ML and then remains constant while the peak for sodium is centred at 21meV for comparison. The high frequency vibrations of lithium give rise to quantum properties observed, such as those presented by Huang *et.al* [42] on copper (001). And it is well known that charge donation from alkali metals has a dramatic effect on force constants, phonon spectra and the structural behaviour of alkali metals with the effect largest for the lithium [42, 114, 125].

Some theoretical work on the diffusion of alkali metals has been performed, for example transition state theory applied to theoretical parametrised DFT pseudo-potentials by Padilla-Campos *et. al.* [137], has been used to predict the adsorption sites and diffusion pathways for sodium, lithium and potassium on the copper substrate. The work builds on a previous DFT study by Scheffler and co-workers [138] on the gold surface, however the results are found to be heavily dependent on the number of layers of the adsorbate used in the calculation.

5.2 Experimental methods

A Cu(111) sample was mounted on the sample manipulator, providing position and cryogenic temperature control. The sample preparation procedure is the same as that for sodium and is described in detail in chapter 4 section 4.2. Throughout the measurement program the base pressure was maintained at less than 2×10^{-11} mbar and the sample was cleaned daily, using cycles of argon ion sputtering ($I_{\text{emiss}} \approx 6 \mu\text{A}/\text{cm}^2$, 800 V Ar⁺ ions, $T_s = 300$ K for 30 mins) followed by surface annealing ($T_s = 800$ K, 30 secs). Surface quality was monitored though measurement of helium reflectivity using a quadrupole mass spectrometer in the sample chamber. A high quality surface was confirmed regularly by exceptionally strong helium reflectivity (> 34%) measured at $T_s = 300$ K. The temperature of the source nozzle was main-

tained at 37K using a helium cryostat refrigerator. The source produces a typical kinetic energy of 8 meV, with full width half maximum of 0.2 meV. The precise beam properties were recorded at regular intervals and the corresponding values used in data analysis. More detail on the procedures and instrumentation are given in chapter 3. The clean crystal is aligned to the [11 $\bar{2}$] surface azimuth, by optimising the pattern of helium scattered from high purity carbon monoxide adsorbed to saturation. The temperature of the sample was monitored using a type-K¹ thermocouple spot welded onto a sample mount constructed from tantalum as described in chapter 3. Temperature control is achieved with cryogenic sample cooling using liquid nitrogen ($T_s > 120$ K), balanced against radiative heating from a coiled tungsten filament.

5.3 Coverage calibration

The degassed alkali metal dosing arm described in section 4.2, fitted with a lithium dispenser from SAES Getters [120] was used to dose the sample. The method is the same as that for sodium, and is outlined with reference to figure 4.3 in chapter 4. Coverage is calculated by monitoring the change in specular helium reflectivity as a function of time while lithium is deposited. A dispensing current, typically 7.2 A is passed through the getter (**G**) for a period of approximately 5 minutes with the dosing arm, shown as (**A**) in figure 4.3a retracted and the flag (**H**) closed. Residual gasses are pumped during initial heating such that the clean sample is not contaminated. The dosing arm is placed in front of the sample and the flag opened to commence deposition, which is monitored using specular helium reflectivity. Finally the flag is closed and arm retracted to complete the dose.

The results of an uptake measurement are presented in figure 5.2. Initially lithium adsorbs in fcc and hcp hollow sites [136]. As in other cases of alkali metal adsorption the specular reflected signal decreases strongly at first, as shown in the region starting at *A* in figure 5.2, suggesting the adsorbates are well-separated. As the lithium dose is increased the nearest-neighbour separation reduces, causing the reflectivity to rise due to the formation of ordered compressed structures. Onset of different compressed structures are identified by the gradient changes at *B*. At the saturation

¹type-K thermocouple : chromel (90 % nickel and 10 % chromium) alumel (95 % nickel, 2 % manganese, 2 % aluminium and 1 % silicon) [83]

coverage all of the available sites are filled in a commensurate p(2x2) structure [136], which occurs at C . Doses past the saturation are reported to result in 2-D island formation and copper-lithium substitution configurations, with the precise structures dependent on the temperature of the crystal as shown by Mizuno *et. al.* [134], structural changes would be evident as changes in gradient of the trend in helium reflectivity during dosing, for which there is some evidence marked D in figure 5.2.

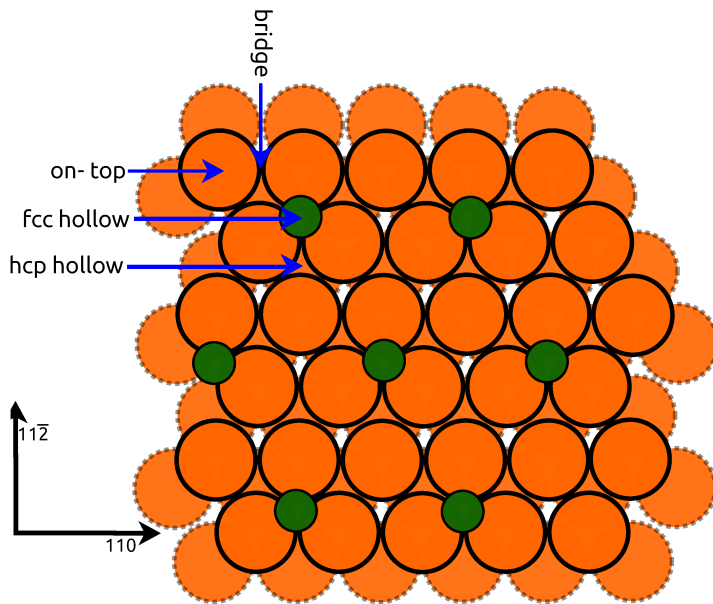


Figure 5.1: Position of lithium atoms on the copper(111) surface at saturation coverage, at a sample temperature 180 K. Top layer copper atoms are shown as solid orange circles and second layer atoms shown beneath. Lithium atoms are shown in green for the $\Theta = 1 \text{ ML}$ p(2x2) structure determined using LEED [134], work-function [136] and photoemission spectroscopy [135].

For the experiments reported later in the chapter, the dosing was stopped at a specular attenuation $I = I_0/5$, remaining in the low coverage limit, where the adsorbate atoms are well separated and only weakly interacting. Assuming a sticking coefficient of unity, which photoemission studies confirm to be appropriate for coverages below first layer saturation [135]; the uptake curve in figure 5.2 can be used to estimate the coverage. For the measurements of Lithium, where saturation coverage contains 1/4 of the substrate layer atoms, the $I = I_0/5$ dose equates to a coverage $\Theta = 0.025 \text{ ML}$ with respect to the number of atoms in the first substrate layer.

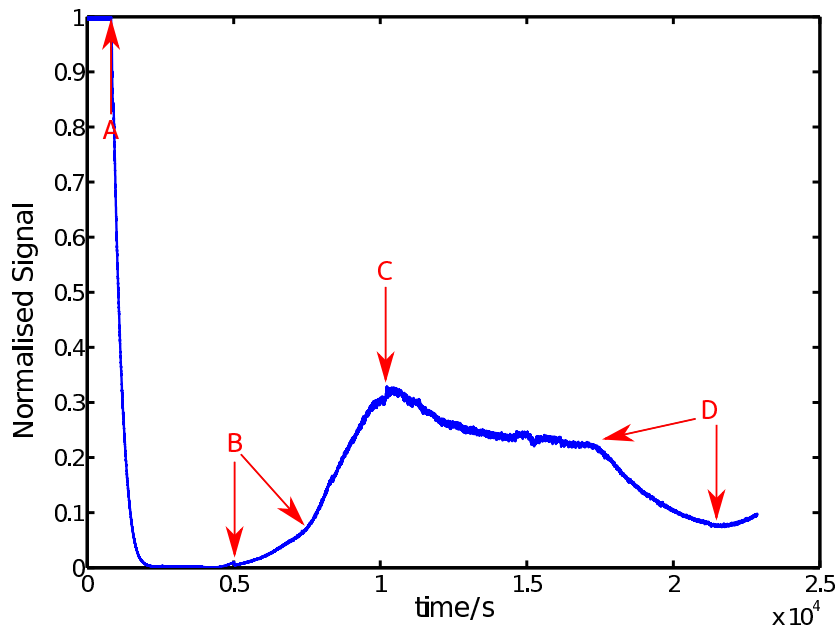


Figure 5.2: Normalised uptake curves of Li/Cu(111) taken at a surface temperature of 200 K. Specular helium reflectivity is shown as a function of time. The dosing flag is opened at A, and an initial decrease in reflectivity is observed as the surface order decreases, followed by an increase as the surface stabilises approaching the saturation coverage, shown at C. At the points indicated by B, different compressed surface structures are formed. After saturation at C, a decrease in reflectivity is observed as more complex structures build up occurs with some evidence of further compressed structures forming at D, which may be consistent with reported substitution processes at higher coverage [134].

5.4 Measurement of Lithium dynamics

Having considered static scattering we now consider dynamics measurements employing surface spin-echo spectroscopy. ISFs were recorded at a coverage $\Theta = 0.025$ at typically 140 K sample temperature. Figure 5.3 presents a typical ISF, with the real contribution shown as red crosses and the imaginary as blue crosses. In addition to

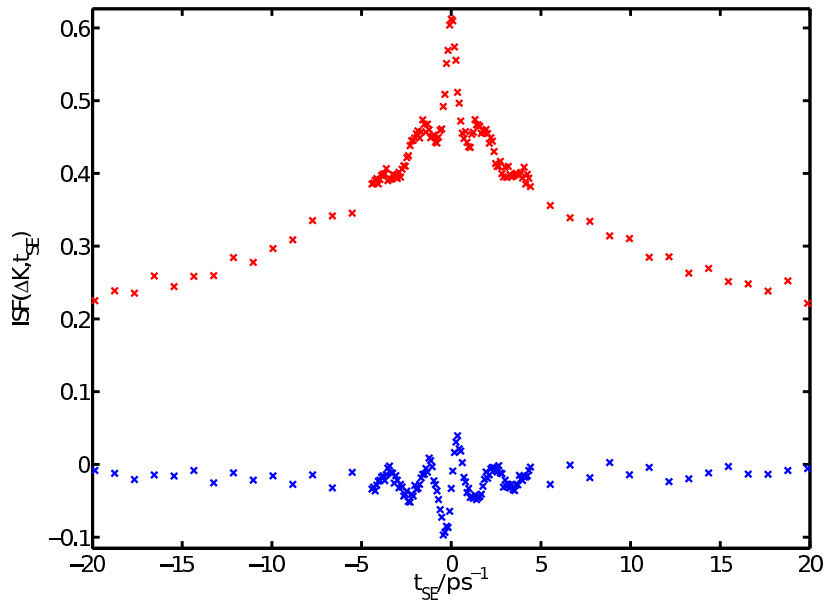


Figure 5.3: Li/Cu(111) ISF measured in the $[11\bar{2}]$ surface direction at a sample temperature of 140 K with momentum transfer, $\Delta K = -0.307 \text{ \AA}^{-1}$ and beam energy $7.92 \pm 0.06 \text{ meV}$. Red crosses show the real part of the spectrum and blue crosses the imaginary part. At spin-echo times faster than $\pm 10 \text{ ps}$, an oscillation is visible in the real and imaginary parts of the spectrum. There is a phase difference between the real and imaginary spectra, consistent with an inelastic scattering process.

the expected exponential decay at long times, there is an oscillatory contribution to the ISF that is clearly visible in figure 5.3, particularly at spin-echo times less than 10 ps. Inelastic scattering from substrate modes is the most likely cause of these features as the adsorbate modes occur at much higher frequencies [21]. It is desirable to remove these vibrational features from the data and in the present work we remove them using a Fourier filter method described previously in section 4.3.1 and appendix D, Figure 5.5 shows the oscillatory component that is identified and subtracted.

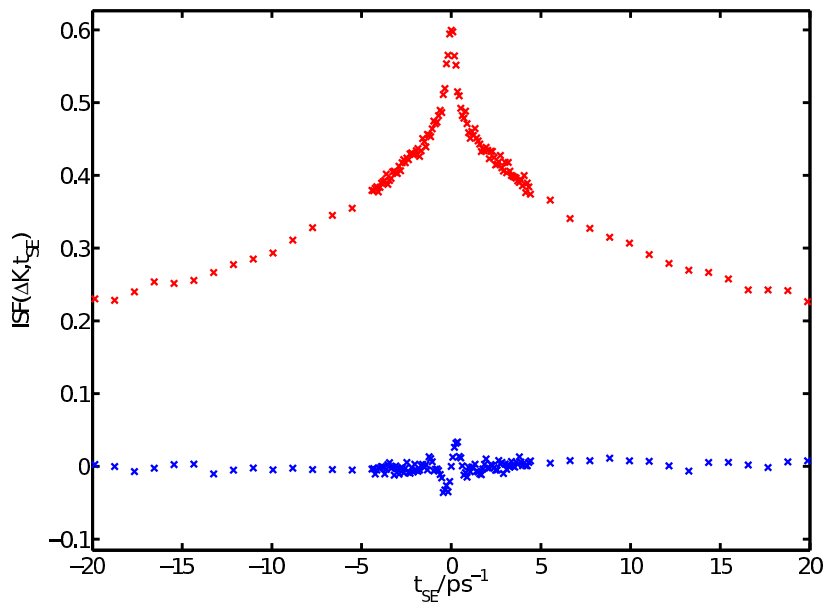


Figure 5.4: Li/Cu(111) ISF measured in the $[11\bar{2}]$ surface direction, taken at a sample temperature of 140 K with momentum transfer, $\Delta K = -0.307 \text{ \AA}^{-1}$. Red crosses show the real part of the spectrum and blue crosses the imaginary part. The inelastic scattered signal, shown in figure 5.3 has been removed using a Fourier transform filter presented in section 4.3.1. At times faster than about ± 3 ps there is evidence of an energy shift in the quasi-elastic scattering, most visible in the imaginary signal.

Comparing figure 5.3 with figures 5.4 and 5.5 demonstrates that a simple filtering technique applied in the frequency domain can significantly enhance the ability to separate and analyse the inelastic and quasi-elastic processes which are not easily separable in the time domain. In the current work we focus on the analysis of the quasi-elastically scattered signal, figure 5.4, but note that the removed part of the spectrum shown in figure 5.5 takes the form of decaying sinusoidal oscillation with a π phase shift between real and imaginary, consistent with expectations for inelastic scattering.

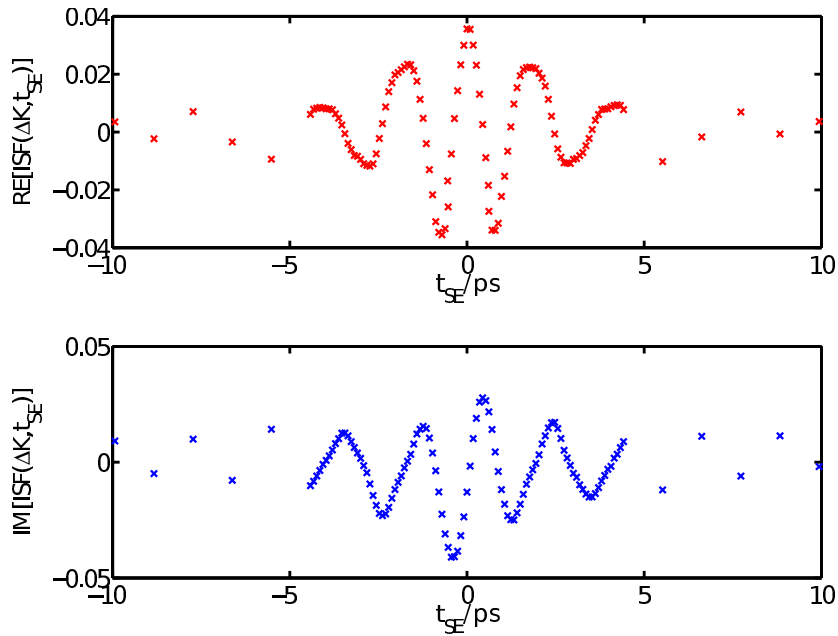


Figure 5.5: Contribution to the spectra shown in 5.3 associated with an inelastic scattering process and filtered using a Fourier filtering process detailed in section 4.3.1. the real part of the spectrum is shown in red and takes the form of a decaying cosine function. The imaginary spectrum is shown in blue and is a decaying sine function. The total form is typical of the spectra resulting from inelastic scattering from a substrate phonon.

We now consider an analysis of the quasielastic signal. The real part of the spectra shown in figure 5.4 consists of several decaying processes and finally settles at a constant level. The imaginary contribution is negligible except for a small asymmetric peak at times less than ≈ 3 ps.

To begin we consider the real part of the spectrum. Initial analysis is performed

using the same method used previously; the spectrum is separated in time and individual processes analysed separately. The constant level and slowest decay parameters are modelled with an exponential of the form $A_1 \exp(-\alpha t) + A_0$ with the parameters A_1, α and A_0 found using least squares optimisation. Since there are several decaying processes in the ISF, it is necessary to specify a cut-off time over which to optimise the model. The applicability of the model and particularly the cut off time is quantified using the R squared value, R_{adj}^2 , adjusted for the number of degrees of freedom of the model, where R^2 is the square of the correlation between the response value of the data and the predicted response value. If the data is defined as a series $y_{i=1}^n$ and the fit as $f_{i=1}^n$, then R_{adj}^2 is defined:

$$R_{adj}^2 = 1 - \frac{(n-1) \sum_{i=1}^n (y_i - f_i)^2}{(n-m) \sum_{i=1}^n (y_i - \bar{y})^2}. \quad (5.1)$$

Starting with the slowest 5 data points and incrementing towards $t=0$, the model is iteratively compared with the data by virtue of the R^2 parameter, and the best cut-off time for each spectra determined. The results are very similar to those used for sodium and presented in section 4.3.2 of chapter 4.

The ISF in figure 5.4 is shown with the model $A_1 \exp(-\alpha t) + A_0$ subtracted in figure 5.6 as red circles. The remaining data is fitted, at very small momentum transfers ($< 0.2 \text{ \AA}^{-1}$) the spectra consists of a single Gaussian function, but at larger momentum transfers a clear second exponential decay process is present. The faster parts of the ISF, shown in figure 5.6 are compared with the model $A_2 \exp(-\alpha_2 t) + A_3 \exp(-t^2/(2\sigma^2))$, with A_2, α_2, A_3 and σ found using a least squares optimisation. Figure 5.7, presents a summary of the extracted optimisation parameters used to characterise the diffusion process. Panel (c) of figure 5.7 presents the decay rate α , of the exponential function $A_1 \exp(-\alpha t) + A_0$, there is generally a periodic dependence on momentum transfer with some weak evidence of interactions. Panel (b) shows the exponential decay rate α_2 , of the function, $A_2 \exp(-\alpha_2 t) + A_3 \exp(-t^2/(2\sigma^2))$ there are no data points for $\Delta K < 0.25 \text{ \AA}^{-1}$ as there is no evidence of a second decay process at small momentum transfers. The Gaussian part of the residual model is treated separately later. Panel (a) shows the ratio of the amplitude A_1/A_2 for the two

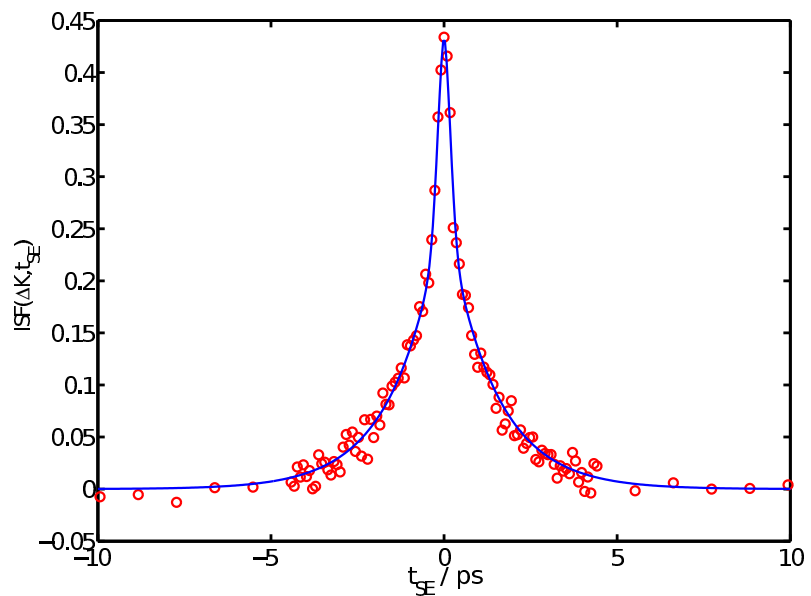


Figure 5.6: Red points show the ISF after the slowest decaying exponential function has been subtracted, measured in the $[11\bar{2}]$ surface direction, taken at a sample temperature of 140 K with momentum transfer, $\Delta K = -0.307 \text{ \AA}^{-1}$. The blue line is a model line of the form $A_2 \exp(-\alpha_2 t) + A_3 \exp(-t^2/(2\sigma^2))$ with A_2, α_2, A_3 and σ optimised using a non-linear least squares optimisation.

exponential functions in the model, the data is constant with a hopping between fcc and hcp non-equivalent adsorption sites as described in reference [139], and applied by McIntosh [103], Hedgelend [98] and Lechner [89].

Figure 5.8 presents the decay rates, α and α_2 , of the function, $A_2 \exp(-\alpha_2 t) + A_3 \exp(-t^2/(2\sigma^2))$, fitted to the slowest decaying process, as a function of temperature, between 125 K and 150 K on a log y axis. The lines represent a linear regression to the data, whose gradient is related to the activation energy through Arrhenius' equation [93]. From the plot the activation energy for both processes is found to be the same at 8.3 ± 0.2 meV, which provides a starting point for the potential energy landscape in Langevin simulations later in the chapter. While the activation energy is the same it is noted from the figure that the intercept is different, this may be understood from noting that the intercept is related to the pre-exponential factor in Arrhenius' equation and therefore suggests that the rate of forward and backward hopping changes due to the energy degeneracy of the two adsorption sites.

Before considering the final, fastest part of the real spectrum, we turn to the small inelastic component present in figure 5.4. This asymmetric peak is smaller in amplitude but otherwise reminiscent of the peak observed for Na/Cu(111) which was attributed to the effect of the form factor on scattering and resulted in an energy shift in the quasi-elastic spectrum. The ISFs are analysed in the same way as for sodium, in this case the two exponentially decaying components are subtracted, leaving only the fastest decaying process in the real spectrum. An example of the complex spectrum on a ± 5 ps scale is shown in figure 5.9a, which shows a symmetric peak in the real part of the spectrum and an asymmetric peak in the imaginary part. The complex spectrum is then divided by $\cos(\Delta\omega t) + i \sin(\Delta\omega t)$, and the value of $\Delta\omega$ optimised to make the complex function completely real. Comparing panels (a) and (b) in figure 5.9, the effect of the process is to shift the imaginary polarisation into the real part of the spectrum, and therefore determine the shift in energy experienced in the observed data. The frequency shift $\Delta\omega$ is converted into an energy shift ΔE and is shown as a function of ΔK in figure 5.10, and is consistent with scattering from a form factor similar to that observed for sodium in chapter 4.

The ISFs obtained after removing the results of scattering from the form factor are entirely real and only contain the fastest decaying contribution which we turn to analyse now. We expect to observe a fast decay due to ballistic motion which

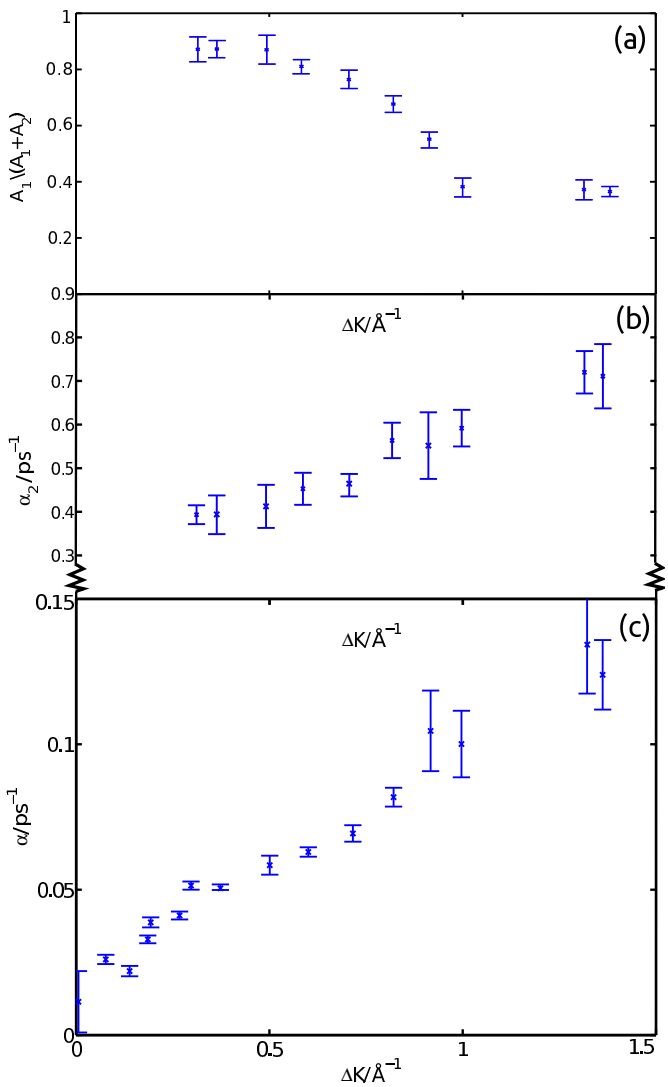


Figure 5.7: Plots of the diffusion characteristics of Li/Cu(111) in the $[1\bar{1}\bar{2}]$ surface direction, taken at a sample temperature of 140 K over a range of the absolute values of momentum transfer, ΔK . Blue points are optimised parameters from experimental ISFs, and the red lines are optimised to the same model functions for ISFs determined using the Generalised Langevin equation model detailed in section 5.5. From the bottom of the figure, panel *c* presents the decay rate α , of an exponential function $A_1 \exp(-\alpha t) + A_0$ applied to the slowest decay process in the ISF. Panel *b* shows the exponential decay rate α_2 , of the function $A_2 \exp(-\alpha_2 t) + A_3 \exp(-t^2/(2\sigma^2))$ applied to the residual ISF after subtracting the slowest exponential part, the Gaussian part of the model is treated separately. Panel *a* presents the ratio of the amplitude of the two exponential functions, the data is constant with hopping between several non-equivalent sites [139].

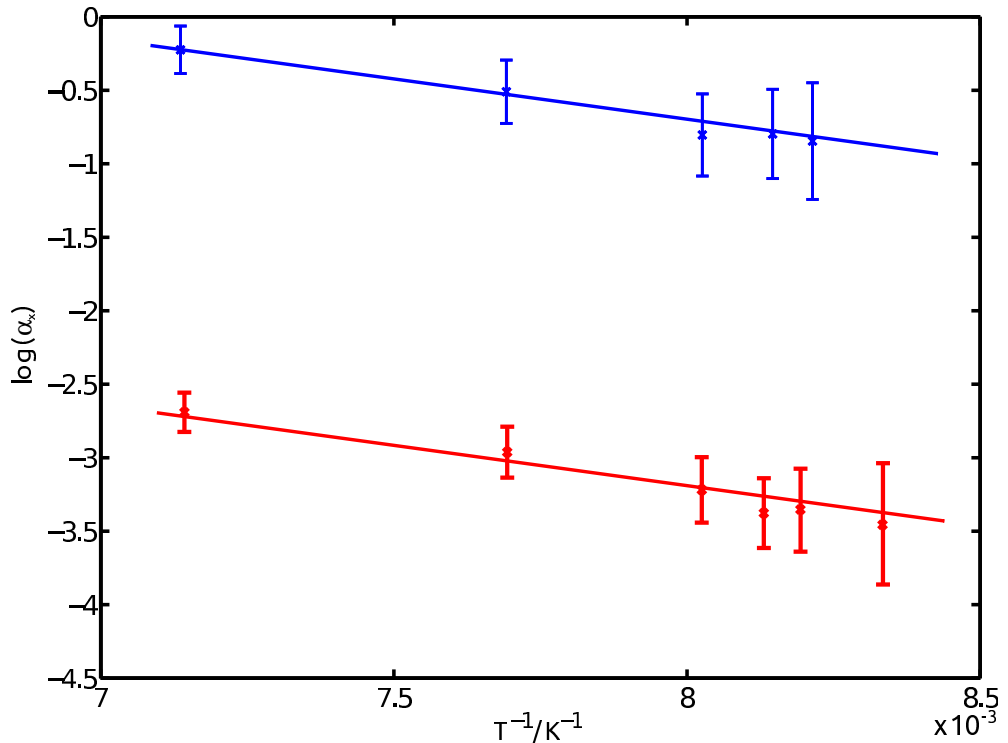


Figure 5.8: Decay rates α_1 (red) and α_2 (blue) of the two exponentials used to model the ISFs for Li/Cu(111) shown as a function of surface temperature at $\Delta K = 1 \text{ \AA}^{-1}$ in the [11\bar{2}] surface direction. Data is shown on $\log(\alpha)$ vs $1/T$ scales and demonstrates a linear dependence consistent with a classical activated process. The activation energy may be determined using an Arrhenius' law to be $8.3 \pm 0.2 \text{ meV}$. The activation energy of the two decays is the same as they relate to the same process, while the intercept is different as the rate of forward and backward hopping changes due to the energy degeneracy of the two adsorption sites.

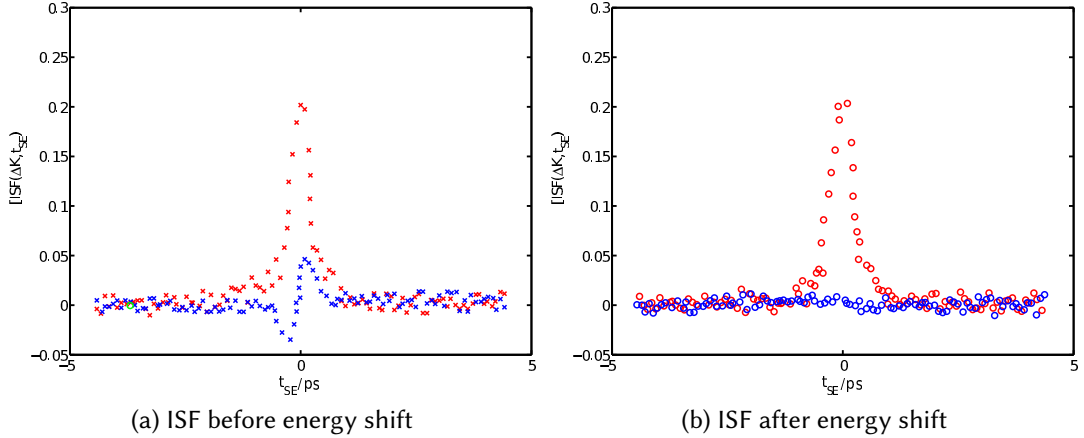


Figure 5.9: Li/Cu(111) in the $[11\bar{2}]$ surface direction, taken at a sample temperature of 140 K, momentum transfer, $\Delta K = -0.307 \text{ \AA}^{-1}$. The ISF has been filtered using a Fourier filter detailed in the text, the fastest decay contribution in the real spectra, shown as red crosses in panel (a), is isolated and the complex ISF divided by $\cos(\Delta\omega t) + i \sin(\Delta\omega t)$, with $\Delta\omega$ optimised to make the ISF completely real, the results for the spectra are shown in panel (b), highlighting the enforced symmetric quasi-elastic peak shape.

should have a Gaussian shape [54]. The complete functional form used to model the ISF is $A_0 + A_1 \exp(-\alpha t) + A_2 \exp(-\alpha_2 t) + A_3 \exp(-t^2/(2\sigma^2))$ and we are now considering the Gaussian part, $A_3 \exp(-t^2/(2\sigma^2))$ where $1/\sigma$ is expected to have a linear dependence on ΔK . Figure 5.11 presents the experimental data as red points with the blue line representing the simplest model for ballistic motion, atoms moving as an ideal 2-D gas [54], where the ISF will have the form¹:

$$I(\Delta K, t) = \exp\left(-\frac{\Delta K^2 \nu_0^2 t^2}{4}\right), \quad (5.2)$$

where $\nu_0 = \sqrt{2k_B T/m^*}$ and m^* is the effective mass of the gas particle. Thus, the width, σ should increase inversely with ΔK ;

$$\sigma = \frac{\sqrt{2}}{\Delta K \nu_0}. \quad (5.3)$$

It is clear from the line in figure 5.11 that we observe lithium moving ballisti-

¹See Appendix A section A.3 for a detailed derivation of the relationship between σ and ΔK .

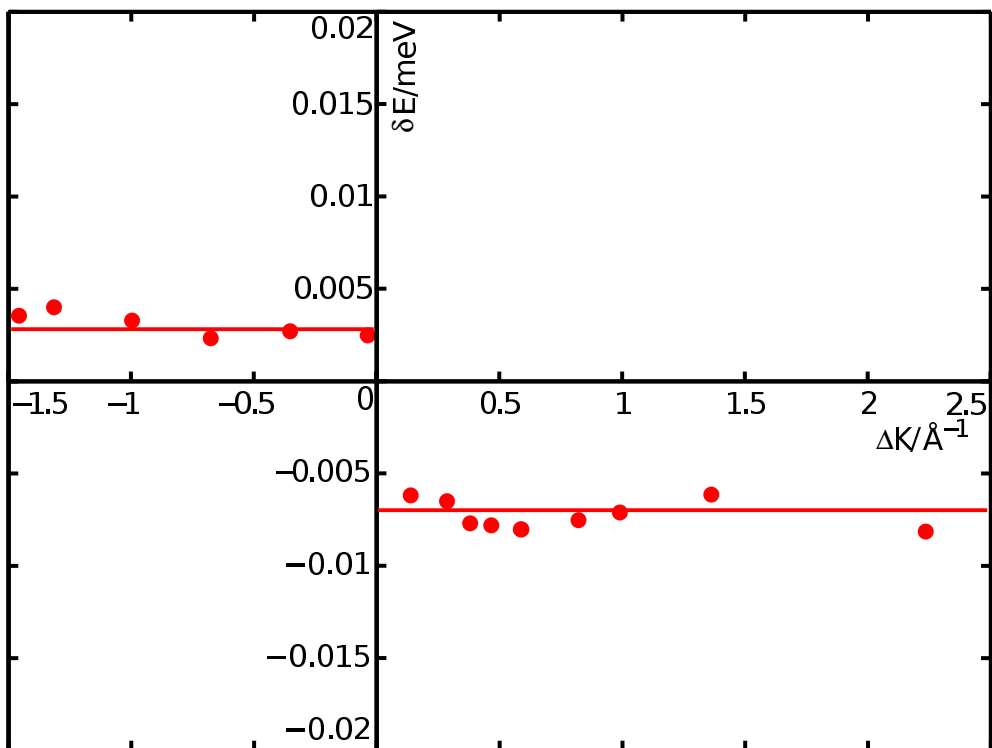


Figure 5.10: Dependence of the energy shift in the quasi-elastically scattered peak with respect to momentum transfer, ΔK , for Li/Cu(111) [11̄2] direction, coverage $\Theta = 0.025$ ML determined from the experimental ISFs measured at a surface temperature of 140 K with a He^3 beam of incident energy 8 ± 0.4 meV. The solid red line is a guide to the eye and it suggests that the energy shift is approximately independent of ΔK , except for the clear discontinuity at $\Delta K = 0$, and is in agreement with previously observed effects seen for sodium, but with consistently smaller shift, $\approx 1/10$ of the sodium value in chapter 4 figure 4.26.

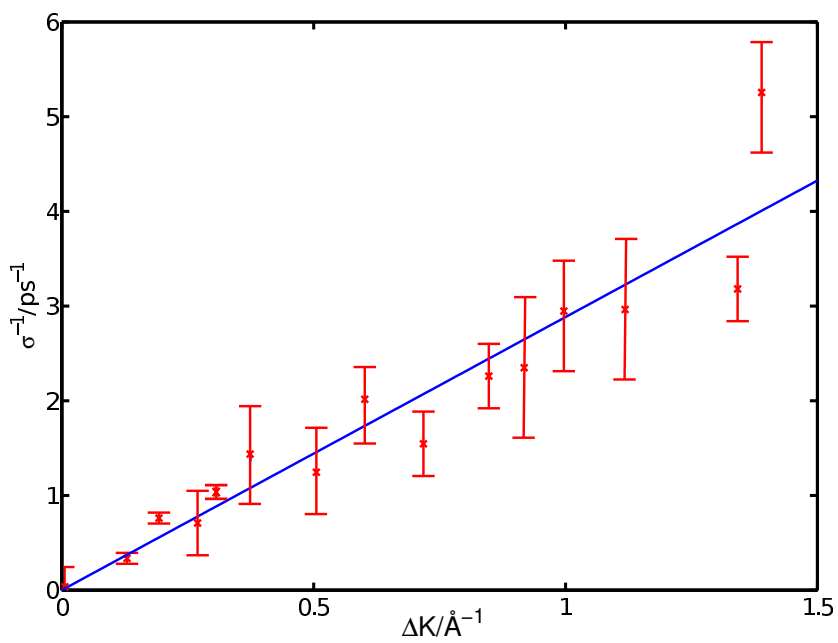


Figure 5.11: Momentum transfer dependence of the inverse variance of a Gaussian model for Li/Cu(111) in the [112] surface direction, taken at a sample temperature of 140 K. Shown as a blue line is the 2-D ideal gas law as described by equation 5.3, with an effective mass the same as the atomic mass of lithium.

cally as a 2-D ideal gas on the copper surface at short times, before a transition to a diffusion process characterised by a double exponential decay, suggesting non-degenerate hopping between adsorption sites [139], with the main results already presented in figure 5.7. In some respects the observation of a combined ballistic/diffusive lineshape, is similar to the work presented on Xe/Pt(111) in chapter 2. Density Functional Theory (DFT) calculations of alkali metals on a Cu(001) substrate by Fratesi [116], have suggested that a cosine adsorbate-substrate potential is appropriate which should be equally valid in the (111) surface, however like the xenon system, the relative magnitude of the ballistic to diffusive motion appears too large. As reported in figure 5.8 the diffusion process observed exhibits a low activation energy and suggest a weakly corrugated substrate; it is therefore not practical to flatten the Potential Energy Surface (PES) further as was the case in the xenon measurements and therefore the relatively large ballistic contribution is explained through a derivation of a coloured excitation spectrum in the Langevin framework referenced in chapter 1 section 1.3.

5.5 Simulating the ballistic/diffusive transition using the Generalised Langevin Equation (GLE)

Having considered the experimental observations we now turn to computer simulations with the aim of investigating the adsorbate substrate interactions. Specifically, the spectrum of excitations contributing to the nano-scale friction and excitation of the lithium and how this affects the transition between ballistic and diffusive motions. The Generalised Langevin Equation (GLE) can be written

$$m\dot{\mathbf{r}} = -\nabla V(\mathbf{r}) - m\eta \int_{-\infty}^t K(t-t')\dot{\mathbf{r}}(t')dt' + \zeta(t), \quad (5.4)$$

where

$$\zeta(t) = \int_{-\infty}^t K(t-t')\xi(t)(t')dt', \quad (5.5)$$

∇ is the standard gradient operator, $V(\mathbf{r})$ is the fixed potential energy surface representing the degrees of freedom of the substrate as ‘seen’ by a Li atom, m is

the mass of Li and \mathbf{r} is the position vector [35]. The middle term in equation 5.4, $-m\eta \int_{-\infty}^t K(t-t')\dot{\mathbf{r}}(t')dt'$ is related to energy dissipation processes, while the final term $\zeta(t)$ represents the contributions from thermal impulses coupling to the system. If the adsorbate and substrate are in thermal equilibrium the final two terms of equation 5.4 must balance on average, such that the dissipative processes energetically balance with energy gained through thermal fluctuations. The noise term $\zeta(t)$ is defined through,

$$\langle \zeta(t) \rangle = 0, \quad (5.6)$$

$$\langle \zeta(t)\zeta(t') \rangle = 2\eta k_B T/mK(t-t'). \quad (5.7)$$

When applying the GLE, the energy loss and gain terms are not separable and are relate to the history of the system $(t - t')$ in a complicated way defined by the transfer function $K(t, t')$ as explained in chapter 1 section 1.3. The statement of the Langevin equation in 5.4 is not directly solvable as it does not define the transfer function K , and requires knowledge of the infinite history of the whole system. As explained in chapter 1, the transfer function 5.5 is equivalent to a digital filter applied to a white noise distribution $\xi(t)$.

5.5.1 Implementation of a digital noise filter to solve the generalised Langevin equation

A number of implementations of the GLE have been presented recently [39, 140–142]. In the present work, a different approach is taken. A coloured noise Langevin molecular dynamics framework has been built using the Mathworks Simulink systems modelling environment. A block diagram of the Simulink solver is shown in figure 5.12, where the lines represent vectors of parameters with dimensions NxM where N is the number of degrees of freedom; 2 in this case, and M is the number of timesteps in the simulation. The basis of the simulation is to sum the force components in a Langevin sum shown as **(c)**, and then perform numerical integration between $\ddot{\mathbf{r}}$, $\dot{\mathbf{r}}$ and \mathbf{r} is marked by **(e)** and **(f)** respectively. During one simulation timestep, δt , the acceleration due to the forces indicated by the terms of equation 5.4 are determined and the resultant velocity and position calculated, which is fed back as the starting conditions for the next timestep such that over the full simulation a position and

velocity trajectory for the atom is recorded at **(h)**. The initial conditions are shown as secondary inputs to the numerical integration blocks in orange, and define the initial positions and velocities of the atom at the start of the simulation.

We will consider the physical nature of the digital filter used in the simulations shortly, which is treated as a black box at this stage. Starting from **(a)**, in the bottom right of figure 5.12, A random number from a white noise spectrum is selected, which is then filtered in block **(b)** to form ‘coloured’ noise, $\zeta(t)$, before entering the Langevin sum in block **(c)**. The other two terms fed into the sum are the dissipative energy term and the effect of the frozen potential energy landscape $V(r)$. In order to maintain thermal equilibrium and satisfy the second fluctuation dissipation theorem, the dissipative term must be filtered in the same way as the noise term, through the block **(d)**. The potential energy landscape is modelled using a digitised potential defining a unit cell and since the whole surface is represented by a tiling of the unit cell the effect of the potential on the atom can be determined by considering the modulus of the atom position on the surface with the size of the cell, shown as the two outputs of block **(g)**. The key blocks that define the noise spectrum in the generalised Langevin equation are the digital filters **(b)** and **(d)**, we now consider the detail of filter used in the current work.

The simplest filter is one with a band limited noise spectrum. All adsorbates will experience a maximum frequency in their excitation spectrum and the effect can be described with a simple memory kernel $K(t) = \eta \exp(-t/\tau)/\tau$, [39] which corresponds to the frequency spectrum

$$|K(\omega)|^2 \propto \frac{1}{(1 + \tau^2\omega^2)}, \quad (5.8)$$

where the band limit of the noise is defined by a cut-off frequency, $\omega_c = 1/\tau$. The factor η , in $K(t)$, results in a scaling that gives the same behaviour in the long-time limit, $t \gg \tau$, as is observed in the conventional Langevin equation. The filter blocks **(b)** and **(d)** can be set for the filter in equation 5.8, as shown for a 2-D case in figure 5.12 **(ii)**.

As noted previously the simulation produces an output consisting of trajectories in position and velocity, shown in the simulation in block **(h)** of figure 5.12. In order to compare the results of the simulation to experimental data, the trajectories are

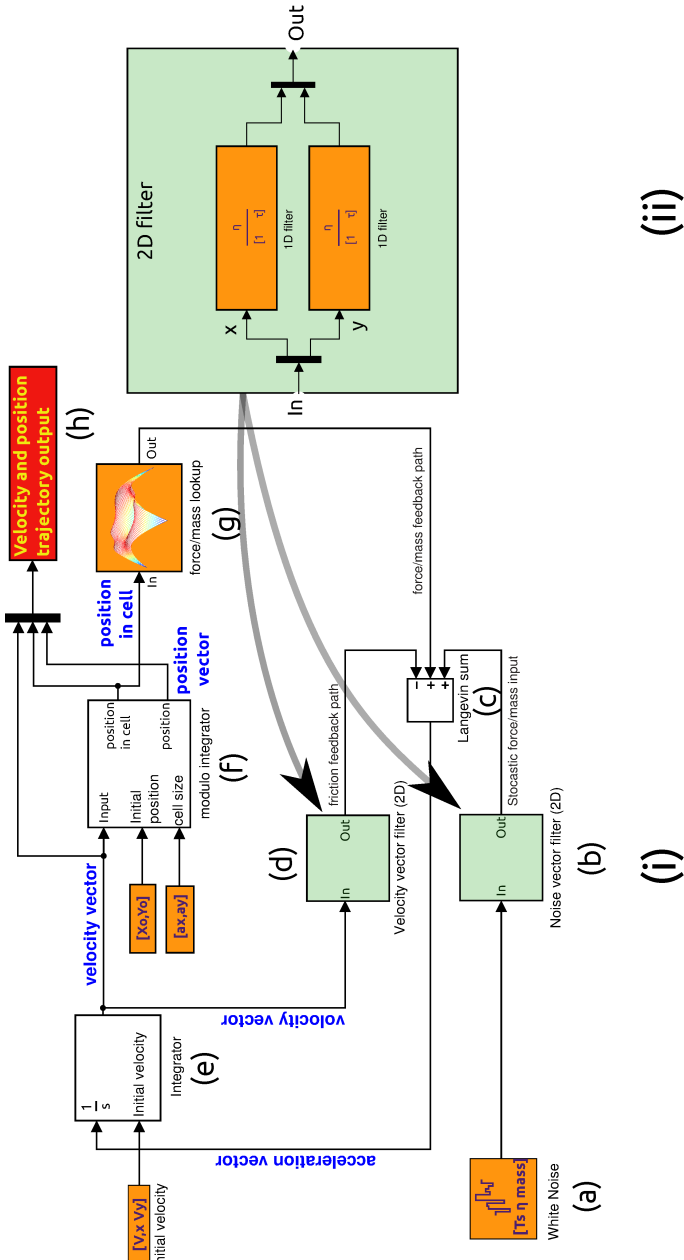


Figure 5.12: Schematic diagram of the coloured noise molecular dynamics simulation system, written using a digital filter design in Simulink software. All of the lines in the diagram represent 2-D vectors in \vec{r} , $\vec{dot{r}}$ or \vec{r} , which is emphasised in the block design of the digital filters shown in **ii**. In the bottom right of the figure, white noise is generated at **(a)**, before a digital filter is applied in the blow marked **(b)** before being collected at the Langevin sum **(c)**. The Langevin sum is performed in units of \vec{r} , which is proportional to the force on the particle via its atomic mass. The blocks **(e)** and **(f)** numerically integrate $\vec{r}(t)$ to determine $\vec{dot{r}}(t)$ and $\vec{r}(t)$ vectors respectively. The velocity is fed to the Langevin sum via the filter **(d)**, which applies the same digital filter that is applied to the white noise in **(b)** to take into consideration dissipative forces on the atom. The final force that is considered results from the interaction from the substrate determined by a frozen potential energy surface, a digitised potential is read in as an input parameter and the position of the adsorbate within the cell is used to calculate the force due to $-\nabla V(\vec{r})$ at **(g)** before the velocity and position trajectories are output at **(h)**. Panel **(ii)** shows in greater detail the filter used in the simulations in the current work, and highlight the split in the pathway to deal with both Cartesian dimensions of the simulation. In the displayed model, panel **(ii)** also shows the digital filter represented in equation 5.8 with poles at η and τ .

converted to the correlation function measured on long time-scales - the familiar Intermediate Scattering Function, $I(\Delta K, t)$ (ISF). The method follows a similar procedure to the initial derivation of the ISF in chapter 1. For a single simulation run we can write the total scattered amplitude at that time as:

$$A(K, t) = \exp(-i(k_x \cdot x(t) + k_y \cdot y(t))); \quad (5.9)$$

$A(K, t)$ is accumulated through the position vector $r(t)$ which, in Cartesian co-ordinates is $\sqrt{x(t)^2 + y(t)^2}$, at each time-step, δt , of the simulation. $A(K, t)$ is multiplied by the form factor, F , which for these studies is assumed to be unity for all values of ΔK , and can be Fourier transformed to determine the amplitude in energy space,

$$A(K, \omega) = \hat{F}(F \cdot A(K, t)); \quad (5.10)$$

where \hat{F} denotes the forward Fourier transform, in Cartesian co-ordinates, and k_x and k_y define the momentum vector in Cartesian co-ordinates, defining the surface direction. If $A(K, \omega)$ is multiplied by its complex conjugate, the energy self correlation function is recovered, which can then be inverse transformed to recover the self correlation function in time, the ISF:

$$I(K, t) = \hat{f}(A(K, \omega)A^*(K, \omega)), \quad (5.11)$$

where \hat{f} is the inverse Fourier transform.

We now move on to consider the results of the coloured noise simulations. Starting with the simplest case of flat adsorbate substrate potentials; we investigate the transition between ballistic and simple Brownian motion, with respect to the noise frequency response, building on the work in chapter 1, and then move on to consider sinusoidal adsorbate-substrate potentials and compare the results with experimental data for the Lithium system. Position trajectories in 2-D of the generalised Langevin model with a flat potential ($\nabla V(\mathbf{r})=0$) have been shown in chapter 1 already and are reproduced in figure 5.13. As expected the overall motion on longer time scales remains the same, while the motion resulting from individual impulses, on shorter time scales changes in response to the exact nature of the fluctuation distribution. The main conclusion from figure 5.13 is that the simple filter used in this

case gives an element of control over the impulse spectrum, giving a better representation of the interaction between the environment and the atom, without affecting the macroscopic friction parameter and its known physical significance. A check on

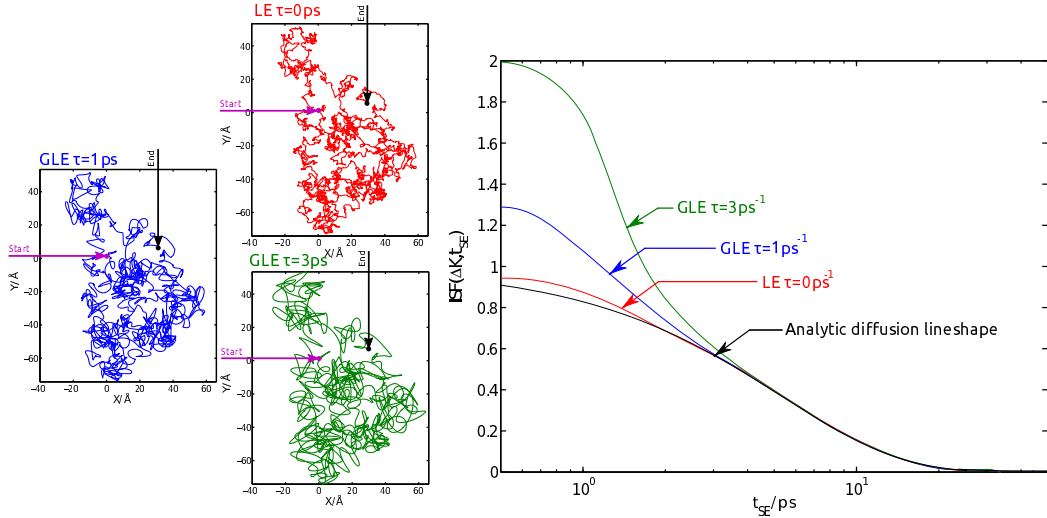


Figure 5.13: Trajectories calculated using the Simulink GLE molecular dynamics simulations, using a potential energy surface with $\nabla V(\mathbf{r}) = 0$. A filter with an exponential response of exponent τ is used to generate a coloured stochastic force so that frequency impulses are damped. The static friction η , in all of the simulations is 5 ps^{-1} and the temperature is 140 K for a particle of mass 7 amu . Between the red and green lines τ is increased from 0 (white noise) to 3 ps^{-1} , and the intermediate scattering functions calculated for the trajectories are shown normalised to the amplitude of the diffusion contribution.

the accuracy of the implementation is provided by an analysis of the kinetic energy distribution. In particular the kinetic energy distribution of an atom in thermal equilibrium is given by the law of equipartition of energy. The kinetic energy is described by a Boltzmann distribution $(P(E)) = \exp^{-mV_x^2/K_B T}$ in one dimension, which is proportional to the square of the velocity distribution V^2 , where

$$\begin{aligned} P(E).dE &= P(V^2).d(V^2), \\ P(V^2) &= P(E)/2V, \end{aligned} \tag{5.12}$$

Figure 5.14 shows a histogram of the velocity V_x^2 against the probability of a certain

velocity $\log(V_x^2).2V_x$, for an atom of mass 7, moving with a friction of $\eta = 2 \text{ ps}^{-1}$ and $\tau = 0.8 \text{ ps}^{-1}$ with a target temperature of 200 K. If the velocity distribution follows the expected Boltzmann distribution it will have a gradient $-\frac{m}{K_b T}$. Simulations were conducted at various temperatures and with different values of η and τ , and in all cases the temperature calculated from the velocity distribution was found to be in agreement with the target temperature of the simulation, in the case of figure 5.14 the temperature, from the slope of the line, was found to be $199.8 \pm 0.4 \text{ K}$ against a set point of 200 K.

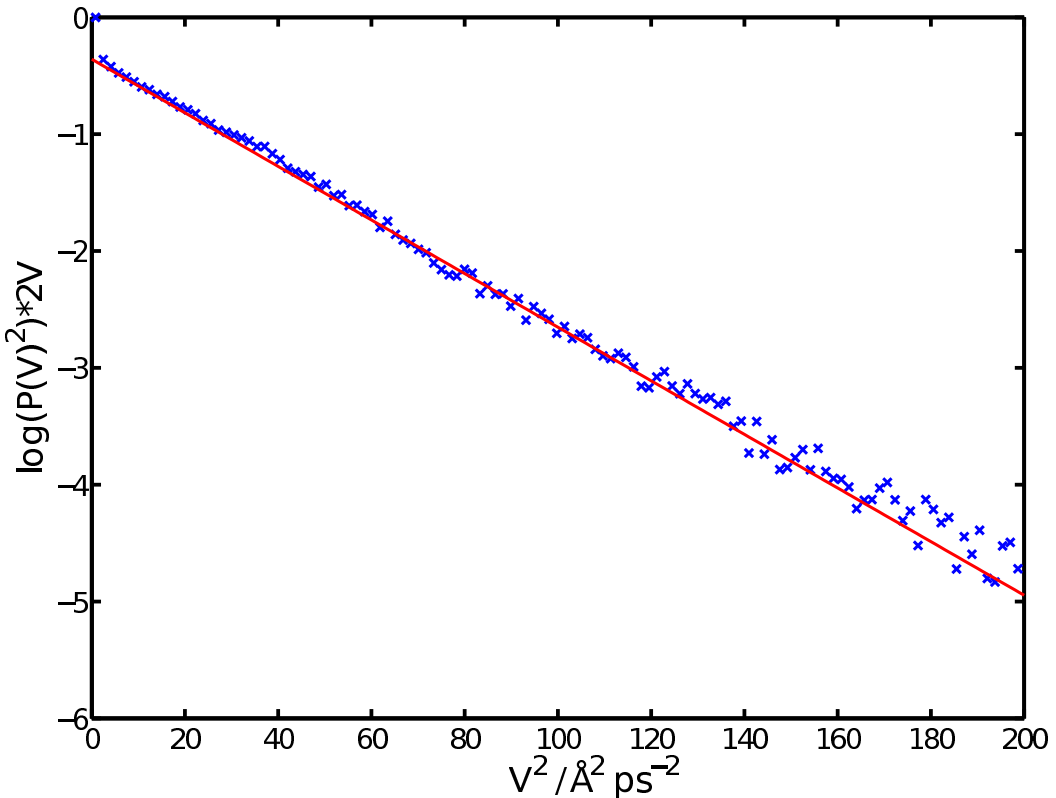


Figure 5.14: Kinetic energy distribution for an atom of mass 7 amu moving across a flat potential energy landscape, $\nabla V(\mathbf{r}) = 0$, at 200 K sample temperature with a friction, $\eta = 2 \text{ ps}^{-1}$ and $\tau = 5 \text{ ps}^{-1}$. The line is determined using linear regression and has a gradient of $-m/K_b T$, for a temperature $199.8 \pm 0.4 \text{ K}$, in good agreement with the simulation temperature.

Now turning to the analysis of the experimental data, we employ a sinusoidal potential energy landscape as has been previously simulated for the Cu(001) surface by Fratesi [116]. The PES has the hexagonal symmetry of the substrate and we use

degenerate hcp/fcc hollow sites, justified by the weak corrugation suggested by the experimental data 5.8 and the theoretical predictions in [137]. The sinusoidal PES is attractively simple and defined by a single amplitude parameter. In total there are three parameters that may be optimised in the simulations, the amplitude of the PES, the friction η and the cut-off frequency in the excitation spectra τ .

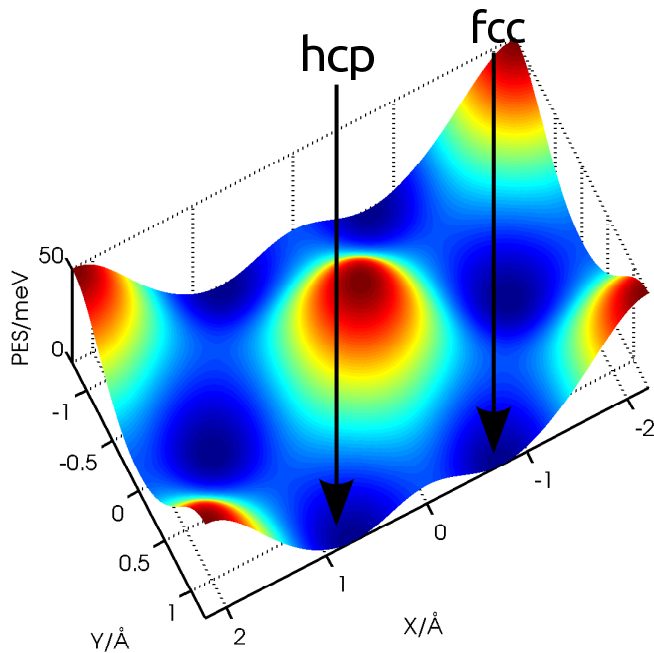


Figure 5.15: Example PES for Li/Cu(111) as used in the Langevin molecular dynamics simulations. The two hollow sites are marked and are equivalent in energy. The amplitude of the potential is 45 meV between the top and hollow sites and 8 meV over the saddle point, which is the route for diffusion for this system.

Figures 5.16 and 5.17 present the main results of the GLE simulations. Experimental data is shown using blue points and the simulation results as red crosses, with a smooth line to show the trends. The simulation was conducted over 800 ps with a 1 fs time-step, a 9 meV barrier between the fcc and hcp hollow sites, a coefficient of friction $\eta = 1.2 \text{ ps}^{-1}$ and noise cut-off $\tau = 0.8 \pm 0.1 \text{ ps}^{-1}$. The lower panel, (c), shows the decay rate for the slowest decay component, and the agreement is excellent, a similar agreement with the conventional Langevin equation could be achieved. The middle plot, panel (b), presents the second decay component attributed to hopping between non-equivalent lattice sites, and the top panel,

(a) shows the ratio of the two processes. Both show acceptable qualitative agreement with differences expected to be associated with the approximated form of the PES, which cannot be overcome by simply changing the barrier height, and therefore would require a more complicated model. Overall the agreement to the diffusive behaviour is excellent.

Figure 5.17 presents the width of a Gaussian function representing the ballistic component, again the experimental data is shown in blue with the results of the simulation shown in red, and the thermodynamic model described in equation 5.3 shown as a black line. As expected the result shows excellent agreement between simulation and experimental data, since it depends only on the effective mass of the adsorbate and the temperature of the system.

Finally I turn to comparison of complete ISFs. Figure 5.18 shows two specific ISFs, at particular values of ΔK , 0.6 \AA^{-1} in panel (a), and 1.2 \AA^{-1} in panel (b). Experimental data points are shown as black crosses and simulation results shown as red, blue and green lines for different values of the cut-off time τ . The simulation was conducted performed for a total time of 800 ps with a 1 fs time-step, a 9 meV barrier between the fcc and hcp hollow sites and repeated 200 times to collect good statistics over the full time scale.

In panel (a), the ISF is shown to be well separated into diffusive and ballistic regions, as expected since α_1 is 15 ps^{-1} for this value of momentum transfer. Panel (b) shows a wider transition between the processes, as expected. In both cases the best fit, shown in blue for $\tau = 0.8 \pm 0.1 \text{ ps}^{-1}$, is in excellent agreement with the data. For comparison two values either side of the best fit are provided in green and red, with the traditional Langevin equation ($\tau = 0$) appearing with a lower amplitude than $\tau = 0.4$, if scaled to fit the diffusion signature. All of the simulations correctly describe the diffusion process however the amplitude of the ballistic component in the data is not reproduced. Overall it is possible to determine that the optimum cut off frequency is 0.8 ps^{-1} .

The frequency cut off corresponding to the noise spectrum is 1.2 THz. On the basis of the current work alone it is not possible to determine if the origin of the friction is phononic or electronic however the availability of results of the quality shown here provides a unique opportunity for future theoretical models. Results such as these provide one of the few avenues through which the physical origin of

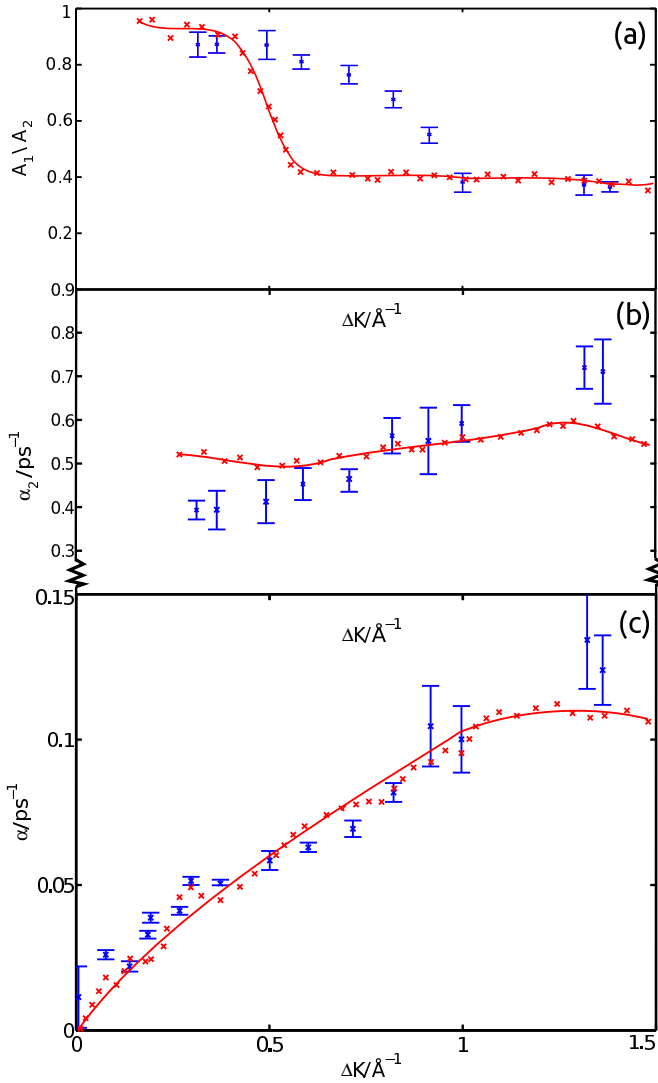


Figure 5.16: Plots of the diffusion characteristics of Li/Cu(111) in the [11̄2] surface direction, taken at a sample temperature of 140 K over a range of the absolute values of momentum transfer, ΔK . Blue points are optimised parameters from experimental ISFs, and the red lines are optimised to the same model functions for ISFs determined using the Generalised Langevin equation model detailed in section 5.5, with optimised parameters of a sinusoidal PES of amplitude 10 mev across the saddle point, with friction $\eta = 2 \text{ ps}^{-1}$ and $\tau = 0.8 \text{ ps}^{-1}$. From the bottom of the figure, panel (c) presents the decay rate α , of an exponential function $A_1 \exp(-\alpha t) + A_0$ applied to the slowest decay process in the ISF. Panel (b) shows the exponential decay rate α_2 , of the function $A_2 \exp(-\alpha_2 t) + A_3 \exp(-t^2/(2\sigma^2))$ applied to the residual ISFs after subtracting the slowest exponential part, the Gaussian part of the model is treated separately. Panel (a) presents the ratio of the amplitude of the two exponential functions, the data is constant with hopping between several non equivalent sites [139].

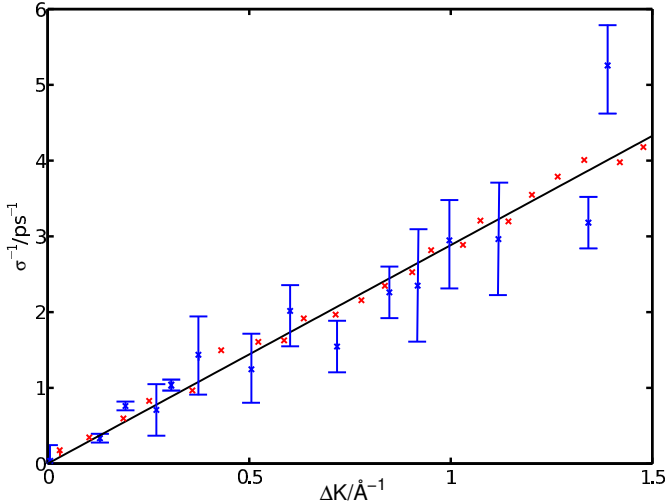


Figure 5.17: Inverse variance of a Gaussian fitted to the fastest decay process of measured and simulated ISFs of Li/Cu(111) in the [11̄2] surface direction, taken at a sample temperature of 140 K. Experimental data is shown as blue crosses and simulation results using the GLE implementation described in the text are shown as red crosses. The black line is the 2-D ideal gas law as described by equation 5.3, with an effective mass the same as the atomic mass of lithium.

nano-scale friction can be probed.

5.6 Discussion

In this chapter I have presented experimental results for the dynamic processes of lithium on a copper(111) surface. The results provide evidence for an activated surface diffusion process, with hopping motion observed between non-equivalent lattice sites with a barrier height $\Delta E \approx 8 \text{ meV}$ and friction co-efficient $1.2 \pm 0.3 \text{ ps}^{-1}$ assuming degenerate hollow sites. The resolution of the data allows the separation of a ballistic motion with lithium moving as a classical particle of effective mass close to its atomic mass. A novel method of applying a Generalised Langevin Equation (GLE) is used to simulate the whole experimental ISF and the results indicate a cut off frequency in the excitation spectrum of the system.

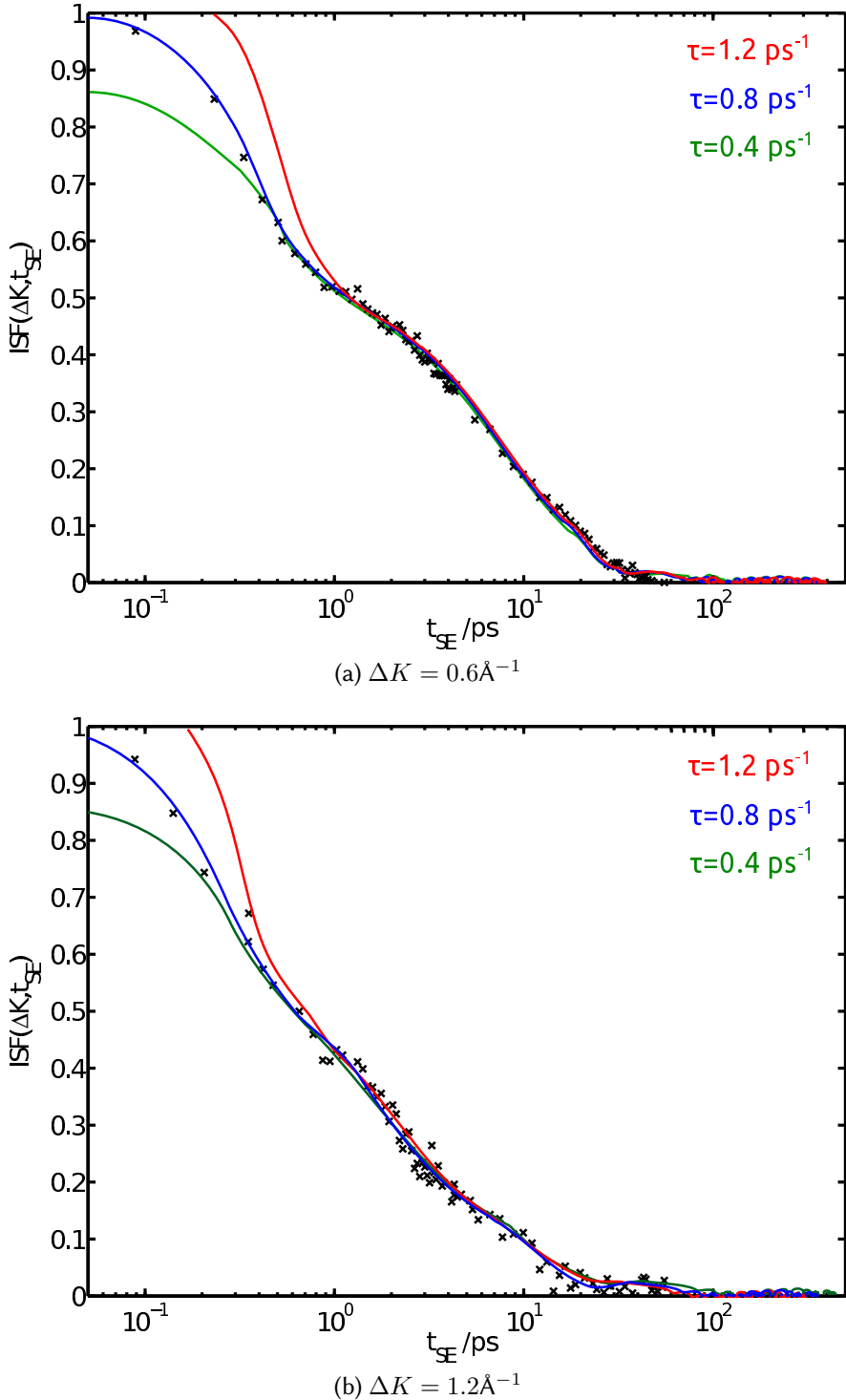


Figure 5.18: ISF for Li/Cu(111) at 140 K in the $[11\bar{2}]$ direction. Experimental data is presented as black crosses and simulation results for different values of a cut off time in the excitation spectra, shown as green blue and red lines. The simulations were performed for a total time of 800 ps with a 1 fs time-step, a 9 meV barrier between the fcc and hcp hollow sites and repeated 200 times to collect good statistics over all time scales.

Chapter 6

Outlook and future work

The present thesis has demonstrated the applicability of the established helium spin-echo technique to study dynamic processes on a range of prototypical ‘simple’ surfaces, ranging from Xe/Pt(111) to Li/Cu(111). All the data presented in the thesis demonstrated a significant degree of complexity, representing the breadth of physics that the technique can access. I have shown that a particularly rich area of physics is the transition between ballistic and diffusive regimes.

In analysis of the quasi-elastically scattered experimental data, the existing methodology, which uses the Langevin equation, has been shown to be insufficient for the simulation of the complete dynamic range. The first application of the generalised Langevin equation to experimental dynamics data has been presented using a systems approach to implement the analysis.

Chapter 2 showed that xenon and the platinum(111) surface behaved as a low friction adsorbate, moving across a flat surface landscape with low barriers. The experimental data revealed aspects of the motion that correspond to jump diffusion as well as 2-D ideal gas like behaviour. While the latter motion had been observed previously [54], the impact of the present work lies in the recognition that, on different time-scales, the motion displays a radically different character.

The experimental data was analysed using a conventional Langevin molecular dynamics simulation for a cosine potential energy surface. The comparison between the simulation and data was conducted using parameters fitted to correlation functions, particularly demonstrating the applicability of the Intermediate Scattering Function, $I(\Delta K, t)$ (ISF) for analysing dynamics systems. It was noted that while

the ballistic portion of the data agrees with a thermodynamic model, and the diffusion can be simulated using a simple potential energy landscape, the whole ISF is not comparable between experiment and simulation. To achieve a better agreement for the ISF, the potential energy surface was flattened to increase the ballistic contribution and an improved agreement was achieved.

Chapter 2 shows the importance of measuring the Intermediate Scattering Function, $I(\Delta K, t)$ (ISF) over the whole timescale for the system of study. To achieve a higher dynamic range, high resolution power supplies coupled with methods of measuring the real and imaginary ISF are required. Chapter 3 presented improvements in the calibration of the spin-echo point, and shows the importance of precise measurement of the real and imaginary parts of the ISF at small timescales. Secondly, the effect of the environmental conditions on the spin-echo calibration is investigated and a procedure for calibration determined.

In chapters 4 and 5, the dynamics of alkali metals on Cu(111) were investigated. Similar phenomenology to that of the Xe system is noted, but on a different timescale. Other features of small time scale dynamics measurements, such as inelastic scattering contributions are shown and a method for separating the quasi-elastic dynamics is developed. Improvements in the measurement technique from chapter 3 are demonstrated in the ability to measure the real and imaginary ISF at high precision on time-scales previously inaccessible. The quasi-elastic spectrum is shown to be asymmetric, which is attributed to scattering from the form factor, and limits the ability to investigate the ballistic/diffusive transition in the ISF.

In chapter 5, the fast part of the ISF for lithium is analysed using the same techniques applied for sodium in chapter 4. In this case a smaller form factor contribution is observed. It was not possible to analyse the whole ISF using the traditional Langevin equation. A molecular dynamics simulation using the Generalised Langevin equation with coloured noise is used to investigate the properties of the noise spectrum incident on the adsorbate.

Further instrumental developments are possible, for example the phase coil method of rotating the spin vector is ideal for measurements where the velocity spread of the beam is small; however if there are large energy changes, due to inelastic processes, it is desirable to increase the beam energy and spread to excite more processes. A better method would be to install ‘flipper coils’ that produce an additional, controlled,

magnetic alignment field between the hexapole and start of the precession field (see figure 3.3 between sections (c) and (d)). By varying the alignment of the additional field the polarisation of the beam can be rotated in a plane perpendicular to the direction of propagation. A mechanism for measuring the real and imaginary parts of the spectrum in this way has been implemented as part of an earlier work [104], and was employed in a recent work of Kole *et. al.* [143], however this method is currently limited to measuring a range of 90° of one spin orbit and requires a careful magnetic field design, manufacture and testing procedure to extend it to measuring a full rotation, which as shown in chapter 3 is necessary to truly calibrate the spin-echo point.

Previous work on surface diffusion has focussed almost exclusively on the long-time behaviour, which provide insights into the two key parameters - potential energy landscape and atom-scale friction (η). The present work has contributed to understanding of the dynamics occurring at the times before the onset of diffusion, and the transition region between the two extremes.

Relatively little information is available on the physical origin of the friction. For example the work of Persson, Tosatti *et. al.* discusses the electronic and phononic contributions to friction in relation to vibrational dephasing [144]. The present work, particularly chapter 5, has shown that one important aspect is the transition region between ballistic and diffusive motion. The nature of the interpolation between the two regions contains information on the frequency spectrum of the excitations experienced by the adsorbate. That spectrum provides new information on the underlying mechanism of friction and it will be a valuable source for future theoretical work.

The next logical step is to develop an understanding the relationship between the excitation spectrum in the Langevin equation and the origin of the friction. Experimentally there is scope to continue the work started in this thesis, to study a range of adsorbate/substrate systems to systematically to collect comparative results for a range of interactions. Recent successes in measuring more complicated systems using spin-echo spectroscopy has revealed interesting insights on the internal motion of molecules [89, 98] as well as rotational and translational motions [100, 102], which would benefit from the additional understanding through the current work. The systems presented in the current work support a bottom-up approach, and are

specifically chosen for their relative simplicity, significant discoveries are still to be realised. One goal would be to apply the methods and ideas developed here to more complex systems such as those mentioned in chapter 1, the methods are particularly applicable to molecular size devices, and as an example would give a deeper understanding of the physics driving the ‘molecular SUV’ [10].

Appendices

Appendix A

Useful Fourier relationships

In this section several useful transforms relating properties of measured scattering function and physical properties.

A.1 Relationship between the variance of a Gaussian function in time with Full Width Half Maximum in frequency and Energy

If we have a Gaussian defined;

$$f(t) = Ae^{-\frac{t^2}{2\sigma^2}}; \quad (\text{A.1})$$

at the FWHM, $f(t)$ has the value $\frac{A}{2}$;

$$\frac{A}{2} = Ae^{-\frac{\frac{A}{2}^2}{2\sigma^2}}; \quad (\text{A.2})$$

solving for t;

$$t = \sigma^\pm \sqrt{2\ln(2)}; \quad (\text{A.3})$$

Since $f(t)=A$ at $t=0$, the full width half maximum can be defined;

$$FWHM = 2\sigma^\pm \sqrt{2\ln(2)}. \quad (\text{A.4})$$

A.1.1 Fourier relationship

If we define the Fourier transform relationship as;

$$F(\omega) = \frac{1}{\sqrt{2\pi}} \int_{-\infty}^{\infty} f(t) \cdot e^{-it\omega} \cdot dt; \quad (\text{A.5})$$

then substituting equation A.1;

$$F(\omega) = \frac{1}{\sqrt{2\pi}} \int_{-\infty}^{\infty} Ae^{-\frac{t^2}{2\sigma^2}} \cdot e^{-it\omega} \cdot dt; \quad (\text{A.6})$$

which can be re-written;

$$F(\omega) = \frac{A}{\sqrt{2\pi}} \int_{-\infty}^{\infty} e^{-(\frac{t^2}{2\sigma^2} + it\omega)} \cdot dt. \quad (\text{A.7})$$

Since the integrand in equation A.7 cant be solved directly we can separate the parameters of t by “completing the square”;

$$\frac{t^2}{2\sigma^2} + it\omega = \frac{1}{2\sigma^2}(t + i\omega\sigma^2)^2 + \frac{\omega^2\sigma^2}{2} \quad (\text{A.8})$$

Substituting back into equation A.7;

$$F(\omega) = \frac{A}{\sqrt{2\pi}} \int_{-\infty}^{\infty} e^{-\frac{1}{2\sigma^2}(t+i\omega\sigma^2)^2 - \frac{\omega^2\sigma^2}{2}} \cdot dt \quad (\text{A.9})$$

$$F(\omega) = \frac{A}{\sqrt{2\pi}} e^{-\frac{\omega^2\sigma^2}{2}} \int_{-\infty}^{\infty} e^{-\frac{1}{2\sigma^2}(t+i\omega\sigma^2)^2} \cdot dt \quad (\text{A.10})$$

which is of the form of a Gaussian in ω multiplied by the integral of a Gaussian in time. Using the standard integral for a Gaussian¹

¹Standard Integral of a Gaussian: If we take a square integral method in Cartesian co-ordinates for solving the integral of a Gaussian described as e^{-x^2} , then a method for solution was demonstrated by Laplace in 1812 [145] Let $y = xs$; then $dy = x.ds$;

e^{-x^2} is a symmetric function and therefore; $\int_{-\infty}^{\infty} e^{-x^2} dx = 2 \int_0^{\infty} e^{-x^2} dx$;
if y and s have the same limits ;

$$\begin{aligned} I^2 &= 4 \int_0^{\infty} \int_0^{\infty} e^{-(x^2+y^2)} dy dx \\ \frac{I^2}{4} &= \int_0^{\infty} \left(\int_0^{\infty} e^{-(x^2+y^2)} dy \right) dx = \int_0^{\infty} \left(\int_0^{\infty} e^{-x^2(1+s^2)} x ds \right) dx \\ &= \int_0^{\infty} \left(\int_0^{\infty} e^{-x^2(1+s^2)} x dx \right) ds \\ &= \int_0^{\infty} \left[\frac{1}{-2(1+s^2)} e^{-x^2(1+s^2)} \right]_0^{\infty} ds = \frac{1}{2} \int_0^{\infty} \frac{ds}{1+s^2} \end{aligned}$$

$$\int_{-\infty}^{\infty} e^{-\frac{(t+i\omega\sigma^2)^2}{2\sigma^2}} dt = \sqrt{2\pi}\sigma; \quad (\text{A.11})$$

therefore the functional form of the Gaussian in ω space;

$$F(\omega) = A\sigma e^{-\frac{\omega^2\sigma^2}{2}} \quad (\text{A.12})$$

now using the same method as above to find the FWHM

$$\frac{A\sigma}{2} = A\sigma e^{-\frac{\omega^2\sigma^2}{2}}; \quad (\text{A.13})$$

$$\ln(2) = \frac{\omega^2\sigma^2}{2}; \quad (\text{A.14})$$

$$\omega = \frac{\sqrt{2\ln(2)}}{\sigma}; \quad (\text{A.15})$$

$$\text{FWHM} = \frac{+2\sqrt{2\ln(2)}}{\sigma}; \quad (\text{A.16})$$

since $E = \hbar\omega$;

$$\text{FWHM in Energy} = \frac{2\hbar^+\sqrt{2\ln(2)}}{\sigma}$$

A.2 Relationship between α in time and Full Width Half Maximum of a Lorentzian in frequency and energy

If we have a symmetric exponential function in time defined

$$f(t) = Ae^{-\alpha|t|} = \begin{cases} Ae^{\alpha t} & \text{if } t \leq 0 \\ Ae^{-\alpha t} & \text{if } t \geq 0 \end{cases} \quad (\text{A.17})$$

If we define the Fourier transform relationship as;

$$= \frac{1}{2} \arctan s|_0^\infty = \frac{\pi}{4}.$$

$$I = \sqrt{\pi}.$$

$$F(\omega) = \frac{A}{\sqrt{2\pi}} \int_{-\infty}^{\infty} f(t) \cdot e^{-it\omega} \cdot dt; \quad (\text{A.18})$$

substituting in equation A.18;

$$F(\omega) = \frac{A}{\sqrt{2\pi}} \int_0^{\infty} e^{-\alpha t} \cdot e^{-it\omega} \cdot dt + \int_{-\infty}^0 e^{\alpha t} \cdot e^{-it\omega} \cdot dt; \quad (\text{A.19})$$

$$F(\omega) = \frac{A}{\sqrt{2\pi}} \int_0^{\infty} e^{-(\alpha+i\omega)t} \cdot dt + \int_{-\infty}^0 e^{(\alpha-i\omega)t} \cdot dt; \quad (\text{A.20})$$

$$F(\omega) = \frac{A}{\sqrt{2\pi}} \left[\frac{[-e^{-(\alpha+i\omega)t}]_0^{\infty}}{\alpha + i\omega} + \frac{[e^{(\alpha-i\omega)t}]_{-\infty}^0}{\alpha - i\omega} \right]; \quad (\text{A.21})$$

$$F(\omega) = \frac{A}{\sqrt{2\pi}} \left[\frac{1}{\alpha + i\omega} + \frac{1}{\alpha - i\omega} \right]; \quad (\text{A.22})$$

$$F(\omega) = \frac{A}{2\pi} \frac{\alpha - i\omega + \alpha + i\omega}{\alpha^2 + \omega^2} = A \sqrt{\frac{2}{\pi}} \frac{\alpha}{\alpha^2 + \omega^2}. \quad (\text{A.23})$$

$F(\omega)$ is, as expected a Lorentzian function with amplitude $\sqrt{\frac{2}{\pi}} \frac{A}{\alpha}$ @ $\omega = 0$

The FWHM of $F(\omega)$ in terms of the de-phasing rate α is then;

$$\sqrt{\frac{2}{\pi}} \frac{A}{2\alpha} = A \sqrt{\frac{2}{\pi}} \frac{\alpha}{\alpha^2 + \omega^2} \quad (\text{A.24})$$

$$\frac{1}{2\alpha} = \frac{\alpha}{\alpha^2 + \omega^2} \quad (\text{A.25})$$

$$\omega = \pm\alpha \quad (\text{A.26})$$

Therefore;

$$FWHM(\omega) = 2\alpha \quad (\text{A.27})$$

since $E = \hbar\omega$;

$$FWHM(Energy) = 2\hbar\alpha \quad (\text{A.28})$$

A.3 Derivation of the ballistic gas line for an ISF in time

If the self-diffusion function $G_s(R, t)$ is defined [27, 54]:

$$G_s(R, t) = \frac{1}{\pi(\nu_0 t)^2} \exp\left(\frac{-R^2}{(\nu_0 t)^2}\right) \quad (\text{A.29})$$

where

$$\nu_0^2 = \frac{2k_B T}{m} \quad (\text{A.30})$$

If the Fourier transform of a Gaussian is defined

$$\exp(-ax^2) = \sqrt{\frac{\pi}{a}} \exp\left(\frac{-\pi^2 K^2}{a}\right) \quad (\text{A.31})$$

then

$$a = \frac{1}{(\nu_0 t)^2} \quad (\text{A.32})$$

and if $2\pi K = \Delta K$ ad $R^2 = x^2 + y^2$, we must do a 2D Fourier transform with respect to x and y, however the time dependence for y is 1 such that the ISF is defined:

$$I(\Delta K, t) = \frac{1}{\pi(\nu_0 t)^2} \cdot \sqrt{(\pi)^2} \cdot (\nu_0 t)^2 \exp\left(-\frac{\Delta K^2 \nu_0^2 t^2}{4}\right) \quad (\text{A.33})$$

$$I(\Delta K, t) = \exp\left(-\frac{\Delta K^2 \nu_0^2 t^2}{4}\right) \quad (\text{A.34})$$

which is a Gaussian line shape, which can be written in the standard form of $\exp(-t^2/2\sigma^2)$ such that σ is;

$$\frac{1}{2\sigma^2} = \frac{\Delta K^2 \nu_0^2}{4}, \quad (\text{A.35})$$

$$\sigma = \frac{\sqrt{2}}{\Delta K \nu_0}. \quad (\text{A.36})$$

For an exponential in time, as α gets bigger the decay rate gets faster, or in other words the FWHM of the exponential defined $\exp(-\alpha|t|)$ gets narrower. So to compare α of an exponential in time, we should use $1/\sigma$ of a Gaussian.

Finally for completeness, remembering that $\nu_0^2 = \frac{2k_B T}{m}$ and that $FWHM =$

$2\sigma^+ \sqrt{2\ln(2)}$, The FWHM of a Gaussian in time spectrum;

$$FWHM = \frac{2}{\Delta K} \sqrt{\frac{2\ln(2)k_B T}{m}} \quad (\text{A.37})$$

Appendix B

All Na/Cu(111) ISFs

Figures B.11 to B.15 present Na/Cu(111) ISFs, recorded with the best temporal resolution, inelastic contributions associated with surface phonons are removed according to the method in section 4.3.1 and not presented in the data. Figures B.16 to B.20 present the ISFs in figures B.11 to B.15, with the diffusion signature removed.

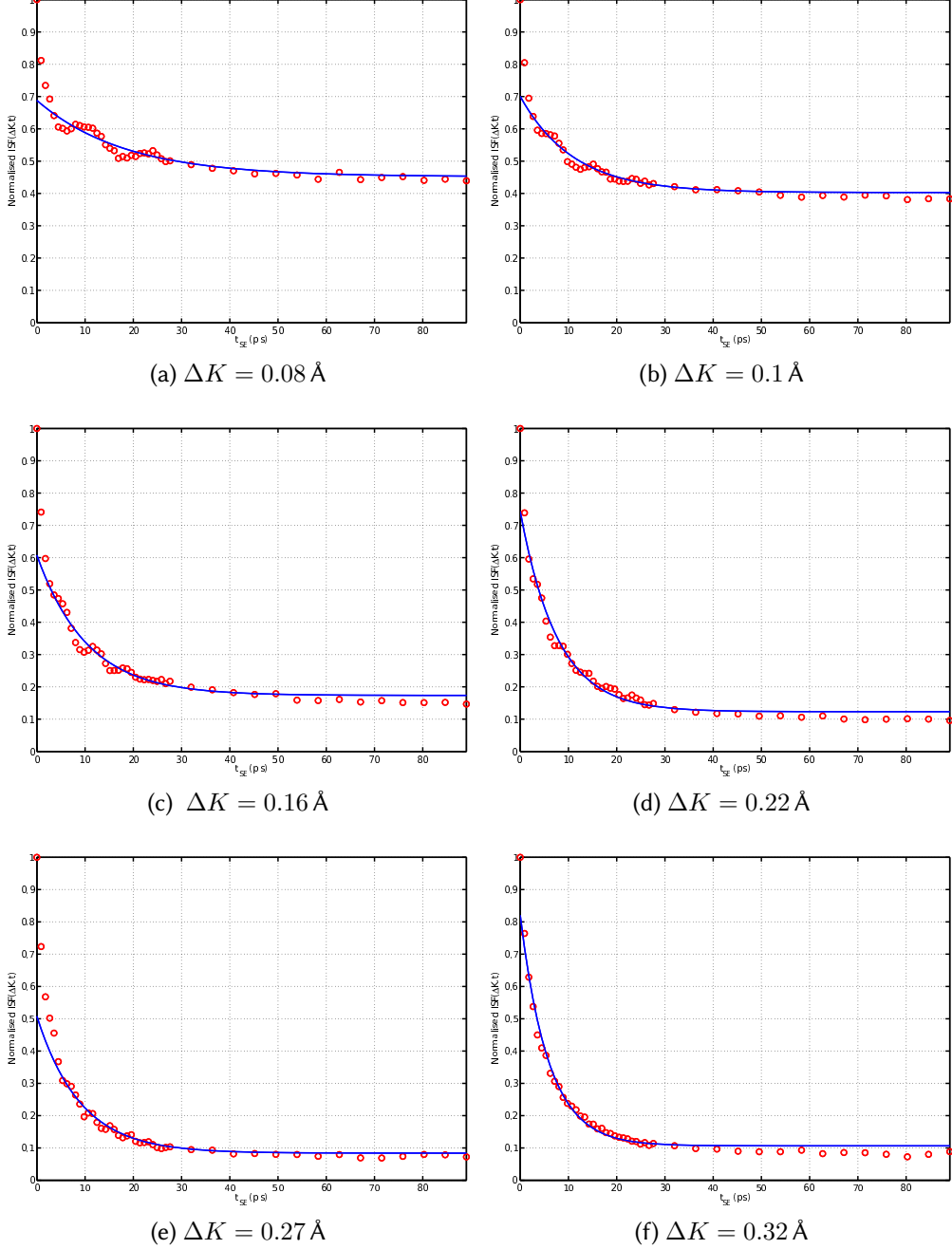


Figure B.1: Experimental ISFs for Na/Cu(111) recorded with a sample temperature 155 K and a Na coverage of $\theta = 0.025 \text{ ML}$. The spectra are fitted to $A_1 e^{-\alpha t} + A_2$, shown as blue lines in the figures. In some of the figures an oscillatory component is observed, for example the ISF in panel (a) and figure B.5. Oscillations in time spectra relate to inelastic scattering, i.e. energy losses or gains proportional to the oscillation frequency, in the present work they are associated with Cu phonons and are extracted from the spectra before further analysis, detailed in section 4.3.1.

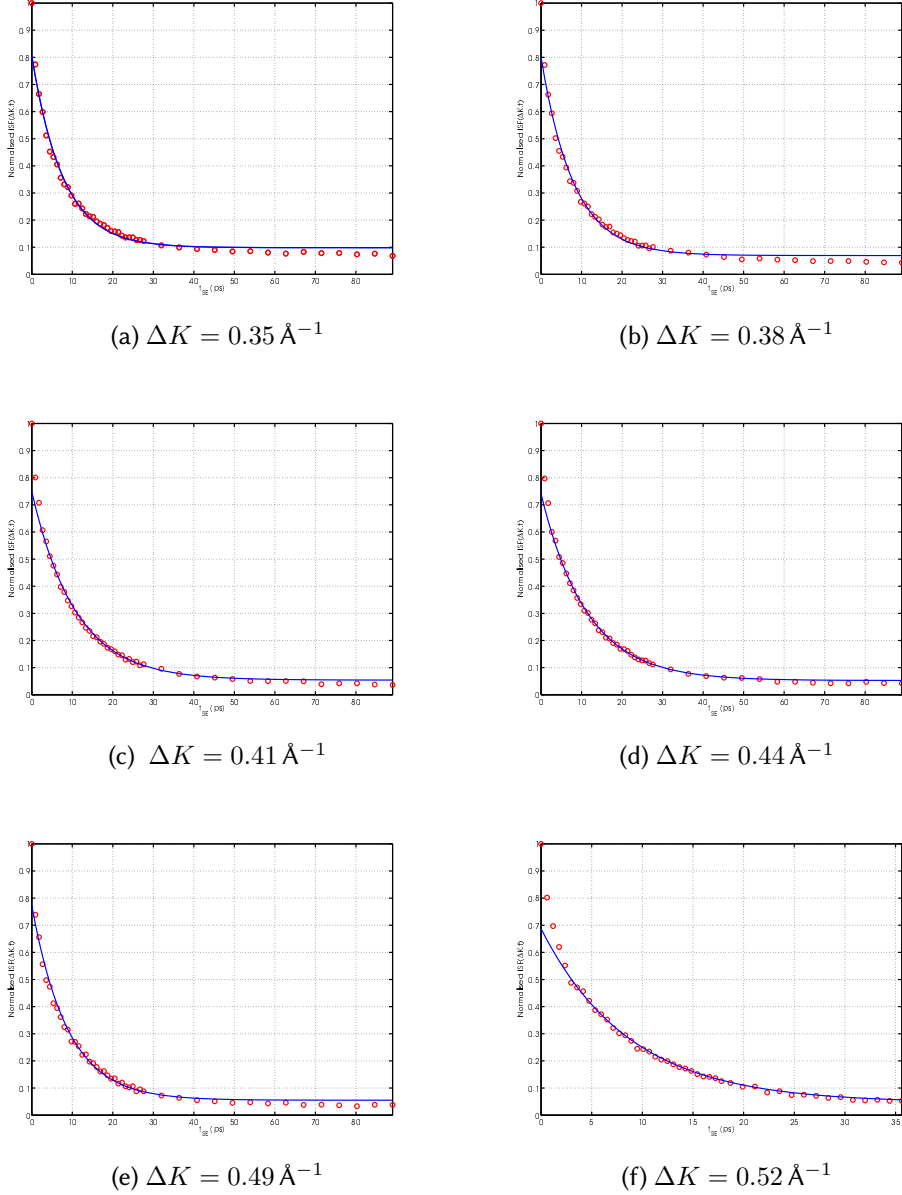


Figure B.2: See caption of figure B.1

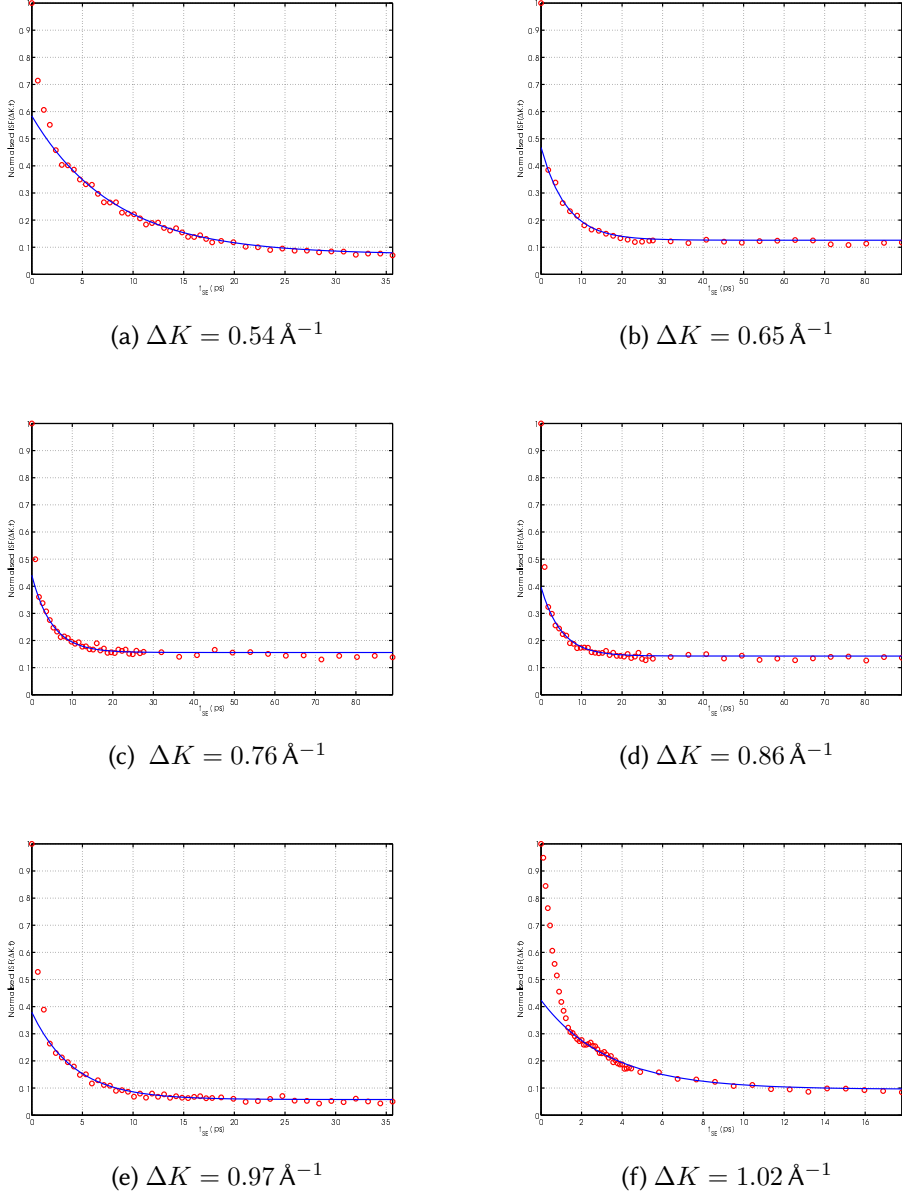


Figure B.3: See caption of figure B.1

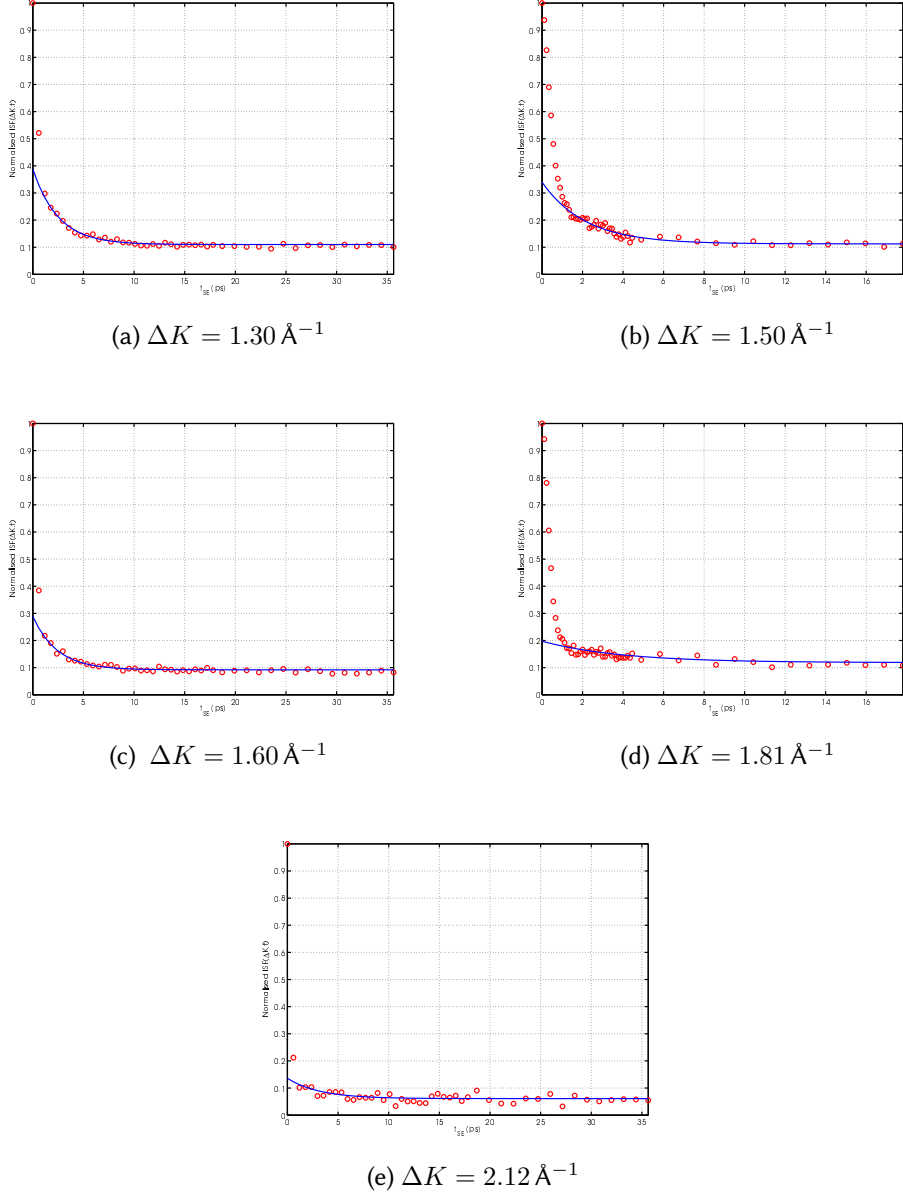


Figure B.4: See caption of figure B.1

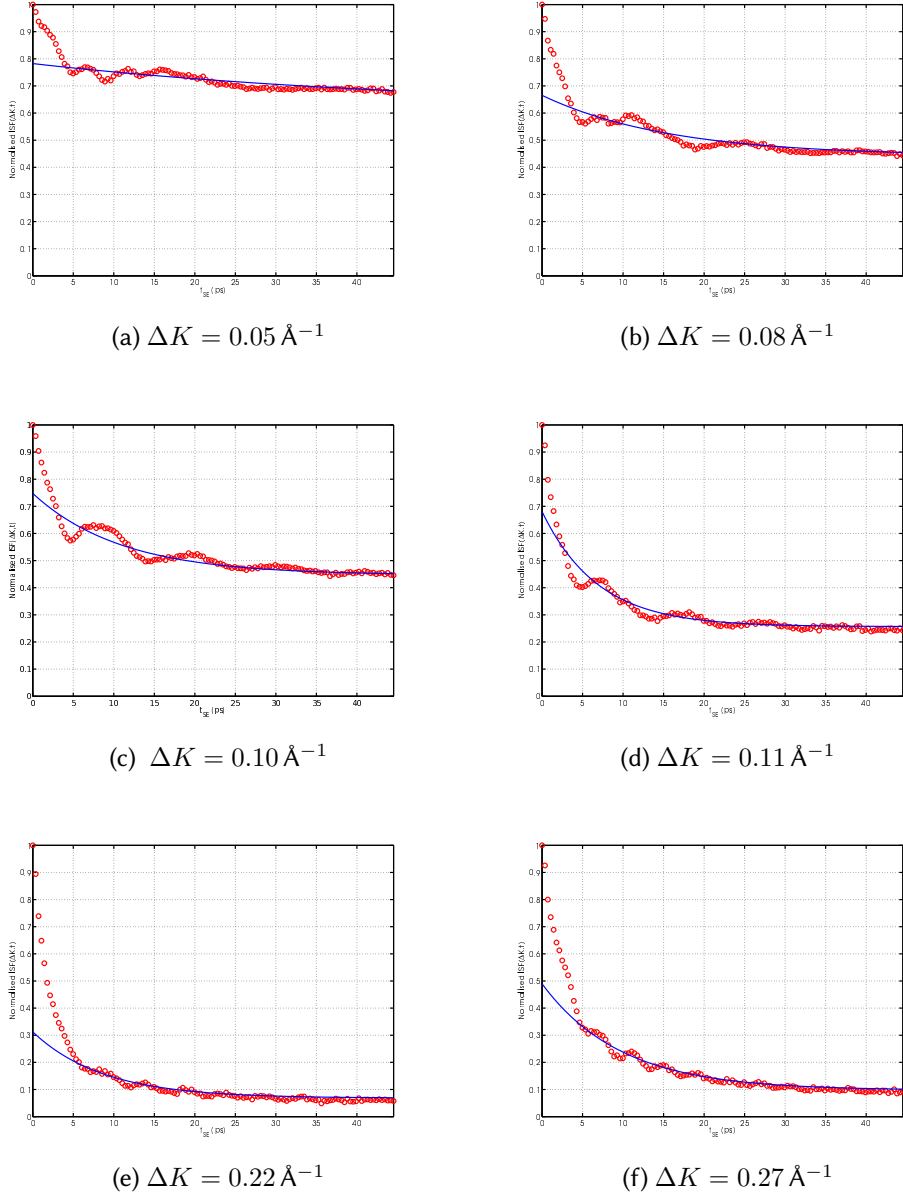


Figure B.5: Experimental ISFs for Na/Cu(111) recorded with a sample temperature 155 K and a Na coverage of $\theta = 0.08$ ML. The spectra fitted to $A_1 e^{-\alpha t} + A_2$, shown as blue lines in the figures, see caption of figure B.1.

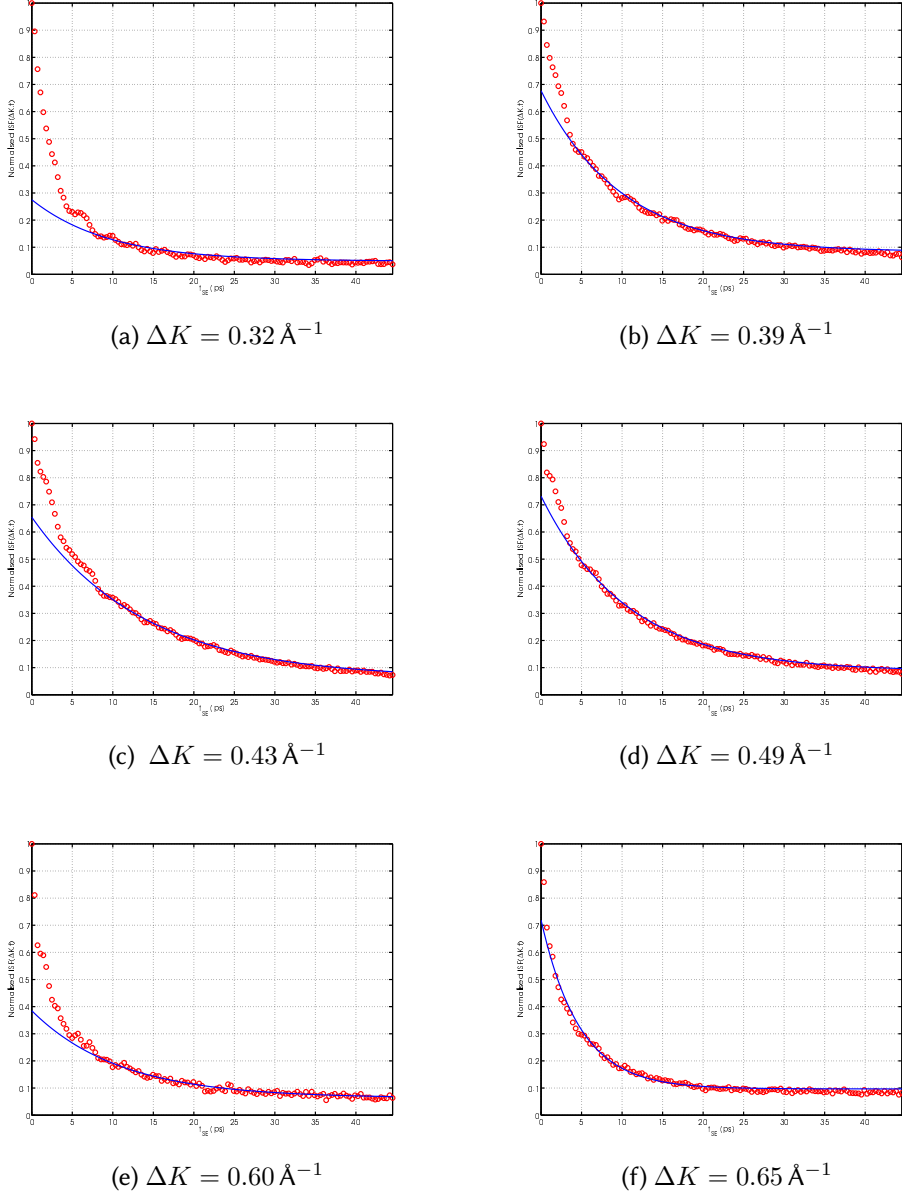


Figure B.6: See caption of figure B.5

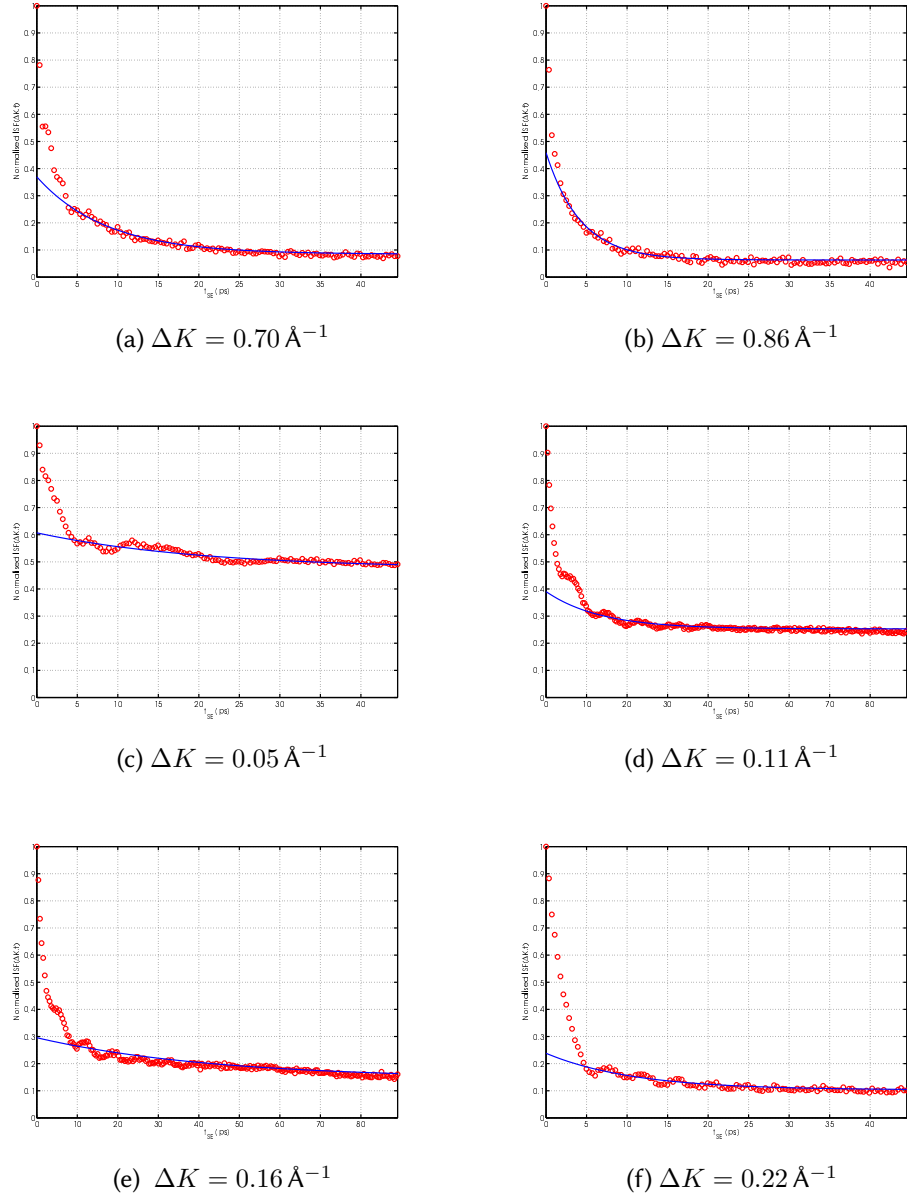


Figure B.7: See caption of figure B.5, panels (a) and (b) are quoted for a coverage of $\Theta = 0.08 \text{ ML}$, while the other panels are presented with a coverage $\Theta = 0.12 \text{ ML}$.

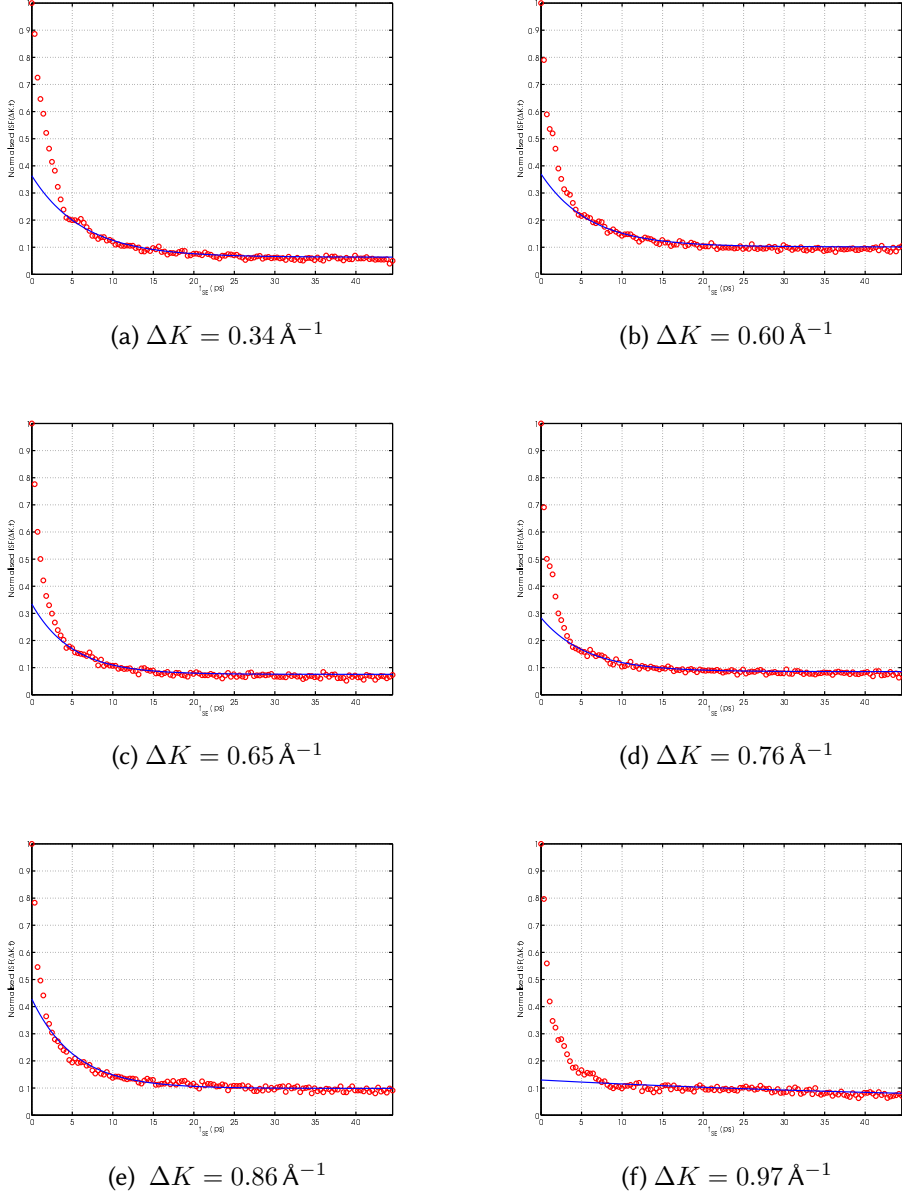
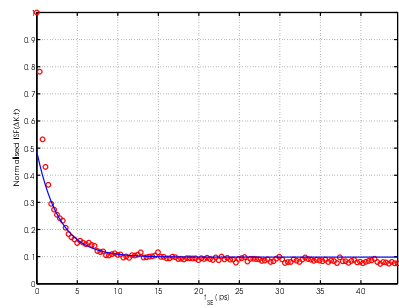
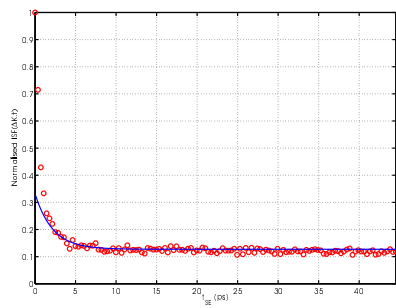


Figure B.8: See caption of figure B.5, coverage for this figure is $\Theta = 0.12 \text{ ML}$.

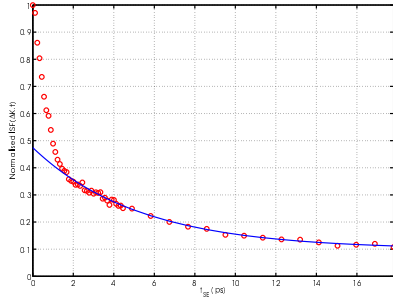


(a) $\Delta K = 1.08 \text{ \AA}^{-1}$

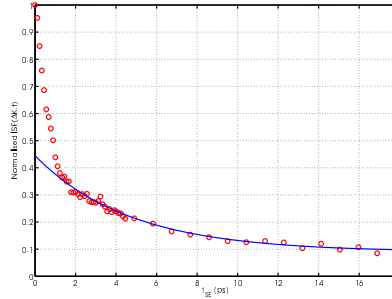


(b) $\Delta K = 1.18 \text{ \AA}^{-1}$

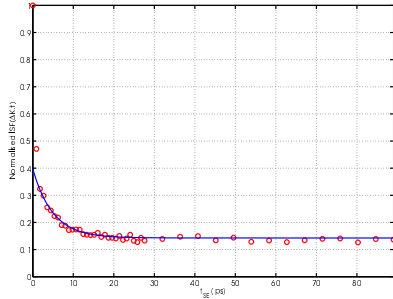
Figure B.9: See caption of figure B.5, coverage for this figure is $\Theta = 0.12 \text{ ML}$



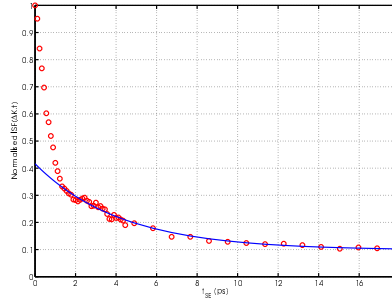
(a) $T_s = 130 \text{ K}$



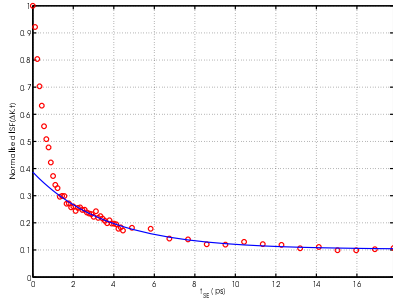
(b) $T_s = 140 \text{ K}$



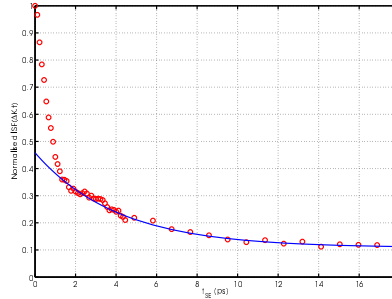
(c) $T_s = 155 \text{ K}$



(d) $T_s = 170 \text{ K}$



(e) $T_s = 175 \text{ K}$



(f) $T_s = 185 \text{ K}$

Figure B.10: Shown as red point are experimentally measured ISFs for Na/Cu recorded with a sample temperature between 130 K to 185 K and a Na at an angle relating to momentum transfer $\Delta K = 0.86 \text{ \AA}^{-1}$ coverage of $\theta = 0.025 \text{ ML}$. The spectra are fitted to $A_1 e^{-\alpha t} + A_2$, shown as blue lines in the figures.

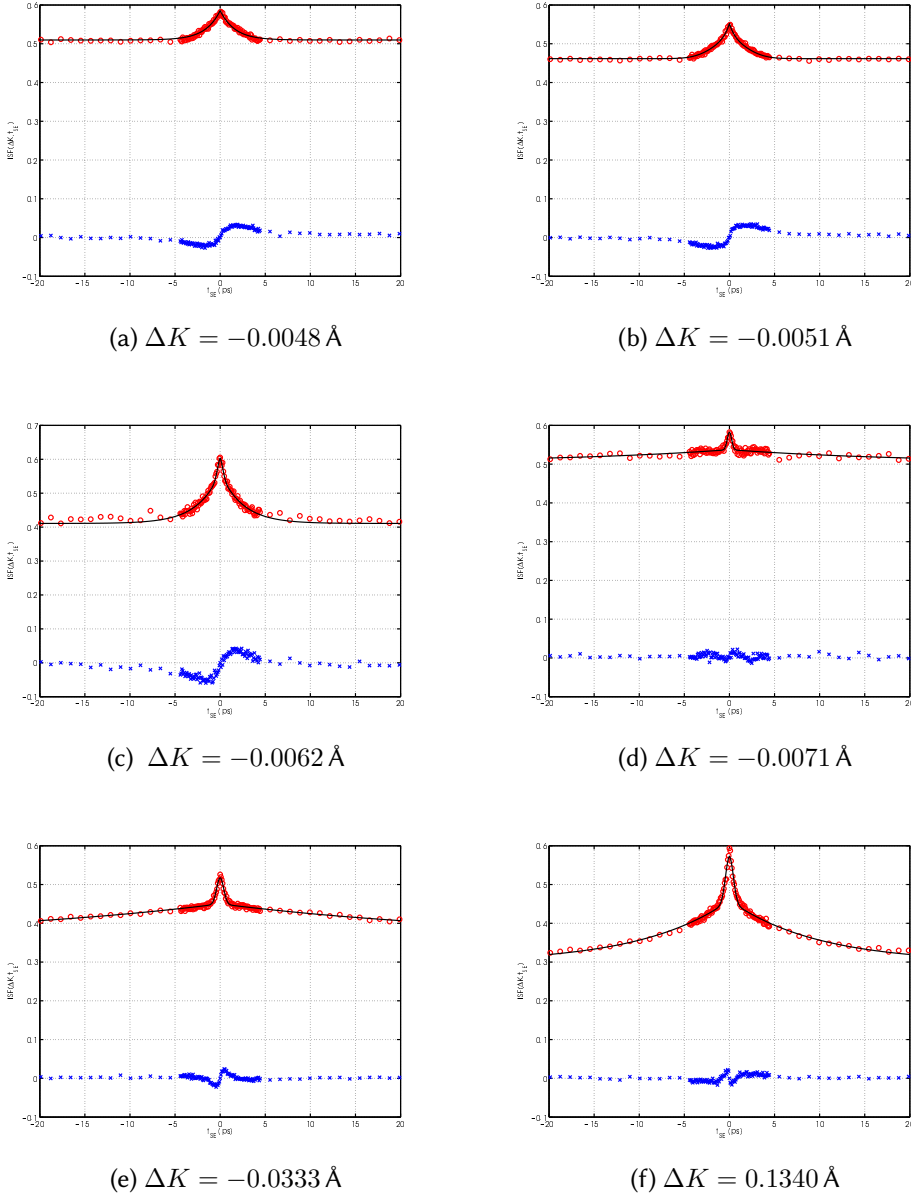


Figure B.11: Experimental ISFs measured at high temporal resolution and short times for Na/Cu(111) recorded with a sample temperature 120 K and a Na coverage of $\theta = 0.025$ ML. The spectra fitted to $A_0 e^{-\frac{t^2}{2\sigma^2}} + A_1 e^{-\alpha t} + A_2$, shown as black lines in the figures. Inelastic scattering features (oscillations in time spectra) are extracted, as explained in section 4.3.1, and not displayed.

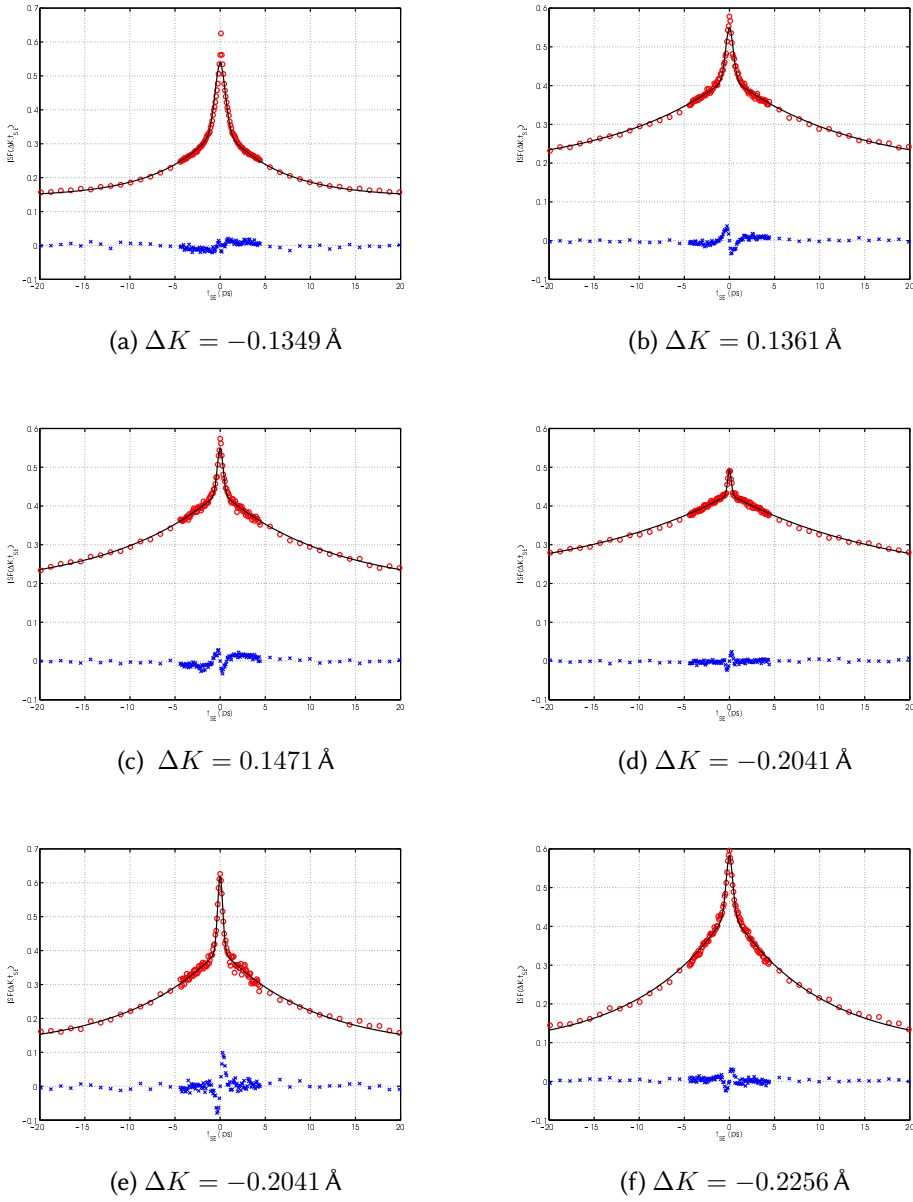


Figure B.12: see B.11

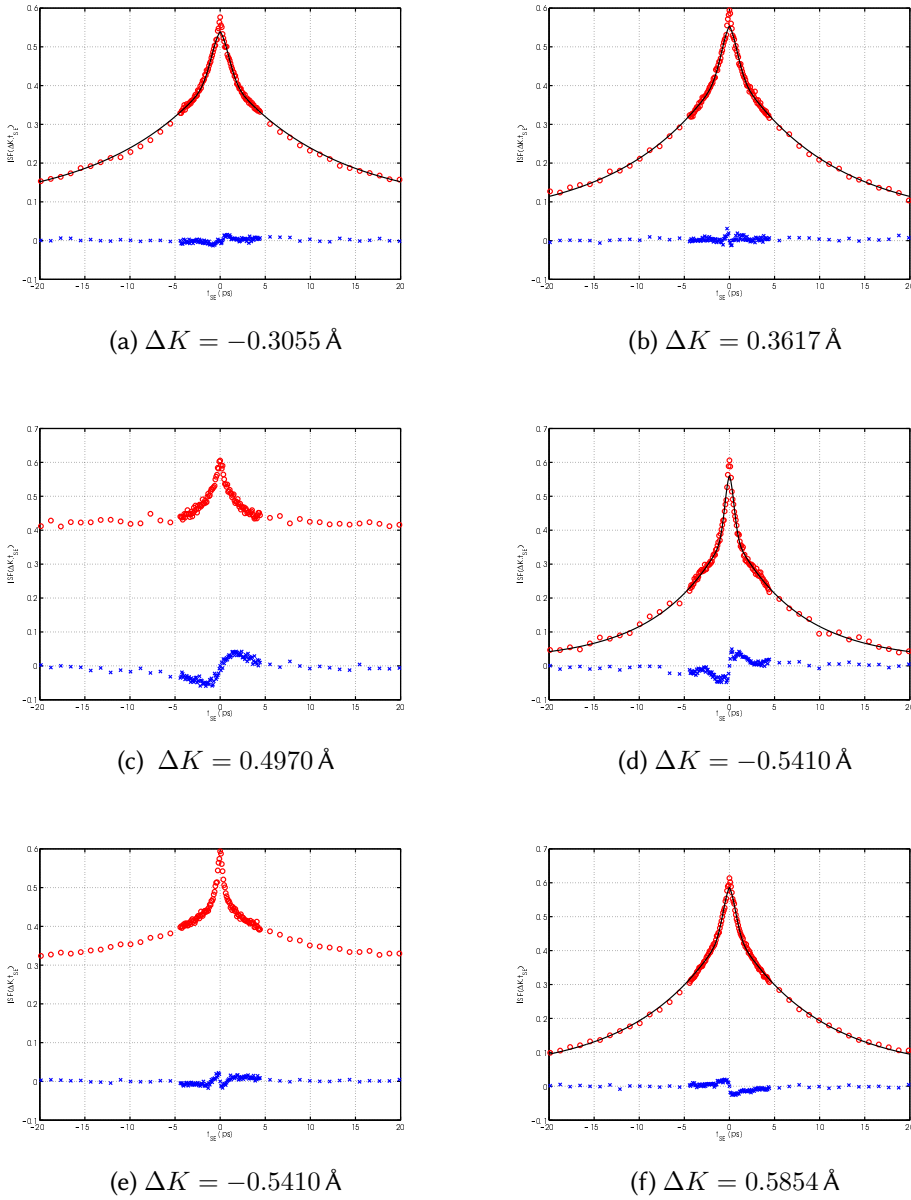


Figure B.13: see B.11

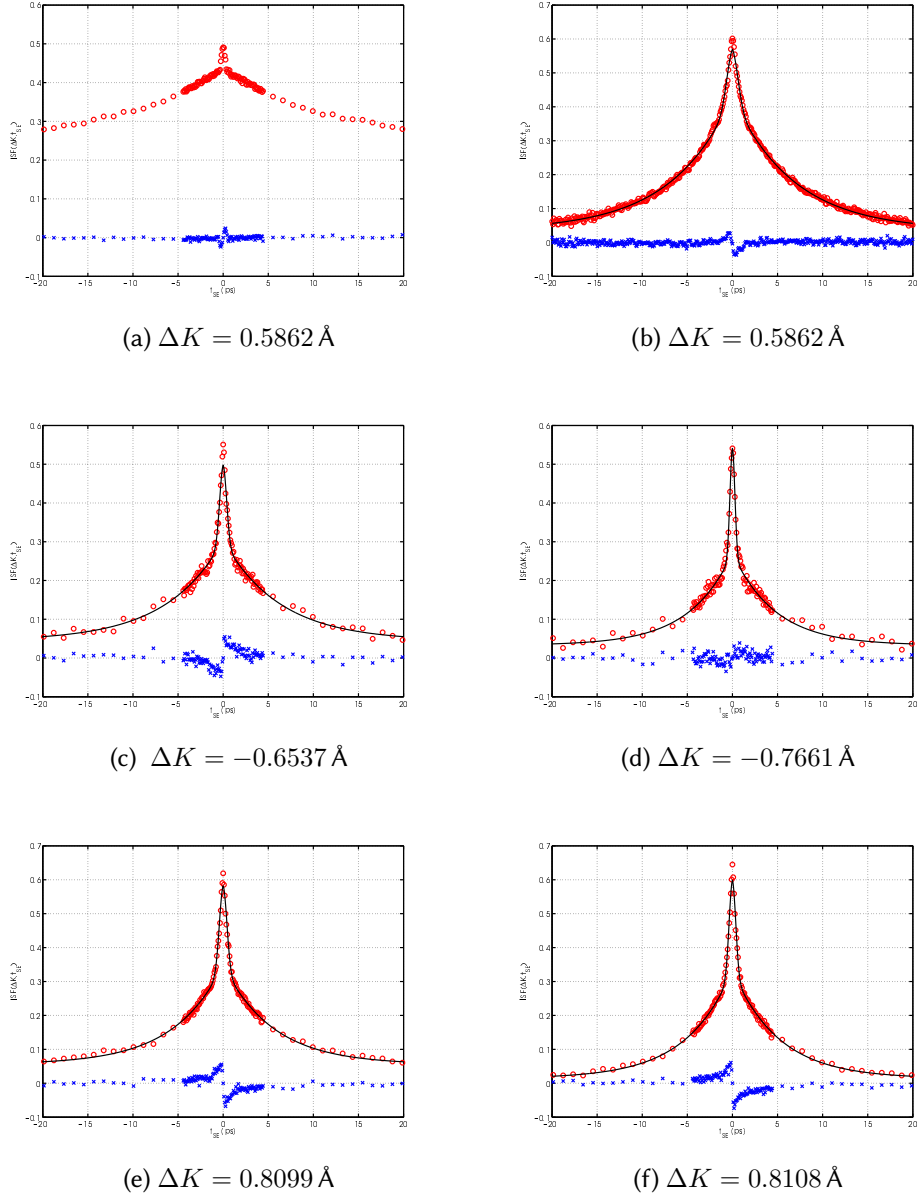


Figure B.14: see B.11

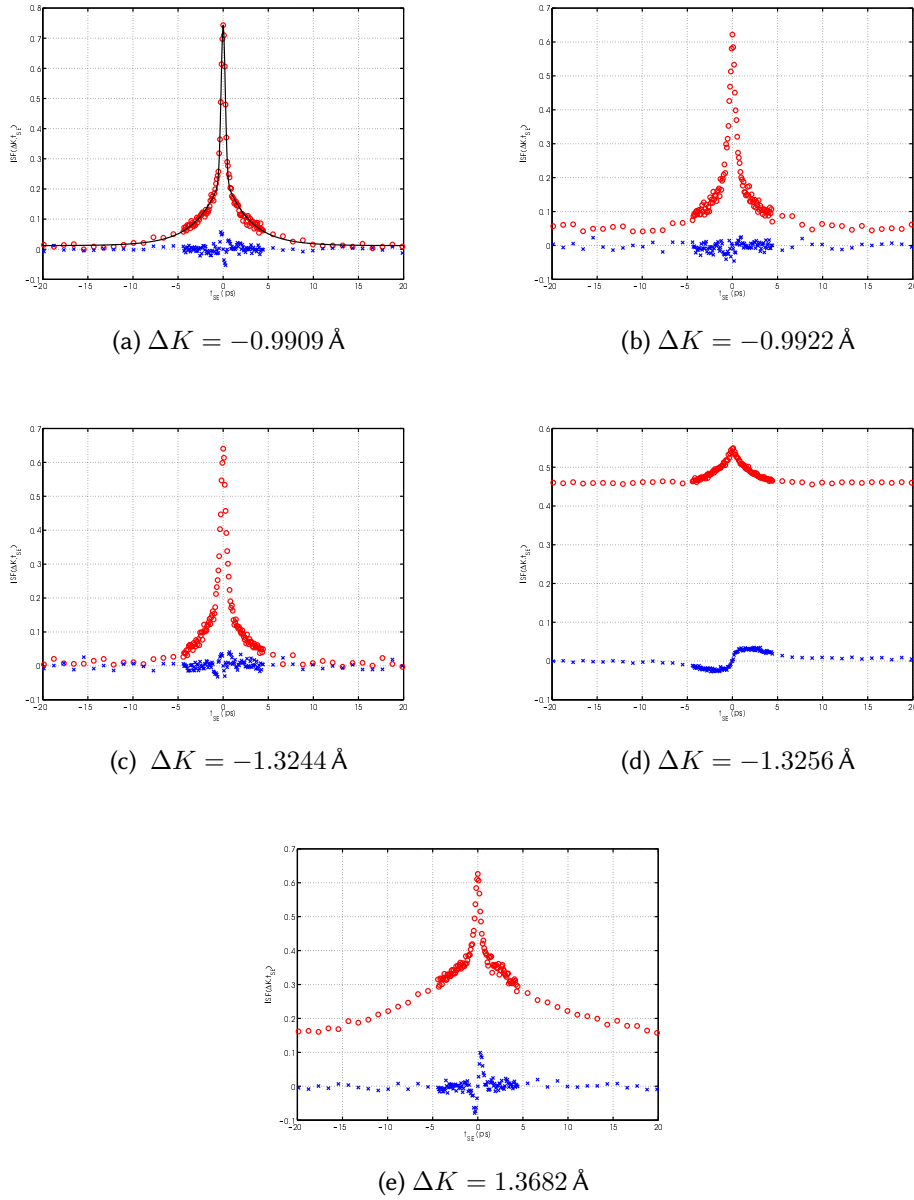


Figure B.15: see B.11

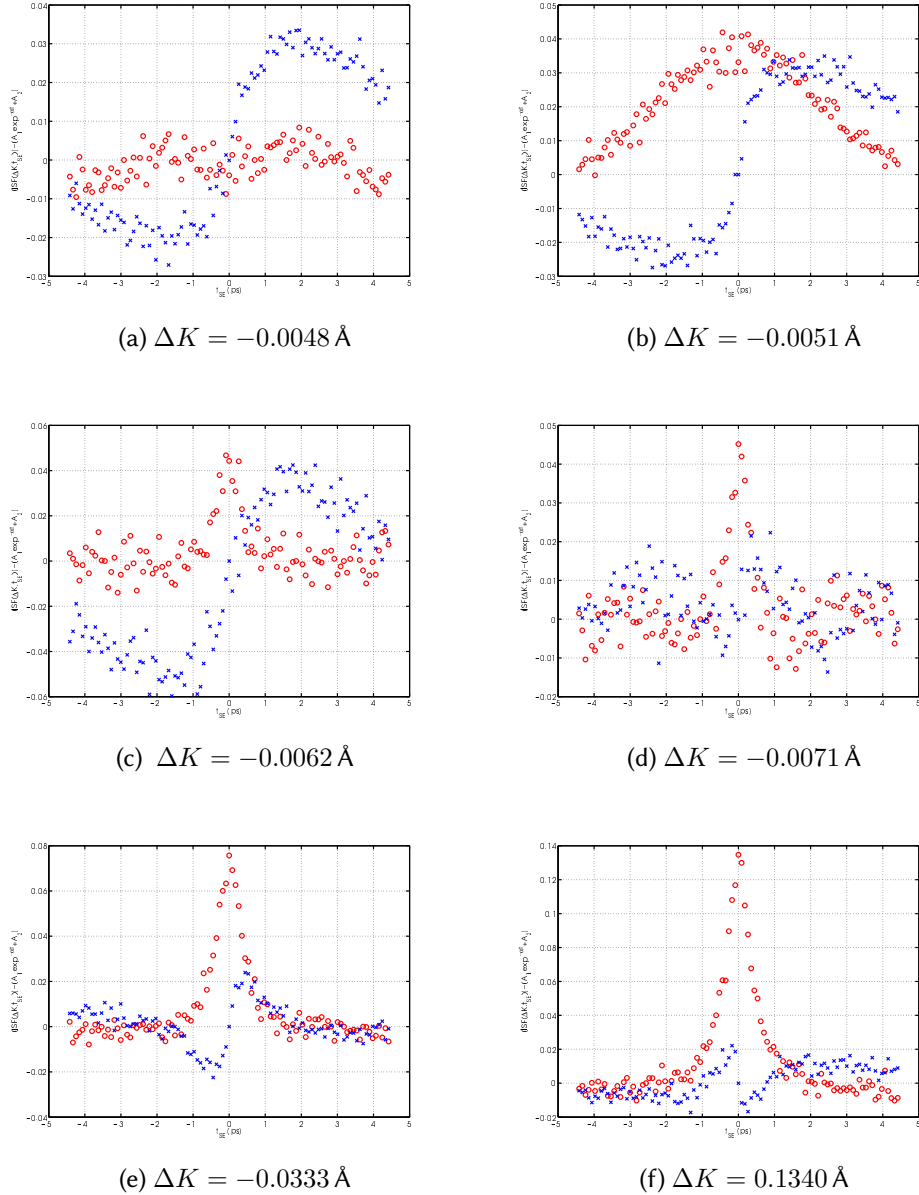


Figure B.16: Experimental Na/Cu(111) ISFs with diffusive signature subtracted, measured at $\Theta = 0.025 \text{ ML}$

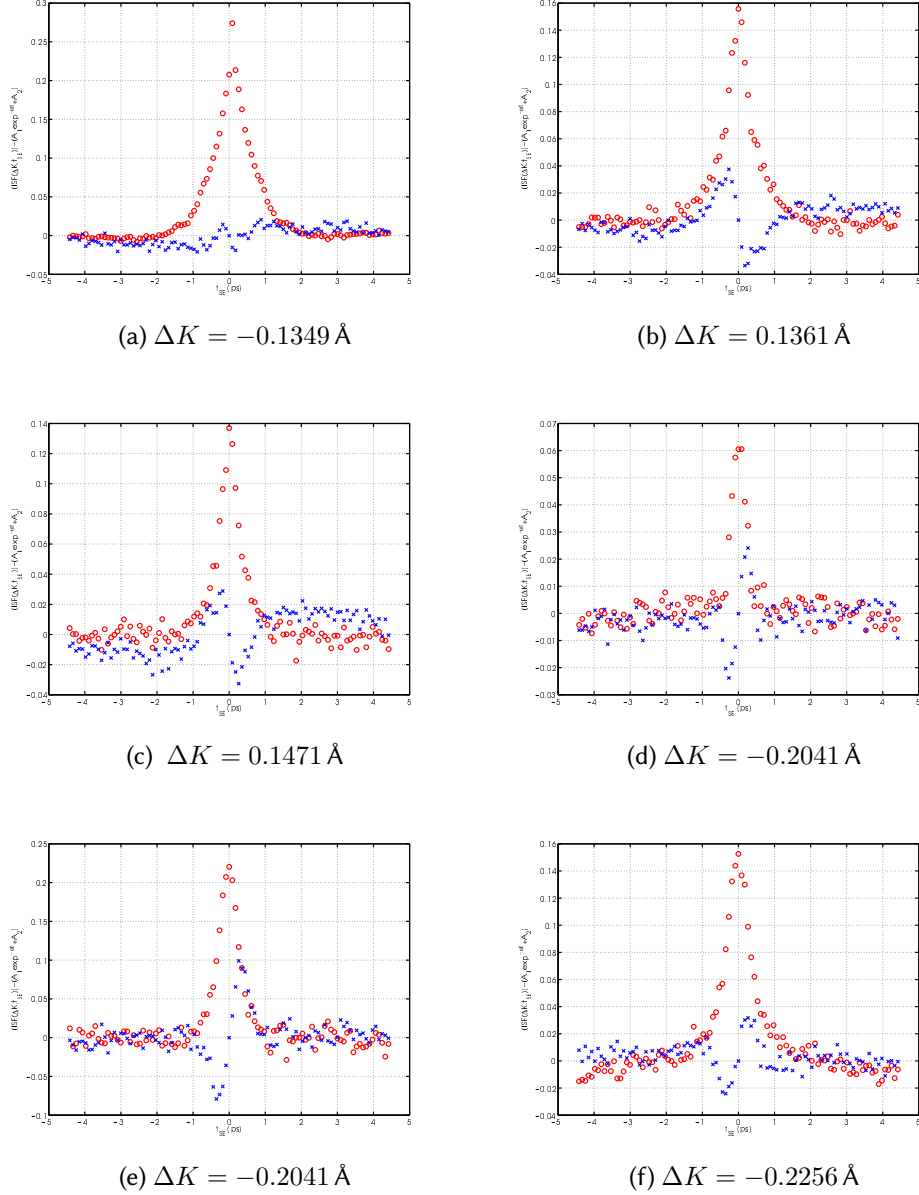


Figure B.17: see B.16

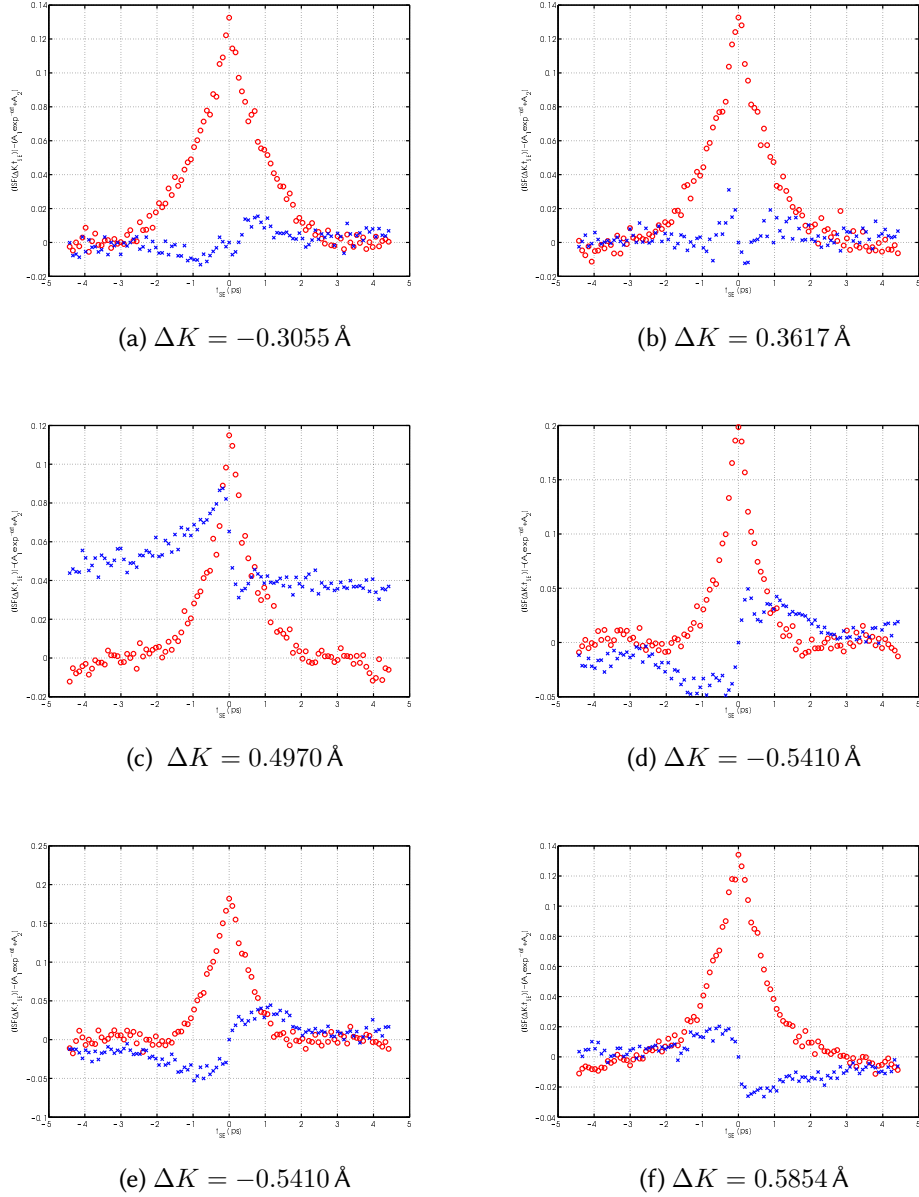


Figure B.18: see B.16

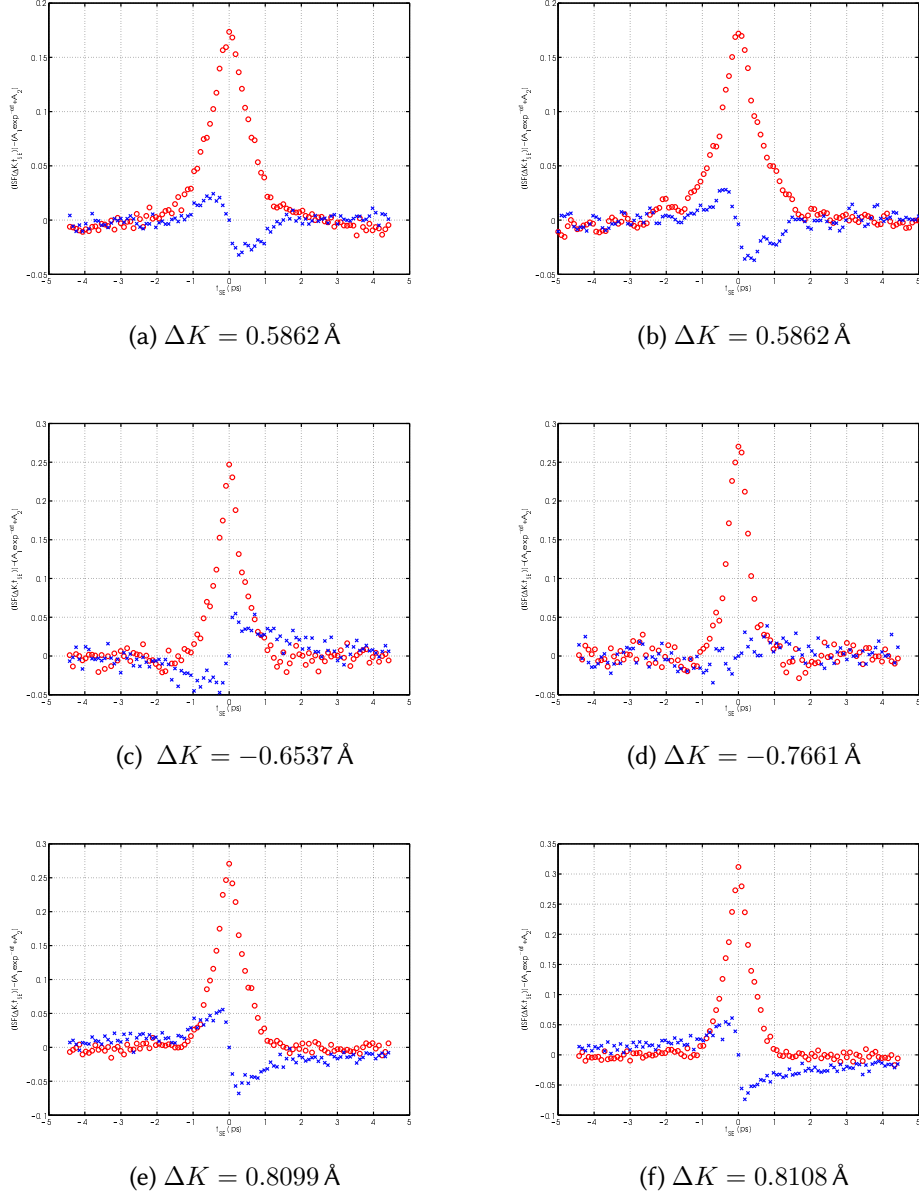


Figure B.19: see B.16

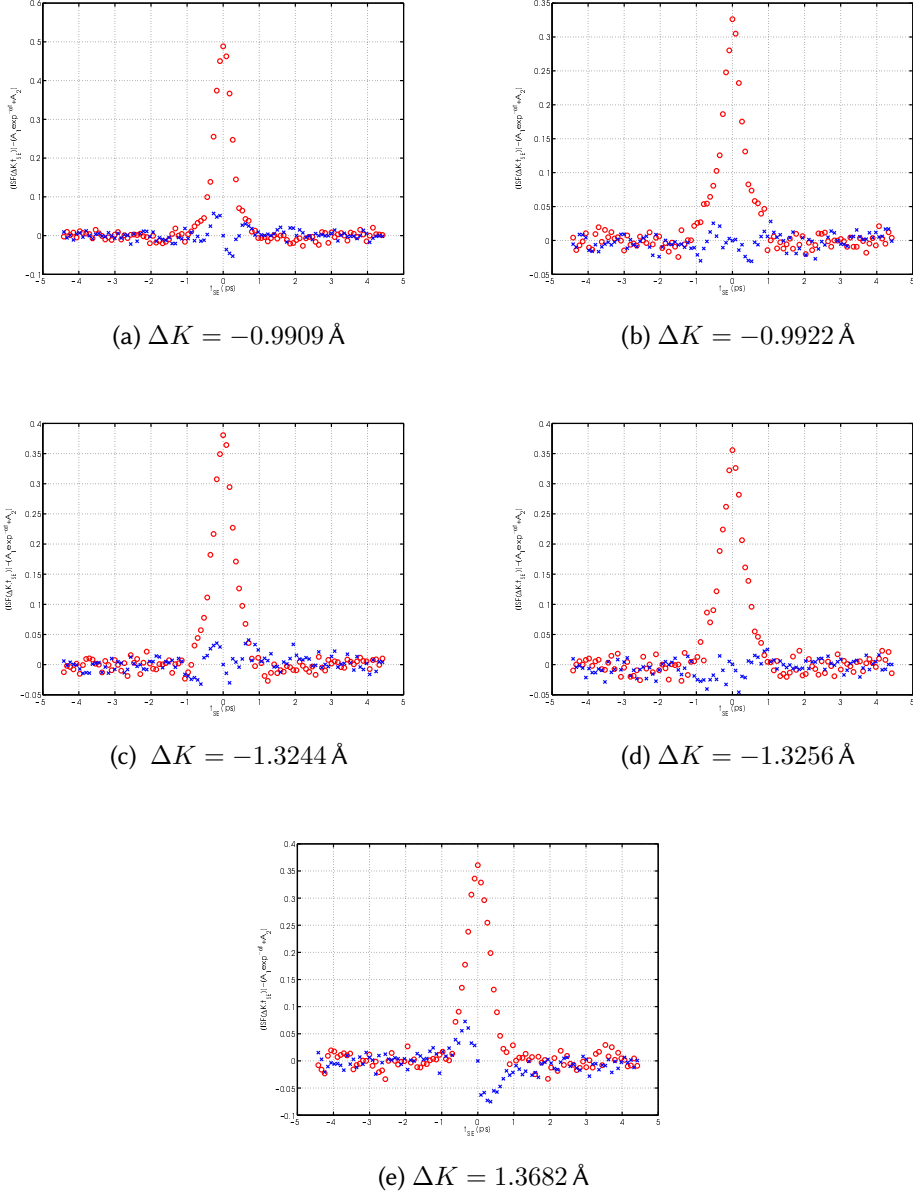


Figure B.20: see B.16

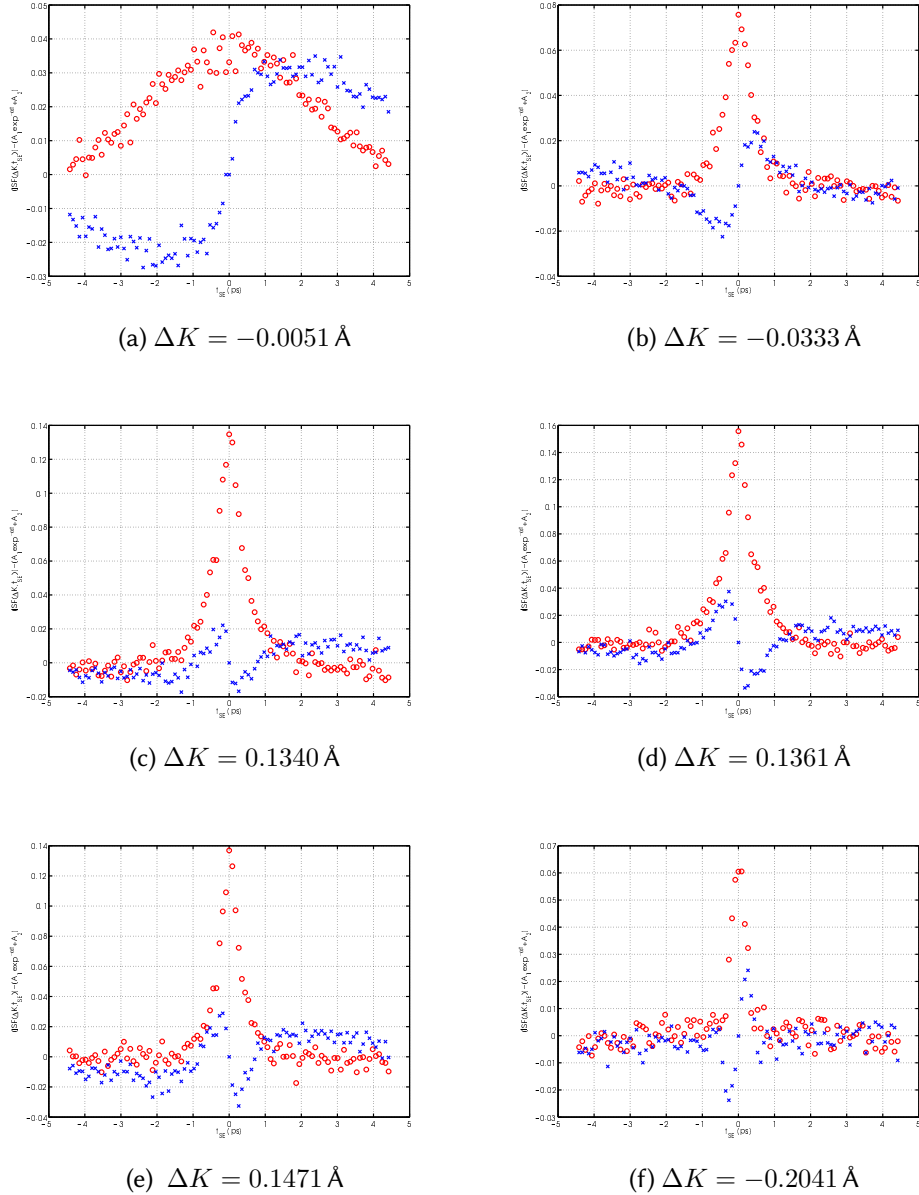


Figure B.21: Figures showing the fast decay process in the spectra which is used to measure the energy shift, related to the frequency of the imaginary peak. The experimental data is shown in red crosses (real) and blue crosses (imaginary) and the result after application of frequency optimisation in the form $ISF = ISF/\cos(\omega t) + i\sin(\omega t)$ are presented in figure 5.10 of chapter 5.

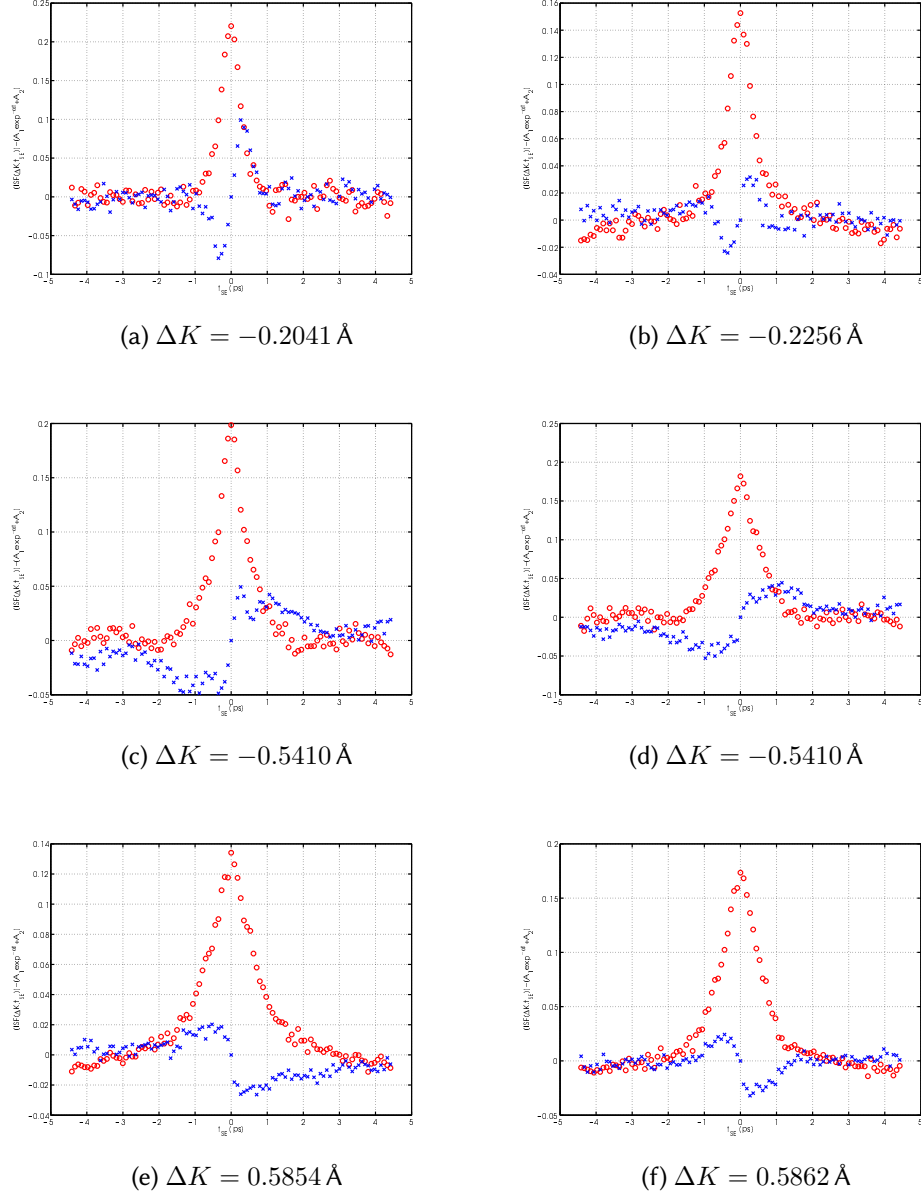


Figure B.22: See caption of figure B.21.

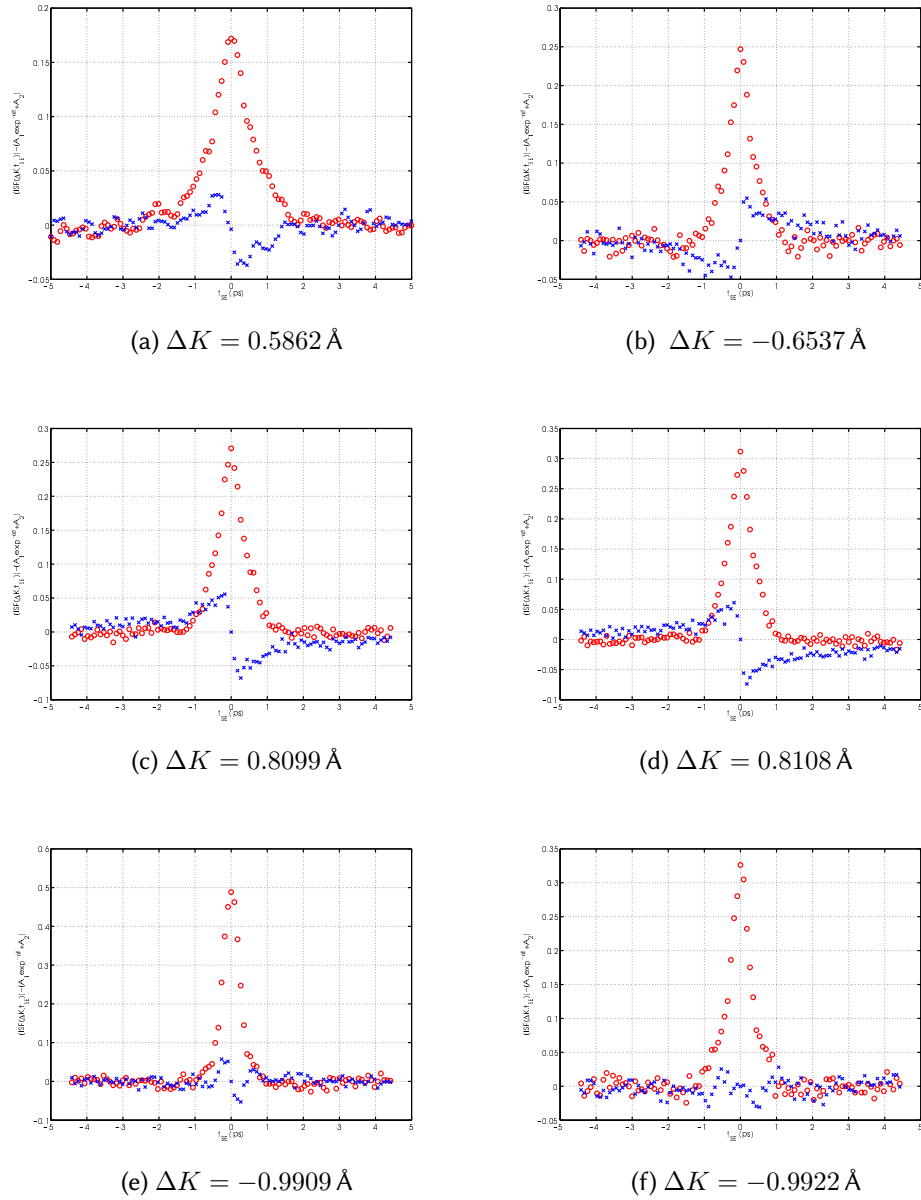


Figure B.23: See caption of figure B.21.

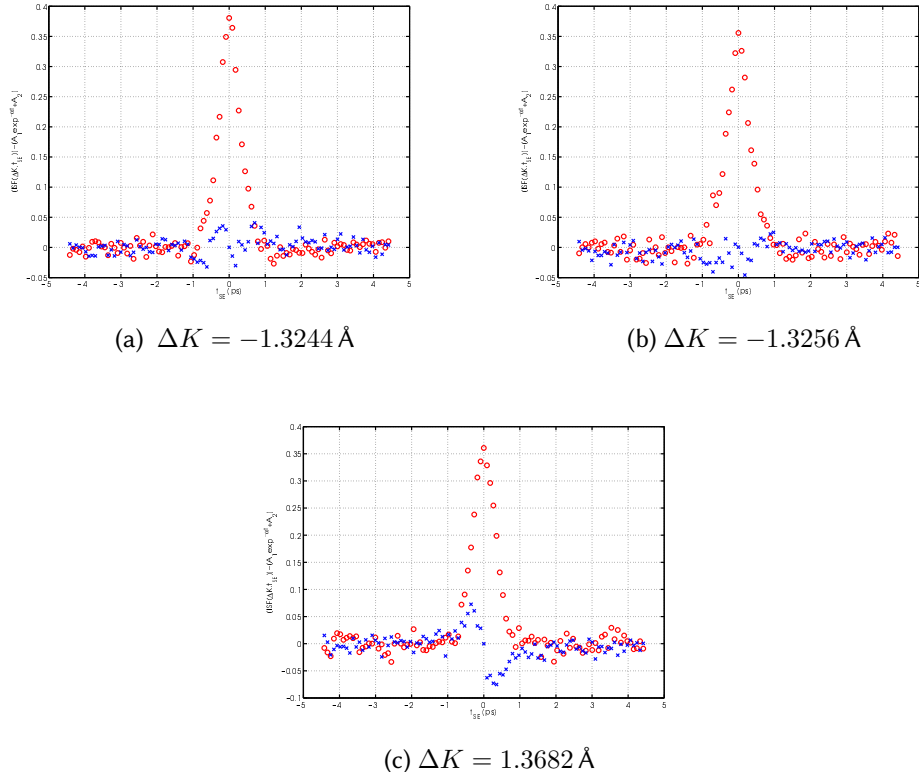


Figure B.24: See caption of figure B.21.

Appendix C

All Li/Cu(111) ISFs

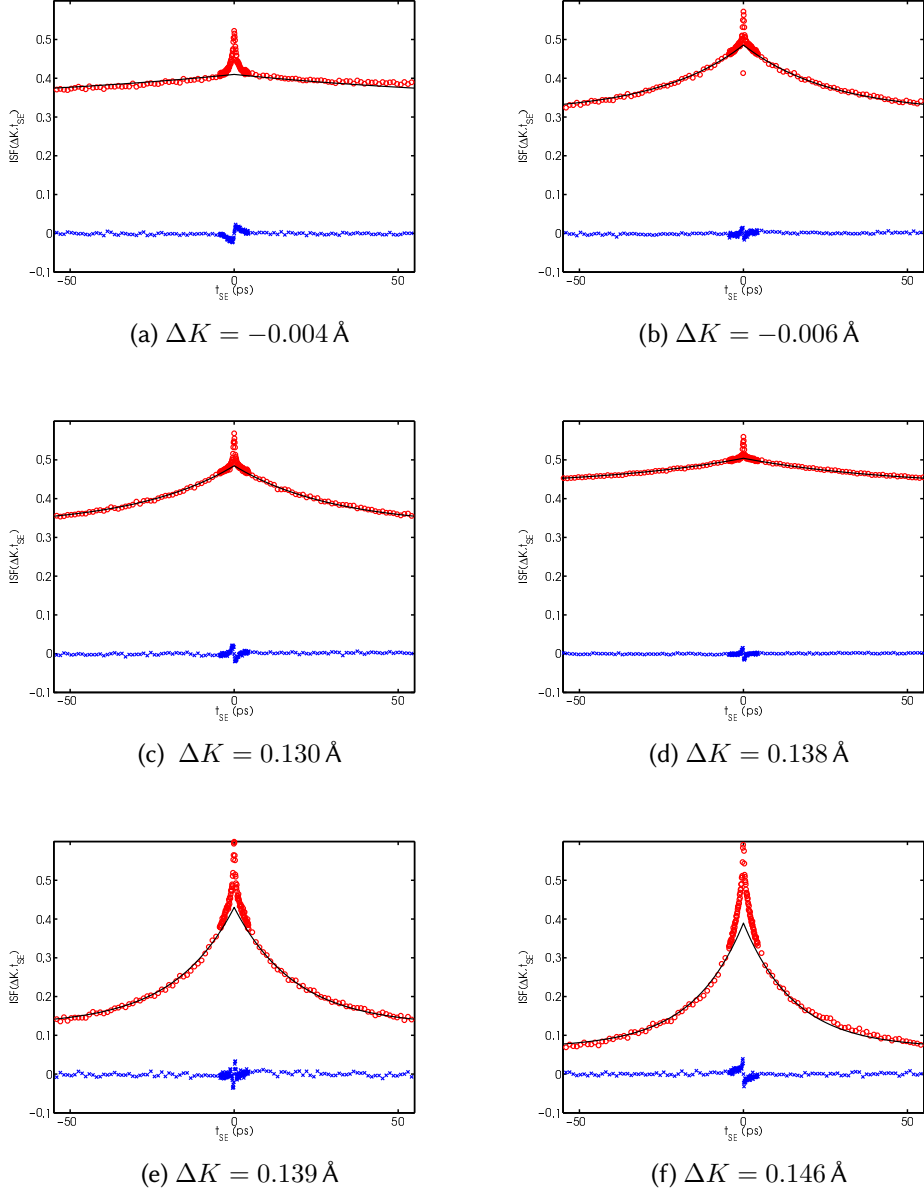


Figure C.1: Experimental ISFs for Li/Cu(111) recorded with a sample temperature 155 K and a Li coverage of $\theta = 0.025 \text{ ML}$. The spectra are fitted to $A_1 e^{-\alpha t} + A_2$, shown as black lines in the figures. Oscillations in time spectra related to inelastic scattering, i.e. energy losses or gains proportional to the oscillation frequency, in the present work they are associated with Cu phonons and are extracted in the displayed spectra using the method detailed in section 4.3.1.

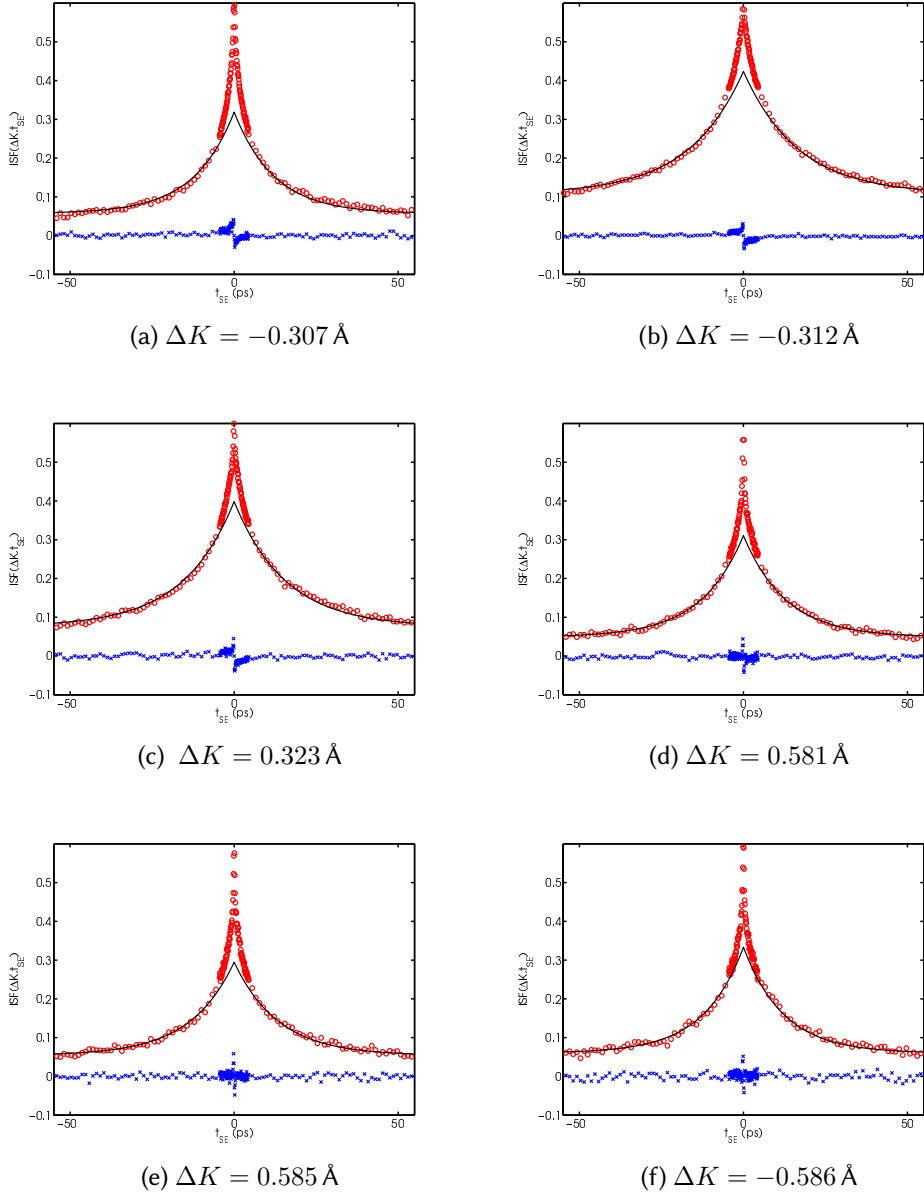


Figure C.2: See caption of figure C.1.

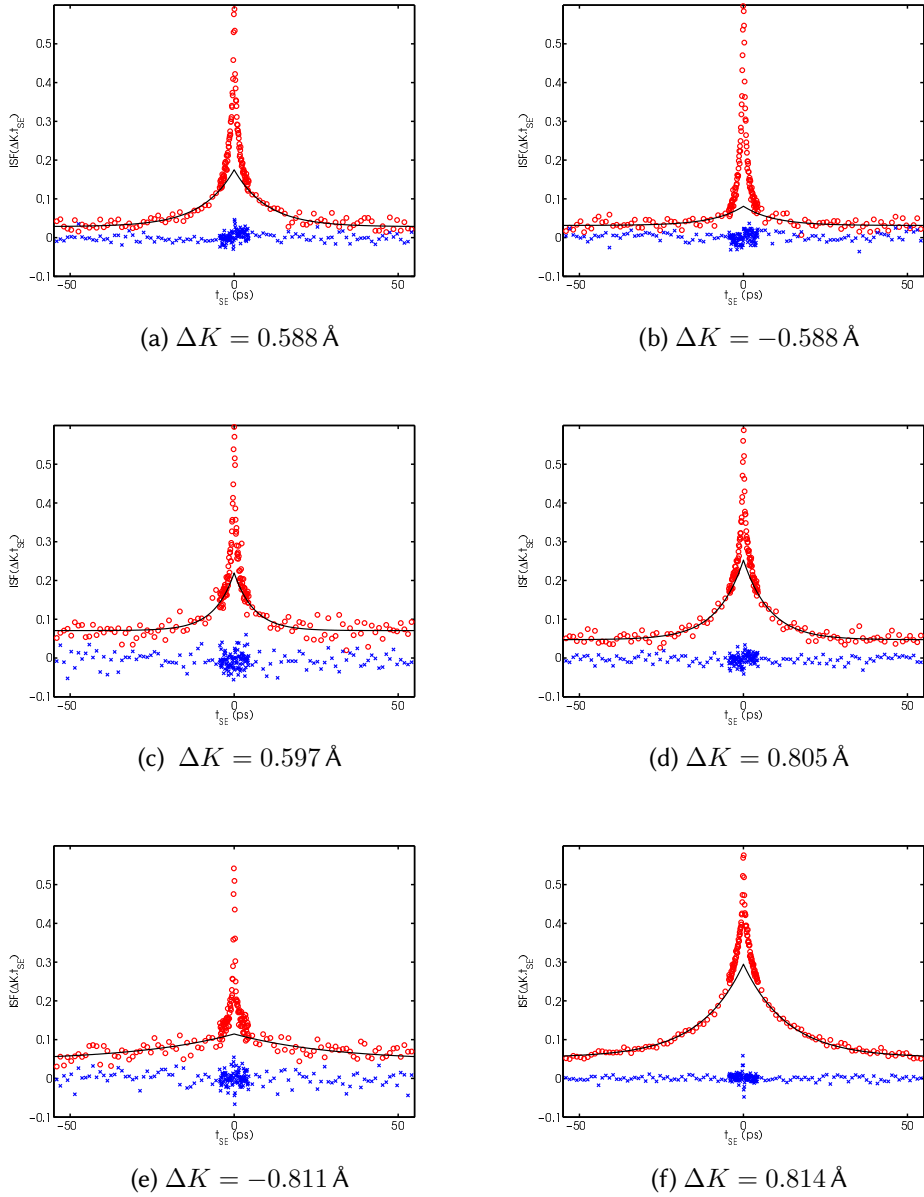


Figure C.3: See caption of figure C.1.

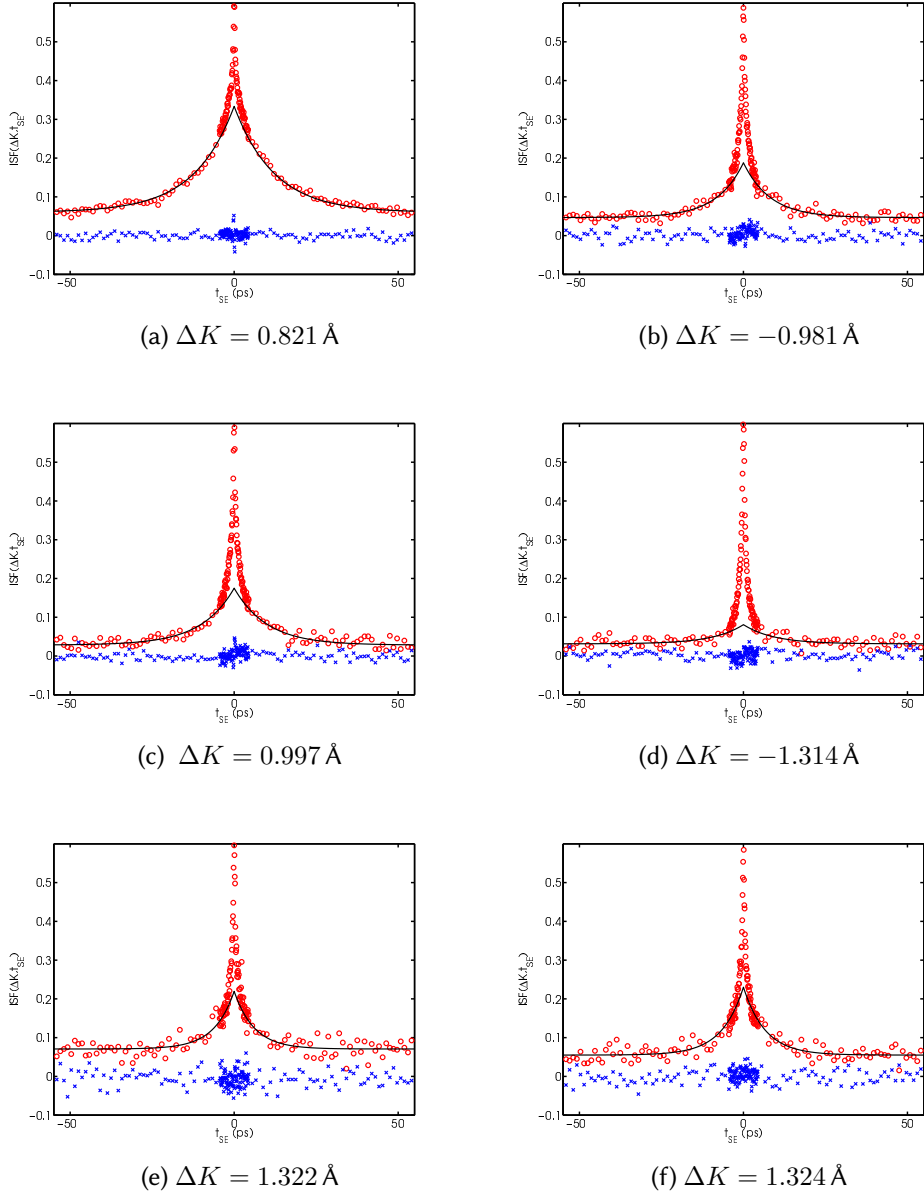


Figure C.4: See caption of figure C.1.

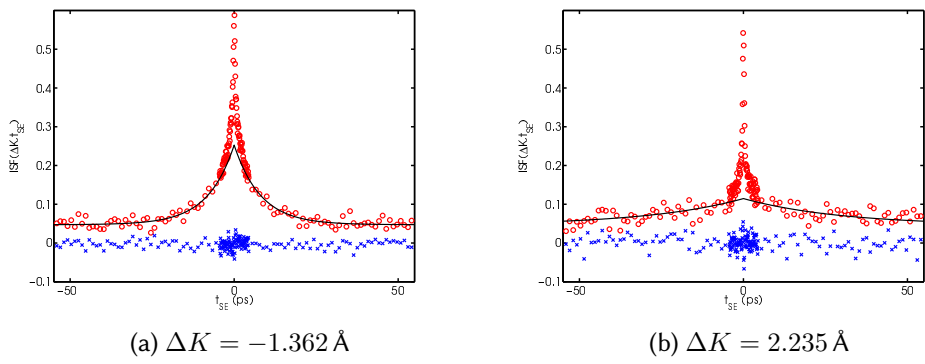


Figure C.5: See caption of figure C.1.

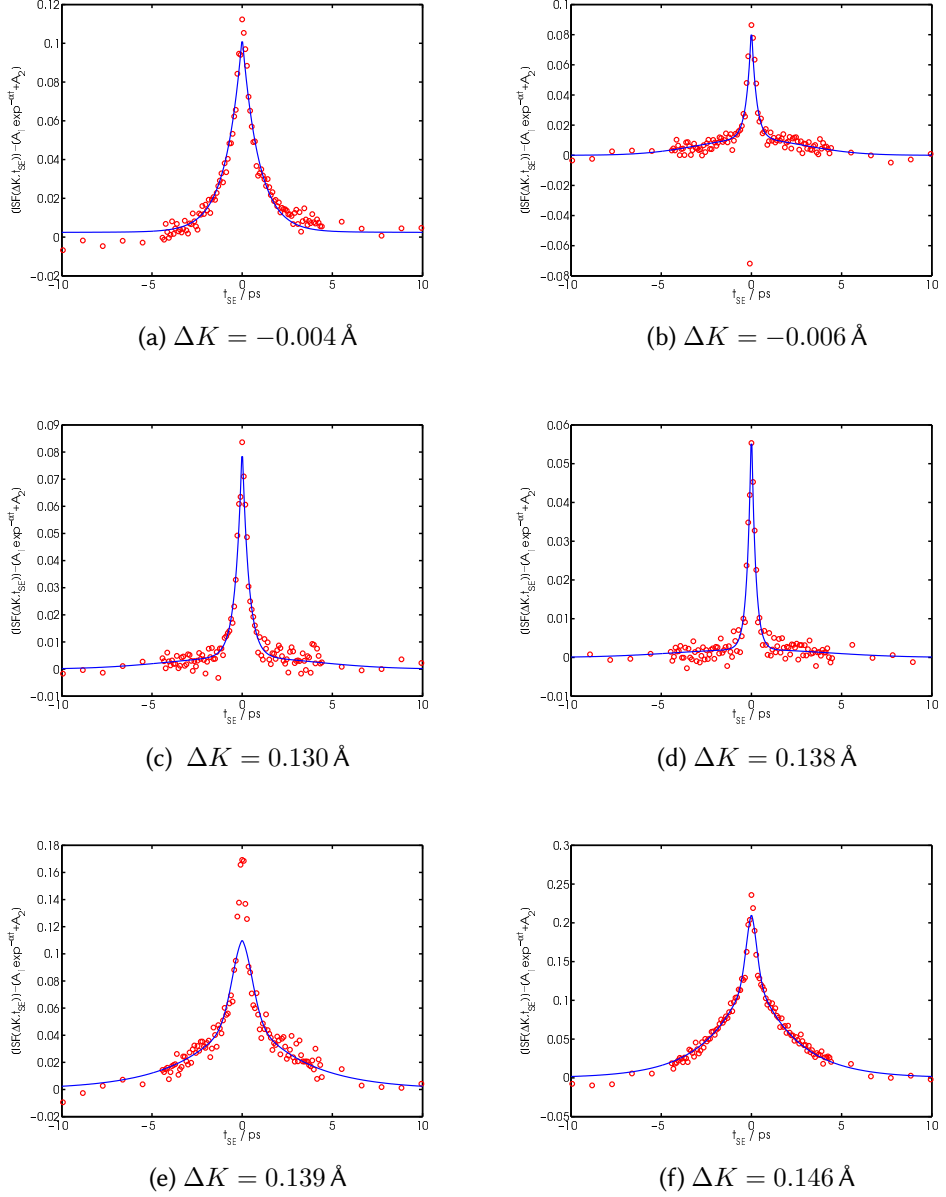


Figure C.6: Experimental ISFs for Li/Cu(111) recorded with a sample temperature 140 K and a Li coverage of $\theta = 0.025 \text{ ML}$. The diffusion signature characterised by the model $A_1 e^{-\alpha t} + A_2$, is extracted from the residual spectrum shown.

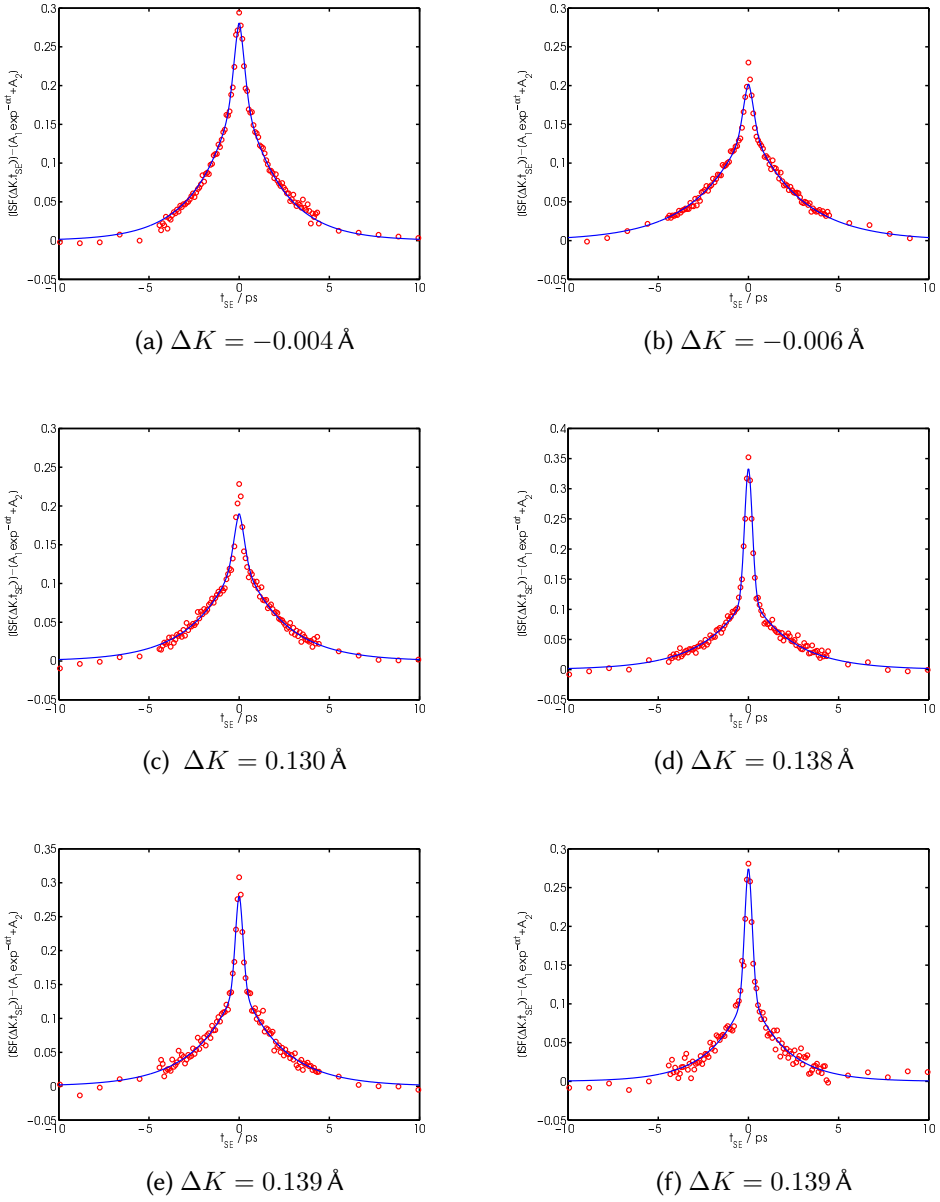


Figure C.7: See caption of figure C.6.

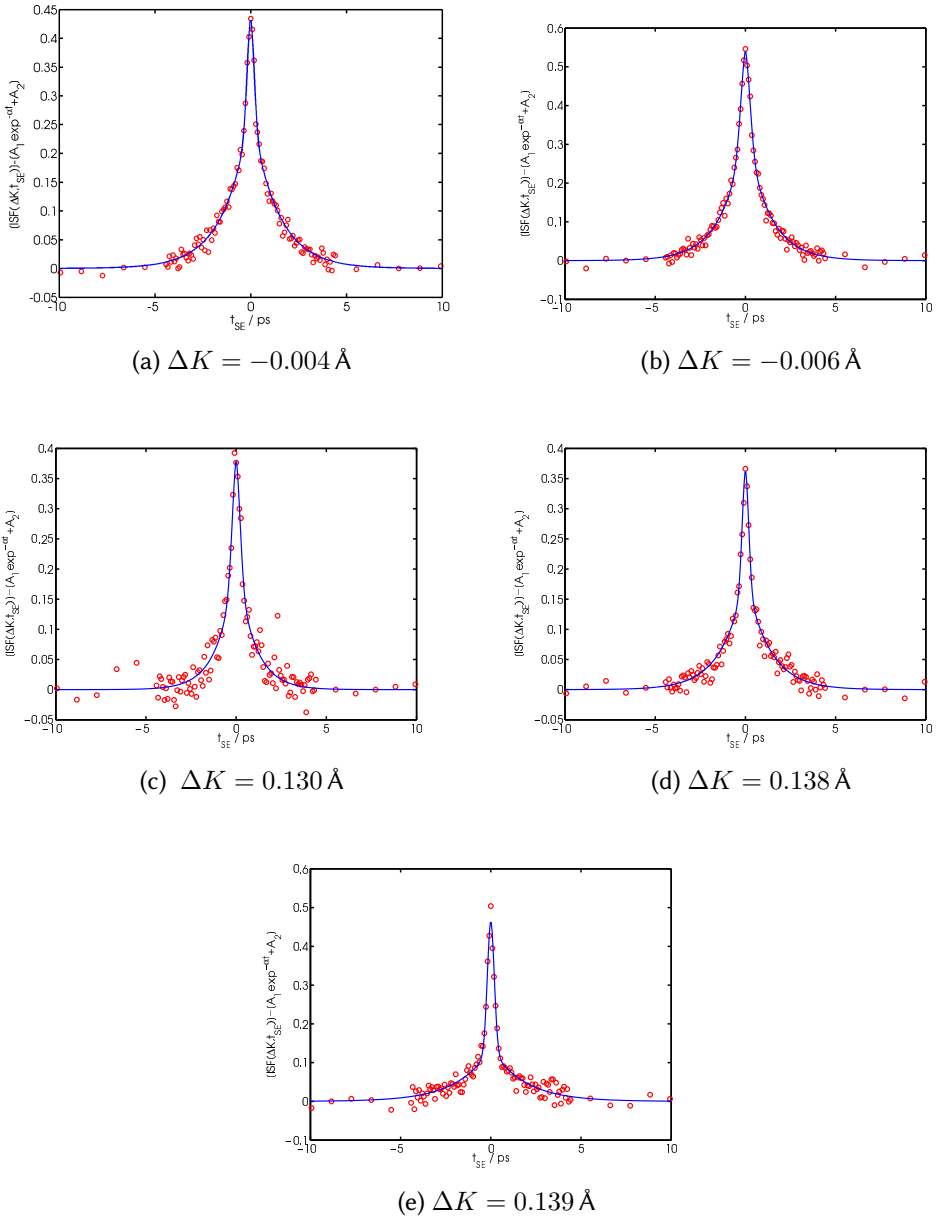


Figure C.8: See caption of figure C.6.

Appendix D

Protocol for Fourier filtering ISFs

A major theme in the current work is the analysis of the ‘fast’ part, or ‘initial drop’ in the ISF. In all of the experimental data presented there is evidence of inelastic phenomena in the spectra which occur on the same time scales as the dynamics processes of interest, which makes analysis more challenging. Here details of the protocol used in the application of the Fourier filter are described, and the resilience of the method examined.

If we consider a typical, high resolution ISF, presented in figure D.1 (in this case lithium on copper(111) in the $[11\bar{2}]$ direction, at $\Delta K = 0.5^{-1}$ with temperature 140 K at a coverage of $\Theta = 0.025$ ML). The real part of the spectrum is shown in blue and the imaginary part in red of panel (a). It is clear that there is an oscillatory contribution on top of a generally decaying spectra. It is desirable to extract the oscillating contribution to help analyse the rest of the spectra, which is difficult in the time domain. If we now consider the Fourier transform of the spectra in the right hand panel, it is clear that there is a central large peak which is related to the elastic and quasielastic scattering, with a much smaller peak resulting from inelastic scattering to the left of it which is much easier to identify and separate.

One simple method of removing the inelastic peak is to select a point on either side of it and linearly interpolate between the two points, which is the method applied in this case. There are several points that may be chosen in order to apply the interpolation. In all of the presented work a method has been used that involves manually selecting points either side of the peak at the steep take-off points of the peak, as demonstrated by the blue line on the right hand side of panel (b) (the orig-

inal data is shown as a dashed black line for reference). The left hand side of the panel presents the inverse transform of the data on the right and demonstrates that a significant amount of the inelastic process has been removed from the spectrum.

To investigate the effect of choice of the start and end points, the result of two different, more drastically selections is presented in panels (a) and (b). The results clearly demonstrate that there is very little sensitivity to the start and end point, with slightly more or less of the oscillating intensity removed.

A more sophisticated procedure for removing inelastic peaks from the transform could be applied, with a simultaneous fit in real and Fourier space to fit the whole spectra in one go; however such a procedure would be time-consuming and dependant on the exact form and symmetry of the instrument function as well as the scattering processed involved. Since the purpose of the current work is to analyse the quasielastic spectrum which appears to be relatively insensitive to the selection criteria, the method outlined here is used.

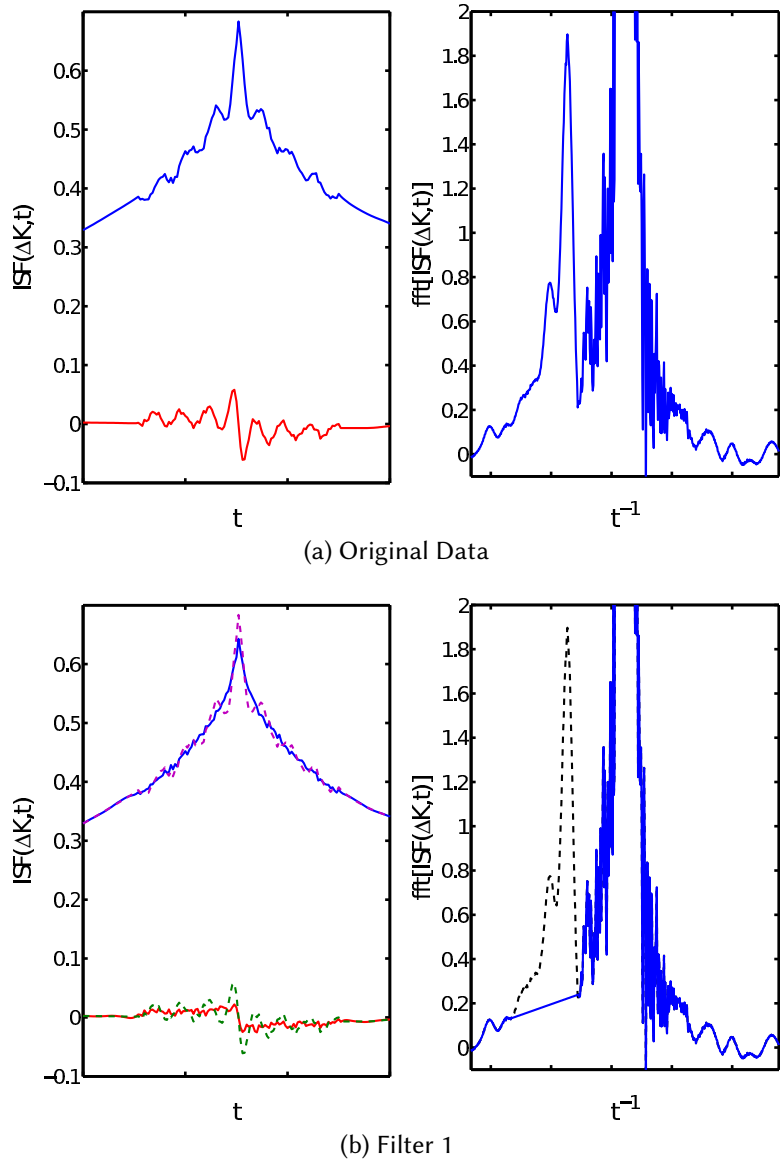


Figure D.1: The left hand side of panel (a) shows the real and imaginary parts (blue and red respectively) of a typical high resolution ISF, in this case for lithium on copper(111) in the $[11\bar{2}]$ direction at $\Delta K = 0.5^{-1}$ with temperature 140 K at a coverage of $\Theta = 0.025$ ML. The right hand side of panel (a) is the Fourier transform of the left, real part only shown as the imaginary contribution is not physical and of insignificant magnitude to be seen on this scale. The central elastic peak in the transform has a magnitude several orders larger than the rest of the spectrum and is not shown for clarity. It is clear from the figure that there is an inelastic feature on the left of the elastic peak. The right hand sides of panel (b) shows the inelastic peak removed in blue using the linear interpolation method employed generally in this work, with start and end point picked to minimise the removed intensity. The dashed black line shows the original data for reference. The left hand sides of panel (b) shows the real and imaginary parts of the inverse Fourier transforms of the right hand figures in blue and red respectively.

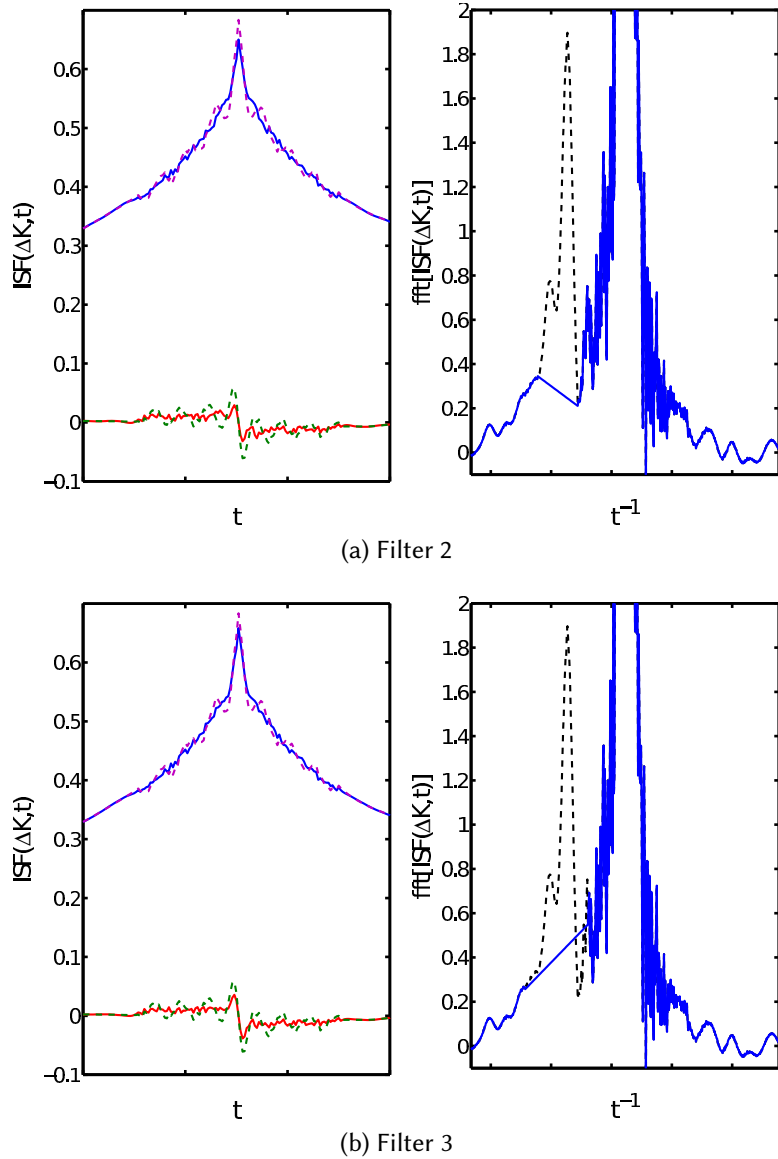


Figure D.2: The right hand sides of panel (a) and (b) show two different start and end points from the ‘standard’ shown in figure (b) with the dashed black line again showing the original data, and the blue line showing a section replaced with a linear interpolation between selected start and end points. The left hand sides of panels (a) and (b) show the real and imaginary parts of the inverse Fourier transforms of right hand spectra in blue and red respectively, by comparing the results of the different points used to select the peaks it is clear that a significant amount of the oscillating component of the ISF is removed in all cases with the resulting spectra relatively insensitive to the precise selection in the process.

UHV Ultra High Vacuum**ISF** Intermediate Scattering Function, $I(\Delta K, t)$ v $G(R, t)$ Pair correlation function $G(R, t)$ **$^3\text{HeSE}$** helium-3 Spin-echo 20**QHAS** Quasi-Elastic Helium Atom Scattering i**TOF** Time Of Flight 10**Xe** xenon i**Na** sodium**Li** lithium**Pt** platinum i**Pd** palladium 22**Cu** copper 24**LEED** Low Energy Electron Diffraction 22

TPD Temperature Programmed Desorption	
HAS Helium Atom Scattering	8
LITPD Laser Induced Temperature Programmed Desorption	28
LITD Laser Induced Thermal Desorption	
DFT Density Functional Theory	24
FWHM Full Width Half Maximum	48
STM Scanning Tunnelling Microscopy	3
AFM Atomic Force Microscopy.....	3
MD Molecular Dynamics	108
LE Langevin Equation	16
GLE Generalised Langevin Equation	17
RGA Residual Gas Analysis	30
PES Potential Energy Surface	59

fcc face centred cubic

hcp hexagonal close packed

rms root mean squared 17

References

- [1] H. Yang, J. Heo, S. Park, H. J. Song, D. H. Seo, K.-E. Byun, P. Kim, I. Yoo, H.-J. Chung & K. Kim. *Science* (New York, NY) **336** (2012)(6085), pp. 1140. doi:10.1126/science.1220527.
- [2] P. a. Pandey, G. R. Bell, J. P. Rourke, A. M. Sanchez, M. D. Elkin, B. J. Hickey & N. R. Wilson. *Small* (Weinheim an der Bergstrasse, Germany) **7** (2011)(22), pp. 3202. doi:10.1002/smll.201101430.
- [3] T. Ala-Nissila, R. Ferrando & S. C. Ying. *Advances in Physics* **51** (2002)(3), pp. 949. doi:10.1080/00018730110107902.
- [4] G. Antczak & G. Ehrlich. *Surface Diffusion: Metals, Metal Atoms, and Clusters*. Cambridge University Press, **2010**. ISBN 0521899834.
- [5] R. Gomer. *Reports on Progress in Physics* **53** (1990)(7), pp. 917. doi: 10.1088/0034-4885/53/7/002.
- [6] E. W. Müller. *Zeitschrift für Physik* (1938).
- [7] E. W. Muller. *Field Ion Microscopy*, vol. 160 of *Springer Series in Materials Science*. Springer New York, **1969**. ISBN 978-1-4614-3435-1.
- [8] D. Barredo, F. Calleja, P. Nieto, J. J. Hinarejos, G. Laurent, A. L. V. de Parga, D. Fariás & R. Miranda. *Advanced Materials* **20** (2008)(18), pp. 3492. doi: 10.1002/adma.200800866.
- [9] S. Hahne, J. Ikonomov, M. Sokolowski & P. Maass. *Physical Review B* **87** (2013)(8), p. 085409. doi:10.1103/PhysRevB.87.085409.

- [10] T. Kudernac, N. Ruangsapichat, M. Parschau, B. Maciá, N. Katsonis, S. R. Harutyunyan, K. Ernst & B. L. Feringa. *Nature* **479** (2011)(7372), pp. 208. doi: 10.1038/nature10587.
- [11] A. V. Akimov, C. Williams & A. B. Kolomeisky. *The Journal of Physical Chemistry C* **116** (2012)(25), pp. 13816. doi:10.1021/jp303549u.
- [12] I. Brihuega, a. Cano, M. Ugeda, J. Sáenz, a. Levanyuk & J. Gómez-Rodríguez. *Physical Review Letters* **98** (2007)(15), p. 156102. doi: 10.1103/PhysRevLett.98.156102.
- [13] A. P. Jardine, H. Hedgeland, G. Alexandrowicz, W. Allison & J. Ellis. *Progress in Surface Science* **84** (2009)(11-12), pp. 323. doi:10.1016/j.progsurf.2009.07.001.
- [14] P. R. Kole. *Dynamics and morphology of metal and metal oxide surfaces*. Ph.D. thesis, Cambridge University, **2011**.
- [15] K. L. Wong, B. V. Rao, G. Pawin, E. Ulin-Avila & L. Bartels. *The Journal of chemical physics* **123** (2005)(20), p. 201102. doi:10.1063/1.2124687.
- [16] I. Estermann & O. Stern. *Zeitschrift für Physik A Hadrons and Nuclei* **95** (1930)(15), pp. 95.
- [17] F. Knauer & O. Stern. *Zeitschrift für Physik* **53** (1929)(11-12), pp. 779. doi: 10.1007/BF01341278.
- [18] G. Bracco & B. Holst. *Surface Science Techniques*, **2013**. ISBN 978-3642342424.
- [19] D. Farias & K. Rieder. *Reports on Progress in Physics* **61** (1998)(12), pp. 1575. doi:10.1088/0034-4885/61/12/001.
- [20] E. Hulpke. *Helium Atom Scattering from Surfaces*, vol. 27 of *Springer Series in Surface Sciences*. Springer Berlin Heidelberg, Berlin, Heidelberg, **1992**. ISBN 978-3-642-08115-6. doi:10.1007/978-3-662-02774-5.
- [21] G. Comsa & K. Kern. *Advances in Chemical Physics* (1989).

- [22] B. Poelsema & G. Comsa. *Scattering of Thermal Energy Atoms*, vol. 115 of *Springer Tracts in Modern Physics*. Springer Berlin Heidelberg, **1989**. ISBN 978-3-540-50358-3. doi:10.1007/BFb0045229.
- [23] T. Engel & K. H. Rieder. In *Structural Studies of Surfaces SE - 2*, vol. 91 of *Springer Tracts in Modern Physics*, pp. 55–180. Springer Berlin Heidelberg, **1982**. ISBN 978-3-540-10964-8. doi:10.1007/BFb0041342.
URL <http://dx.doi.org/10.1007/BFb0041342>
- [24] G. Brusdeylins, R. Doak & J. Toennies. *Physical Review Letters* **46** (1981)(6), pp. 437.
- [25] A. P. Graham. *Surface Science Reports* **49** (2003)(4-5), pp. 115. doi: 10.1016/S0167-5729(03)00012-8.
- [26] D. A. McLaren. *Development of a Single Crystal Mirror for Scanning Helium Microscopy*. Ph.D. thesis, University of Cambridge, **2002**.
- [27] G. Vineyard. *Physical Review* **110** (1958)(5), pp. 999. doi: 10.1103/PhysRev.110.999.
- [28] L. Van Hove. *Phys Rev* **95** (1954)(1), pp. 249. doi:10.1103/PhysRev.95.249.
- [29] J. Ellis & J. P. Toennies. *Physical Review Letters* **70** (1993)(14), pp. 2118. doi: 10.1103/PhysRevLett.70.2118.
- [30] P. Fouquet, A. P. Jardine, S. Dworski, G. Alexandrowicz, W. Allison & J. Ellis. *Review of Scientific Instruments* **76** (2005)(5), p. 053109. doi:10.1063/1.1896945.
- [31] B. A. J. Lechner, H. Hedgeland, W. Allison, J. Ellis & A. P. Jardine. *The Review of scientific instruments* **84** (2013)(2), p. 026105. doi:10.1063/1.4791929.
- [32] A. P. Jardine, P. Fouquet, J. Ellis & W. Allison. *Review of Scientific Instruments* **72** (2001)(10), p. 3834. doi:10.1063/1.1405794.
- [33] J. M. Cowley. *Diffraction Physics*. Elsevier B.V., 1 ed., **1995**. ISBN 978-0-444-82218-5.

- [34] A. P. Jardine, G. Alexandrowicz, H. Hedgeland, W. Allison & J. Ellis. Physical chemistry chemical physics : PCCP **11** (2009)(18), pp. 3355. doi: 10.1039/b810769f.
- [35] R. Zwanzig. *Non equilibrium statistical mechanics*. Oxford University Press, **1991**. ISBN 0195140184.
- [36] P. Hänggi & P. Jung. Advances in chemical physics (1995).
- [37] J. L. Vega, R. Guantes & S. Miret-Artés. Journal of Physics: Condensed Matter **14** (2002)(24), pp. 6191. doi:10.1088/0953-8984/14/24/316.
- [38] Hansen J P. *Theory of simple liquids*. Elsevier Academic Press, London, 3rd ed ed., **2007**. ISBN 9780123705358.
- [39] M. Ceriotti, G. Bussi & M. Parrinello. Physical Review Letters **102** (2009)(2), pp. 1. doi:10.1103/PhysRevLett.102.020601.
- [40] R. Martínez-Casado, J. L. Vega, A. S. Sanz & S. Miret-Artés. Journal of Physics: Condensed Matter **19** (2007)(17), p. 176006. doi:10.1088/0953-8984/19/17/176006.
- [41] P. N. Pusey. Science (New York, NY) **332** (2011)(6031), pp. 802. doi: 10.1126/science.1192222.
- [42] C. Huang, G. Fratesi, D. A. MacLaren, W. Luo, G. P. Brivio & W. Allison. Physical Review B **82** (2010)(8), p. 081413. doi:10.1103/PhysRevB.82.081413.
- [43] M. Ceriotti, G. Bussi & M. Parrinello. Journal of Chemical Theory and Computation **6** (2010)(4), pp. 1170. doi:10.1021/ct900563s.
- [44] B. Girod. *Signals and systems*. John Wiley & Sons, Chichester, **2001**. ISBN 0471988006.
- [45] R. Martínez-Casado, A. S. Sanz, J. L. Vega, G. Rojas-Lorenzo & S. Miret-Artés. Chemical Physics **370** (2009)(1-3), p. 40. doi:10.1016/j.chemphys.2010.02.013.

- [46] P. R. Kole, H. Hedgeland, A. P. Jardine, W. Allison, J. Ellis & G. Alexandrowicz. *Journal of physics Condensed matter : an Institute of Physics journal* **24** (2012)(10), p. 104016. doi:10.1088/0953-8984/24/10/104016.
- [47] H. Hedgeland, P. Fouquet, A. P. Jardine, G. Alexandrowicz, W. Allison & J. Ellis. *Nature Physics* **5** (2009)(8), pp. 561. doi:10.1038/nphys1335.
- [48] H. Hedgeland, P. R. Kole, H. Davies, A. P. Jardine, G. Alexandrowicz, W. Allison, J. Ellis, G. Fratesi & G. Brivio. *Physical Review B* **80** (2009)(12), p. 125426. doi: 10.1103/PhysRevB.80.125426.
- [49] A. P. Jardine, G. Alexandrowicz, H. Hedgeland, R. D. Diehl, W. Allison & J. Ellis. *Journal of Physics: Condensed Matter* **19** (2007)(30), p. 305010. doi: 10.1088/0953-8984/19/30/305010.
- [50] G. Alexandrowicz, A. P. Jardine, H. Hedgeland, W. Allison & J. Ellis. *Physical Review Letters* **97** (2006)(15), pp. 156103. doi:10.1103/PhysRevLett.97.156103.
- [51] G. Alexandrowicz, A. P. Jardine, P. Fouquet, S. Dworski, W. Allison & J. Ellis. *Physical Review Letters* **93** (2004)(15), pp. 156103. doi: 10.1103/PhysRevLett.93.156103.
- [52] I. Langmuir. *Journal of the American Chemical Society* **345** (1918)(1914). doi: 10.1021/ja02242a004.
- [53] J. D. Silva, C. Stampfl & M. Scheffler. *Physical Review B* **72** (2005)(7), pp. 075424. doi:10.1103/PhysRevB.72.075424.
- [54] J. Ellis, A. P. Graham & J. P. Toennies. *Physical Review Letters* **82** (1999)(25), pp. 5072. doi:10.1103/PhysRevLett.82.5072.
- [55] G. Vidali, G. Ihm, H. Kim & M. W. Cole. *Surface Science Reports* **12** (1991)(4), pp. 135. doi:10.1016/0167-5729(91)90012-M.
- [56] G. Hilgers, M. Potthoff, S. Wirth, N. Müller, U. Heinzmann, L. Haunert, J. Braun & G. Borstel. *Surface Science* **251-252** (1991), pp. 612. doi: 10.1016/0039-6028(91)91065-6.

- [57] G. Hilgers, M. Potthoff, N. Müller & U. Heinzmann. *Surface Science* **322** (1995)(1-3), pp. 207. doi:10.1016/0039-6028(95)90031-4.
- [58] J. Gottlieb. *Physical Review B* **42** (1990)(8), pp. 5377. doi:10.1103/PhysRevB.42.5377.
- [59] J. Gottlieb & L. W. Bruch. *Physical Review B* **44** (1991)(11), pp. 5759. doi:10.1103/PhysRevB.44.5759.
- [60] J. Black & A. Janzen. *Surface Science* **217** (1989)(1-2), pp. 199. doi:10.1016/0039-6028(89)90544-X.
- [61] J. A. Barker & C. T. Rettner. *The Journal of Chemical Physics* **97** (1992)(8), p. 5844. doi:10.1063/1.463743.
- [62] T. Seyller. *Chemical Physics Letters* **291** (1998)(5-6), pp. 567. doi:10.1016/S0009-2614(98)00622-8.
- [63] T. Seyller, M. Caragiu, R. D. Diehl, P. Kaukasoina & M. Lindroos. *Physical Review B* **60** (1999)(15), pp. 11084. doi:10.1103/PhysRevB.60.11084.
- [64] M. Caragiu, T. Seyller & R. D. Diehl. *Physical Review B* **66** (2002)(19), pp. 1. doi:10.1103/PhysRevB.66.195411.
- [65] B. Narloch. *Chemical Physics Letters* **270** (1997)(1-2), pp. 163. doi:10.1016/S0009-2614(97)00327-8.
- [66] P. Zeppenfeld, G. Comsa & J. Barker. *Physical Review B* **46** (1992)(14).
- [67] S. Horch, P. Zeppenfeld & G. Comsa. *Applied Physics A Materials Science and Processing* **60** (1995)(2), pp. 147. doi:10.1007/BF01538240.
- [68] A. E. Betancourt & D. M. Bird. *Journal of physics Condensed matter* **7077** (2000), pp. 7077. doi:10.1088/0953-8984/12/31/309.
- [69] J. C. Tully. *The Journal of Chemical Physics* **73** (1980)(4), p. 1975. doi:10.1063/1.440287.

- [70] L. W. Bruch, R. D. Diehl & J. Venables. *Reviews of Modern Physics* **79** (2007)(4), pp. 1381. doi:10.1103/RevModPhys.79.1381.
- [71] P. Lazić, v. Crljen, R. Brako & B. Gumhalter. *Physical Review B* **72** (2005)(24), pp. 245407. doi:10.1103/PhysRevB.72.245407.
- [72] D.-L. Chen, W. Al-Saidi & J. Johnson. *Physical Review B* **84** (2011)(24). doi:10.1103/PhysRevB.84.241405.
- [73] K. Kern. *Surface Science* **195** (1988)(3), pp. 353. doi:10.1016/0039-6028(88)90347-0.
- [74] K. Kern, R. David, R. Palmer & G. Comsa. *Surface Science* **175** (1986)(1), pp. L669. doi:10.1016/0039-6028(86)90072-5.
- [75] K. Kern. *Solid State Communications* **62** (1987)(6), pp. 391. doi:10.1016/0038-1098(87)91040-4.
- [76] K. Kern, P. Zeppenfeld, R. David & G. Comsa. *Physical Review B* **35** (1987)(2), pp. 886. doi:10.1103/PhysRevB.35.886.
- [77] B. Poelsema, L. Verheij & G. Comsa. *Surface Science* **152-153** (1985)(Part 2), pp. 851. doi:10.1016/0039-6028(85)90496-0.
- [78] F. Brunet. *Surface Science* **512** (2002)(3), pp. 201. doi:10.1016/S0039-6028(02)01518-2.
- [79] D. L. Meixner & S. M. George. *The Journal of Chemical Physics* **98** (1993)(11), p. 9115. doi:10.1063/1.464419.
- [80] L. W. Bruch, A. P. Graham & J. P. Toennies. *Molecular Physics* **95** (1998)(3), pp. 579. doi:10.1080/00268979809483191.
- [81] A. P. Jardine, J. Ellis & W. Allison. *The Journal of chemical physics* **120** (2004)(18), pp. 8724. doi:10.1063/1.1695320.
- [82] D. Sholl & R. Skodje. *Physical Review Letters* **75** (1995)(17), pp. 3158. doi:10.1103/PhysRevLett.75.3158.

- [83] *Manual on the Use of Thermocouples in Temperature Measurement*. ASTM International, **1993**. ISBN 0803114664.
- [84] B. Poelsema, L. Verheij & G. Comsa. Physical Review Letters **51** (1983)(26), pp. 2410. doi:10.1103/PhysRevLett.51.2410.
- [85] P. A. Redhead. Vacuum (1962)(June), pp. 203.
- [86] D. L. Meixner & S. M. George. Surface Science **297** (1993)(1), pp. 27. doi: 10.1016/0039-6028(93)90012-9.
- [87] A. P. J. Jansen. The Journal of Chemical Physics **97** (1992)(7), p. 5205. doi: 10.1063/1.463819.
- [88] J. L. Vega, R. Guantes & S. Miret-Artés. Journal of Physics: Condensed Matter **16** (2004)(29), pp. S2879. doi:10.1088/0953-8984/16/29/003.
- [89] B. A. J. Lechner. *Studying complex surface dynamical systems using helium-3 spin-echo spectroscopy*. Ph.D. thesis, Cambridge University, **2012**.
- [90] C. T. Chudley & R. J. Elliott. Proceedings of the Physical Society **77** (1961)(2), pp. 353. doi:10.1088/0370-1328/77/2/319.
- [91] P. Degennes. Physica **25** (1959)(7-12), pp. 825. doi:10.1016/0031-8914(59)90006-0.
- [92] K. Connors. *Chemical Kinetics*. VCH Publishers, **1990**.
- [93] R. Arrhenius. *No Title*. Ph.D. thesis, **1899**.
- [94] G. Uhlenbeck & L. Ornstein. Physical Review **36** (1930)(5), pp. 823. doi: 10.1103/PhysRev.36.823.
- [95] P. Langevin. Comptes Rendus de l'Académie des Sciences **146** (1908), pp. 530.
- [96] H. Kramers. Physica **7** (1940)(4), pp. 284. doi:10.1016/S0031-8914(40)90098-2.
- [97] C. E. Shannon. PROCEEDINGS OF THE IRE (1949), pp. 10.

- [98] H. Hedgeland, B. A. J. Lechner, F. E. Tuddenham, A. P. Jardine, W. Allison, J. Ellis, M. Sacchi, S. J. Jenkins & B. J. Hinch. *Physical Review Letters* **106** (2011)(18), p. 186101. doi:10.1103/PhysRevLett.106.186101.
- [99] F. E. Tuddenham. *Helium atom scattering as a probe of hydrogen adsorption and dynamics*. Ph.D. thesis, **2011**.
- [100] S. Paterson, C. J. Aas & A. P. Jardine. *Surface Science* **606** (2012)(3-4), pp. 426. doi:10.1016/j.susc.2011.11.003.
- [101] S. Paterson. *Elucidating surface dynamics in systems of atomic and molecular adsorbates*. Ph.D. thesis, Cambridge University, **2012**.
- [102] S. Paterson, W. Allison, H. Hedgeland, J. Ellis & A. P. Jardine. *Physical Review Letters* **106** (2011)(25), pp. 1. doi:10.1103/PhysRevLett.106.256101.
- [103] E. M. McIntosh. *Adsorption and dynamics of interacting surface systems*. Ph.D. thesis, **2013**.
- [104] D. J. Ward. *Measuring the Diffusion of Sub-Monolayer Xe on Pt (111) - developing the Cambridge 3 He SpinEcho spectrometer for fourier analysis*. First year report, Cambridge University, **2010**.
- [105] J. W. Doeberiner. *Annalen der Physik und Chemie* **140** (1845)(1), pp. 94. doi: 10.1002/andp.18451400110.
- [106] G. Ertl, M. Weiss & S. Lee. *Chemical Physics Letters* **60** (1979)(3), pp. 391. doi:10.1016/0009-2614(79)80595-3.
- [107] G. Ertl. *Catalysis Reviews* **21** (1980)(2), pp. 201. doi: 10.1080/03602458008067533.
- [108] G. Ertl. *Zeitschrift für anorganische und allgemeine Chemie* **638** (2012)(3-4), pp. 487. doi:10.1002/zaac.201190458.
- [109] W. D. Mross. *Catalysis Reviews* **25** (1983)(4), pp. 591. doi: 10.1080/01614948308078057.
- [110] R. D. Diehl & R. McGrath. *Journal of Physics: Condensed Matter* **951** (1999).

- [111] R. D. Diehl & R. McGrath. *Surface Science Reports* **23** (1996)(2-5), pp. 43. doi:10.1016/0167-5729(95)00010-0.
- [112] R. Gurney. *Physical Review* **47** (1935)(6), pp. 479. doi:10.1103/PhysRev.47.479.
- [113] T. Aruga. *Progress in Surface Science* **31** (1989)(1-2), pp. 61. doi:10.1016/0079-6816(89)90013-0.
- [114] P. Fouquet & G. Witte. *Physical Review Letters* **83** (1999)(2), pp. 360. doi:10.1103/PhysRevLett.83.360.
- [115] G. Fratesi, G. Alexandrowicz, M. I. Trioni, G. P. Brivio & W. Allison. *Physical Review B* **77** (2008)(23), p. 235444. doi:10.1103/PhysRevB.77.235444.
- [116] G. Fratesi. *Physical Review B* **80** (2009)(4), p. 045422. doi:10.1103/PhysRevB.80.045422.
- [117] X. Shi, D. Tang, D. Heskett, K. Tsuei, H. Ishida & Y. Morikawa. *Surface Science* **290** (1993)(1-2), pp. 69. doi:10.1016/0039-6028(93)90589-C.
- [118] D. Tang, D. Mcilroy, X. Shi, C. Su & D. Heskett. *Surface Science* **255** (1991)(1-2), pp. L497. doi:10.1016/0039-6028(91)90002-A.
- [119] S. Borisova, G. Rusina, S. Eremeev, G. Benedek, P. Echenique, I. Sklyadneva & E. Chulkov. *Physical Review B* **74** (2006)(16), p. 165412. doi:10.1103/PhysRevB.74.165412.
- [120] Saes Getters. *Alkali Metal Dispensers*. 1 ed., **2009**.
- [121] A. Carlsson, S. Lindgren, C. Svensson & L. Wallden. *Physical Review B* **50** (1994)(12), pp. 8926.
- [122] G. Witte. *Journal of Physics: Condensed Matter* **16** (2004)(29), pp. S2937. doi:10.1088/0953-8984/16/29/009.
- [123] J. Ellis & A. P. Graham. *Surface Science* **377-379** (1997), pp. 833. doi:10.1016/S0039-6028(96)01514-2.

- [124] J. Ellis, A. P. Graham, F. Hofmann & J. P. Toennies. *Physical Review B* **63** (2001)(19), pp. 1. doi:10.1103/PhysRevB.63.195408.
- [125] P. Fouquet & G. Witte. *Applied surface science* **180** (2001), pp. 286.
- [126] R. Kubo. *Reports on Progress in Physics* **29** (1966)(1), pp. 255. doi:10.1088/0034-4885/29/1/306.
- [127] W. Kohn & K. Lau. *Solid State Communications* **18** (1976)(5), pp. 553. doi:10.1016/0038-1098(76)91479-4.
- [128] J. Topping. *Proceedings of the Royal Society A: Mathematical, Physical and Engineering Sciences* **114** (1927)(766), pp. 67. doi:10.1098/rspa.1927.0025.
- [129] N. Fischer, S. Schuppler, T. Fauster & W. Steinmann. *Surface Science* **314** (1994)(1), pp. 89. doi:10.1016/0039-6028(94)90215-1.
- [130] A. P. Jardine, J. Ellis & W. Allison. *Journal of Physics: Condensed Matter* **14** (2002)(24), pp. 6173. doi:10.1088/0953-8984/14/24/315.
- [131] R. Martínez-Casado, A. S. Sanz & S. Miret-Artés. *The Journal of chemical physics* **129** (2008)(18), p. 184704. doi:10.1063/1.3009624.
- [132] G. Vandegrift & B. Fultz. *American Journal of Physics* **66** (1998)(7), p. 593. doi:10.1119/1.18911.
- [133] A. M. Lahee, J. R. Manson, J. P. Toennies & C. Wołłii. *The Journal of Chemical Physics* **86** (1987)(12), p. 7194. doi:10.1063/1.452321.
- [134] S. Mizuno, H. Tochihara, A. Barbieri & M. V. Hove. *Physical Review B* **51** (1995)(12), pp. 7981.
- [135] A. Carlsson, D. Claesson & G. Katrich. *Physical Review B* **57** (1998)(20), pp. 192.
- [136] S. Lindgren, C. Svensson, L. Walldén, a. Carlsson & E. Wahlström. *Physical review B, Condensed matter* **54** (1996)(15), pp. 10912.
- [137] L. Padilla-Campos & A. Toro-Labbé. *Journal of Molecular Structure: ...* (1997).

- [138] J. Neugebauer & M. Scheffler. Physical Review B **46** (1992)(24), pp. 16067. doi:10.1103/PhysRevB.46.16067.
- [139] F. E. Tuddenham, H. Hedgeland, A. P. Jardine, B. A. J. Lechner, B. J. Hinch & W. Allison. Surface Science **604** (2010)(17-18), pp. 1459. doi: 10.1016/j.susc.2010.05.009.
- [140] D. Gordon, V. Krishnamurthy & S.-H. Chung. The Journal of chemical physics **131** (2009)(13), p. 134102. doi:10.1063/1.3233945.
- [141] M. Ceriotti, D. E. Manolopoulos & M. Parrinello. The Journal of chemical physics **134** (2011)(8), p. 084104. doi:10.1063/1.3556661.
- [142] M. Ceriotti. *A novel framework for enhanced molecular dynamics based on the generalized Langevin equation* Presented by. Ph.D. thesis.
- [143] P. R. Kole, A. P. Jardine, H. Hedgeland & G. Alexandrowicz. Journal of Physics: Condensed Matter **22** (2010)(30), p. 304018. doi:10.1088/0953-8984/22/30/304018.
- [144] B. Persson, E. Tosatti, D. Fuhrmann, G. Witte & C. Wöll. Physical Review B **59** (1999)(18), pp. 11777. doi:10.1103/PhysRevB.59.11777.
- [145] P. S. Laplace. *Théorie analytique des probabilités*. Courcier, **1812**.